Employment of semi-rigid *N*-donor ligands towards the synthesis of functional coordination polymers with low dimensionality

Edouardos Loukopoulos

Submitted for degree of Doctor of Philosophy

University of Sussex

August 2018

DECLARATION

This thesis conforms to an 'article format' in which Chapters 1 (in part), 2-6 consist of discrete articles written in a style that is appropriate for publication in peer-reviewed journals in the field. The remaining parts of Chapter 1 present discussion of the field related to this work and include currently unpublished content. Chapter 7 summarizes the results of the previous chapters and proposes future work directions based on preliminary investigations; it is therefore not written in an article format. Chapters 8 and 9 include all synthetic overviews and crystallographic data presented in this work.

Parts of **Chapter 1** (Sections 1.1.1 and 1.1.4) are published as a review in *Journal of Coordination Chemistry* as:

"Recent advances of one-dimensional coordination polymers as catalysts"
E. Loukopoulos, G. E. Kostakis, *J. Coord. Chem.*, **2018**, 71, 371.

The author contributions are as follows: E. Loukopoulos (E.L.) was responsible for all aspects of literature reviewing and writing of the manuscript. G. E. Kostakis (G.E.K.) was responsible for providing feedback and corrections to the manuscript.

Chapter 2 is published in *Crystal Growth and Design* as:

"Exploring the Coordination Capabilities of a Family of Flexible Benzotriazole-Based Ligands Using Cobalt(II) Sources"
E. Loukopoulos, N. F. Chilton, A. Abdul-Sada, G. E. Kostakis,
Cryst. Growth Des., **2017**, *17*, 2718

The author contributions are as follows: E.L. was responsible for the synthesis and characterisation of the compounds. N. F. Chilton (N.F.C.) was responsible for the collection and interpretation of magnetic data. A. Abdul-Sada (A.A-S) was responsible for the

collection of ESI-MS data. E.L and G.E.K. were collectively responsible for the initial conception of the research and the writing of the paper.

Chapter 3 is published in *Advanced Synthesis and Catalysis* as:

"A Copper-Benzotriazole-Based Coordination Polymer Catalyzes the Efficient One-Pot Synthesis of (N'-Substituted)-hydrazo-4-aryl-1,4-dihydropyridines from Azines"

E. Loukopoulos[*], M. Kallitsakis[*], A. Abdul-Sada, G. J. Tizzard, S. J. Coles, G. E. Kostakis, I. N. Lykakis, *Adv. Synth. Cat*., **2017**, 359, 138.

([*] notes equal contribution)

The author contributions are as follows: E.L. was responsible for the synthesis and characterisation of all coordination compounds as well as crystallization of all reported products. M. Kallitsakis (M.K.) was responsible for the development of catalytic protocols. E.L. and M.K. were responsible for all catalytic studies. A.A-S was responsible for the collection of ESI-MS data. G. J. Tizzard (G.J.T.) and S. J. Coles (S.J.C.) were responsible for the collection of some crystallographic data. I. N. Lykakis (I.N.L.) was responsible for the design of the synthetic method towards dihydropyridines. E.L, M.K., I.N.L. and G.E.K. were collectively responsible for the initial conception of the research and the writing of the paper.

Chapter 4 is published in *Inorganic Chemistry* as:

"Cu(II) Coordination Polymers as Vehicles in the A^3 Coupling"

E. Loukopoulos, M. Kallitsakis, N. Tsoureas, A. Abdul-Sada, N. F. Chilton, I. N. Lykakis, G. E. Kostakis, *Inorg. Chem.*, **2017**, 56, 4898.

The author contributions are as follows: E.L. was responsible for the synthesis and characterisation of the compounds, development of the catalytic protocols and catalytic

studies. M.K. was responsible for providing feedback during the development of the catalytic protocols and catalytic studies. N. Tsoureas was responsible for the collection and interpretation of cyclic voltammetry data. A.A-S was responsible for the collection of ESI-MS data. N.F.C. was responsible for the collection and interpretation of magnetic data. I.N.L. was responsible for providing feedback to the manuscript. E.L and G.E.K. were collectively responsible for the initial conception of the research and the writing of the paper.

Chapter 5 is published in *Dalton Transactions* as:

"Copper(II)-benzotriazole coordination compounds in click chemistry: A diagnostic reactivity study"

E. Loukopoulos, A. Abdul-Sada, G. Csire, C. Kallay, A. Brookfield, G. J. Tizzard, S. J. Coles, I. N. Lykakis, G. E. Kostakis, *Dalton Trans.*, **2018**, 47, 10491.

The author contributions are as follows: E.L. was responsible for the synthesis and characterisation of the compounds, development of the catalytic protocols and catalytic studies. A.A-S was responsible for the collection of ESI-MS data. G. Csire and C. Kallay were collectively responsible for the collection and interpretation of cyclic voltammetry data. A. Brookfield was responsible for the collection and interpretation of EPR data. G.J.T. and S.J.C. were responsible for the collection of some crystallographic data. I.N.L. was responsible for providing feedback to the manuscript. E.L and G.E.K. were collectively responsible for the initial conception of the research and the writing of the paper.

Chapter 6 has been accepted for publication to *Crystal Growth and Design* as:

"Structural diversity and catalytic properties in a family of Ag(I)-benzotriazole based coordination compounds"

E. Loukopoulos, A. Abdul-Sada, E. M. E. Viseux, I. N. Lykakis, G. E. Kostakis, *Cryst. Growth Des.*, **2018**, 18, 5638.

The author contributions are as follows: E.L. was responsible for the synthesis and characterisation of the compounds, development of the catalytic protocols and catalytic studies. A.A-S was responsible for the collection of ESI-MS data. E. M. E. Viseux was responsible for providing feedback on the alkyne hydration reaction and on the manuscript. I.N.L. was responsible for providing feedback to the manuscript. E.L and G.E.K. were collectively responsible for the initial conception of the research and the writing of the paper.

I hereby declare that this thesis has not been and will not be, submitted in whole or in part to another University for the award of any other degree.

Signature:

ACKNOWLEDGEMENTS

Firstly, I would like to thank Dr George E. Kostakis for giving me the opportunity to join his group, and for his invaluable guidance and support throughout these years. I would also like to thank the University of Sussex and the EPSRC for funding my PhD, and Prof. Vassilios Nastopoulos, as I would not have been able to start this PhD without his help and support.

I am eternally grateful to all project collaborators who provided me with important measurements and feedback that made this thesis possible. Many thanks to Dr Ioannis Lykakis (University of Thessaloniki), for his critical insight in organic chemistry and catalysis, and the members of his group for our collaboration in various catalysis projects. I would like to thank Dr Graham Tizzard and Dr Simon J Coles (University of Southampton) for their invaluable help with the more difficult crystal stuctures. I am also grateful to Dr Alaa Abdul-Sada, for performing all ESI-MS measurements and providing important advice, and Dr Nikolaos Tsoureas for cyclic voltammetry measurements and many helpful discussions. Many thanks to Dr Nicholas Chilton and Adam Brookfield (University of Manchester), for performing magnetic and EPR studies reported in this thesis. I would also like to thank Dr Csilla Kállay and Gizella Csire (University of Debrecen) who provided additional cyclic voltammetry measurements. The help of Prof. Anastasios Tasiopoulos (University of Cyprus, PXRD measurements) and Dr Stephen Boyer (London Metropolitan University, Elemental Analysis measurements) is also hugely acknowledged. I also thank Dr Iain Day for feedback and advice on NMR spectra and Dr Eddy Viseux for helpful discussions and advice on silver chemistry. Finally, a big thank you to Mick and Fran for allowing me to work in their lab during my first year.

I would also like to thank Stavroula, James, Magda, Joe, Adam and all other past and present members of Lab 10 and 5th floor Offices, for all the good times we had during these years. Special thanks to Alexia and Michael for being great colleagues and greater friends. I would also like to thank John and Bernadette for their constant support and for making me feel like home. Many thanks to my friends and fellow PhD candidates Vassilis and Helen for their support and pain-sharing discussions. I am also grateful to Olympia for her love, endless support, patience, food and knitwear. Above all, I would like to thank my mother Sharon, my brother Pano, my sister Evie and my nephew Kosmas for always being there for me.

ABSTRACT

The focus of this thesis is the design of low-dimensional coordination polymers (CPs) using semi-rigid *N*-donor ligands based on heterocyclic molecules, especially benzotriazole, and the investigation of their potential magnetic and catalytic properties.

Chapter 1 serves as a general introduction to the chemistry discussed in the thesis. The first part emphasizes on the synthetic aspects and applications of CPs. The second part presents the unique chemical characteristics of benzotriazole and includes a thorough literature review on its use as a ligand in coordination chemistry, culminating to the development of a ligand system for the design of the targeted materials.

Chapter 2 introduces the main family of benzotriazole-based ligands (**L^1-L^3**) employed in this thesis, focusing on their coordination chemistry with cobalt salts. The synthesis and characterisation of a series of novel 0D, 1D and 2D compounds with a large structural variety is reported. Synthetic aspects and magnetic properties of selected compounds are discussed.

Chapters 3, **4** and **5** report a series of copper coordination compounds employing **L^1-L^3** as well as analogous *N*-donor ligands (**L^4-L^8**). A system of 1D CPs is established and investigated for its catalytic properties in a range of organic transformations that includes the synthesis of 1,4-dihydropyridines through a previously unreported route, the A^3 coupling and the 'click' azide-alkyne cycloaddition reaction. Investigations into optimising the catalytic behaviour and mechanistic aspects of this system are presented.

In **Chapter 6** the coordination capabilities of **L^1-L^3** are combined with the rich chemistry of silver salts to generate a structurally diverse family of 0D, 1D and 2D compounds. Investigations of their potential catalytic properties in the A^3 coupling and alkyne hydration reactions are additionally presented.

Chapter 7 provides an overall conclusion to the work presented in the thesis, including its contributions to the reported literature as well as potential future directions. Finally, experimental and synthetic details as well as crystallographic data are presented in **Chapter 8** and **Chapter 9** respectively.

LIST OF ABBREVIATIONS

0D	zero-dimensional
1,4-DHP	1,4-dihydropyridine
1D	one-dimensional
2D	two-dimensional
3D	three-dimensional
Å	Angström
Ac	acetate
acac	acetylacetonate
atm	atmosphere
bbdp	bis(benzotriazol-1-yl)-1,3-dioxapropane
bbtm	bis(benzotriazol-1-yl)methane
bipy	4,4´-bipyridine
btc	benzene-1,3,5- tricarboxylate
BTP	2H-benzotriazol-2-yl phenolate
^{C1DMe}IBTPH	2-(2H-benzotriazol-2-yl)-6-(((2,6-dimethylphenyl)imino)methyl)-4-methylphenol
^{C8}BTPH	2-(2H-benzotriazol-2-yl)-4-(2,4,4-trimethylpentan-2-yl)phenol
ClbtaH	5-chlorobenzotriazole
CP	coordination polymer
Cp	cyclopentadienyl
CSD	Cambridge Structural Database
CV	Cyclic Voltammetry
D	axial anisotropy component
DCE	1,2-dichloroethane
DCM	dichloromethane
D-H_2cam	D-camphoric acid
DMAD	dimethyl acetylenedicarboxylate
DMF	*N*,*N*-dimethylformamide
DMSO	dimethylsulfoxide

E	rhombic anisotropy component
E	*trans or anti*
EA	Elemental Analysis
ee	enantiomeric excess
EPR	Electron Paramagnetic Resonance
ESI-MS	electrospray ionization mass spectrometry
Et	ethyl
Et_3N	triethylamine
EtOH	ethanol
FTIR	Fourier-Transform Infrared Spectroscopy
g	grams
H	magnetic field
h/hr	hour
H_2abdc	2-amino-1,4-benzenedicarboxylic acid
H_2aipa	5-acetamidoisophthalic acid
H_2apa	adipic acid
H_2bdc	1,4-benzenedicarboxylic acid
H_2bpdc	4,4´-biphenyldicarboxylic acid
H_2btca	benzotriazole-5-carboxylic acid
H_2cdc	1,4-cyclohexanedicarboxylic acid
H_2gta	glutaric acid
H_2ina	isonicotinic acid
H_2ipa	isophthalic acid
H_2mbdc	1,3-benzenedicarboxylic acid
H_2ndc	1,4-naphthalenedicarboxylic acid
H_2sdba	4,4´-dicarboxybiphenyl sulfone
H_2tma	benzene-1,3,5-tricarboxylic acid
H_3bpt	biphenyl-3,4',5-tricarboxylic acid
H_3ccb	3-(carboxymethyl-amino)-4-chlorobenzoic acid
H_3cia	*N*-(4-carboxybenzyl) iminodiacetic acid
H_3oadbc	5-oxyacetatoisophthalic acid

H_3qbtcb	4,4′,4′′-[1,3,5-benzenetriyltris(carbonylimino)]tris(benzoate)
H_3tbtcb	3,3′,3′′-[1,3,5-benzenetriyltris(carbonylimino)]tris(benzoate)
H_3tea	triethanolamine
H_4bced	N,N′-bis(4-carboxysalicylidene)ethylenediamine
H_4pdada	4,4′-((pyridine-2,6-dicarbonyl)bis(azanediyl))dibenzoic acid
H_4pma	pyromellitic acid
HA-1,4-DHPs	*N*′-substituted-hydrazo-4-aryl-1,4-DHPs
Hbta	benzotriazole
Hhpp	(S)-3-hydroxy-2-(pyridine-4-ylmethylamino)propanoic acid
HRMS	high resolution mass spectrometry
ibta	1-(1H-benzotriazol-1-yl)isoquinoline
iPrOH	2-propanol
J	exchange coupling constant
K	Kelvin
L	ligand
lac	lactate
M	magnetization
M	metal
M.W.	microwave
MCR	multicomponent reaction
Me	methyl
Me_2btaH	5,6-dimethylbenzotriazole
Me_2CO	acetone
MebtaH	5-methylbenzotriazole
MeCN	acetonitrile
MeOH	methanol
mg	milli-gram
min	minute
mL	milli-litre
mmol	milli-mole
MOF	metal–organic framework

NMR	Nuclear Magnetic Resonance
^{o}	degrees (angles)
^{o}C	degrees Celsius
OMe_2btaH	5,6-dimethoxybenzotriazole
OTf	triflate
pbta	1-(pyridin-2-yl)-1H-benzotriazole
pmbta	1-(pyridin-2-ylmethyl)-1H-benzotriazole
PXRD	Powder X-Ray Diffraction
pybz	4-pyridyl benzoate
ROP	ring-opening polymerization
rt	room temperature
salen	*N*,*N*´-Ethylenebis(salicylimine)
SET	single electron transfer
SMM	single-molecule magnet
SQUID	Superconducting Quantum Interference Device
TBHP	*tert*-Butyl hydroperoxide
T_c	Curie temperature
TCNQ	7,7,8,8-tetracyano-p-quinodimethane
TGA	Thermogravimetric Analysis
THF	tetrahydrofuran
TMB	1,2,3-trimethoxybenzene
^{TMCl}BTPH	2-tert-butyl-6-(5-chloro-2Hbenzotriazol-2-yl)-4-methylphenol
TMSCN	trimethylsilyl cyanide
T_N	Néel temperature
TOF	turnover frequency
TON	turnover number
tpb	*N*,*N*,*N*-tris(3-pyridinyl)-1,3,5-benzenetricarboxamide
tpdc	p-terphenyl-4,4″-dicarboxylate
tppz	2,3,5,6-tetrakis(2-pyridyl)pyrazine
UV-Vis	ultraviolet–visible spectroscopy
Z	*cis* or *syn*

ZFS	Zero-Field Splitting
μL	micro-litre
τ	structural parameter
χ	magnetic susceptibility
χ_M	molar magnetic susceptibility

Abbreviations in NMR spectroscopic data

d	doublet
dd	doublet of doublets
Hz	hertz
Jx	coupling constant over x bonds
m	multiplet
MHz	megahertz
ppm	parts per million
q	quartet
s	singlet
t	triplet
δ	chemical shift in ppm

Abbreviations in FT-IR data

br	broad
m	medium
s	strong
w	weak

TABLE OF CONTENTS

Chapter 1: General Introduction

1.1. Coordination Polymers

1.1.1. Classifications and Brief History

Throughout the numerous amount of studies performed in the fields of Inorganic and Coordination Chemistry during the last 50 years, research on Coordination Polymers (CPs) holds a leading position. CPs are infinite, hybrid organic-inorganic compounds; they are constructed from metal centres linked to each other via organic ligands (linkers) through coordination bonds, thus forming structures that extend into one, two or three dimensions[1,2] (Scheme 1.1). Metal-Organic Frameworks (MOFs), a term popularized by Yaghi *et al*. in 1995[3,4], refers to compounds also included in this class. They may be defined as high-dimensional porous CPs that are capable of including guest species within their cavities.

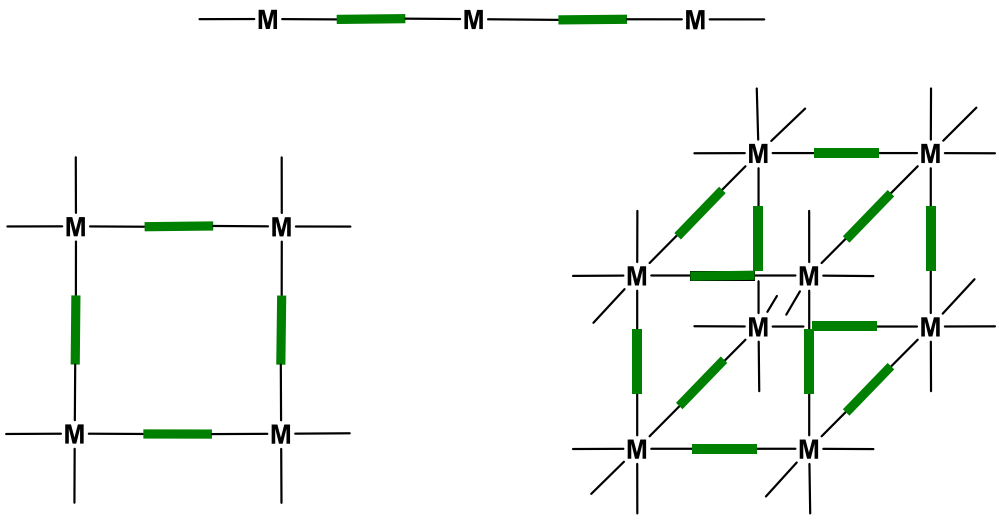

Scheme 1.1. A schematic representation of one-, two- and three-dimensional coordination polymers.

While the term of "coordination polymer" has been regularly used in scientific reports since the 1950s[5], interest in this field exploded rapidly in the early 1990s (Scheme 1.2) when Robson and others published a series of papers[6–11] proposing a design approach towards CPs with targeted structures. The development of this concept was further aided by the rising

growth of crystal engineering, which concerns the study and understanding of intermolecular interactions (eg. hydrogen bonds, halogen bonds, π···π interactions etc.) in a crystal structure, towards the design of new molecules with desired applications[12–14]. These concepts have been widely used for the production of CPs ever since[15]: synthetic variables such as ligand and metal source selection, or experimental conditions (e.g., solvent, temperature) may be controlled and manipulated to afford polymeric compounds with the desired shape and dimensionality, and most importantly the desired applications. The most important of these aspects will be further discussed in the following section.

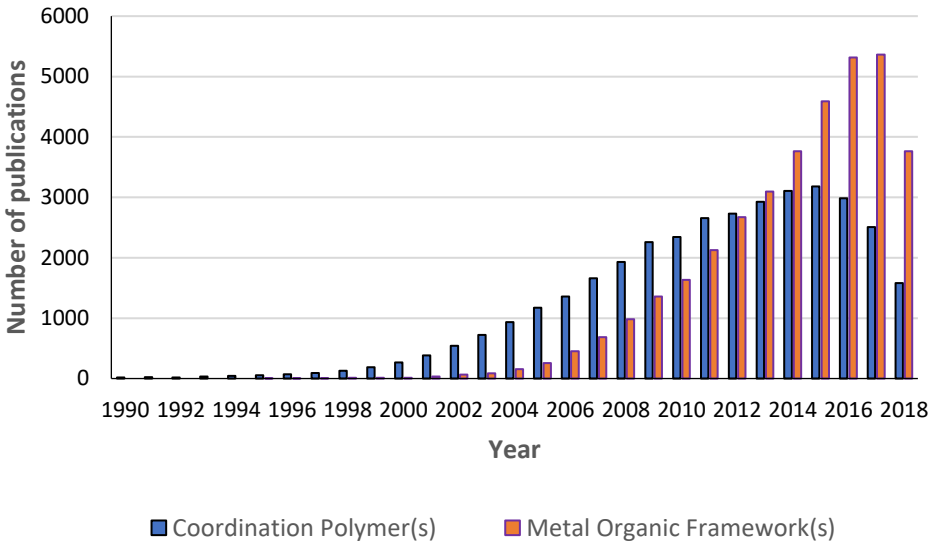

Scheme 1.2. Number of publications per year on the topics of "coordination polymer(s)" or "metal organic framework(s)". Based on a Web of Science search (June 2018).

1.1.2. Synthetic Aspects of Coordination Polymers

When approaching the design of CPs/MOFs, the initial step involves the choice of appropriate organic linker(s) and metallic sources. The following subsections will explore the plethora of options available for both of these parameters.

1.1.2.1. Ligand Selection

1.1.2.1.1. Rigid Ligands

During the emergence of MOFs and rational design concepts rigid organic linkers with a fixed geometry quickly became the popular choice amongst researchers. In particular, several studies have reported the use of polycarboxylate ligands towards the construction of CPs and especially MOFs. These *O*-donor ligands can easily coordinate to a range of transition metals and lanthanides under various binding modes (mono- or multi-dentate, chelating or bridging). Their fixed geometry provides an excellent opportunity to tune the architecture of the resulting network in accordance with the chemical nature of their backbone. A well-known example of this concept was reported by Yaghi and others in multiple studies[16,17]. The authors employed 1,4-benzenedicarboxylate (bdc), a rigid linker with a fixed angle of 180° between the two carboxylic groups, towards the construction of a MOF formulated as $[Zn_4O(bdc)_3]\cdot$(solvent) (**1.1**). The main building unit of this compound contains a Zn_4O tetrahedron in which the oxide ion is located in the centre (Figure 1.1, left). These units are linked to each other by bridging bdc ligands which coordinate to the metal centres, completing the charge balance and contributing towards the tetrahedral geometry of each Zn^{II} ion. Owed to the geometrical characteristics of the bdc linkers, the resulting structure is a three-dimensional cubic framework with large pores (Figure 1.1, right). Further optimization was made possible by extending the length of the polycarboxylate linker while retaining the same building unit (iso-reticular synthesis), which in turn increased the size of the pores. Notably, the use of p-terphenyl-4,4″-dicarboxylate (tpdc) resulted in the analogous $[Zn_4O(tpdc)_3]$ 3D CP which exhibited an extremely high porous volume of 91.1% in the absence of guest solvent molecules.

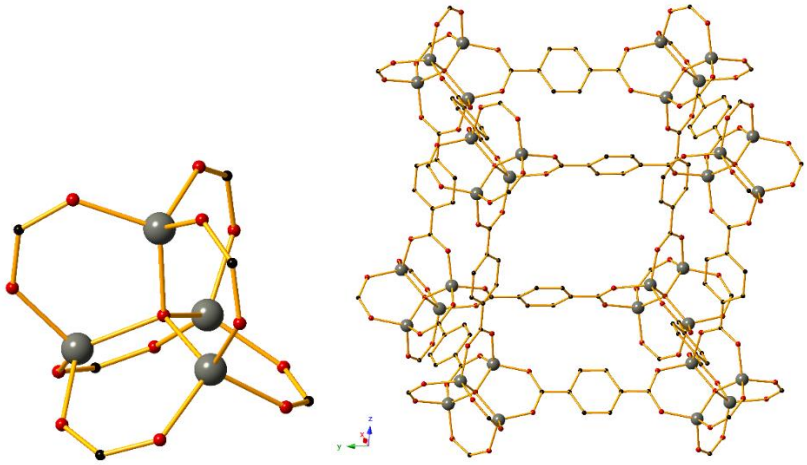

Figure 1.1. The building unit (left) and the porous 3D framework (right) in compound **1.1**. Hydrogen atoms and guest molecules are omitted for clarity. Colour code Zn (grey), C (black), O (red).

Another design approach involves the use of *N*-donor ligands. Initially, a popular use of this type of linkers was as a secondary (co-) ligand in polycarboxylate-based CPs to increase the dimensionality in the resulting framework. The linear bridging linker 4,4´-bipyridine (bipy) has been commonly used in such a fashion. For example, compound $[Ni_6(btc)_4(bipy)_6(H_2O)_9(MeOH)_3]$ (**1.2**, where btc = benzene-1,3,5- tricarboxylate) synthesized by Rosseinsky's group[18] contains $[Ni_3(btc)_2]$-based nodes that expand infinitely to generate porous 2D sheets with a honeycomb-like architecture. Bipy molecules occupy the axial positions of the Ni^{II} centres and are perpendicular to these sheets, resulting in a pillared 3D MOF structure (Figure 1.2). The porous volume of **1.2** was determined at 74% after guest solvents were removed.

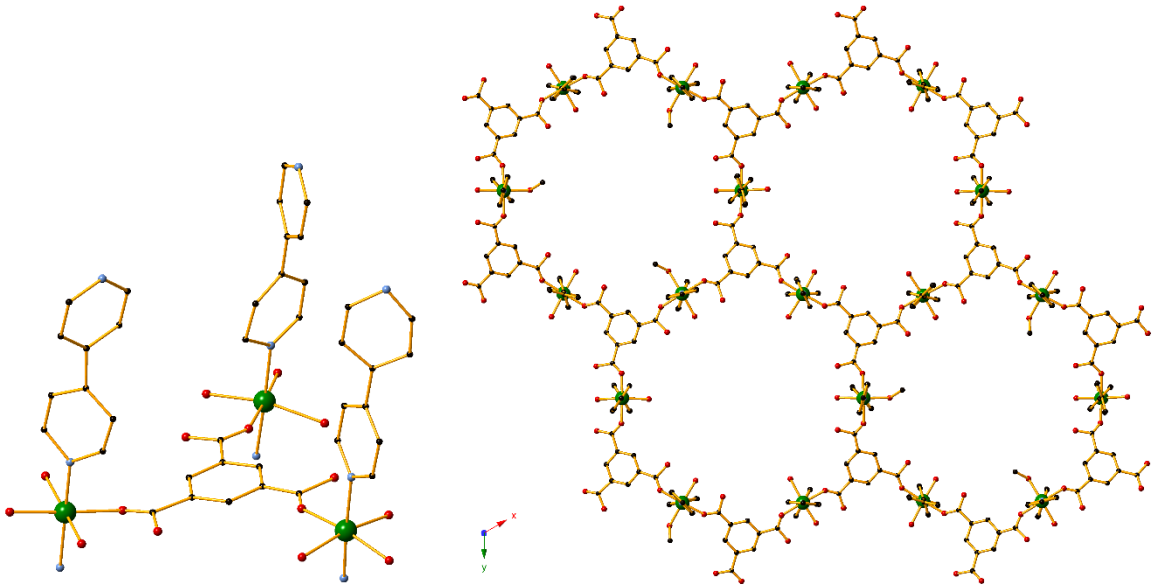

Figure 1.2. The building unit (left) and the porous honeycomb-like framework (right) in compound **1.2**. Hydrogen atoms and certain guest molecules are omitted for clarity. Colour code Ni (green), C (black), N (light blue), O (red).

However, an increasing number of reports have recently surfaced in which rigid *N*-donor linkers based on heterocyclic molecules are employed as primary ligands. Most of the ligands used in this category are neutral, resulting to architectures that are cationic as the charge balance is completed by the anion component of the metal salt. This strategy can cause certain disadvantages compared to polycarboxylate-based linkers, depending on the coordinating nature of the employed anion. Non-coordinating anions are usually found within the voids of the framework, reducing its porosity. They can also participate in various non-covalent interactions which further hinders their removal from the framework. Stronger-coordinating anions with multi-dentate or bridging capabilities can lead to unanticipated architectures, making prediction of the resulting framework more difficult.

On the other hand, M-N coordination bonds (M = metal) are generally weaker and more labile compared to the M-$O_{carboxylate}$ coordination bond. As a result the constructed frameworks are more dynamic and more flexible to rearrangements during the self-assembly process, allowing for further optimization. Some of the manipulations towards improved properties include anion exchange, removal/exchange of guest molecules or temperature-

induced crystal transformations. For example, Kitagawa and co-workers[19] report a dynamic Cu^{II}/bipy system with AF_6 type anions (A = Si, Ge, P) that can undergo multiple anion-induced transformations or guest exchanges to engineer a variety of CP frameworks with different dimensionalities and pore sizes.

1.1.2.1.2. Flexible Ligands

For many years the synthesis of CPs or MOFs was conducted almost entirely using rigid bridging ligands, largely due to their convenience and ease of use when it comes to rational design strategies and prognosis of the resulting structures. In contrast, flexible ligands (i.e., ligands in which rotation around single bonds occurs) can adopt more than one conformation and are therefore more likely to lead to various frameworks throughout the self-assembly process. Moreover, the adjustability of these linkers further increases the influence of reaction parameters such as temperature or time, as subtle changes can drastically affect the resulting frameworks and make the prediction of structures even more difficult.

Despite these drawbacks, the conformational freedom of flexible ligands can also provide unique advantages to this approach. The versatility in coordination and conformation modes leads to a large structural diversity that in many cases cannot be achieved in strategies that include rigid linkers. As a result, this diversity can lead to an unparalleled variety of structural topologies and offer exceptional understanding of these systems, which in turn may provide more efficient optimization of any potential applications. Moreover, the malleability of the ligand backbone allows the network to respond reversibly to the presence or absence of guest molecules; in contrast, many frameworks based on rigid building blocks have been found to collapse when guest molecules are removed[20,21]. Another important aspect of these linkers is the potential induction of chirality within the final structures. Flexible chiral ligands, such as amino acids or peptides[22,23], are much more common and less expensive compared to conformationally rigid chiral molecules. Their use promotes the construction of homochiral CPs which can be then employed in the fields of asymmetric catalysis or enantioselective separation. For all these reasons, flexible ligands have gathered increasing attention in recent years and are also being used to generate frameworks despite the challenges they pose[24].

An example reported by Wu and co-workers[25] was $[Cu_2(hpp)_2Cl_2]\cdot H_2O$ (**1.3**), a homochiral CP constructed using the serine-based ligand (S)-3-hydroxy-2-(pyridine-4-ylmethylamino)propanoic acid (Hhpp). **1.3** presents a framework that extends to two dimensions: each ligand coordinates to one copper centre through its serine-based functional groups (amino, hydroxyl and carboxyl), while its pyridyl nitrogen coordinates to a second metal centre; this arrangement results in polymeric 1D Cu/hpp chains which are then further connected by chloride bridges to generate the final architecture (Scheme 1.3, inset). This compound was found to catalyse the asymmetric 1,2-addition of a Grignard reagent to various α,β-unsaturated ketones with excellent (88–98%) conversions and very good enantioselectivities, with enantiomeric excess (*ee*) values up to 99%. The conditions for this reaction are presented in Scheme 1.3.

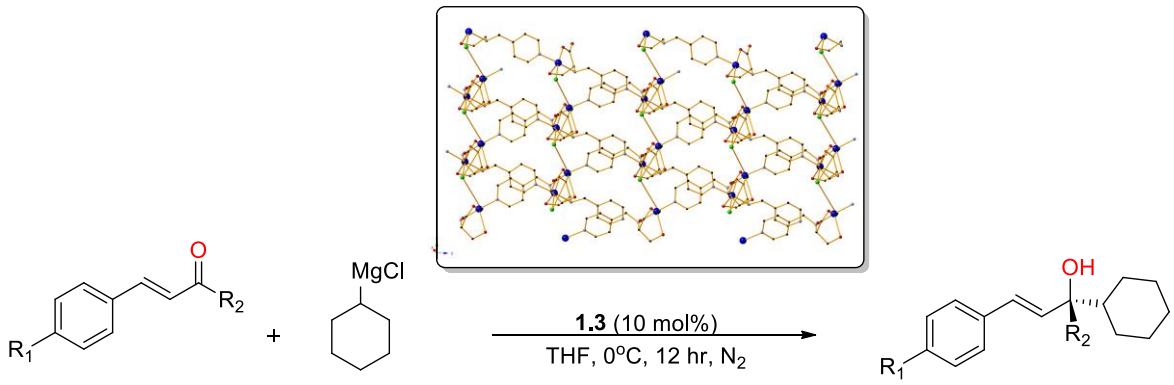

Scheme 1.3. Asymmetric 1,2-addition to various α,β-unsaturated ketones as catalysed by **1.3**. Inset: Part of the 2D architecture of **1.3**. H-atoms have been removed for clarity. Colour code Cu (blue), C (black), N (light blue), O (red), Cl (green).

1.1.2.2. Metal Selection

When choosing the appropriate metal sources for CP design, multiple parameters have to be taken into consideration. These are: i) their ease of coordination to the donor atom of the linker(s), as the strength of these interactions will determine the robustness or dynamism of the resulting structure; ii) their structural flexibility and capabilities, such as the possible coordination numbers and metal geometries. For example, Ag^{I} and Cu^{I} sources are often used when linear or trigonal metal geometries are desired, while Cu^{II}, Zn^{II}, Co^{II} or Mn^{II} favour octahedral geometry; iii) their electronic functionality and properties. Several transition

metals, such as copper, iron, cobalt or manganese may exist in multiple oxidation states and are thus ideal for the design of CPs with potential catalytic activity in redox reactions. On the other hand, lanthanide-based compounds are mostly investigated for their magnetic properties due to the high number of unpaired electrons in the now-used 4f orbitals; iv) the nature of the counter anion, which can easily influence the resulting structure e.g. through coordination or participation in other (hydrogen bond, $\pi\cdots\pi$ stacking) interactions; v) their general ease of chemistry (e.g., solubility in common organic solvents, air sensitivity); vi) their abundance and cost; vii) the intended resulting application. Most of the above criteria can be satisfied by transition metals of the first and (in a lesser extent) second row, and as a result a large percentage of CPs are based on such sources.

Another common synthetic approach concerns the use of heterometallic (mixed-metal) systems. In this method the CPs are usually constructed in a stepwise manner: first, a metal centre reacts with a suitable ligand to form an initial coordination complex, which in this case acts as a building unit ("metalloligand"[26]). These units are linked to each other through heterometallic nodes, providing the final structure.

The metalloligand approach offers even greater control and predictability over the resulting framework and is especially beneficial in the design of CPs with catalytic properties, as it can efficiently provide unsaturated catalytically active metal sites. An example of this was reported by Bhunia and others[27] who employed a targeted synthesis of Mn^{II}/Ln^{III} CPs based on the ligand N,N´-bis(4-carboxysalicylidene)ethylenediamine (H_4bced) to generate 1D frameworks with Mn^{II} metal centres as the active sites. The CPs were then successfully used as catalysts in the epoxidation of olefins. A total of five isostructural compounds were synthesized, formulated as $\{Ln_2[Mn(bced)Cl]_2(NO_3)_2(DMF)_5\}$ (**1.4 - 1.8**), where Ln=Nd (**1.4**), Eu (**1.5**), Gd (**1.6**), Dy (**1.7**), Tb (**1.8**). The frameworks are constructed by two different Mn-based units, [Mn(bced)Cl(DMF)] and [Mn(bced)Cl], which are then connected by lanthanide-based nodes (Figure 1.3). Regarding their catalytic activity, **1.4 - 1.8** afforded similarly good (60-66%) yields in the epoxidation of trans-stilbene with molecular oxygen in order to form stilbene oxide. Further tests were made using an analogous zero-dimensional Mn^{II} complex, affording significantly lower conversions. These results show that the choice

of lanthanide has zero effect on the catalytic activity directly; however, its role as a node in the generation of the 1D framework is essential in order to optimize the catalytic performance.

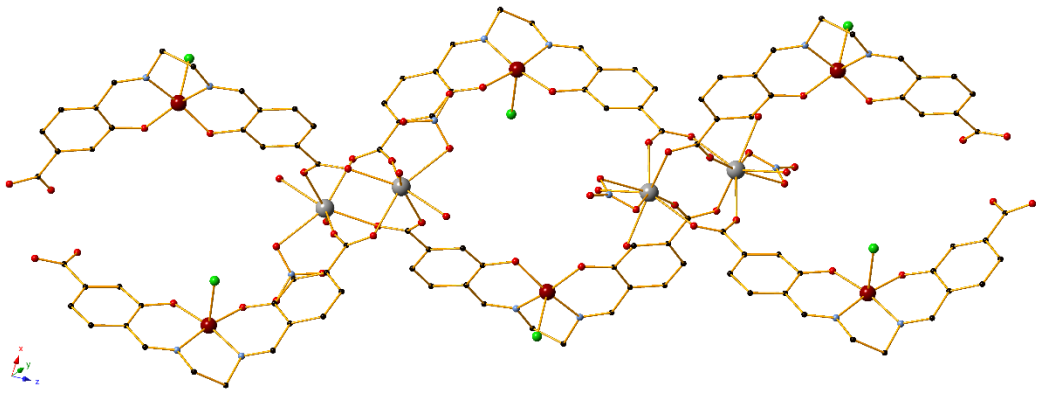

Figure 1.3. Part of the polymeric framework observed in compounds **1.4 – 1.8**. Hydrogen atoms and certain solvent molecules are omitted for clarity. Colour code Ln (grey), Mn (maroon), C (black), N (light blue), O (red), Cl (green).

1.1.2.3. Synthetic Conditions

After a suitable metal/ligand system is chosen, special attention must be paid to the synthetic approach as certain factors can drastically affect the resulting structures. In particular, the selection of solvent is of significant importance for the system: depending on its coordination capabilities, it is possible that the solvent occupies coordination sites of the metal, limiting the number of available sites for ligand binding and affecting the final architecture. Furthermore, certain solvents can participate in various interactions (such as hydrogen bonding) which stabilize the framework. In the case of porous CPs solvent compounds may also act as guest molecules and will have to be removed in order to assess the porosity, as detailed in Section 1.1.3.1.

The temperature of the conducted experiments also plays an important role in CPs. While most reactions are typically performed at room temperature, an increasingly common technique in order to generate CPs is the use of solvothermal conditions. In this case, the reaction mixture is sealed in a vessel and heated above the boiling point of the solvent under autogenous pressure. It is therefore possible for the system to undergo unexpected chemical

changes due to the significant amount of energy provided under these conditions, affording CPs which would not be achievable by conventional methods.

1.1.3. Selected Applications

As the rational design of CPs is constantly optimized to produce targeted compounds, the application range of such materials has greatly expanded beyond the scope of Coordination Chemistry and includes fields such as chemical and biological sensing[28–30], luminescence[31], drug delivery[32] and conductivity[33]. In the context of this thesis, the current section will highlight the use of CPs in the selected topics of porosity, magnetism and catalysis along with particular examples.

1.1.3.1. Porosity

The porous nature of some CPs has been of significant interest to researchers with several applications emerging from this field in recent decades. While the presence of voids can be determined through visual inspection of the structure, conclusive proof of porosity is typically established by gas adsorption-desorption isotherm studies. These experiments provide information on the pore size and determine whether the material retains its structural identity during adsorption and desorption of guest molecules. The latter property, known as permanent porosity, is especially important in CPs: since nature tends to avoid empty space, porous CPs are generally synthesized containing various guest molecules within the cavities, such as solvents, free ligands or anions. Therefore, any related applications may only be studied when these molecules are removed without causing the remaining “activated” framework to collapse.

Perhaps the most important of these applications is gas sorption, for which several porous CPs have been found to be excellent candidates. Compared to other porous materials, CPs can have tuneable pore size through targeted ligand design. Additionally, the hydrocarbons and aromatic groups contained within the linkers can attract guest molecules by forming weak interactions (typically physisorptive). For these reasons, CPs have been reported to store and/or separate gases of various size and chemical nature through safe, efficient and

cost-effective methods. Characteristic examples include the storage of hydrogen[34], carbon dioxide[35], methane[36], and the selective adsorption of acetylene over other gases[37].

1.1.3.2. Catalysis

Another key application of CPs involves their use as homogeneous or heterogeneous catalysts in various chemical reactions. The field has attracted increased interest especially after the emergence of MOFs, as researchers immediately drew comparisons between these porous materials and aluminosilicate minerals, commonly known as zeolites. The latter have been regularly used in commercial catalysis due to their high surface area, porosity and thermal stability. CPs may also show some of these characteristics, but their lower thermal stability makes them unsuitable for reactions under extreme conditions. On the other hand, they can be efficient catalysts in sensitive reactions which involve delicate molecules and require milder conditions. Furthermore, the plethora of options in metal and ligand selection means that CPs can be synthesized in greater chemical variety compared to zeolites, providing plenty of room for catalyst tuning and optimization.

A seminal example of a CP with heterogeneous catalytic activity was presented by Kaskel and co-workers, who investigated[38] the catalytic potential of an already known[39] Cu^{II}-based MOF, formulated as $[Cu_3(tma)_2(H_2O)_3]$ (**1.9**, where H_2tma = benzene-1,3,5-tricarboxylic acid). The compound consists of dicopper tetracarboxylate building blocks that are linked to form a 3D network with large diamond-shaped pores (Scheme 1.4, inset). In particular, **1.9** was employed in the cyanosilylation of carbonyl compounds. The resulting cyanohydrins are versatile components in synthetic chemistry and act as intermediates in the preparation of compounds such as β-amino alcohols or α-hydroxy aldehydes. Trimethylsilyl cyanide (TMSCN) is the most commonly used cyanide source for the formation of cyanohydrins, however the use of a catalyst is also necessary in order to activate both the substrate and the cyanide precursor. **1.9** was first activated at high temperature under vacuum to remove guest solvents and the axially coordinated water molecules, leaving Lewis acidic Cu^{II} centres with unsaturated sites. This dehydrated framework was found to promote the cyanosilylation of benzaldehyde (Scheme 1.4) in a protocol that involved stirring TMSCN and benzaldehyde in pentane, for 72 hours and under 40°C. Encouraging yields of 57% were afforded using this

method, while the reaction gave trace amounts of the cyanohydrin product when no catalyst was used. It is worth noting that zero conversion was observed when the reaction took place in the coordinating solvent THF, further confirming the role of the unsaturated Cu^{II} sites.

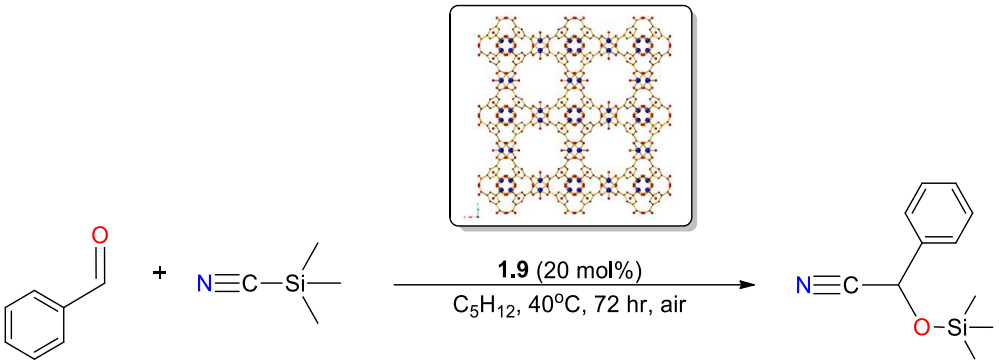

Scheme 1.4. Cyanosilylation of benzaldehyde as catalysed by **1.9**. Inset: The porous 3D architecture of **1.9**. H-atoms have been removed for clarity. Colour code Cu (blue), C (black), O (red).

1.1.3.3. Magnetism

The generation of materials that exhibit magnetic ordering is an important topic in coordination chemistry, as well as one of the primary investigations in Chapter 2 of this thesis. To facilitate the presentation of these results, this subsection will first introduce related measures and definitions before expanding on the use of CPs in this area.

Introduction

In general, the magnetic properties in an atom or a compound arise from the total spin and orbital angular momentum of its unpaired electrons. As a result, magnetic moment (expressed in bohr magneton, μ_B) is created under the presence of an applied magnetic field (H); magnetization (M), i.e., the quantity of magnetic moment per unit volume, is typically used to measure this behaviour. Another common measure is magnetic susceptibility (χ), i.e. the ratio of magnetization M to the applied field strength H, which is often used to indicate whether the material is attracted or repelled by the presence of this field. Furthermore, χ has been found to be inversely proportional to the effects of temperature in what is known as the

Curie's law, showing that the magnetic properties of materials increase at lower temperatures.

In the case of paramagnetic materials, the individual magnetic moments do not interact with each other and as a consequence their magnetization *M* is zero when the field is no longer applied. Additional phenomena (Figure 1.4), however, may be observed in chemical compounds (in the crystalline phase) where magnetic interactions between the spins of neighbouring atoms also occur. These exchange interactions (coupling) provide magnetic ordering in the compounds and are typically described by the exchange coupling constant *J*. Common types of magnetic ordering observed in structures are:

i) Ferromagnetism ($J > 0$), in which spins are coupled in a parallel alignment. This results in a large net magnetization and susceptibility even in the absence of an external field as the magnetic moments of the individual spins add to each other. While this electronic interaction is strong enough to align spins, the effect of thermal energy can overcome this exchange at a particular temperature, also known as the Curie temperature (T_c). As a result, ferromagnetic materials lose this behaviour and their magnetic ordering above T_c, becoming paramagnets.

ii) Ferrimagnetism, in which materials exhibit the same characteristics as ferromagnets (spontaneous magnetization, temperature dependence). However, they show different magnetic ordering, as antiparallel coupling of unequal spins occurs.

iii) Antiferromagnetism ($J < 0$), in which antiparallel coupling of equal spins is observed. The magnetization and susceptibility in such materials is therefore low, as the individual magnetic moments cancel each other. Such coupling interactions are common in transition metal-based compounds. As with ferromagnets, antiferromagnetic materials exhibit ordering until a critical temperature, in this case called the Néel temperature (T_N).

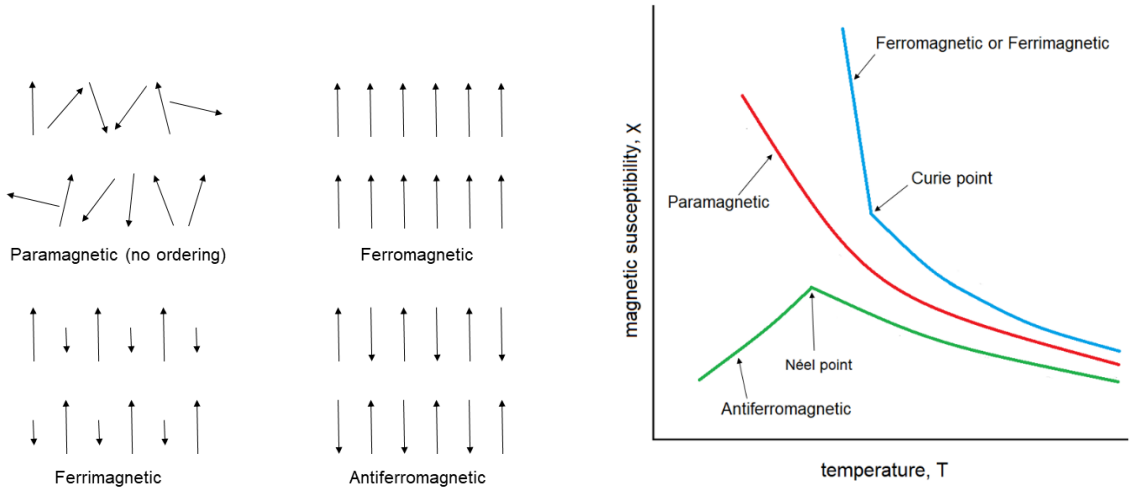

Figure 1.4. The arrangement of spins (left) and characteristic χ vs T plots (right) in magnetic materials.

The exact nature of the magnetic phenomena in compounds can be established through temperature-dependent molar magnetic susceptibility (χ_M) measurements as well as investigations on the dependence of H on the magnetization M below the Curie temperature. The main instrument used for these determinations is the Superconducting Quantum Interference Device (SQUID), providing magnetic measurements of (micro)crystalline samples in temperatures as low as 2 K. The susceptibility is typically plotted as $\chi_M T$ versus T, as it can visually provide more information on the type of magnetic coupling.

Another considerable factor during investigations of magnetic properties is the presence of spin-orbit coupling, which may cause a weak interaction of the spins even in the absence of a magnetic field, eventually leading to a split of the spin state levels. The phenomenon is known as Zero-Field Splitting (ZFS). In magnetism ZFS can have a profound effect in the resulting properties, causing unequal distribution of the magnetic moment to the three dimensions (magnetoanisotropy). ZFS is usually found in transition metal complexes which have a molecular spin $S \geq 1$ and consists of an axial (D) as well as a rhombic (E) component. The determination of ZFS in a material with magnetic properties is typically done through Electron Paramagnetic Resonance (EPR) studies. The data are then modeled against theoretical spin Hamiltonian equations in order to derive the most accurate fits for the D and E values.

CPs in magnetism

CPs are an excellent option for the purposes of studying such phenomena, as they can incorporate paramagnetic metal centres and carefully chosen organic linkers to connect them within interacting range through direct coordination bonds. These parameters are ideal for the formation of exchange interactions between the spins of the paramagnetic metals, establishing cooperative magnetic behaviour. As such, CPs have been extensively studied for their magnetic properties in recent decades.

An interesting example of a CP with such capabilities was recently reported by Zeng and co-workers[40]. The authors constructed the 3D CP $[Co^{II}_3(lac)_2(pybz)_2]\cdot 3DMF$ (**1.10**, where pybz = 4-pyridyl benzoate, lac = D- and L-lactate) which consists of Co^{II}-lac nodes bridged by pybz linkers that also act as pillars and form a porous 3D architecture (Figure 1.5). DMF solvent molecules are found within the pores, however they may be easily exchanged post-synthetically with other molecules through single-crystal to single-crystal transformation: selected compounds $[Co^{II}_3(lac)_2(pybz)_2]\cdot 6MeOH$ (**1.11**), $[Co^{II}_3(pybz)_2(lac)_2(H_2O)_2]\cdot 7H_2O$ (**1.12**) and $[Co^{III}Co^{II}_2(pybz)_2(lac)_2(H_2O)_2]I\cdot 2H_2O\cdot 1.5DMSO$ (**1.13**) were obtained through immersion of the material in MeOH, H_2O and I_2/H_2O/DMSO solutions respectively. **1.10** and **1.11** are isostructural and both showed antiferromagnetic behaviour when tested for their magnetic properties. However, **1.12** and **1.13** show structural differences which affect the metal centres, as coordination of water molecules and oxidation of Co^{II} ions takes place in each case. These variations account for significant differences in the magnetic behaviour, with **1.12** behaving as a ferrimagnet and **1.13** showing ferromagnetic interactions between the metal ions.

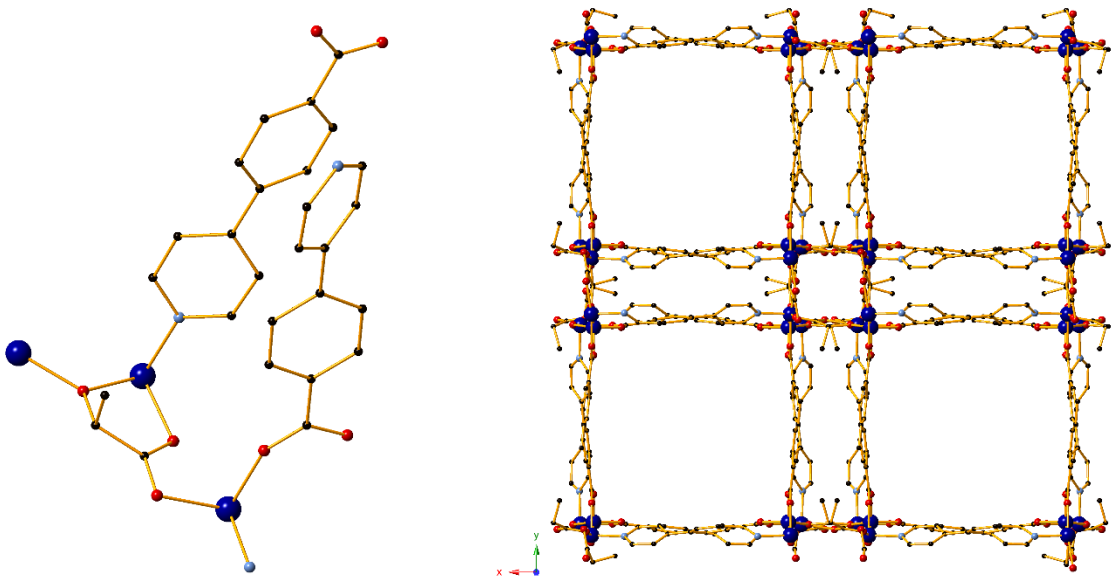

Figure 1.5. The building unit (left) and the porous architecture (right) in compound **1.10**. Hydrogen atoms and solvent molecules are omitted for clarity. Colour code Co (blue), C (black), N (light blue), O (red).

1.1.4. One-dimensional coordination polymers

Amongst the thousands of reports on CPs that have been studied for their applications, a large majority of those consists of porous 2D and 3D CPs especially since the emergence of the "MOF" term in the literature. Consequently, lesser attention has been paid towards one-dimensional CPs and their potential properties. However, more efforts to systematically study these materials have been made recently[29,33,41]. Despite their structural simplicity compared to MOFs, 1D CPs in particular are generally easier to synthesize and the resulting framework can be tuned more effectively in order to generate structures with maximized application potential[42,43]. A number of detailed reviews regarding the potential of 1D CPs have been published. In 1993 Chen and Suslick[44] reported the uses of 1D CPs in various topics of materials science. In 2011, a comprehensive review by Leong and Vittal[45] covered the literature on 1D CPs from 1993 up to the end of the previous decade, focusing on structural motifs and supramolecular architecture issues as well as their applications. More recently, a study by Slabbert and Rademeyer[46] published in 2015 focused on the structural trends of 1D halide-bridged CPs.

In all these reviews, the catalytic properties of 1D CPs received minimal focus; however, efforts towards more systematic studies in this field have been made recently. 1D CPs can catalyse an organic transformation via homo- or heterogeneous pathways depending on their solubility; this can introduce ambiguity when determining the active catalytic species and is therefore considered as a disadvantage when compared to the capabilities of 2D/3D MOFs. On the other hand, their easy synthesis and tuning offers greater potential and unrivalled variability for mechanism unravelling or catalyst development in an existing system. Therefore, 1D CPs with catalytic activity present a unique opportunity to connect Inorganic and Organic Chemistry, providing invaluable information.

For these reasons, Section 1.1.4.1 will provide selected reports of 1D CPs that have been used as catalysts in various organic reactions in the last decade. The CPs have been mainly categorized into homometallic and heterometallic compounds; additional parameters such as the metal and ligand selection for the CP are discussed, to provide a more detailed look into each system.

1.1.4.1. Recent advances of one-dimensional coordination polymers as catalysts

Homometallic

Several cases of 1D CPs with catalytic activity in oxidation reactions have been reported. Such reactions are a very useful tool for synthetic organic chemists, however due to the high activation energies involved they often require the use of a catalyst as well as harsh conditions. The first related compound was introduced by Karabach and co-workers[47], synthesized through the self-assembly of Cu^{II} nitrate, triethanolamine (H_3tea) and pyromellitic acid (H_4pma) in an aqueous medium. The ligand selection was intended to promote the synthesis of CPs with a targeted Cu^{II} coordination environment to mimic the respective environment in methane monooxygenase, a copper enzyme that can catalyse the oxidation of alkanes. Indeed, the resulting compound, $[Cu_2(tea)_2(pma)]$ (**1.14**), forms 1D ladder-like polymeric chains in which each Cu centre possesses a $\{NO_5\}$ coordination environment. **1.14** was used as a catalyst precursor in the mild oxidation of cyclohexane (Scheme 1.5) at room temperature and in $MeCN/H_2O$, providing moderate conversion to cyclohexanol and cyclohexanone (29% overall yield based on cyclohexane); this result was

comparable to other copper catalysts for this reaction. The catalyst was also found to largely retain its activity when reused in the reaction (26% overall yield after three recycles).

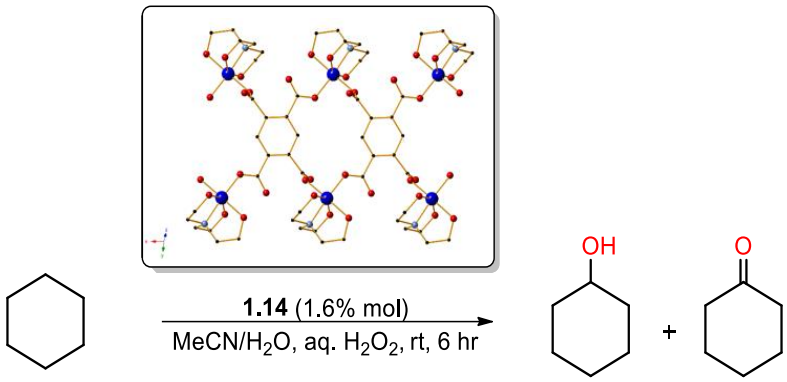

Scheme 1.5. Oxidation of cyclohexane as catalysed by **1.14**. Inset: Part of the 1D architecture of **1.14**. H-atoms have been removed for clarity. Colour code Cu (blue), C (black), N (light blue), O (red).

Very recently, Wang and co-workers[48] came up with a series of catalysts for the selective oxidation of arylalkanes to ketones. The synthetic procedure for the catalysts involves the use of various Cu^{I} halogen sources and the tpb ligand (tpb = *N*,*N*,*N*-tris(3-pyridinyl)-1,3,5-benzenetricarboxamide). Out of the reported compounds, the iodine analogue formulated as [CuI(tpb)] (**1.15**) features a 1D framework along the *a* axis, which consists of a herringbone-like chain due to the conformation of the tpb molecules. Each Cu^{I} centre possesses a trigonal geometry and a $\{N_2I\}$ coordination environment. **1.15** acts as an excellent heterogeneous catalyst for the oxidation of a series of arylalkanes to the corresponding ketones (Scheme 1.6), providing the highest yields (72-99%) out of all the compared catalysts in the study. The ketones are afforded in very high selectivity and the reaction takes place under easy and eco-friendly conditions (air atmosphere, H_2O as solvent, room temperature and only 4 hours stirring time). Additionally, only 5 mol% of the catalyst is employed, which can be then recovered and reused for at least six cycles with small losses in activity. Interestingly, the authors attribute the superiority of **1.15** to its coordination environment; it is proposed that the iodide anions enhance the activity of the metal centres and further facilitate the substrate binding.

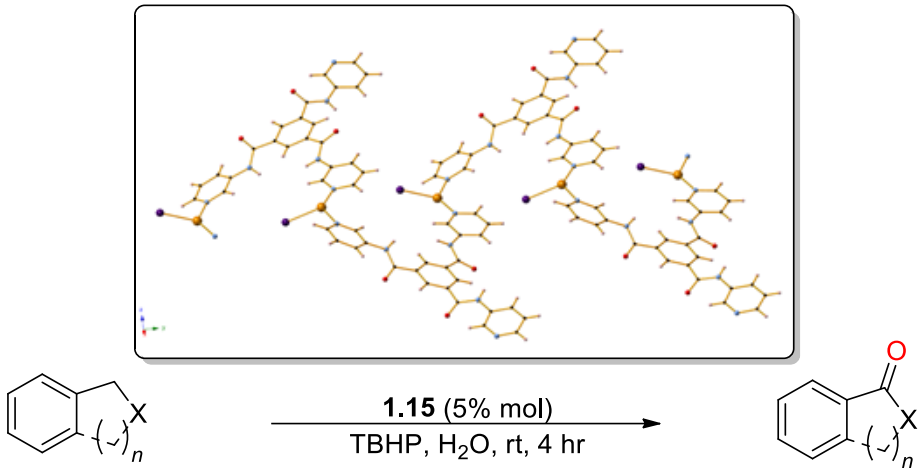

Scheme 1.6. Oxidation of arylalkanes to corresponding ketones as catalysed by **1.15**. Inset: The 1D herringbone-like chain in **1.15**. H-atoms have been removed for clarity. Colour code Cu (light orange), C (black), N (light blue), O (red), I (purple).

Furthermore, a Mn^{II} 1D CP with the ligand *N*-(4-carboxybenzyl) iminodiacetic acid (H_3cia) was reported by Lymperopoulou[49] and co-workers, showing catalytic activity in the epoxidation of alkenes. The compound, formulated as [Mn(Hcia)(H_2O)] (**1.16**), forms 1D ladder-like chains with the ligand being only partially deprotonated, as the benzoic group remains intact and participates in hydrogen bonding interactions. Catalysis-wise, **1.16** promotes the epoxidation of a large range of olefins when hydrogen peroxide and ammonium acetate were added respectively as oxidant and additive (Scheme 1.7). Typically the reactions proceeded under room temperature and were completed at 6 hours, providing epoxide products with moderate to high conversions (up to 81%) and excellent selectivities (up to 100%).

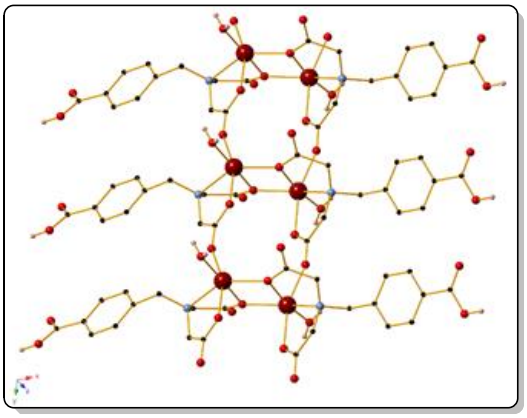

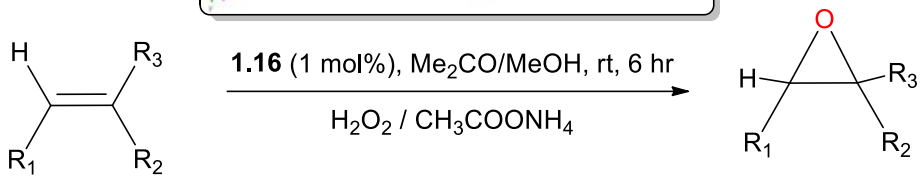

Scheme 1.7. Olefin epoxidation catalysed by **1.16**. Inset: The 1D ladder-like structure of **1.16**. Certain H-atoms have been removed for clarity. Colour code Mn (maroon), C (black), N (light blue), O (red).

The use of 1D CPs as catalysts, however, is not limited to oxidation reactions only. In a recent study by Wani[50] and co-workers a zinc-based 1D CP, [Zn(tppz)(Hccb)] (**1.17**), is tested for its catalytic efficiency in the transesterification reaction. In this transformation, synthesis of esters is achieved as the organic component of the alkoxy group of a different starting ester is exchanged with the organic group of an alcohol. Two different organic linkers, 2,3,5,6-tetrakis(2-pyridyl)pyrazine (tppz) and 3-(carboxymethyl-amino)-4-chlorobenzoic acid (H_3ccb) are used for the synthesis of **1.17** providing multiple potential coordination sites to the metal centres. The resulting compound comprises of M(tppz) units linked by Hccb ligands with deprotonated carboxyl groups, which provide the dimensionality to the framework. This forms a 1D zig-zag chain where each zinc centre is penta-coordinated in a square pyramidal geometry. In regards to its catalytic activity, very good yields were achieved when the transesterification reactions proceeded in DMSO, under 80^{o}C and within 4 to 16 hrs, when 2 mol% of **1.17** was used (Scheme 1.8). The catalyst may also be reused for at least four cycles without any loss in yield. As **1.17** has a superior activity compared to Zn^{II} salts, the authors propose that this may be attributed to the unsaturated penta-coordinated Zn^{II} centres which provide a free site for substrate binding.

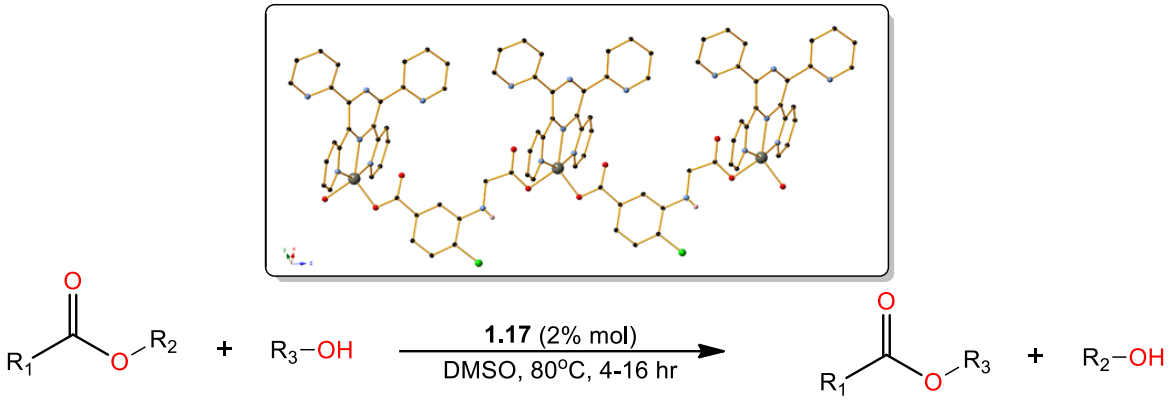

Scheme 1.8. Transesterification reaction as catalysed by **1.17**. Inset: The 1D zig-zag chain in **1.17**. Solvent molecules and H-atoms have been removed for clarity. Colour code Zn (grey), C (black), N (light blue), O (red), Cl (green).

The Knoevenagel reaction[51] is another chemical transformation in which the catalytic potential of 1D CPs has been studied recently. This C-C bond formation reaction affords α,β-unsaturated compounds from the condensation of a carbonyl compound and an active hydrogen compound, which is then deprotonated by the catalyst. Recently, Karmakar and co-workers[52] reported the synthesis of a 1D zig-zag CP, [Zn(aipa)(H_2O)$_2$] (**1.18**), using 5-acetamidoisophthalic acid (H_2aipa) as the primary linker. This compound was found to have very good performance as a heterogeneous catalyst for the Knoevenagel condensation reaction (Scheme 1.9) with various aldehydes and malononitrile used to produce the corresponding benzylidenemalononitriles. Moreover, the catalyst was found to be recyclable without any considerable loss of activity. The suggested mechanism by the authors involves a synergistic effect by the Lewis acid (Zn centres) and basic (carboxylate-O or amide-O) sites, highlighting the importance of the metal and ligand selection when choosing the synthetic and catalytic systems.

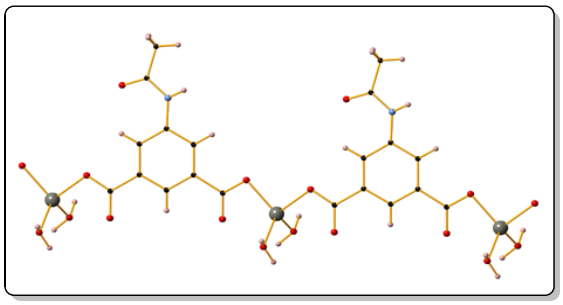

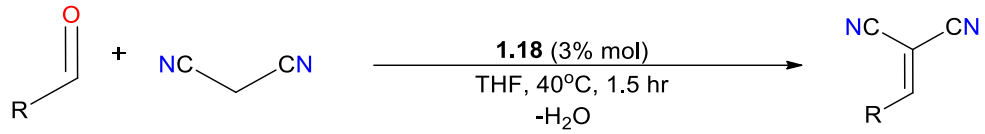

Scheme 1.9. Knoevenagel reaction as catalysed by **1.18**. Inset: Part of the 1D zig-zag framework in **1.18**. Lattice solvent molecules have been removed for clarity. Colour code Zn (grey), C (black), N (light blue), O (red).

Heterometallic

As the search for new and effective metal catalysts carries on, the concept of multimetallic catalytic systems has been growing increasingly[53]. The use of two or more different metal elements in order to promote a reaction can be very rewarding and enhance the catalytic performance in various ways: firstly, the potential cooperativity and synergy effects[54,55] can lead to improvements in the catalytic activity, as the multimetallic system may provide greater performance than the individual homometallic components. Furthermore, reports have shown that the binding affinity of a substrate to a metal centre may increase when another metal centre is in close proximity[56].

Section 1.1.2.2. included compounds **1.4** – **1.8** as examples of mixed-metal (3d/4f) 1D CPs with catalytic activity. Another heterometallic one-dimensional coordination polymer based on a lanthanide element was presented by Kumar and co-workers[57] in a recent study. The CP contains a Co^{III}/Eu^{III} core and was found to be a suitable catalyst for various ring opening reactions of epoxides. The metalloligand approach is once again used in the synthetic method, as a Co^{III} precursor (**1.19**) with the ligand 4,4'-((pyridine-2,6-dicarbonyl)bis(azanediyl))dibenzoic acid (H_4pdada) is employed. Addition of the lanthanide source follows, as the 1D CP $[Co(pdada)_2Eu(H_2O)_5]\cdot 8H_2O$ (**1.20**) is constructed. Each metalloligand as a whole coordinates to two Eu(III) centres, generating a zig-zag framework.

1.20 was found to be an efficient heterogeneous catalyst in the ring opening reactions of cyclohexene oxide and styrene oxide with various nucleophiles (Scheme 1.10), including anilines (aminolysis), trimethylsilyl azide (azidolysis), alcohols (alcoholysis) and thiols (thiolysis). The corresponding products are afforded at excellent yields (78-100%) and under mild conditions, as the reactions are treated with 2 mol% catalyst under ambient conditions and for 4 hours. Reusability tests showed that the catalyst may be recycled at least five times with very minor losses in yield. The activity of this heterometallic CP is mainly attributed to the strong Lewis acidic nature of the Eu^{III} centres, as well as their coordinating environment. Many of the coordination sites of the lanthanide are occupied by labile water molecules, providing an easy access to substrates.

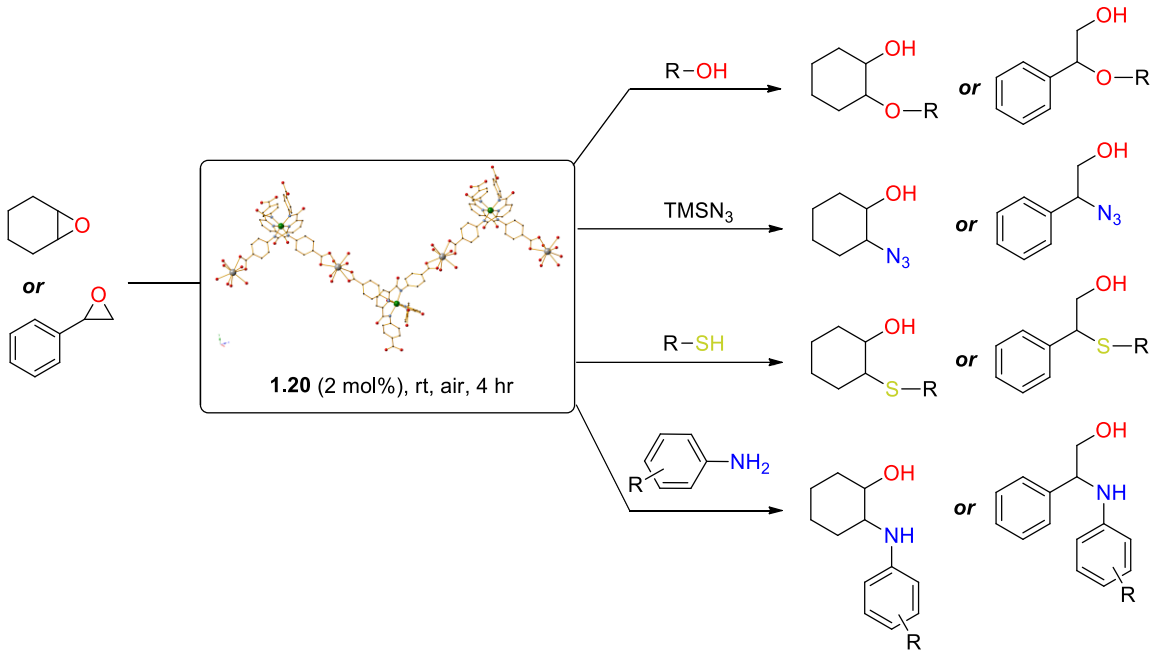

Scheme 1.10. A scope of the ring-opening reactions catalysed by **1.20**. Inset: Part of the zig-zag chain in **1.20**. Lattice solvent molecules and H-atoms have been removed for clarity. Colour code Co (green), Eu (grey), C (black), N (light blue), O (red).

1.2. Benzotriazole

Section 1.1.2.1 of this Chapter discussed the importance of ligand selection towards the construction of functional CPs. Particularly noted amongst the plethora of available choices were *N*-donor ligands based on heterocyclic molecules. This category has been recently attracting increased interest with several reported frameworks based on imidazole-, benzimidazole-, triazole- and tetrazole-derived ligands[58–60]. The following section will focus on the analogous aspects of benzotriazole, since the use of this molecule will be a key feature of this thesis in regards to the ligand design.

1.2.1. Introduction

Benzotriazole (Hbta) is an aromatic heterocyclic compound that has been widely popular in organic as well as inorganic chemistry. It belongs in the general category of azoles, along with other well-known heterocyclic molecules such as pyrazole, imidazole, 1,2,3-triazole, 1,2,4-triazole and tetrazole. Hbta contains a benzene ring that is fused with a five-membered aromatic ring which incorporates the 1,2,3-triazole moiety.

Since the proton in this moiety can easily relocate between the nitrogen atoms, Hbta can exist in two tautomeric forms, 1H- and 2H-Benzotriazole (Scheme 1.11, Forms **A** and **B** respectively). Investigation of this phenomenon has been the subject of multiple studies throughout the years, which showed that the 1H-tautomer (**A**) is the predominant species in solution. This has been attributed to its high dipole moment (μ = 4.3 D in **A**, 0.38 D in **B**, according to theoretical calculations) which favours interactions with the solvent and therefore provides better solvation than in the case of the 2H-tautomer[61]. Furthermore, the 1H-tautomer has been found to be the only stable isomer in the solid state, as shown by X-Ray crystallography[62] and other spectroscopic studies.

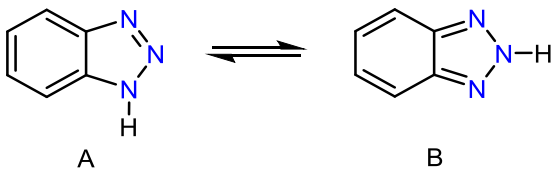

Scheme 1.11. The two tautomeric forms in Hbta.

Historically, the synthesis of the first benzotriazole derivative dates back to the late 19th century. A study by Zinin in 1860 reports efforts towards the nitration of azoxybenzene[63]. One of the afforded products was 2-phenylbenzotriazole-1-oxide, although this was not recognised until 1899 by Werner and Stiasny[64]. Other studies in that period by Hofmann[65] and Ladenburg[66] investigated the effect of nitrous acid on various phenylenediamines, noting that the use of o-phenylenediamines resulted in products with unique properties compared to the rest. These products were later found to be benzotriazole derivatives and the synthetic method to obtain Hbta remains similar today (Scheme 1.12), albeit with certain improvements in the reaction conditions[67].

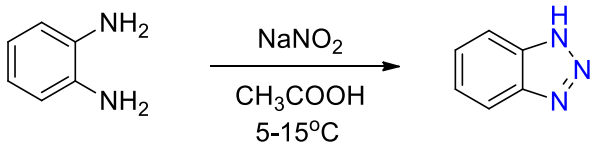

Scheme 1.12. Common synthetic method to obtain benzotriazole.

The popularity of benzotriazole derivatives amongst organic chemists is in no small part due to their attractive properties. Hbta is an odourless, non-toxic, non-sensitive chemical that shows excellent solubility in a variety of organic solvents and is almost insoluble in water. Additionally, it is inexpensive and easy to synthesize. More importantly, Hbta exhibits both electron donating and electron attracting capabilities; it can either act as a weak acid (pKa = 8.2) through proton loss, or as a very weak Brønsted base (pKa < 0) through accepting a proton using the lone pair electrons available on the nitrogen atoms. As such, it is also soluble in aqueous Na_2CO_3 as well as HCl, meaning that it can be easily separated from reaction mixtures. Finally, its ring system shows remarkable thermal (up to 400°C) and chemical (in the presence of H_2SO_4, KOH, $LiAlH_4$ etc.) stability. For these reasons, benzotriazole and its derivatives have been extensively used in synthetic organic chemistry as auxiliary tools towards a great range of reactions and syntheses. Relevant work by Katritzky should be noted in particular, as his group contributed more than 600 research papers as well as multiple reviews and books related to this field in the span of three decades. This enormous work revolving around the synthetic utilities of benzotriazole derivatives extends well beyond the

scope of this thesis. Characteristic examples include benzotriazole-mediated alkylation reactions or the synthesis of heterocycles, peptides and amino-acid derivatives[68–72].

1.2.2. Benzotriazole-based Molecules as Ligands in Coordination Chemistry

1.2.2.1. Brief History

The unique properties and synthetic versatility of Hbta are not limited within the realm of synthetic organic transformations. In 1947, Procter and Gamble Ltd submitted a patent[73] on the use of Hbta as a corrosion inhibitor for metallic copper. In particular, subjection of copper to a solution containing Hbta formed a barrier layer that was insoluble in water and many organic solvents, protecting the metal from potential surface reactions. Subsequent studies[74] by Cotton and co-workers in the 1960s suggested that this protective layer consisted of a polymeric Cu^{I}-bta complex in which each benzotriazole molecule is deprotonated and uses its two non-central nitrogen atoms of the 1,2,3-triazole moiety to coordinate to two different copper centres, forming a linear polymeric structure (Scheme 1.13).

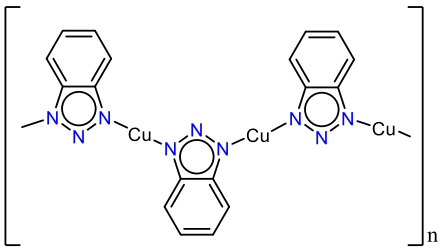

Scheme 1.13. Proposed structure of the formed copper-benzotriazole complex as suggested by Cotton and co-workers.

As a result of these reports Hbta was introduced in inorganic synthesis as a potential ligand towards the formation of coordination complexes. The first related coordination compound that was characterized by X-Ray crystallography was presented in 1976 when Meunier-Piret and co-workers reported[75] the structure of a Ni^{II}/benzotriazole coordination complex, while studies in the 1980s also investigated the coordination capabilities of Hbta with other transition metals[76,77]. However, the increased popularity of *N*-donor linkers in the late 1990s allowed researchers to fully realize the advantages that benzotriazole-based ligands could

offer in coordination chemistry: i) being *N*-donor ligands, they can provide dynamic and flexible frameworks (as previously explained in Section 1.1.2.1); ii) the 1,2,3-triazole moiety provides multiple potential coordination modes and allows Hbta to be utilized as a terminal or a bridging ligand (Scheme 1.14); iii) they can participate in various interactions (e.g. hydrogen bonds, $\pi\cdots\pi$ stacking) which stabilize the resulting structures and provide a better understanding of the system; iv) due to the synthetic versatility of Hbta it is very easy to synthesize benzotriazole-based ligands with various levels of flexibility, although in some cases it can be difficult to separate the resulting 1H- and 2H-isomers.

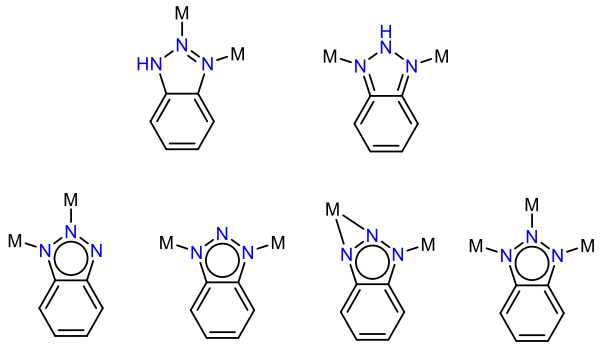

Scheme 1.14. Bridging coordination modes of benzotriazole (top, modes $\mu_{2,3}$, $\mu_{1,3}$) and benzotriazolate (bottom, modes $\mu_{1,2}$, $\mu_{1,3}$, μ-η^2:η^1, $\mu_{1,2,3}$).

As a result of the above, a search in the Cambridge Structural Database (CSD)[78] for coordination compounds based on benzotriazole-derived ligands reveals a high number of studies with the majority published after 2000. However, the relevant reviews on this subject are surprisingly scarce. In 2010 Mohamed reported[58] the coordination chemistry of various *N*-donor ligands employing coinage metals, however only complexes based on 1,2,4-triazole are mentioned. A review by Aromí and co-workers in 2011 presents the use of triazole and tetrazole ligands in coordination chemistry and includes some examples of benzotriazole-based complexes[59]. Similarly, a 2012 review[60] by Zhang covers the subject of metal azolate frameworks, however only a few selected cases are mentioned in regards to benzotriazolate compounds. As such, in order to fully realise the potential of benzotriazole-based linkers in coordination chemistry, Section 1.2.2.2 will present a more detailed, non-exhaustive list of related coordination complexes (Scheme 1.15) covering the literature as of April 2018. This list will include certain structural information on the compounds as well as notable reported

applications. In order to facilitate this presentation, the complexes have been primarily categorized in regards to the exact linker used (Hbta or some derivative) and its role in the resulting architecture (either as a main or as a supporting co-ligand).

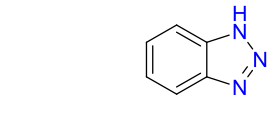

Hbta

Compounds **1.21** - **1.47** (as main ligand)
1.48 - **1.73** (as co-ligand)

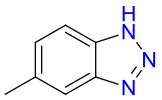

MebtaH

Compound **1.77**

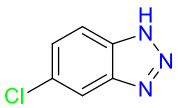

ClbtaH

Compound **1.78**

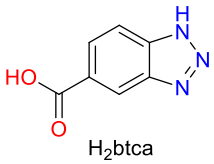

H_2btca

Compounds **1.80** - **1.84**

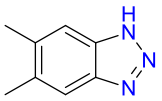

Me_2btaH

Compounds **1.74**, **1.75, 1.79**

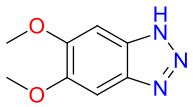

OMe_2btaH

Compound **1.76**

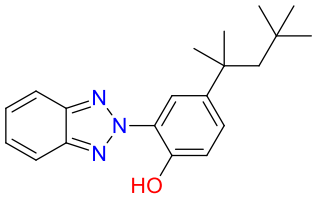

^{C8}BTPH

Compound **1.85**

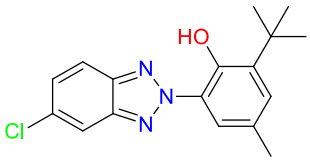

^{TMCl}BTPH

Compound **1.86**

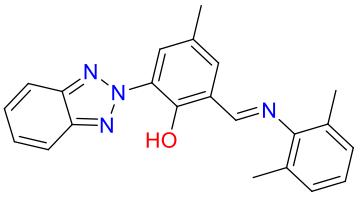

^{C1DMe}IBTPH

Compound **1.87**

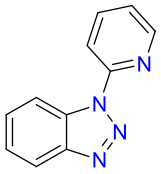

pbta

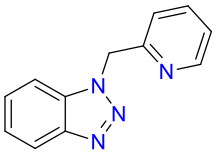

pmbta

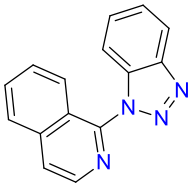

ibta

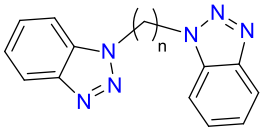

bbtm (n = 1)
bbte (n = 2)
bbtp (n = 3)
bbtb (n = 4)
bbth (n = 6)

Compound **1.88** (n = 1)

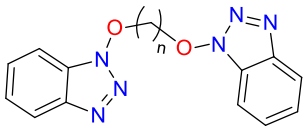

bbdp (n = 1)
bbdpt (n = 3)
bbdh (n = 4)

Compounds **1.89**, **1.90** (n = 1)

Scheme 1.15. A list of the benzotriazole-based ligands and the respective coordination compounds mentioned in Section 1.2.2.2.

1.2.2.2. Recent Advances

1.2.2.2.1. Benzotriazole as a Main Ligand

Polynuclear Coordination Clusters

Long-time investigations of the coordination capabilities of Hbta using M^{II} transition metals have shown that the system frequently leads towards polynuclear coordination complexes with similar structural motifs. Notably, a family of pentanuclear compounds with the general formula $[M_5(OH)x(bta)_{6-x}(acac)_4(H_2O)_{4x}]$ (where M = Cu^{II}, Ni^{II}, acac = acetylacetonate, x = 0, 1) have been commonly reported[79–81] in previous decades. These compounds consist of four penta-coordinated M^{II} centres that are found in the corners of an imaginary tetrahedron, while the fifth M^{II} ion is found at the centre of this arrangement and is hexa-coordinated. These metal centres are bridged exclusively by deprotonated benzotriazole (bta) molecules in a $\mu_{1,2,3}$-bridging fashion, as the N1, N3 nitrogen atoms coordinate to metal ions of the tetrahedron while the six N2 atoms coordinate to the central octahedral metal. The remaining coordination sites are occupied by oxygen atoms deriving from acetyloacetonate units, which simply act as chelating terminal ligands. In 2008, Biswas and co-workers reported[82] the synthesis of a Zn_5 complex with the same structural characteristics (Figure 1.6), formulated as $[Zn_5(bta)_6(acac)_4]$ (**1.21**), based on the room temperature reaction of $Zn(acac)_2$ and Hbta in CH_2Cl_2.

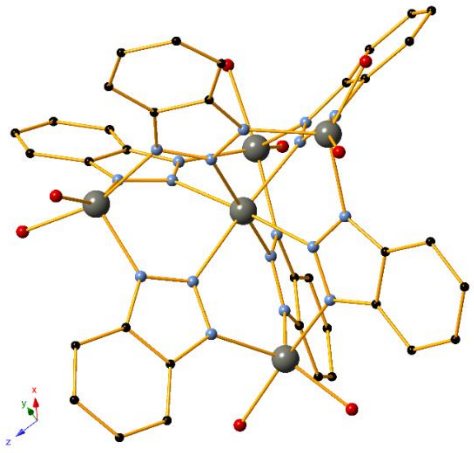

Figure 1.6. The pentanuclear motif as observed in compound **1.21**. Hydrogen atoms and parts of the acetyloacetonates are omitted for clarity. Colour code Zn (grey), C (black), N (light blue), O (red).

Interestingly, a study[83] by Raptopoulou and co-workers in 2009 showed that the same reaction in DMF yields the analogous compounds $[Zn_5(bta)_6(acac)_4(DMF)]\cdot DMF$ and $[Zn_5(bta)_6(acac)_4(DMF)]\cdot 3.7DMF$ (**1.22** and **1.23**), however higher nuclearity may be achieved when the reaction takes place at high temperature and in the presence of pyrazine. The afforded product in this case is a nonanuclear compound, formulated as $[Zn_9(bta)_{12}(acac)_6]\cdot 6DMF$ (**1.24**). Its structure contains seven Zn^{II} centres that are found at the corners of two corner-sharing imaginary tetrahedra, and a Zn^{II} ion at the centre of each tetrahedron (Figure 1.7). As such, this motif may be best described as the addition of two tetrahedral units from **1.21** with the abstraction of one Zn^{II} centre and two $acac^-$ molecules. The benzotriazole molecules also exhibit a similar coordination mode. Further efforts[84] by Volkmer's group resulted in the construction of two more nonanuclear complexes with similar structural motif and coordination characteristics, formulated as $[Ni_9(bta)_{12}(NO_3)_6(MeOH)_6]\cdot 4THF$ (**1.25**) and $[Co_9(bta)_{12}(MeOH)_{18}]\cdot(NO_3)_6\cdot 9C_6H_6$ (**1.26**). Instead of pyrazine, the authors employ a very large excess of Hbta during the synthetic procedure, with metal:ligand ratios of 1:4 and 1:8 respectively. Due to this, the excess ligand acts as the base to deprotonate the coordinated bta molecules. Additionally, magnetic measurements were also performed for **1.25 – 1.26**, revealing the presence of antiferromagnetic interactions between the metal ions in each case.

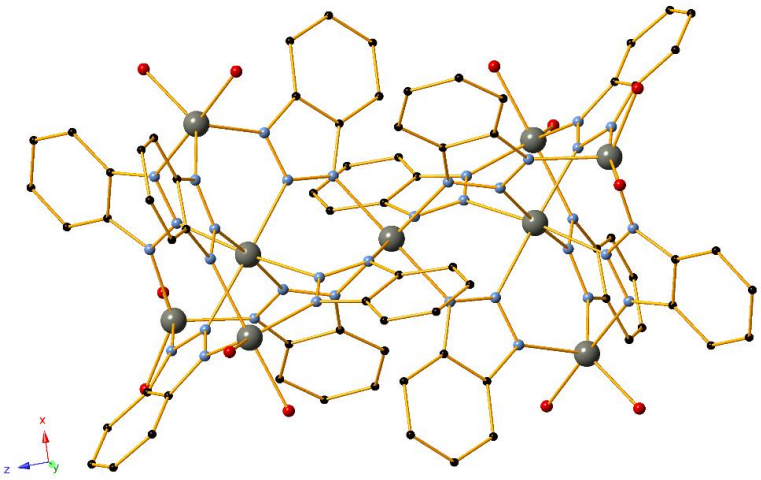

Figure 1.7. The nonaanuclear motif as observed in compound **1.24**. Hydrogen atoms and parts of the acetyloacetonates are omitted for clarity. Colour code Zn (grey), C (black), N (light blue), O (red).

Another example of the pentanuclear structural motif was reported by Yuan and co-workers, who synthesized a mixed valent complex that contains four Cu^{I} ions in the corners of the imaginary tetrahedron and a Cu^{II} ion in the centre[85]. The resulting compound is formulated as $[Cu^{II}Cu^{I}_4(bta)_5Cl(PPh_3)_4]$ (**1.27**). The bta molecules exhibit a similar coordination mode as they bind to the Cu^{II} ion through the N2 atom and bridge two Cu^{I} centres with the remaining nitrogen atoms. In this case, four PPh_3 molecules and one chloride act as the terminal ligands, with the latter also contributing to the charge balance of the complex.

Different motifs and nuclearities, however, may be achieved when M^{3+} metal sources are introduced into the synthetic procedure; this has led to the reports of several benzotriazole-based coordination clusters with interesting magnetic properties. In a series of studies[86–88] Jones and co-workers utilize the physical properties and multimodal capabilities of Hbta with MnF_3 to generate tri-, deca-, and hexaicosametallic Mn^{III} coordination complexes. To overcome the general insolubility of MnF_3 the authors employ Hbta as the solvent; all reactions are performed at 100°C to generate "melt" Hbta, in which the metal is soluble. This results in a simple synthetic route that does not require oxidation of Mn^{II} sources. The trinuclear species $[NHEt_3]_2[Mn_3O(bta)_6F_3]\cdot 2MeOH$ (**1.28**) consists of an anionic $[Mn_3O(bta)_6F_3]^{2-}$ unit in which a central μ_3-bridging oxide links three Mn^{III} centres which are found in a triangular arrangement (Figure 1.8, upper left). Deprotonated benzotriazole units provide further bridging in a $\mu_{1,2}$-fashion as each bta molecule coordinates to two Mn^{III} ions along the edge of the imaginary triangle. The unbound nitrogen atoms form strong O-H···N hydrogen bonds with the lattice methanol solvents to further stabilize this architecture. The use of pyridine, a weaker but coordinating base, increases the aggregation of these units into larger fragments and results in the formation of a decanuclear complex formulated as $[Mn_{10}O_6(OH)_2(bta)_8(py)_8F_8]\cdot 0.75H_2O\cdot 0.5Hbta\cdot 1.4MeOH$ (**1.29**). This compound contains eight edge-sharing $\{Mn_3O\}^{7+}$ triangular units as described before (Figure 1.8, upper right), with py molecules as terminal ligands and the benzotriazolate units participating again in $\mu_{1,2}$-bridging and hydrogen bonding. The protonated Hbta molecule found in the lattice also forms a strong hydrogen bond to increase framework stability. When no base is used during synthesis, aggregation of the $\{Mn_3O\}^{7+}$ units increases even further and results in a hexaicosanuclear compound $[Mn_{26}O_{17}(OH)_8(OMe)_4F_{10}(bta)_{22}(MeOH)_{14}(H_2O)_2]\cdot MeOH$

(**1.30**, Figure 1.8 bottom). The versatility and role of the benzotriazole units is critical for the formation of **1.30**. All 22 units are deprotonated, contributing to the charge balance; four of these exhibit a $\mu_{1,2,3}$-bridging coordination mode, using all nitrogen atoms to coordinate to Mn^{III} ions. The remaining eighteen molecules participate in $\mu_{1,2}$-bridging instead, as the third nitrogen atom forms hydrogen bonds with nearby MeOH, H_2O or OH^- units. Magnetochemical investigations for compounds **1.28 – 1.29** showed that the respective $\chi_M T$ values decrease as temperature decreases, indicating the presence of dominant antiferromagnetic exchange interactions between the metal ions. Additional studies for **1.30** showed that the compound displays single-molecule magnet (SMM) behaviour, i.e. exhibiting magnetization which is of molecular origin, thus retaining it even after the removal of the external field. In particular, **1.30** showed magnetisation relaxation at low temperatures below 1.2 K.

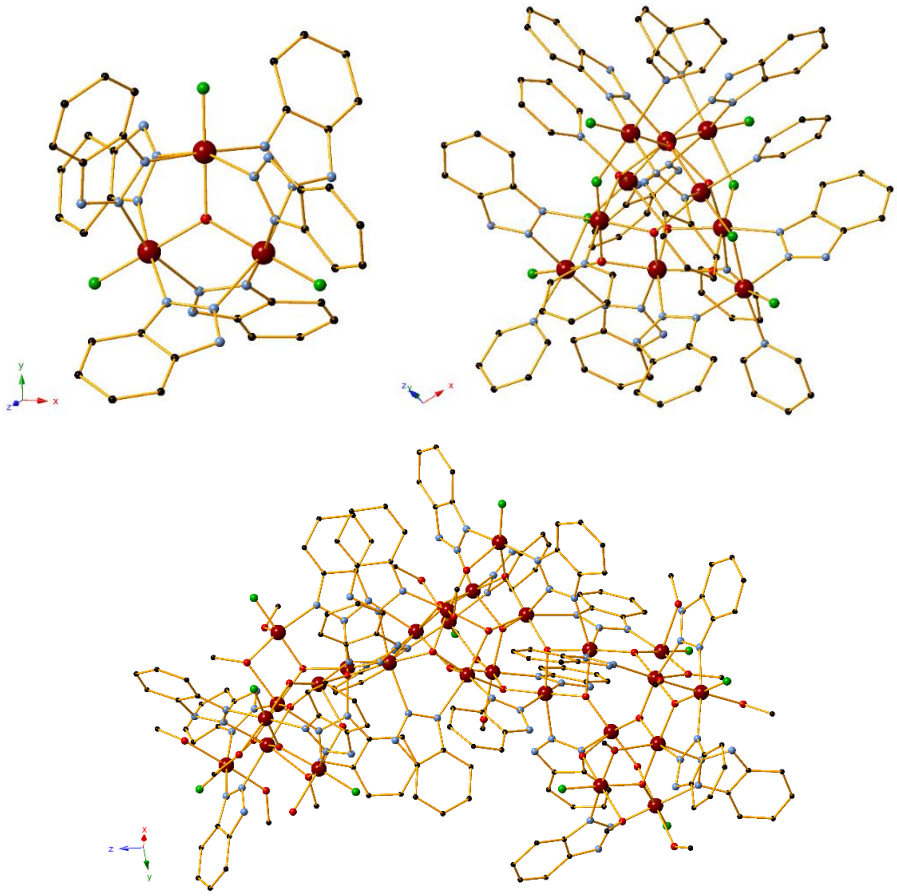

Figure 1.8. (upper left) The anionic trinuclear unit found in compound **1.28**. (upper right) The structure of the decanuclear complex **1.29**. (bottom) The structure of the

hexaicosanuclear compound **1.30**. Hydrogen atoms and all lattice molecules are omitted for clarity. Colour code Mn (maroon), C (black), N (light blue), O (red), F (green).

Similar investigations with various Fe^{III} sources led to the construction of two more polynuclear complexes, formed as $[Fe_5O_2(OMe)_2(bta)_4(Hbta)(MeOH)_5Cl_5]$ (**1.31**) and $[Fe_{14}(bta)_6O_6(OMe)_{18}Cl_6]$ (**1.32**) respectively[89,90]. The former compound exhibits a structural motif that is similar to the one described in compound **1.21**; however, in this case a protonated Hbta unit is also observed, acting as a terminal ligand to one of the Fe^{III} centres. All benzotriazole molecules participate in extensive hydrogen bonding as well as π···π interactions with other Fe_5 clusters in the lattice. Magnetic studies point to an antiferromagnetic coupling of the central Fe^{III} ion to the peripheral metal ions which gives rise to a spin ground state of S = 15/2. In contrast, the tetradecanuclear compound **1.32** was afforded under solvothermal synthetic conditions and shows a completely different motif, consisting of a central hexagonal Fe_6 ring that is linked to a $[Fe_4(bta)_3Cl_3]$ unit on either side through methoxide and oxide bridges (Figure 1.9). All benzotriazolate units exhibit a $\mu_{1,2,3}$-bridging mode, while chloride anions are also present and act as terminal ligands. **1.32** exhibits a very large ground spin state of S = 25, which is attributed by the authors to the competition of antiferromagnetic exchange interactions within the cluster. An analogous synthetic procedure was performed with Cr^{III} and V^{III} sources in a subsequent study to generate the isoskeletal compounds $[Cr_{14}(bta)_6O_6(OMe)_{18}Cl_6]$ (**1.33**) and $[V_{14}(bta)_6O_6(OMe)_{18}Cl_6]$ (**1.34**), however the magnitude of the exchange interactions appears to be much smaller in this case as both complexes were found to have S = 0 spin ground states[90].

In order to obtain compounds with improved SMM behaviour, Layfield and co-authors explored the capabilities of benzotriazole using lanthanide sources[91]. More specifically, reactions with $DyCp_3$ (Cp = cyclopentadienyl) and Hbta resulted in a dimeric compound formulated as $[Cp_2Dy(bta)]_2$ (**1.35**), which was found to behave as an SMM in temperatures below ~12 K. It consists of Dy^{III} centres that are bridged by deprotonated bta ligands. Each of these ligands coordinates to one metal centre through two nitrogen atoms and to the other

one through the remaining nitrogen in a μ-η^2:η^1 bridging mode (Figure 1.10). Notably, **1.35** is one of the first benzotriazole-based complexes in organolanthanide chemistry.

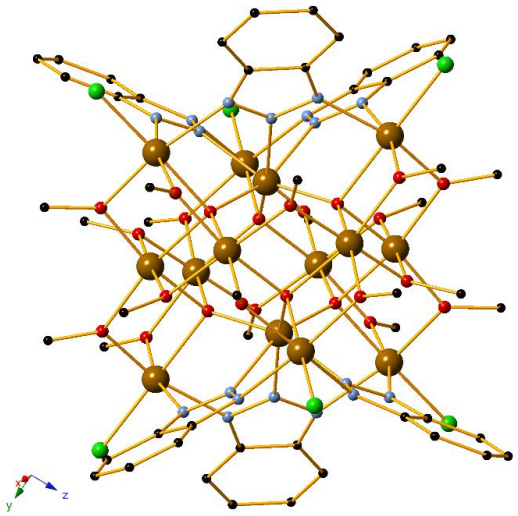

Figure 1.9. The structure of the tetradecanuclear complex **1.32**. Hydrogen atoms are omitted for clarity. Colour code Fe (brown), C (black), N (light blue), O (red), Cl (green).

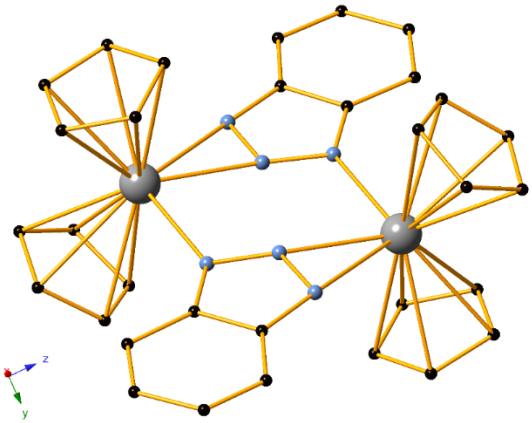

Figure 1.10. The structure of compound **1.35**. Hydrogen atoms are omitted for clarity. Colour code Dy (grey), C (black), N (light blue).

Coordination Polymers

Apart from the formation of zero-dimensional polynuclear coordination clusters, Hbta has also been identified as a suitable linker towards the design of coordination polymers under appropriate synthetic parameters. Few examples of such compounds exist in the literature.

For instance, Shao and co-authors report the isolation of a three-dimensional CP with helix-like network, formulated as $[Zn(bta)_2]$ (**1.36**) under harsh hydrothermal conditions[92]. The framework in **1.36** comprises of tetrahedral zinc centre nodes that are considered asymmetrical, as they are linked through bridging $\mu_{1,3}$-bta molecules with different directions (Figure 1.11).

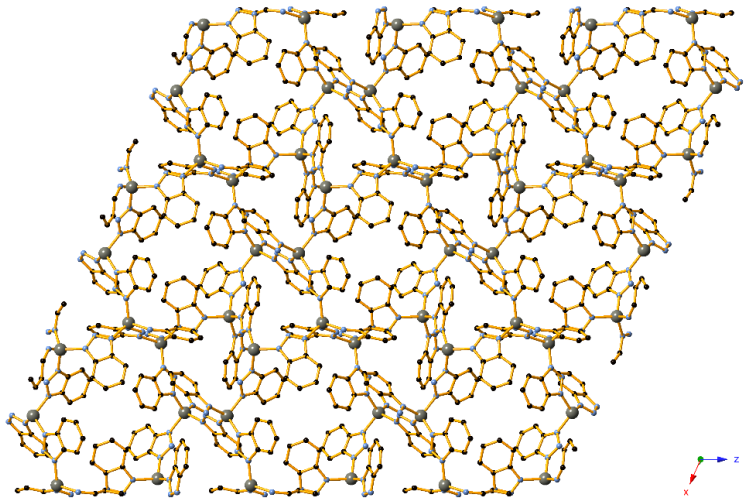

Figure 1.13. Part of the 3D architecture in compound **1.36**. Hydrogen atoms are omitted for clarity. Colour code Zn (grey), C (black), N (light blue).

Furthermore, in a series of studies by Müller-Buschbaum's group various lanthanide sources are employed to produce several CPs with different dimensionalities as the coordination capabilities of Hbta are utilized in full effect[93–96]. In this synthetic procedure the reactants are first heated to 100-120°C to form "melt" Hbta and are then subjected to solvothermal conditions for several days. The method affords 1D CPs that exhibit a chain framework based on a $[Ln(bta)_x(Y)]$ backbone, where Y is a neutral ligand species that is either Hbta or one of its thermal decomposition products, in this case phenylene-diamine or ammonia. These CPs are $[La(bta)_3(Hbta)]$, $[Ce(bta)_3(Hbta)]$, $[Pr(bta)_3(Hbta)]$, $[Nd(bta)_3(Ph(NH_2)_2)]$, $[Tb(bta)_3(Ph(NH_2)_2)]$, $[Yb(bta)_3(Ph(NH_2)_2)]$, $[Ho_2(bta)_6(Hbta)(NH_3)]$ and $[Eu^{II}(bta)_2(Hbta)_2]$ (**1.37 – 1.44**). **1.37 – 1.42** exhibit deca-coordinated lanthanide centres and two different coordination mode are seen in the benzotriazole ligands. In the first one, the ligand shows a μ-η^2:η^1 binding mode, coordinating to one Ln centre through two nitrogen atoms while the third nitrogen coordinates to a neighbouring Ln ion. In the second type of bta ligands the

third nitrogen atom does not coordinate and instead participates in hydrogen bond interactions. The coordination sphere of the Ln ion is filled by either Hbta of $Ph(NH_2)_2$ molecules which bind through two nitrogen atoms. **1.43** exhibits a ladder-like framework which contains nona-coordinate holmium centres; the bta ligands are either in a similar μ-η^2:η^1 binding mode or a $\mu_{1,3}$-bridging type. **1.44** presents a rare case of a divalent lanthanide compound and its Eu^{II} centres are octa-coordinated. To add to this structural variety, crystal transformations of **1.37**, **1.38** and **1.43** were induced in temperatures up to 350°C: in these conditions the neutral ligands are removed from the frameworks and are replaced by symmetry related bta molecules which increase the dimensionality, leading to the 3D CPs $[La(bta)_3]$, $[Ce(bta)_3]$ and $[Eu^{II}(bta)_2]$ (**1.45 – 1.46**).

In another notable example Lin and co-authors presented[97] the first crystal structure of a coordination polymer containing Cu^I sources and Hbta, a feat of significant importance as it could shed light in the mechanistic investigations of the aforementioned corrosion inhibiting effect of benzotriazole in metallic copper. The compound is formulated as $[Cu^I_2(bta)_2]$ (**1.47**) and its structure contains crystallographically independent Cu centres that exhibit linear, trigonal and tetrahedral geometry respectively. These metal ions are linked by $\mu_{1,2,3}$-bridging type deprotonated benzotriazole molecules, as the framework extends to form a 1D chain (Figure 1.12). The formation of $\pi\cdots\pi$ stacking interactions between these bta units further increases the stability of the architecture.

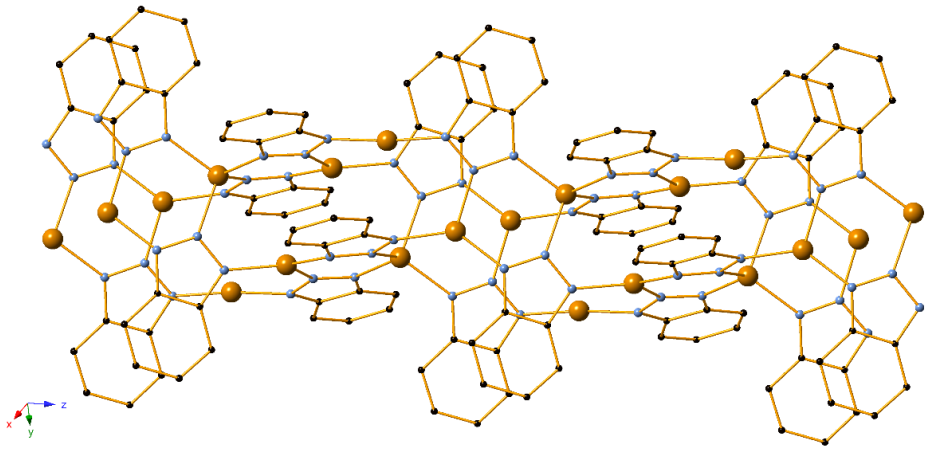

Figure 1.12. Part of the polymeric 1D network in compound **1.47**. Hydrogen atoms are omitted for clarity. Colour code Cu (orange), C (black), N (light blue).

1.2.2.2.2. Benzotriazole as a co-Ligand

A significant portion of studies have incorporated Hbta in coordination chemistry as a potential co-ligand. More specifically, it has been used as a supporting linker in the construction of CPs due to its versatility in coordination modes and bridging capabilities. From a structural point of view, the role of Hbta falls under one of the following categories: i) it forms stable polynuclear coordination clusters which in this case are used as building blocks and are linked by a second ligand (usually of *O*-donor type), forming multi-dimensional materials, ii) it acts as a supporting pillar in otherwise existing metal:ligand frameworks, occupying the remaining coordination sites and increasing the dimensionality of the structure. Some examples of both categories will be presented herein.

Several attempts have been made to utilize the well-established $[M^{II}_5(bta)_6]^{4+}$ unit as a secondary building block and introduce a polytopic bridging co-ligand. The first relevant report came from Bai and co-authors who used $[M_5(bta)_6(NO_3)_4(H_2O)_4]$ ($M = Co^{II}$ or Ni^{II}) as the node, then introduced LiTCNQ (TCNQ = 7,7,8,8-tetracyano-p-quinodimethane) for its radical anions to replace the nitrate and water molecules and occupy their coordination sites[98]. This stepwise assembly led to the synthesis of 3D diamond-like networks (**1.48** and **1.49**) based on the $[M_5(bta)_6(TCNQ^{\cdot-})_4]$ backbone (Figure 1.13). It is worth noting that this benzotriazolate polynuclear node retains its structural stability during this procedure.

Subsequently, employment of the analogous Zn^{II} cluster as precursor along with the introduction of linear polycarboxylates as co-ligands led to additional CPs of similar fashion. Wang and co-workers report the compounds $[Zn_5(bta)_6(bdc)_2(H_2O)_2]$, $[Zn_5(bta)_6(abdc)_2(H_2O)_2]$ and $[Zn_5(bta)_6(bpdc)_2(H_2O)_2]$ (**1.50** – **1.52**, where H_2bdc = 1,4-benzenedicarboxylic acid, H_2abdc = 2-amino-1,4-benzenedicarboxylic acid and H_2bpdc = 4,4'-biphenyldicarboxylic acid), which also exhibit similar 3D microporous diamondoid networks[99]. Similar rational synthesis using 1,4-naphthalenedicarboxylic acid (H_2ndc) by Deng *et al*. led to $[Zn_5(bta)_6(ndc)_2(H_2O)]$ (**1.53**), which exhibits a 3D framework with different topology due to the added steric hindrance of the naphthalene-based co-linker[100]. **1.53** was also tested for its luminescent properties, showing solvent-dependent activity.

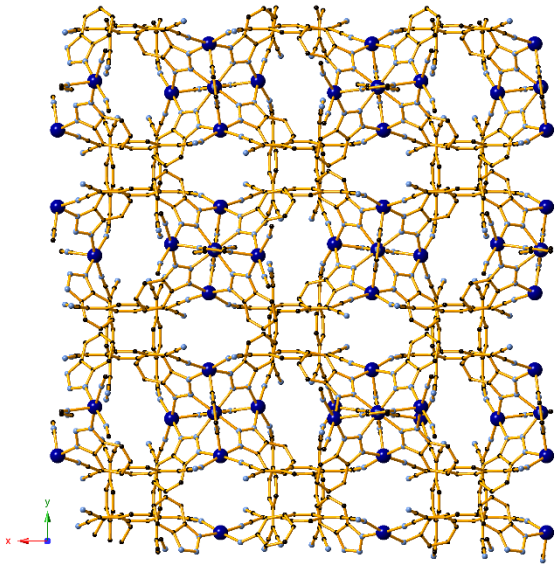

Figure 1.13. View of the diamonoid 3D network found in compound **1.48**. Hydrogen atoms are omitted for clarity. Colour code Co (blue), C (black), N (light blue).

Another diamond-like 3D interpenetrated framework, $[Zn_5(bta)_6(tda)_2]$ (**1.54**, H_2tda = thiophene-2,5-dicarboxylic acid) was reported by Zhang and co-authors, showing selective gas sorption of C_2H_2 or CO_2 over CH_4 at room temperature[101]. Chen and others employed tritopic polycarboxylates (H_3qbtcb = 4,4´,4´´-[1,3,5-benzenetriyltris(carbonylimino)]tris(benzoate) and H_3tbtcb = 3,3´,3´´-[1,3,5-benzenetriyltris(carbonylimino)]tris(benzoate)) as co-linkers using a one-pot synthesis instead of the step-wise assembly[102]. This resulted in the two compounds $[Zn_5(bta)_6(qbtcb)(H_2O)(NO_3)]$ and $[Zn_9(bta)_{12}(tbtcb)_2]$ (**1.55** and **1.56**). The structural characteristics of the cluster building blocks and the behaviour of the bta molecules are similar compared to the pentanuclear and nonanuclear clusters **1.21** and **1.24** respectively, indicating that the formation and stability of such species is heavily favoured regardless of the synthetic method. In both products the structure extends to form microporous 2D networks which exhibited selective uptake of CO_2 over CH_4 and N_2 at room temperature, when guest solvents are removed.

A similar one-pot synthesis was also used by Tan and co-authors[103] to generate a compound based on the analogous pentanuclear Nickel analogue and isonicotinic acid (H_2ina). $[Ni_5(bta)_6(ina)_3(H_2O)(CH_3COO)]$ (**1.57**) reveals a porous 2D layer as the co-linker

coordinates to metal centres through both its pyridinic and carboxylic groups (Figure 1.14). **1.57** also showed selective CO_2 adsorption over CH_4 in its framework.

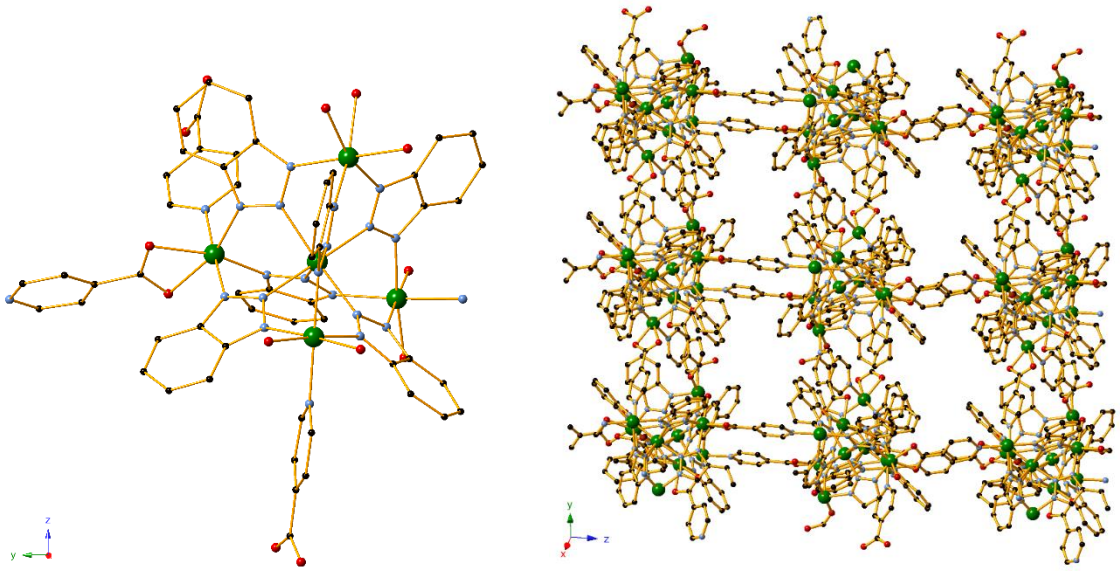

Figure 1.14. The building unit (left) and the porous 2D layer in compound **1.57** along the *b0c* plane (right). Hydrogen atoms and certain solvent molecules are omitted for clarity. Colour code Ni (green), C (black), N (light blue), O (red).

Other types of building block clusters (and consequently, different resulting frameworks) may also be achieved depending on parameters such as the synthetic conditions, the type of co-linker or the binding preference and available coordination sites of the selected metal. For example, Zhong and co-workers report[104] the construction of a 2D layered compound $[Cd_5(bta)_6(bdc)_2(DMF)_4(H_2O)_2]$ (**1.58**) which contains the common pentanuclear motif and the co-ligand H_2bdc, synthesized in room temperature. However, a similar reaction under intense solvothermal conditions promotes the coordination of more bdc molecules over bta and affords the heptanuclear complex $[Cd_7(bta)_2(bdc)_6(DMF)_8]$ (**1.59**). In this case the compound contains two inner trinuclear $[Cd_3(bta)]^{5+}$ cluster units in which the Cd centres are found in a triangular arrangement and are bridged by $\mu_{1,2,3}$-bta molecules (Figure 1.15, left). These units are linked by bdc ligands as the frameworks extends to form a CP with 3D architecture.

Li and co-workers reported another 3D CP based on a trinuclear benzotriazole-built unit, using Co^{II} sources and 1,3-benzenedicarboxylic acid (H_2mbdc) under harsh solvothermal conditions[105]. The afforded compound [Co_4(mbdc)$_3$(bta)$_2$(EtOH)$_2$] (**1.60**) contains tricobalt building blocks bridged by $\mu_{1,2,3}$-bta molecules, with the metal centres forming a rod-shaped chain arrangement (Figure 1.15, right).

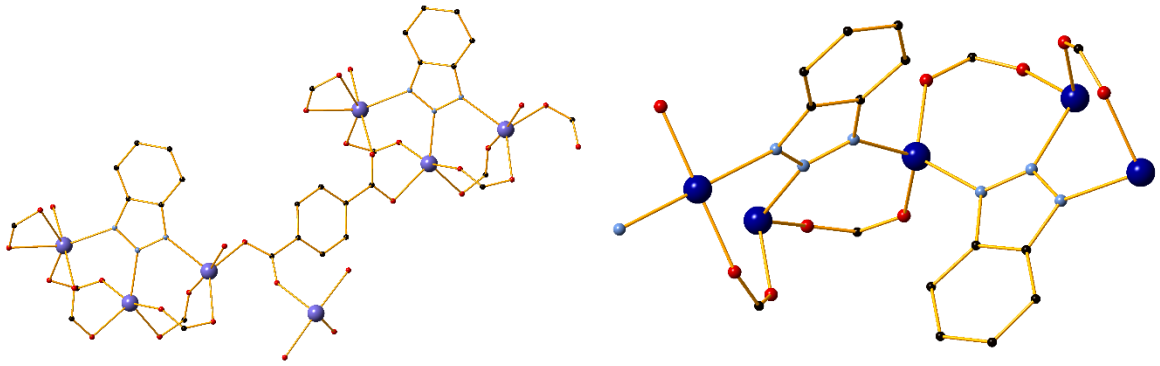

Figure 1.15. The polynuclear building units observed in compounds **1.59** (left) and **1.60** (right). Hydrogen atoms are omitted for clarity. Colour code Cd (light purple), Co (blue), C (black), N (light blue), O (red).

A different bta-based building block cluster is reported in the cationic framework [Zn_4(bta)$_3$(ipa)$_6$] (**1.61**, H_2ipa = isophthalic acid) constructed by Qin and co-authors[106]. Synthesized solvothermally at 160°C, its structure contains unusual plate-like [Zn_4(bta)$_3$]$^{5+}$ units that act as six-coordinated nodes as they are bridged by ipa ligands to form a 3D architecture. Each of these units presents three zinc centres in a triangular arrangement, connecting to the N1, N3 atoms of the bta molecules. A fourth metal ion is found at the centre of this unit, coordinating to the N2 atoms of the benzotriazoles (Figure 1.16, left).

Finally, an unusual heptanuclear [Zn_7(bta)$_7$(oadbc)(μ_3-OH)$_2$(μ_2-OH)$_2$] complex (**1.62**, H_3oadbc = 5-oxyacetatoisophthalic acid) was synthesized by Shao and co-workers, who reacted zinc acetate and H_3oadbc at 180°C for several days[107]. The structure of **1.62** is rather complicated and is based on a rare hexa-zinc subunit that is best formulated as [Zn_6(bta)$_4$(μ_3-OH)$_2$], containing four zinc atoms in a near planar metallomacrocyclic motif as well as two zinc centres inside this cyclic cavity. These ions are connected by $\mu_{1,2,3}$-bta and μ_3-OH

moieties (Figure 1.16, right). The extended framework is three-dimensional as these sub-units are linked by oadbc ligands and $\mu_{1,3}$-bta molecules, while the uncoordinated central N atoms in these benzotriazoles participate in structure-stabilizing hydrogen bonding interactions.

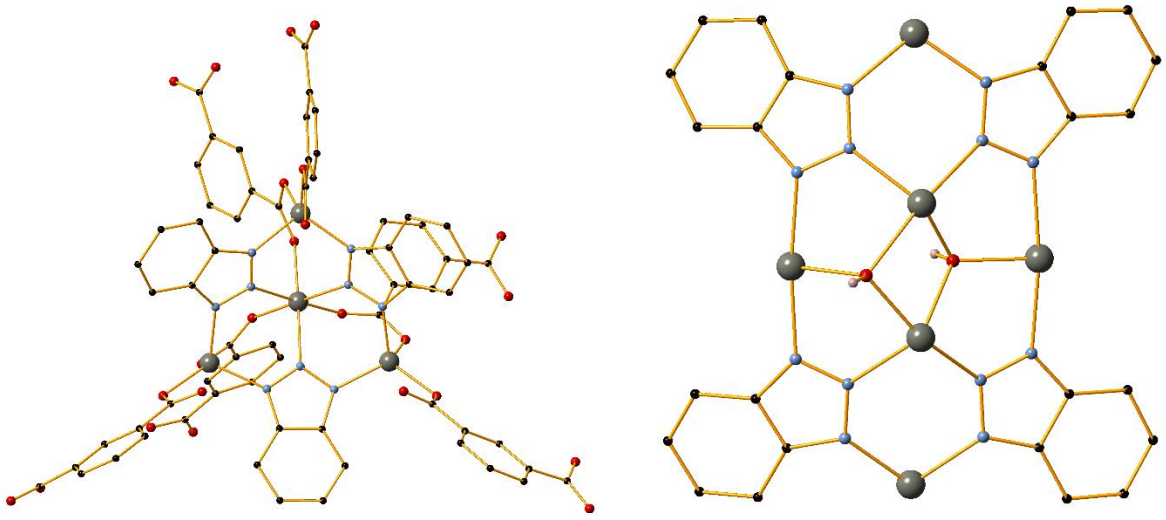

Figure 1.16. The polynuclear building units observed in compounds **1.61** (left) and **1.62** (right). Certain hydrogen atoms are omitted for clarity. Colour code Zn (grey), C (black), H (light pink), N (light blue), O (red).

In regards to the latter category, in which Hbta is utilized as a secondary pillar to increase the dimensionality of coordination compounds, most studies employ carboxylate-based ligands as primary linkers. In order to promote this outcome over the formation of benzotriazole-based cluster building blocks, the synthetic method typically involves careful adjustment of the mixture's pH (usually to 7-8) in accordance to the pKa value of the primary linker in each case. The solution is then subjected to solvothermal conditions for several days. Such procedures are reported in the formation of compounds $[Co_5(\mu_3\text{-}OH)_2(bdc)_3(bta)_2]$, $[Zn_5(\mu_3\text{-}OH)_2(bdc)_3(bta)_2]$, $[Co(cdc)_{0.5}(bta)]$, $[Zn(cdc)_{0.5}(bta)]$, $[Zn(apa)_{0.5}(bta)]$, $[Zn(gta)_{0.5}(bta)]$, $[Co_3(D\text{-}cam)_2(bta)_2]$, $[Zn_3(D\text{-}cam)_2(bta)_2]$, $[Co_3(sdba)_2(bta)_2]$ and $[Cd_2(bpt)(bta)(DMF)]$ (**1.63 – 1.72**, H_2cdc = 1,4-cyclohexanedicarboxylic acid, H_2apa = adipic acid, H_2gta = glutaric acid, D-H_2cam = D-camphoric acid, H_2sdba = 4,4´-dicarboxybiphenyl sulfone and H_3bpt = biphenyl-3,4´,5-tricarboxylic acid)[108–112]. In compounds **1.63** – **1.68** the bta units bridge

metal centres in a $\mu_{1,3}$-fashion to form a M-bta 1D chain, thus increasing the dimensionality of the framework (Figure 1.17). The architectures in the remaining compounds are based on $[M_3(bta)_2(CO_2)_4]$ nodes which contain both linkers and are connected by $L_{carboxylate}$ molecules. In these examples bta adopts a $\mu_{1,2,3}$-bridging coordination mode.

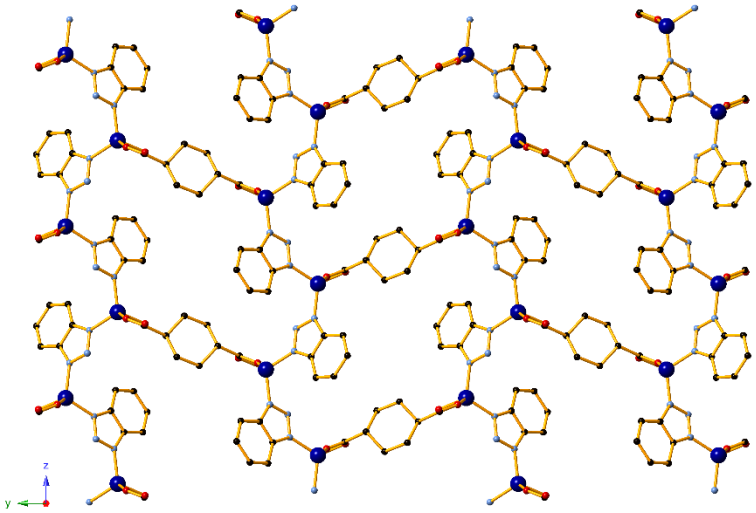

Figure 1.17. Part of the 2D network in compound **1.65** along the *b0c* plane. Hydrogen atoms are omitted for clarity. Colour code Co (blue), C (black), N (light blue), O (red).

A relevant example using non-carboxylate linkers was presented in 2009 by Herchel and co-workers, who opted to use a 0D metalloligand based on Fe^{III} and the salen ligand (salen = *N*,*N*′-Ethylenebis(salicylimine))[113]. The addition of Hbta induces dimensionality and leads to a 1D chain as the $[Fe(salen)]^{1+}$ nodes are bridged by $\mu_{1,3}$-bta molecules to generate [Fe(salen)(bta)] (**1.73**). This compound also showed promising anti-tumour activity against various cancer cell lines.

1.2.2.2.3. Benzotriazole Derivatives as main Ligands

Many derivatives of Hbta have also been used as ligands in coordination chemistry. This section includes: i) benzotriazolates with added functional groups in the 5´ (or 5´,6´) position(s). These compounds retain their triazole moiety intact for coordination and are generally available at low cost. The most common examples are 5-methylbenzotriazole (MebtaH), 5-chlorobenzotriazole (ClbtaH), benzotriazole-5-carboxylic acid (H_2btca), 5,6-

dimethylbenzotriazole (Me_2btaH) and 5,6-dimethoxybenzotriazole (OMe_2btaH). ii) *N*-substituted benzotriazoles (in either the 1´ or 2´ position), which only offer two nitrogen atoms for metal coordination. However, due to the synthetic versatility of Hbta they also provide extended options in ligand design and flexibility.

C-substituted Benzotriazole Derivatives

In regards to this category, employment of M^{II} sources with MebtaH, ClbtaH, Me_2btaH or OMe_2btaH as the main ligand again seems to favour the formation of polynuclear coordination clusters with no major differences compared to the analogous Hbta-based compounds mentioned before, despite the presence of additional chemical groups with potential steric hindrance. As a result, the reported[82,90,114–117] penta-, nona- and tetradecanuclear compounds $[Zn_5Cl_4(Me_2bta)_6]$, $[Zn_9(Me_2bta)_{12}(CH_3COO)_6]$, $[Zn_9Cl_6(OMe_2bta)_{12}]$, $[Fe_{14}O_6(Mebta)_6(OMe)_{18}Cl_6]$, $[Fe_{14}O_6(Clbta)_6(OMe)_{18}Cl_6]$, $[Fe_{14}O_6(Me_2bta)_6(OMe)_{18}Cl_6]$ (**1.74** – **1.79**) exhibit the same structural features noted in compounds **1.21**, **1.24** and **1.32** respectively. Similar isostructural complexes with a heteronuclear $\{M^{II}Zn_4\}$ (where M = Fe, Co, Cu, Ni, Ru)[82,114,115] or $\{M^{II}_3Zn_6\}$ (where M = Fe)[117] core have also been reported; in both cases, the M^{II} ions are located in the centre of the core arrangement.

Perhaps the more interesting ligand in this category, however, is H_2btca, as its carboxylate group provides additional coordination sites and accounts for completely different structures with unique features and properties. In a recent study, Lanza and co-workers report[118] the formation of a polymeric framework $[Co_3(OH)_2(btca)_2]\cdot 2DMF$ (**1.80**) which contains rhombic pores and extends to 3D as each btca unit bridges in total five Co^{II} centres through its carboxylate and triazole moieties (Figure 1.18). These centres are unsaturated (coordination number 5), as the solvent molecules do not coordinate and are instead found within the pores. This framework appears to be very flexible, showing reversible pressure-induced nucleophilic addition of guest molecules; upon increase of pressure, coordination of DMF to one of the unsaturated metal sites occurs as the framework becomes more rigid, while the introduction of MeOH results in solvent exchange and coordination to all Co sites.

After decompression, the framework retains its flexibility as the MeOH molecules are no longer coordinated.

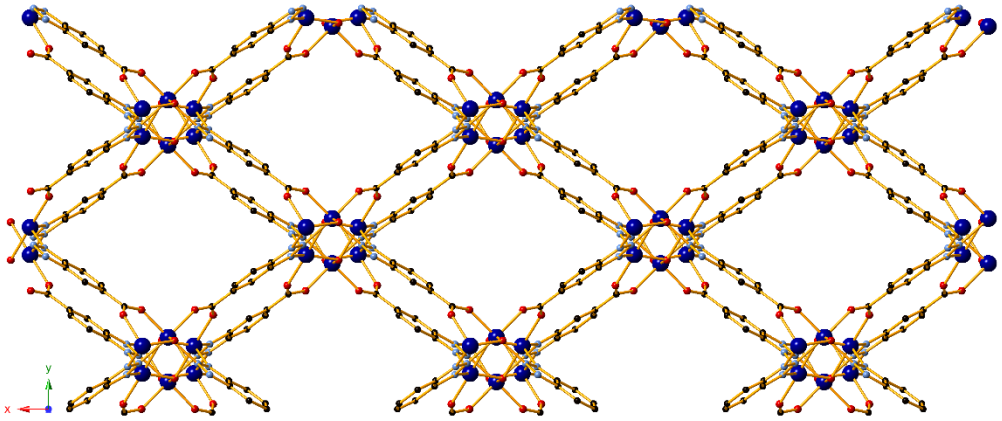

Figure 1.18. View of the rhombic 3D framework in compound **1.80**. Hydrogen atoms and solvent molecules are omitted for clarity. Colour code Co (blue), C (black), N (light blue), O (red).

A similar solvent exchange phenomenon was demonstrated[119] by Qiao *et al.* in the isoskeletal $[Co_3(OH)_2(btca)_2]\cdot 4H_2O$ (**1.81**), which upon immersion to EtOH exchanges its guest molecules to generate $[Co_3(OH)_2(btca)_2]\cdot EtOH$. Additionally, sorption properties for the desolvated compound were studied by Ren and co-authors, who showed that the framework exhibits very good CO_2 uptake of 223.7 and 104.7 mg g^{-1} at 273 and 298 K respectively[120]. Xiao and co-workers showed[121] that the isostructural zinc analogue $[Zn_3(OH)_2(btca)_2]\cdot DMF\cdot H_2O$ (**1.82**) also exhibits large flexibility and a similar "breathing effect". Controlled heating of **1.82** at 220 or 440°C yielded compounds $[Zn_3(OH)_2(btca)_2]\cdot DMF\cdot 0.5H_2O$ (**1.83**) and $[Zn_3(OH)_2(btca)_2]\cdot 2H_2O$ (**1.84**) which showed increased framework narrowing and pore shrinking as the guest molecules were gradually removed.

N-substituted Benzotriazole Derivatives

In recent years there have been several studies that explore the coordination chemistry of ligands based on 2H-benzotriazol-2-yl phenolate (BTP) derivatives towards the design of catalytic systems for ring-opening polymerization (ROP) reactions. More specifically, it has

been shown that the ROP of cyclic esters, which affords biodegradable polyesters, is best promoted by well-defined metal complexes with a limited number of active sites, preventing any side reactions. BTP ligands are therefore ideal for these purposes, offering *N*,*O*-bidentate chelation which ensures the formation of stabilized and well-defined 0D complexes. For example, Li and co-workers designed[122] [(μ-^{C8}BTP)Ti(O^{i}Pr)$_3$]$_2$ (**1.85**, ^{C8}BTPH = 2-(2H-benzotriazol-2-yl)-4-(2,4,4-trimethylpentan-2-yl)phenol, Figure 1.19), a 0D dimeric compound which was found to be an efficient catalyst in the ROP of ε-caprolactone and L-lactide, generating polymers with conversions up to 99% when the reaction occurred in toluene at 30°C and under 0.01 M of the catalyst. The latter reaction may also be catalysed by the monomeric magnesium-based compound [(^{TMCl}BTP)$_2$Mg(THF)$_2$] (**1.86**, ^{TMCl}BTPH = 2-tert-butyl-6-(5-chloro-2Hbenzotriazol-2-yl)-4-methylphenol) in 97% conversion under analogous conditions as shown by the same group[123].

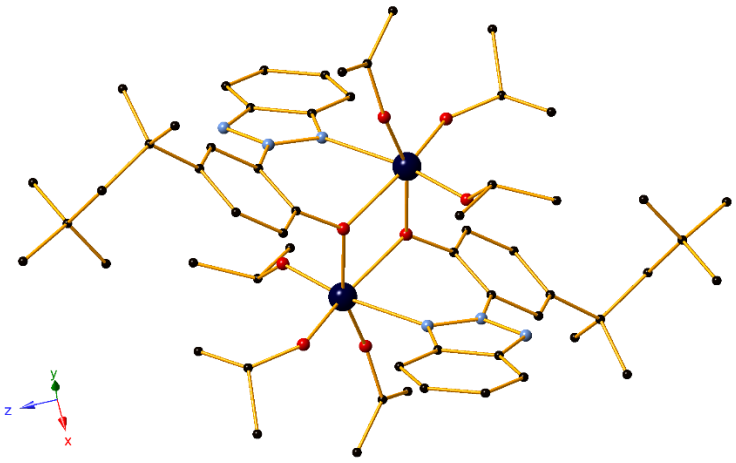

Figure 1.19. The structure of the dimeric compound **1.85**. Hydrogen atoms are omitted for clarity. Colour code Ti (dark blue), C (black), N (light blue), O (red).

In similar fashion, Chang *et al*. constructed[124] a dinuclear zinc compound using the imino-based BTP ligand 2-(2H-benzotriazol-2-yl)-6-(((2,6-dimethylphenyl)imino)methyl)-4-methylphenol (^{C1DMe}IBTPH). [(μ-^{C1DMe}IBTP)ZnEt]$_2$ (**1.87**) catalyses the ROP of ε-caprolactone and β-butyrolactone in toluene at 55°C, as well as the ROP of L-lactide in CH_2Cl_2 at 30°C. In all cases the afforded conversions are excellent (up to 99%), while only 0.01 M of **1.87** is required.

Also prevalent in the literature is the use of 1-substituted benzotriazole ligands with various groups or molecules as substituents. One of the first works that incorporated this strategy was by Richardson and Steel, who explored the chemistry of ligands pbta (1-(pyridin-2-yl)-1H-benzotriazole), pmbta (1-(pyridin-2-ylmethyl)-1H-benzotriazole) and ibta (1-(1H-benzotriazol-1-yl)isoquinoline) with Pd^{II}, Cu^{II} and Ag^{I} sources[125]. This strategy mainly afforded 0D dimers and 1D CPs where metal coordination occurs through the N3 atom of the benzotriazole moieties.

More intriguing, however, is the incorporation of a second benzotriazole unit to generate 1,1´-bis(benzotriazole) ligands with an increased number of potential coordination sites and provide controlled flexibility in the system. For this type of linkers, flexibility is typically introduced with the inclusion of alkyl chain spacer groups between the two benzotriazole units. Alkanes up to hexane have been a popular choice for these purposes, and several compounds have been reported with the respective ligands[125–131]. Most of these studies focus solely on the structural features of the compounds, as mainly $[Cu(bbtm)(NO_3)_2]$ (**1.88**, where bbtm = bis(benzotriazol-1-yl)methane, Figure 1.20) was further tested for any potential properties showing weak antiferromagnetic coupling between the Cu^{II} ions[130]. However, it is worth noting that the use of all linkers in this category consistently produced CPs with low dimensionalities, mainly one-dimensional.

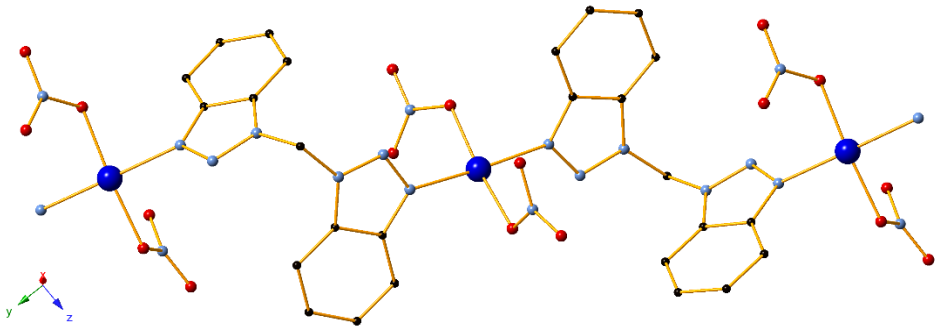

Figure 1.20. Part of the 1D framework in compound **1.88**. Hydrogen atoms are omitted for clarity. Colour code Cu (blue), C (black), N (light blue), O (red).

Analogous bis(benzotriazole)-dioxoalkane ligands have been employed using 1-hydroxybenzotriazole as the starting material, affording compounds similar to the above[132–

[134]. Notably, efforts[133] undertaken by Shit *et al*. resulted in the synthesis of isoskeletal polymeric compounds $[Cu(Br)_2(bbdp)]_2$ and $[Cu(Cl)_2(bbdp)]_2$ (**1.89** – **1.90**, where bbdp = bis(benzotriazol-1-yl)-1,3-dioxapropane) which expand to two dimensions through halide bridging. **1.89** and **1.90** exhibited antiferromagnetic ($\chi_M T$ = 0.79 cm^3 K mol^{-1} at 200 K, 0.09 cm^3 K mol^{-1} at 5 K) and ferromagnetic ($\chi_M T$ = 0.91 cm^3 K mol^{-1} at 200 K, 1.00 cm^3 K mol^{-1} at 5 K) behaviour respectively. Magneto-structural correlation studies by the authors attributed this discrepancy to the different bridging halide atom in each case.

1.3. Aim of This Thesis

Section 1.1 of this chapter explored in detail the synthetic intricacies and application range of CPs, demonstrating their popularity in the last few decades. It also highlighted the underutilization of 1D CPs which have attracted significantly lower interest compared to porous MOFs. For this reason, the primary aim of this thesis is to design 1D CPs with potential applications, focusing on magnetism and catalysis.

To achieve this goal, it was essential to develop a ligand system which would not promote the formation of rigid high-dimensional frameworks and would instead offer a certain degree of freedom for easier tuning and optimization. Emphasis was also placed on factors such as cost of reagents, general ease of chemistry and ligand novelty. Having all these in mind, it was determined that such capabilities and framework dynamism would be best provided by *N*-donor ligands that exhibit some degree of flexibility.

Benzotriazole emerged as an ideal template molecule to design such a system, due to its unique characteristics as shown in Section 1.2. Relevant literature searches (Section 1.2.2.2) showed that simple Hbta as well as *C*-substituted benzotriazoles mostly lead towards the formation of polynuclear coordination clusters. The exception to this was the ligand H_2btca, however it resulted to CPs with characteristics (3D compounds, robust M-O coordination bonds) that were unwanted for the scope of this work. Instead, it was found that the formation of low-dimensional CPs is best achieved by *N*-substituted benzotriazole ligands, especially 1,1´-bis(benzotriazole) ligands which contain spacer groups between the two benzotriazole units. Apart from promoting the desired compound dimensionalities, such linker systems

may provide a contained amount of flexibility and can be easily synthesized through *N*-alkylation (Scheme 1.16), although potential unwanted isomerism should also be considered[135]. Furthermore, it is worth noting that very few of the reported coordination compounds with this type of linkers were investigated for any applications, as more attention was paid to their structural capabilities instead. For this reason, a secondary aim of this thesis is to explore the potential of such ligands towards functional CPs.

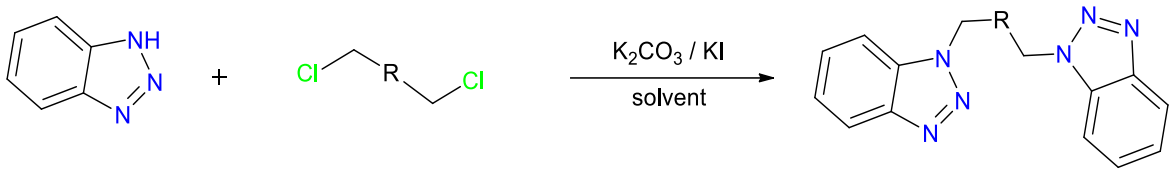

Scheme 1.16. Proposed synthesis of the 1,1´-bis(benzotriazole) ligand system.

The following chapters will present efforts made to achieve both of these targets through a series of coordination compounds synthesized by Co^{II} , $Cu^{I/II}$ and Ag^{I} sources and a family of semi-rigid benzotriazole-based ligands. These transition metals satisfy most of the criteria presented in Section 1.1.2.2, as they show ease of coordination with N atoms and can feature various geometries; they are also relatively low-cost, high-abundance metals with ease of chemistry and stability under ambient conditions. Furthermore, the magnetic properties of cobalt compounds[136], as well as the catalytic activities of systems based on copper[137] and silver[138] have been well documented in the literature.

In order to provide comparison and fully determine the role and effect of the benzotriazole moiety, additional compounds with analogous *N*-donor ligands, including bis(5-methylbenzotriazole), bis(5,6-dimethylbenzotriazole), bis(benzimidazole), bis(imidazole) were also synthesized and tested for the same properties.

Chapter 2: Exploring the coordination capabilities of a family of flexible benzotriazole-based ligands using Co^{II} sources

Abstract: This study focuses on the coordination chemistry of a family of three flexible benzotriazole-based ligands (**L^1**-**L^3**) using Co^{II} salts. These efforts have resulted to the formation of ten novel compounds, formulated as $[Co_2(\mathbf{L^1})_2Cl_4]\cdot 2MeCN$ (**1**), $Co_2(\mathbf{L^1})_2Br_4$ (**2**), $[Co(\mathbf{L^2})Cl_2]\cdot MeCN$ (**3**), $Co(\mathbf{L^2})Cl_2$ (**4**), $[Co_2(\mathbf{L^2})_2Br_4]\cdot 2MeCN$ (**5**), $[Co(\mathbf{L^2})_2(NO_3)_2]\cdot 2MeCN$ (**6**), $[Co_2(\mathbf{L^3})_2Cl_4]\cdot 2MeCN$ (**7**), $Co_2(\mathbf{L^3})_2Cl_4$ (**8**), $Co_2(\mathbf{L^3})_2Br_4$ (**9**), and $Co(\mathbf{L^3})_2(NO_3)_2$ (**10**). The structures have been well characterised through X-Ray crystallography, FT-IR, ESI-MS, PXRD, Elemental Analysis and TGA studies. The compounds show a large structural variety depending on synthetic parameters and the ligand selection. When tuned appropriately, these factors drastically affect dimensionality, metal geometry and the nuclearity of the final product, resulting in a range of 0D dimers (**1**, **3**, **5**, **8**, **9**), 1D (**2**, **7**, **10**) and 2D (**4**, **6**) CPs. A temperature-induced single-crystal to single-crystal transformation of compound **3** to **4** is additionally reported. The magnetic properties of representative compounds (**4**, **7**, **9**) are subject to large changes with only minor structural variations, suggesting that tetrahedral Co^{II} nodes in CPs could function as sensitive reporters of small changes in the local environment.

External Contributions: Nicholas F. Chilton (University of Manchester) was responsible for the collection and interpretation of magnetic and EPR data for compounds **4**, **7** and **9**. Alaa Abdul-Sada (University of Sussex) was responsible for the collection of all ESI-MS data.

2.1. Introduction

The current chapter reports the first efforts towards the development of a system providing functional CPs with low dimensionality based on *N*-donor ligands, particularly benzotriazole-derived. The construction of such a specific system remains a difficult task, despite the advances of the rational design concepts during the last few decades. As discussed in Chapter 1, the resulting architecture of CPs may be manipulated by changing the reaction conditions, leading to a large variety of structurally and topologically unique products[139–141].

However, controlling and predicting the final outcome of the self-assembly procedure remains one of the major challenges in the field[12]. The resulting products are often strongly influenced by factors such as the behaviour of a functional group in a molecule[142], the influence of the crystallization conditions and the various conformations of the components within the crystal[143].

For reasons already detailed in Section 1.3, initial approaches involved the design of 1,1´-bis(benzotriazole) ligands with flexible spacer groups between the two units. Much consideration was given to the exact level of flexibility within the linkers. To maintain an amount of control over the resulting structure while retaining the advantages of flexible linkers, it was determined that the middle ground between these two extremes would be the most sensible option. This would require the use of 'semi-rigid' ligands with a smaller degree of flexibility; such molecules have also been successfully employed to afford CPs[42,144–150]. To satisfy these conditions, a family of benzene-substituted benzotriazole molecules, namely 1,4-bis((1H-benzo[d][1,2,3]triazol-1-yl)methyl)benzene (**L^1**), 1,3-bis((1H-benzo[d][1,2,3]triazol-1-yl)methyl)benzene (**L^2**), and 1,2-bis((1H-benzo[d][1,2,3]triazol-1-yl)methyl)benzene (**L^3**) (Scheme 2.1) was designed and introduced. These ligands contain a flexible C-N bond in an otherwise rigid molecule and when coupled with different positions on the benzene ring (*para*-, *meta*- and *ortho*-substitution for **L^1**, **L^2** and **L^3**, respectively), can lead to a wide array of coordination motifs. In addition, they have been scarcely used in coordination chemistry[151,152].

Cobalt was selected as the most suitable metal for these initial investigations; it is well known that Co^{II} can adopt versatile coordination geometries and often displays large magnetic anisotropy[136,153,154]. Furthermore, detailed studies of the correlation between the coordination geometry of the metal centre and the magnetic parameters of the compounds has already been well established, especially for tetra-[155–158], penta-[159–161] and hexa-coordinated[162,163] Co^{II} complexes.

Having all these in mind, the present work aims to study the coordination capabilities of **L^1**, **L^2**, **L^3** along with Co^{II} salts as metal sources. Ten new compounds, formulated as

$[Co_2(\mathbf{L^1})_2Cl_4]\cdot 2MeCN$ (**1**), $Co_2(\mathbf{L^1})_2Br_4$ (**2**), $[Co(\mathbf{L^2})Cl_2]\cdot MeCN$ (**3**), $Co(\mathbf{L^2})Cl_2$ (**4**), $[Co_2(\mathbf{L^2})_2Br_4]\cdot 2MeCN$ (**5**), $[Co(\mathbf{L^2})_2(NO_3)_2]\cdot 2MeCN$ (**6**), $[Co_2(\mathbf{L^3})_2Cl_4]\cdot 2MeCN$ (**7**), $Co_2(\mathbf{L^3})_2Cl_4$ (**8**), $Co_2(\mathbf{L^3})_2Br_4$ (**9**), and $Co(\mathbf{L^3})_2(NO_3)_2$ (**10**) are reported. Synthetic aspects, as well as the magnetic properties of selected compounds **4**, **7** and **9** are discussed.

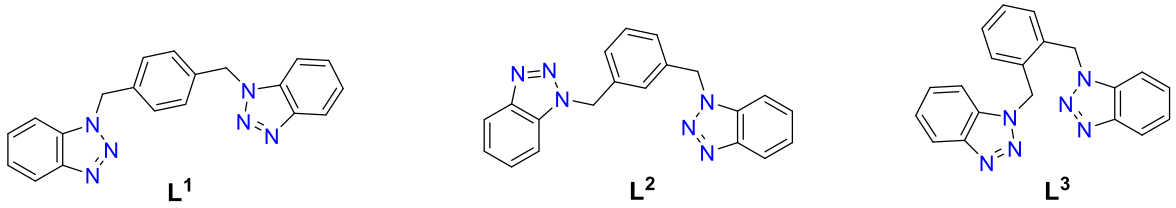

Scheme 2.1. The organic ligands $\mathbf{L^1}$, $\mathbf{L^2}$, and $\mathbf{L^3}$ used in this study.

2.2. Results and Discussion

2.2.1. Crystal Structure Description of Compounds 1 – 10

Compound **1** crystallizes in the triclinic $P\bar{1}$ space group. The asymmetric unit consists of one Co^{II} centre, one $\mathbf{L^1}$ molecule, two chlorine atoms which act as terminal ligands and an acetonitrile molecule in the lattice. X-Ray data further reveal that the structure is finite and does not extend to any dimension (Figure 2.1, upper). Co^{II} is coordinated to four atoms in a $\{N_2Cl_2\}$ environment and exhibits a slightly distorted tetrahedral geometry. In this case, the ligand adopts a boat-like conformation, and its coordination mode is presented in Scheme 2.2 (Mode A). The mean Co-N distances are 2.047(4) and 2.042(4) Å respectively, while the angles of the tetrahedron range from 105.85(12)° to 113.694(14)°. The Co-Cl distances were measured at 2.2439(14) and 2.2393(13) Å. Finally, Co···Co distance was found to be 11.5929(19) Å. While no hydrogen bonds are formed, the supramolecular architecture of the complex is formed and stabilized through inter-molecular π···π stacking interactions of the benzotriazole aromatic rings (Figure S2.1, Appendix). The values for these interactions are detailed in the Appendix (Table S2.1).

Similarly to **1**, compound **2** crystallizes in the triclinic $P\bar{1}$ space group; its asymmetric unit contains one Co^{II} centre, one $\mathbf{L^1}$ molecule and two bromide atoms which act as terminal

ligands. The arrangement of the resulting $\{N_2Br_2\}$ coordination environment around the Co^{II} centre can be described as slightly distorted tetrahedral, in which the angles of the tetrahedron range from 106.27(16)° to 112.77(5)°. As in compound **1**, the metal is coordinated to the ligand through the N3 atom of the benzotriazole units. However, in this case the ligand adopts a chair-like conformation (Scheme 2.2, Mode B). As a result, the structure is extended infinitely into one direction, forming a one-dimensional coordination polymer (Figure 2.1, lower). The Co-N and Co-Br distances are 2.021(5) and 2.030(5), 2.3709(10) and 2.3745(10) Å respectively. No hydrogen bonds or other intermolecular interactions were observed.

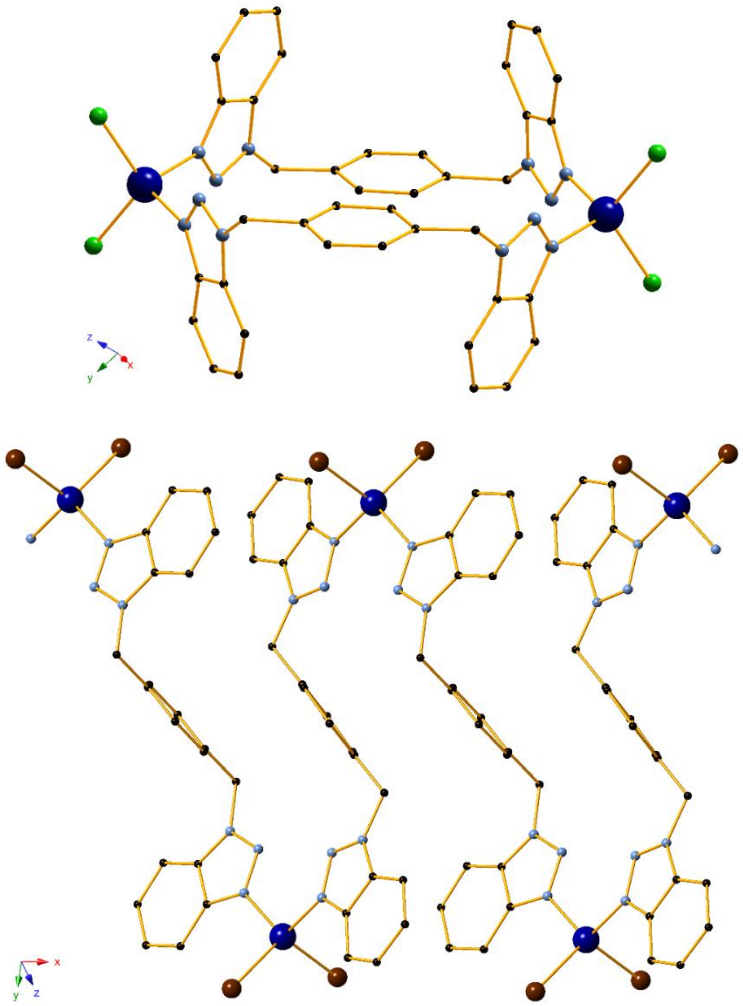

Figure 2.1. (upper) The structure of compound **1**. (lower) Part of the 1D framework of compound **2** along the *a* axis. In each case the ligand adopts a different conformation (boat

or chair). H atoms and solvent molecules are omitted for clarity. Colour code Co (blue), Cl (green), Br (brown), C (black), N (light blue).

L²-based compounds **3** and **5** are isostructural, therefore only the former will be described in detail. **3** crystallizes in the triclinic $P\bar{1}$ space group and forms a zero-dimensional dimer structure as seen in Figure 2.2. The asymmetric unit consists of one Co^{II} centre, one **L²** molecule, two chlorine atoms which act as terminal ligands and an acetonitrile molecule in the lattice. Co^{II} presents a $\{N_2Cl_2\}$ coordination environment and exhibits a slightly distorted tetrahedral geometry. The conformation (boat) and coordination sites of the ligand are detailed in Scheme 2.2 (Mode C). The mean Co-N distances are 2.0341(2) and 2.0352(2) Å respectively, while the Co-Cl distances were measured at 2.0352(17) and 2.0341(17) Å. Angles of the tetrahedron range from 100.470(8)° to 113.250(7)°. Co···Co distance was found to be 11.1122(11) Å. As in the case of compound **1**, the supramolecular architecture is further stabilized by the formation of inter-molecular π···π interactions (Figure S2.2, Appendix), as described in Table S2.2, Appendix. Again, no hydrogen bonds are formed.

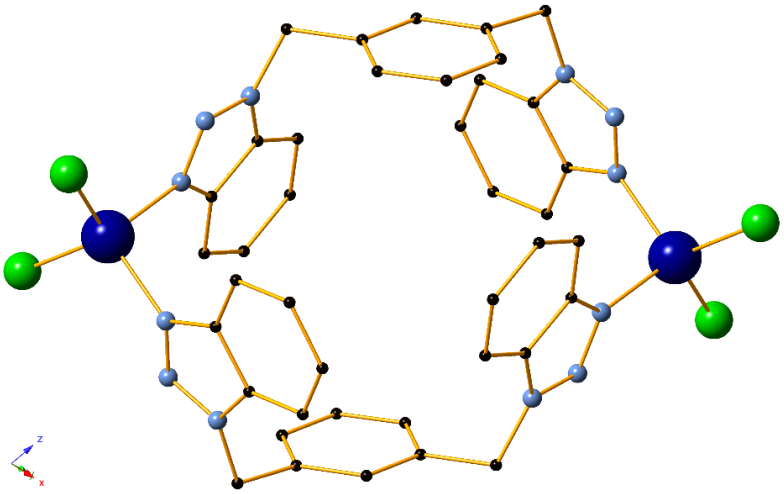

Figure 2.2. The structure of compounds **3** and **5**. X = Cl (**3**), Br (**5**). H atoms and solvent molecules are omitted for clarity. Colour code Co (blue), X (green), C (black), N (light blue).

Compound **4** crystallizes in the monoclinic space group $P2_1/c$ and its asymmetric unit consists of one Co^{II} centre, one **L²** molecule and two chlorine atoms. Co^{II} is coordinated to a total of five atoms and exhibits a distorted trigonal bipyramidal geometry ($\tau = 0.67$).[164] The basal

plane consists of one nitrogen atom from the ligand and the two chlorine atoms, while the apical positions are occupied by a nitrogen and a chlorine atom from symmetry related molecules. In contrast to compound **3**, which has the same molecular formula and its structure is zero-dimensional, the structure of **4** propagates in two directions through the formation of a chlorine bridge and the concurrent rotation of the non-rigid C-N bond (Figure 2.3, left / Scheme 2, Mode D). This results in the construction of a 2D framework, which consists of layers that are formed along the *b*0*c* plane axis (Figure 2.3, right). This packing arrangement allows for the formation of π···π inter-molecular interactions between certain benzotriazole aromatic rings, as detailed in the Appendix (Table S2.3). These weak interactions further facilitate the stability of the framework (Figure S2.3, Appendix). Considering each $Co^{II}_2Cl_2$ unit as a node, the topological evaluation of **4** results in a uninodal 4-connected **sql** network with node distances at 11.724Å.

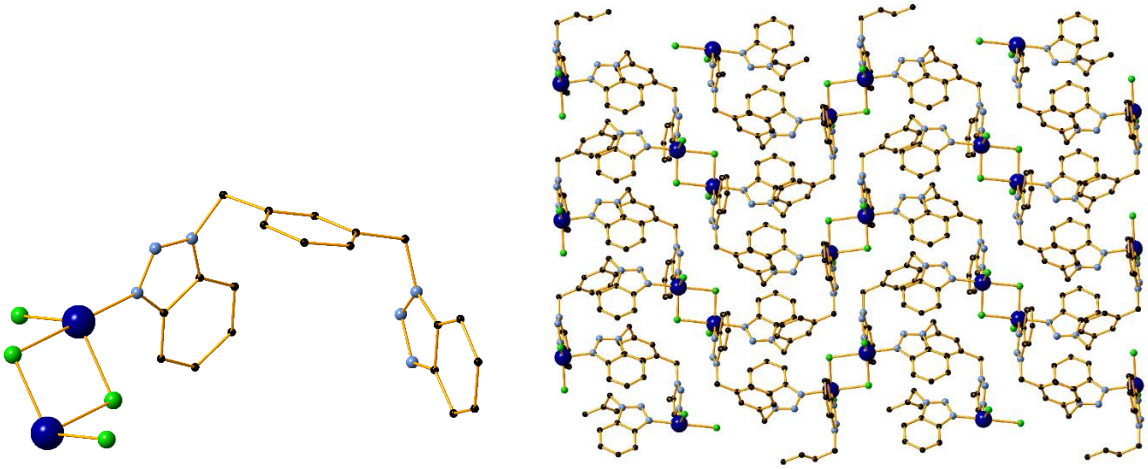

Figure 2.3. (left) The building unit of compound **4**. (right) Part of the 2D framework of compound **4** along the *b*0*c* plane. H atoms are omitted for clarity. Colour code Co (blue), Cl (green), C (black), N (light blue).

Complex **6** crystallizes in the monoclinic space group $P2_1/c$. The asymmetric unit contains a Co^{II} centre, one $\mathbf{L^2}$ molecule, one lattice acetonitrile molecule and one nitrate which acts as a terminal ligand (Figure 2.4, upper). The geometry of Co^{II} is octahedral as it is coordinated to four nitrogen atoms from $\mathbf{L^2}$ molecules, which consist the basal plane and two nitrate oxygen atoms which occupy the axial positions. The respective mean Co-N distances are at

2.15789(10) and 2.19315(8) Å, the longest observed in this Chapter. The relevant Co-O distance was measured at 2.0920(13) Å. In this case, the ligand adopts a chair conformation (Scheme 2.2, Mode E) and as a result the structure extends to two dimensions along the *b*0*c* plane axis, forming a 2D coordination polymer (Figure 2.4, lower). No hydrogen bonds or other supramolecular interactions were observed. Considering each Co^{II} centre as a node, the topological analysis of **6** results, as in the case of compound **4**, in a uninodal four-connected **sql** network with node distances at 12.908Å.

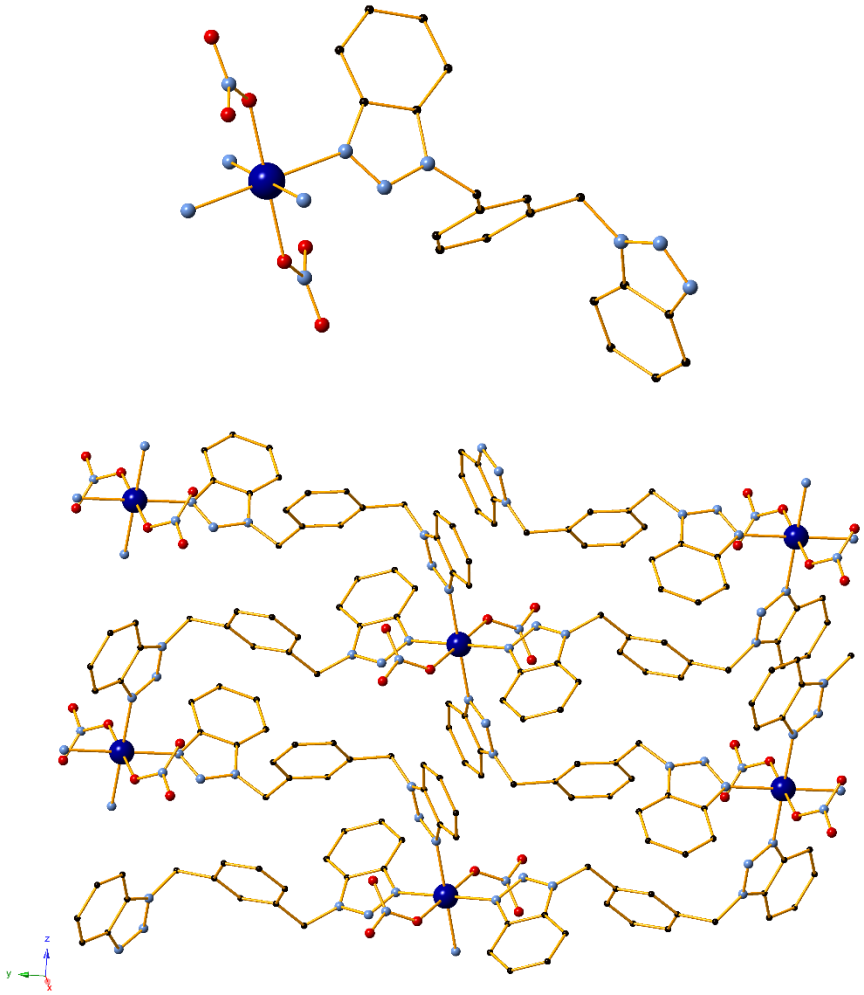

Figure 2.4. (upper) The building unit in compound **6**. (lower) Part of the 2D architecture of compound **6** along the *b*0*c* plane. H atoms and solvent molecules are omitted for clarity. Colour code Co (blue), C (black), N (light blue), O (red).

In regards to the **L^3**-based compounds, **7** was synthesized using $CoCl_2$ as the metal source and crystallizes in the monoclinic space group $P2_1/c$. The asymmetric unit consists of one Co^{II} centre, one organic ligand molecule, two chlorine atoms and a lattice acetonitrile molecule. Co^{II} is coordinated to the two chlorine atoms and to two nitrogen atoms from **L^3** and a symmetry related **L^3** molecule respectively. The metal centre therefore has a coordination number of four and exhibits a slightly distorted tetrahedral geometry, with the angles of the tetrahedron ranging from 105.402(10)° to 114.2428(14)°. The mean Co-N distance is 2.048(2) Å, and the Co-Cl distances are 2.2348(9) and 2.2254(9) Å. In this conformation of the ligand (Scheme 2.2, Mode F), the rotation of the non-rigid C-N bond brings the planes of the benzotriazole molecules to a 44.61(7)° angle. As a result, the structure propagates in one direction with the complex forming one dimensional (1D) chains that unfold in a helix-like manner (Figure 2.5).

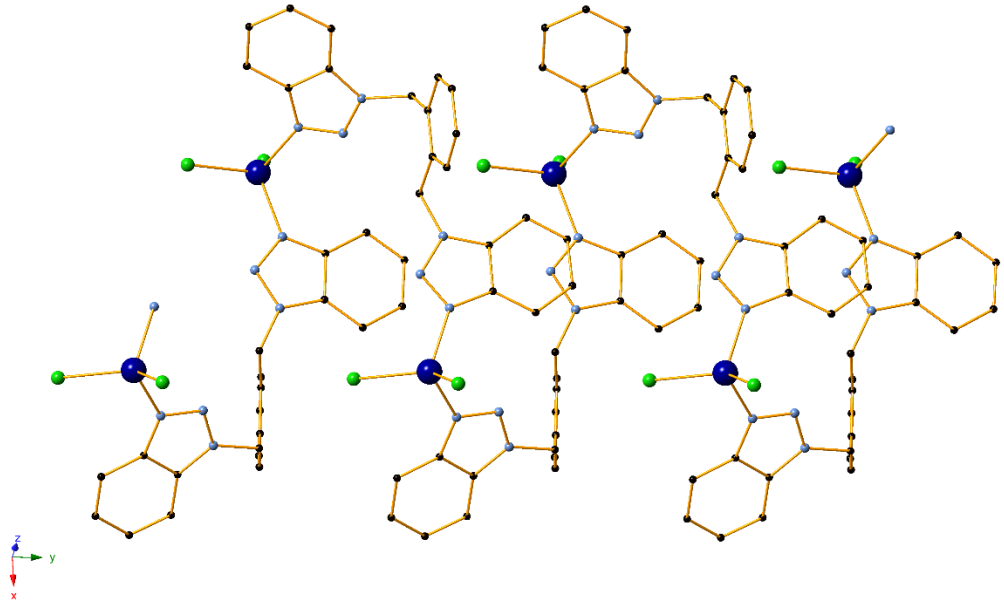

Figure 2.5. Part of the 1D framework of compound **7** along the *b* axis. H atoms and solvent molecules are omitted for clarity. Colour code Co (blue), Cl (green), C (black), N (light blue).

Compounds **8** and **9** are isostructural and as such only **8** will be described below. The compound crystallizes in the triclinic space group $P\bar{1}$. Co^{II} is coordinated to four atoms in a $\{N_2Cl_2\}$ environment and exhibits a slightly distorted tetrahedral geometry. The mean Co-N

distances are 2.041(3) and 2.032(3) Å, and the Co-Cl distances are 2.2350(13) and 2.2378(13) Å. Angles of the tetrahedron range from 104.32(14)° to 119.73(6)°. Co···Co distance was found to be 9.0147(19) Å. In this conformation of the ligand (Scheme 2.2, Mode G), the angle between the planes of the benzotriazole molecules is a 123.05(3)°. As the 1,2,3-triazole moieties are now in a different arrangement compared to **7**, compound **8** is eventually a zero-dimensional dimer structure (Figure 2.6). As in the previous dimers, inter-molecular π···π stacking interactions are formed to facilitate the stability of the supramolecular network (Appendix, Figure S2.4, lower). Additionally, there is an intra-molecular π···π interaction within the dimer, formed between the aromatic rings of benzotriazole molecules (Appendix, Figure S2.4, upper). Details for these interactions are listed in the Appendix (Table S2.4).

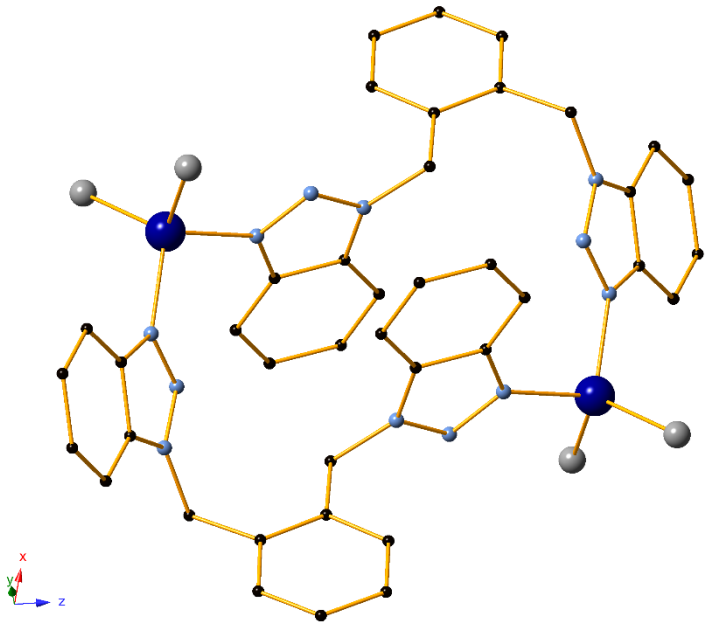

Figure 2.6. The structure of compounds **8** and **9**. X = Cl (**8**), Br (**9**). H atoms and solvent molecules are omitted for clarity. Colour code Co (blue), X (grey), C (black), N (light blue).

Finally, compound **10** crystallizes in the triclinic $P\overline{1}$ space group and contains a Co^{II} centre, a nitrate anion which acts as a terminal ligand, and one organic ligand molecule in the asymmetric unit. The metal centre is coordinated to six atoms and exhibits a distorted octahedral geometry. Four nitrogen atoms from symmetry related ligand molecules occupy the equatorial positions of the octahedron, while two nitrate oxygen atoms occupy the axial

positions. The Co-N and Co-O distances are 2.186(3) and 2.095(2) respectively. The coordination mode and conformation of the ligand in this case is similar to the zero-dimensional dimers **8** and **9** (Scheme 2.2, Mode G). However the octahedral geometry of Co^{II} in compound **10** means that the structure forms a neutral one-dimensional (1D) framework with small voids, which can be seen in Figure 2.7.

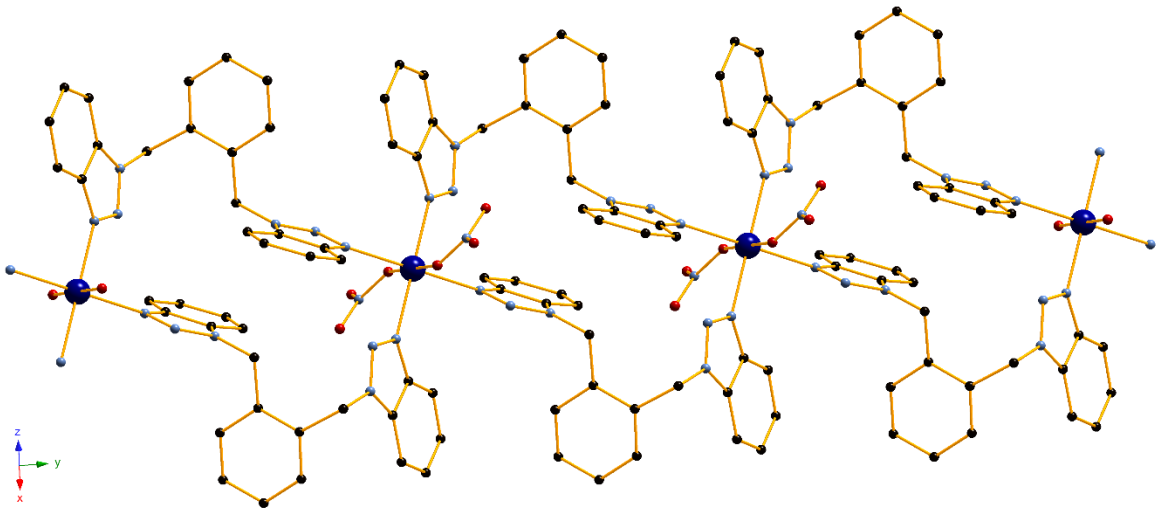

Figure 2.7. Part of the 1D framework of compound **10** along the *b* axis. H atoms are omitted for clarity. Colour code Co (blue), C (black), N (light blue), O (red).

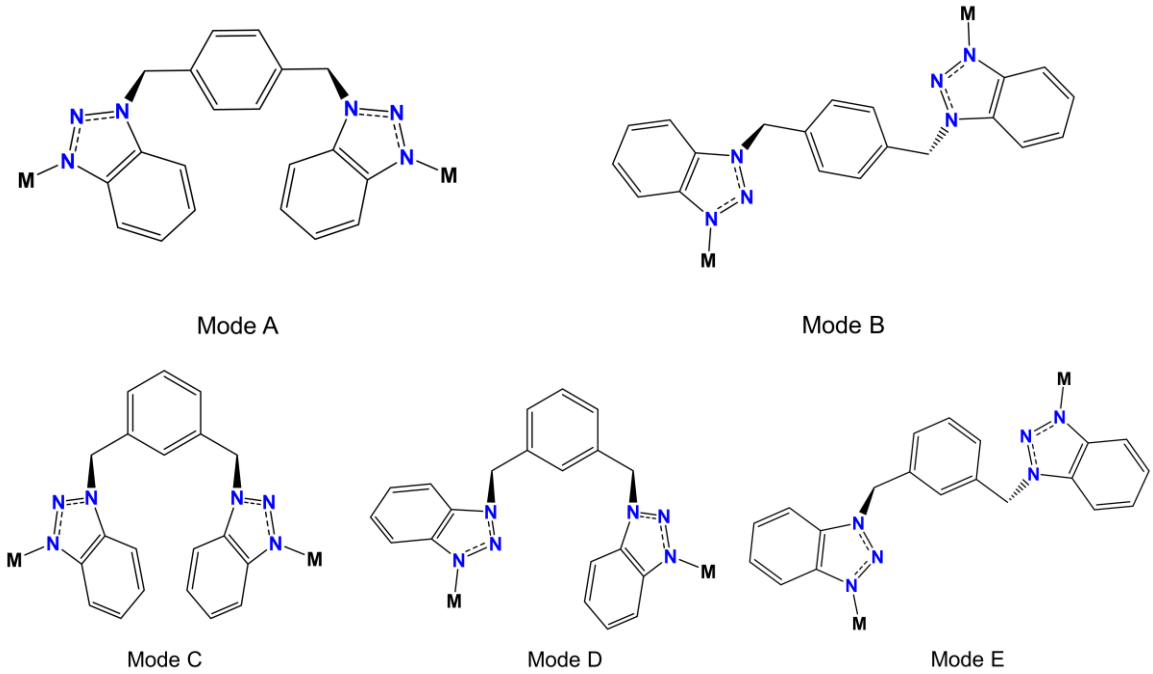

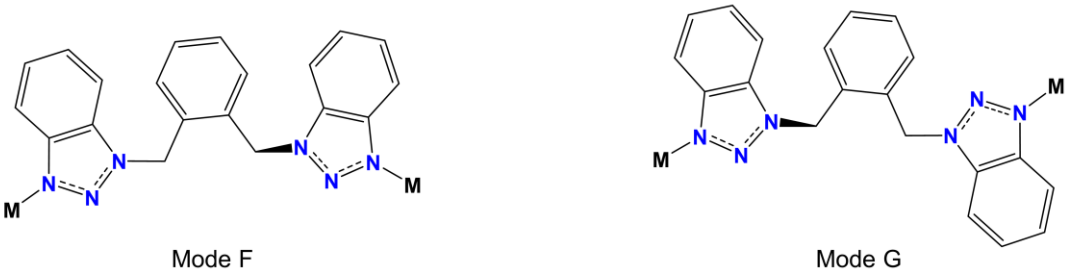

Scheme 2.2. The coordination modes of the ligands **L¹** (upper, modes A, B), **L²** (middle, modes C-E), and **L³** (lower, modes F and G).

Table 2.1. Overview of the coordination characteristics of the compounds reported in this study.

Entry	Ligand	Compound	Geometry of Co^{II}	Coordination Mode	Dimensionality
1	**L¹**	**1**	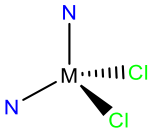	A	0D
2	**L¹**	**2**	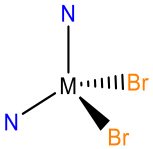	B	1D
3	**L²**	**3**	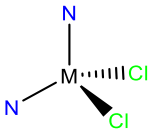	C	0D
4	**L²**	**4**	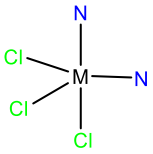	D	2D
5	**L²**	**5**	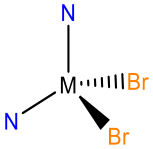	C	0D

6	**L²**	**6**	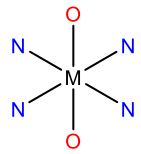	E	2D
7	**L³**	**7**	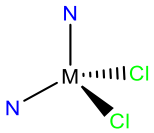	F	1D
8	**L³**	**8**	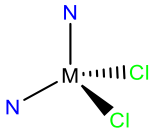	G	0D
9	**L³**	**9**	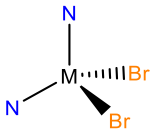	G	0D
10	**L³**	**10**	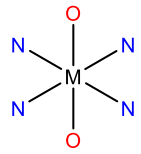	G	1D

2.2.2. Synthetic Aspects

As shown in Table 2.1, the employment of **L¹**, **L²** and **L³** along with Co^{II} sources afforded a variety of compounds, including 0D dimers and 1D or 2D CPs. This structural diversity is owed to the ligand, ratio, temperature and metal source used. As such, these parameters and their importance to this study will be further discussed below. While various solvents were tested during synthesis, only acetonitrile and acetone were successful. The choice of solvent, however, does not seem to play any significant part in the resulting compounds and therefore will not be discussed in further detail.

A close inspection of the ratio and temperature conditions used provides a significant understanding of the system and allows for its finer control. In regards to the ratio, complexes **1**-**5**, **7**, **9** and **10** were synthesized using either a 1:1 or a 2:1 metal-ligand analogy. Interestingly, other ratios were not so successful, resulting mostly in non-crystalline material. The only exceptions to this were **1** and **7**, which were also prepared in a 1:2 ratio, and **6** and

8 which were synthesized in 3:1. None of the ten compounds could be afforded in larger ratios.

Introduction of the temperature parameter through various forms (gentle heating to 50°C, solvothermal reactions to 75-100°C) led to more interesting results. In several cases, an increase in temperature during synthesis allowed for a better control of the resulting product through manipulation of the non-rigid part of the ligands. In the $\mathbf{L^1}$-based compounds **1** and **2**, the former was synthesized at room temperature (rt), while the latter was prepared at 50°C. This temperature effect has a subsequent result in the conformation of the ligand (Scheme 2.2, Modes A and B) which allows for the manipulation of the dimensionality in the structures: **1** is a 0D dimer while **2** is a 1D coordination polymer. Another interesting example is observed in the $\mathbf{L^2}$-based compounds **3** and **4**. Both were prepared by the same method, however **3** was synthesized at rt and produced a 0D dimer, while **4** was subjected to 75°C heating and afforded a 2D coordination polymer. A closer comparison of the structures reveals a rotation of the non-rigid C-N bond in $\mathbf{L^2}$, which can be attributed to the temperature effect in each case. To further investigate this, an acetonitrile solution containing single crystals of **3** was heated to 75°C for 18 hours, and after X-Ray crystallography analysis the crystals were found to have been converted to compound **4**, confirmed also by IR spectra. Thus, compound **3** can undergo a temperature-induced single crystal transformation to **4** (Scheme 2.3), subjecting to significant alterations: the coordination geometry of Co^{II} changes from tetrahedral to trigonal bipyramidal, the dimensionality of the structure changes from 0D to 2D, and the loss of lattice solvent is also observed. In regards to the crystallographic parameters, there are considerable differences in the space group ($P\overline{1}$ to $P2_1/c$) and unit cell dimensions. Efforts to make this transformation reversible were unsuccessful.

Taking these findings up to this point into consideration, it was envisioned that a combination of higher temperatures and large metal:ligand ratios would allow for further structural variety. Indeed, compounds **6** and **8** were synthesized employing a 3:1 ratio and solvothermal conditions. As evident by a comparison of **8** to **7** (synthesized in rt), temperature once again affects the conformation of the ligand's non-rigid part, leading to a 0D dimer and a 1D chain respectively. Efforts to obtain **6** and **8** using different ratios or in the absence of high

temperature proved unsuccessful, indicating the importance of both parameters in controlling the system.

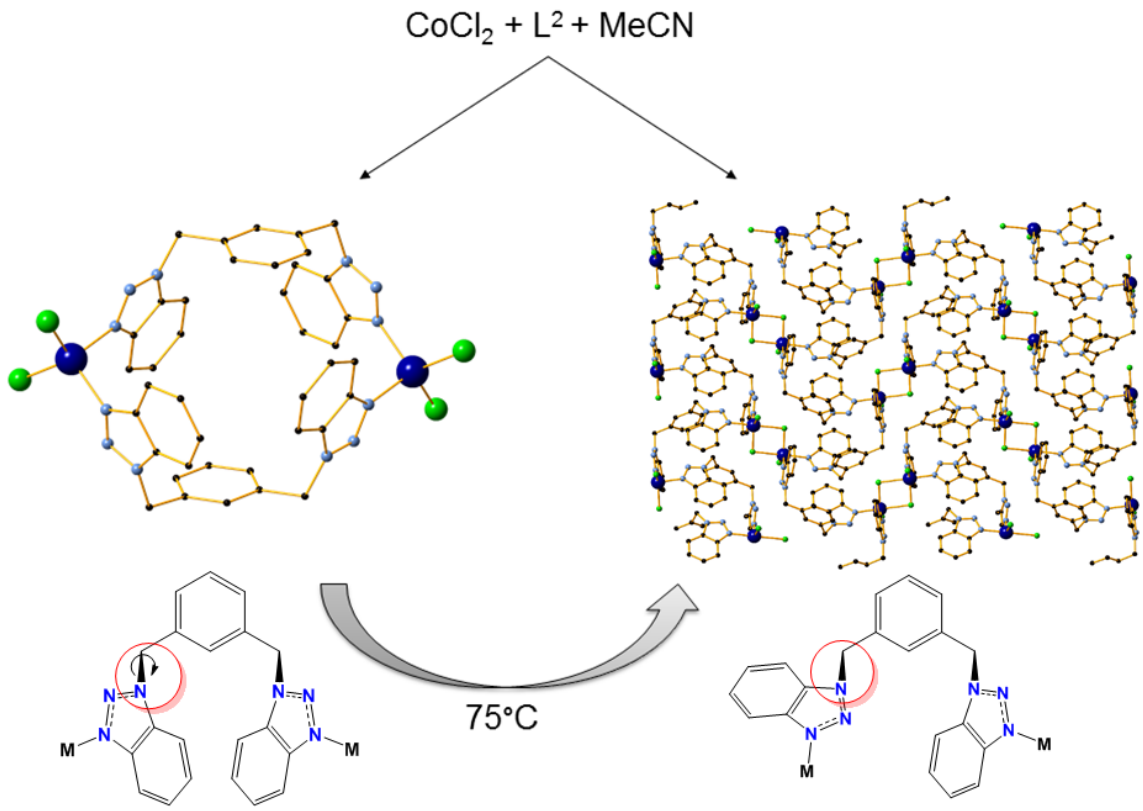

Scheme 2.3. A schematic representation of the temperature-induced single-crystal to single-crystal transformation of **3** to **4.**

A classification of complexes **1**-**10** by ligand reveals that the *para*-substituted ligand $\mathbf{L^1}$ afforded the lowest number of structures, as only a 0D dimer and a 1D CP were obtained. In contrast, four complexes were synthesized using each of the *meta*- and *ortho*-substituted ligands $\mathbf{L^2}$ and $\mathbf{L^3}$ respectively; two 0D dimers and two low-dimensional CPs in each case. Furthermore, $\mathbf{L^1}$-based compounds were afforded in much poorer yields compared to the rest. In all complexes, coordination of the Co^{II} centre takes place only through the N3 atom of the 1,2,3-triazole moiety; coordination through the N2 atom is likely not promoted due to steric effects. $\mathbf{L^1}$, $\mathbf{L^2}$ and $\mathbf{L^3}$ also contribute to the stability of the respective 0D dimers via participation in intermolecular $\pi\cdots\pi$ stacking interactions. The present findings, summarized in Table 2.1, recommend that all ligands are suitable for the construction of dimers and low-

dimensional CPs, however formation of the latter can be easily promoted under the proper synthetic conditions. Taking also into consideration the low yields of the **L^1**-based compounds, it can be deduced that ligands **L^2** and **L^3** with respective substitution in *meta*- and *ortho*- position, are the most appropriate for the synthesis of the desired polymeric structures. These findings were very encouraging, especially having also in mind the little attention that this family of organic ligands has received in coordination chemistry compared to the corresponding derivatives of other heterocyclic *N*-donors, such as benzimidazole[165–174].

In regards to the cobalt sources, a variety of sources were used in order to perform a full systematic study for the metal, including $CoCl_2$, $CoBr_2$, $Co(NO_3)_2$, $Co(OAc)_2$, $Co(BF_4)_2$, $Co(ClO_4)_2$ and $Co(SO_4)_2$. Out of these salts, only the first three afforded any results. Each anion appears to contribute differently to the dimensionality of the structures. Cl plays a significant role in compound **4**, as the structure propagates in two directions through the formation of a chloride bridge. Bromine-based complexes have less frequency and variation, despite efforts to produce results similar to the chloride-based structures. Finally, experiments with Co^{II} nitrate lead exclusively to coordination polymers, as compounds **6** and **10** are 2D and 1D respectively. This change in anion is also accompanied by a drastic change in the geometry of the metal centre, as all nitrate-based compounds exhibit octahedral $\{N_4O_2\}$ coordination motifs.

2.2.3. Characterization of Compounds 1 – 10

ESI-MS Studies

To confirm their identity in solution, electrospray ionization mass spectrometry (ESI-MS) was performed for compounds **1**-**10**. The MS (positive-ion mode) for all complexes shows four peaks at the regions of 369.60, 539.65 and 709.75 and 880.32 m/z which perfectly correspond to the respective $[Co(\mathbf{L})_2 - H]^{2+}$, $[Co(\mathbf{L})_3 - H]^{2+}$ and $[Co(\mathbf{L})_4 - H]^{2+}$ dicationic fragments. Additional peaks, depending on the anion present, are also observed. **1**, **3**, **4**, **7** and **8** show additional peaks at 434.04, 562.24, 774.18 m/z that correspond to the $[Co(\mathbf{L})Cl - H]^{1+}$, $[Co_2(\mathbf{L})Cl_3 - H]^{1+}$ and $[Co(\mathbf{L})_2Cl - H]^{1+}$ monocationic fragments respectively. Compounds **2**, **5** and **9** exhibit peaks at 479.95, 696.75, 820.09, 1036.87 and 1160.24 m/z,

corresponding to $[Co(\mathbf{L})Br - H]^{1+}$, $[Co(\mathbf{L})Br_2 - H]^{1+}$, $[Co(\mathbf{L})_2Br - H]^{1+}$, $[Co_2(\mathbf{L})_2Br_3 - H]^{1+}$, and $[Co(\mathbf{L})_3Br - H]^{1+}$ fragments. For **6** and **10** two peaks appear at 461.06 and 801.20 m/z, that match the $[Co(\mathbf{L})(NO_3) - H]^{1+}$ and $[Co(\mathbf{L})_2(NO_3) - H]^{1+}$ monocationic fragments respectively. The representative ESI-MS spectra are presented in the Appendix (Figures S2.11-S2.15).

TGA and Powder XRD Studies

Thermogravimetric analysis (TGA) between room temperature and 900-1000 °C was carried out on all compounds (Figures S2.16-S2.18, Appendix). All compounds start to decompose in the region of 200-350°C. In compounds with lattice solvent molecules, this loss takes place in the region of 70-190 °C. Furthermore, to confirm phase purity of the samples, representative compounds **7**, **8** and **9** were further characterized through Powder XRD studies. The resulting spectra, as seen in the Appendix (Figures S2.8-S2.10), indicated that the complexes are indeed formed in high purity.

2.2.4. Magnetic and EPR Studies

Selected complexes **4**, **7** and **9** were investigated in order to elucidate their magnetic properties with SQUID magnetometry, Electron Paramagnetic Resonance (EPR) spectroscopy and *ab initio* Complete Active Space Self-Consistent Field Spin-Orbit (CASSCF-SO) calculations. The compounds were chosen based on their characteristic structural features in regards to coordination environment, metal geometry and dimensionality. Complexes **7** and **9** contain Co^{II} in a distorted tetrahedral environment, while the Co^{II} site in **4** is a distorted trigonal bipyramid, giving in all cases an anisotropic $S = {}^3/_2$ ground state. Complex **7** is a 1D CP, the nearest-neighbour Co···Co distance is over 8.5 Å and the through-bond connectivity involves 10 ligand N and C atoms, thus the Co^{II} sites are treated as uncoupled. Complex **9** is a discrete 0D dimeric species with intramolecular π-π stacking, thus some magnetic interaction between the two Co^{II} ions may be present. Complex **4** is a 2D CP featuring a repeat unit of a μ_2-Cl^- bridged dimer and thus it is expected that the magnetic interactions between the Co^{II} ions in could be rather strong. Importantly, for both **4** and **9**, the Co^{II} ions are related by crystallographic inversion symmetry and hence must

have the same local electronic structure. Initial investigations took place for **7**, followed by **9** and **4**, following the expected level of complexity.

The magnetic susceptibility-temperature product, $\chi_M T$, for **7** has a value of 2.71 $cm^3\ mol^{-1}$ K at room temperature and is more-or-less temperature independent until it begins to fall below 30 K to reach a minimum value of 1.67 $cm^3\ mol^{-1}$ K at 2 K (Figure 2.8). The isothermal magnetization, *M*, profiles at 2 and 4 K approach and the same maximum value, but fail to saturate at 7 T (Tesla units) with values of 2.78 and 2.73 $\mu_B\ mol^{-1}$ and are non-superimposible on a reduced magnetization plot, (Figure S2.5, Appendix). The low temperature drop in $\chi_M T$, the lack of saturation of *M* and the non-superimposable reduced *M* plots all suggest significant Zero-Field Splitting (ZFS) of the ground $S = {}^3/_2$ state in this isolated tetrahedral Co^{II} species. The ZFS was estimated by fitting these magnetic data simultaneously with the PHI program[175], using the spin Hamiltonian in Equation 1. With the *E* term fixed to zero to avoid over parameterization, reasonable fits are obtained for $D \approx \pm 7\ cm^{-1}$ and $g \approx 2.3$. The cryogenic X- and Q-band (ca. 9.4 and 34 GHz, respectively) EPR spectra for compound **7** show a reasonably broad feature around 0.15 and 0.45 T, respectively (Figure 2.9). It was found that the relative intensity of the two features in the Q-band spectrum can only be reproduced when $D \approx -7\ cm^{-1}$; subsequent optimization of the parameters against the magnetometry and EPR data yields $D = -6.53\ cm^{-1}$, $E = 0.379\ cm^{-1}$ and $g = 2.26$, with frequency-space Lorentzian linewidths of η(X-band) = 3 GHz and η(Q-band) = 6 GHz. Introducing further flexibility to the Hamiltonian with anisotropic *g*-values and/or anisotropic linewidths does not improve the simulation; furthermore, it is likely that hyperfine coupling of the electron spin to the 100% naturally abundant ^{59}Co nucleus with $I = {}^7/_2$ is responsible for these strange line shapes. Indeed, CASSCF-SO calculations on the Co-containing repeat unit of **7** confirm the experimental findings, suggesting $D = -8.3\ cm^{-1}$, $E = 1.0\ cm^{-1}$ and $g = 2.31$.

$$\hat{H}_1 = D\left(\hat{S}_z{}^2 - \frac{1}{3}\hat{S}^2\right) + E(\hat{S}_+{}^2 + \hat{S}_-{}^2) + g\mu_B\hat{S}\cdot B \quad (1)$$

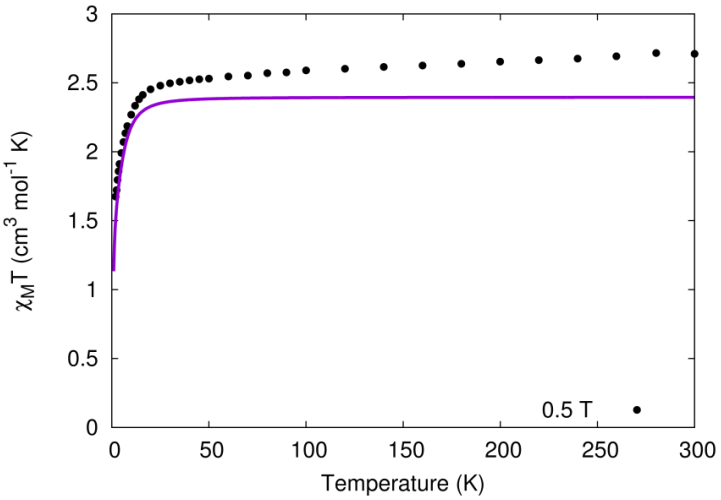

Figure 2.8. Experimental (black circles) and fitted (purple line, parameters in text) $\chi_M T$ for **7** in a 0.5 T field.

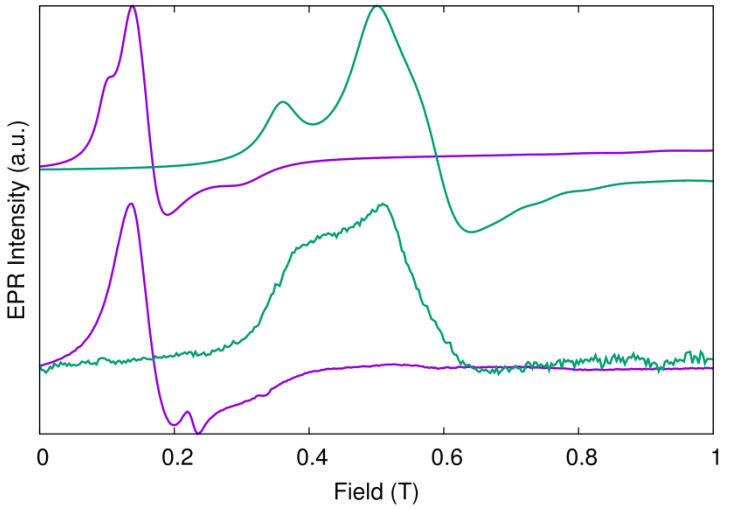

Figure 2.9. Experimental (lower traces) and simulated (upper traces, parameters in text) EPR spectra for a polycrystalline powder of **7** at 9.39557 GHz (purple) and 34.049 GHz (green) at 5 K. Note that the feature at ~ 0.23 T in the X-band spectrum is a background signal.

The $\chi_M T(T)$ for **9** has value of 5.55 cm^3 mol^{-1} K (per dimer) at room temperature that is roughly constant until it declines below 40 K to reach 1.15 cm^3 mol^{-1} K at 2 K (Figure 2.10). While the $\chi_M T(T)$ is broadly similar in profile to that of **7**, the magnetization data at 2 and 4 K show quite different behaviour compared with **7**, where the two isotherms are coincident until ca. 1 T where they separate before approaching one another again at 7 T reaching 4.39 and 4.25 μ_B mol^{-1}, respectively (Figure 2.10, inset). It is impossible to reproduce this data

using the spin Hamiltonian Equation 1 for each site of the dimer, as the strange sigmoidal shape of the magnetization data is directly indicative of antiferromagnetic interactions. Thus, for the initial modelling of the magnetic data the spin Hamiltonian Equation 2 was used, which takes into account an isotropic interaction between the two Co^{II} ions. Using the same initial minimal model as previously with E fixed to zero, the magnetic data fit to find two minima: D = -19.9 cm^{-1}, g = 2.38, J = -0.319 cm^{-1}, and D = 26.8 cm^{-1}, g = 2.41, J = -0.559 cm^{-1}. EPR spectra for **9** at X- and Q-band show only one broad resonance at each frequency (Figure 2.11). Of the two parameter sets determined from the magnetic data, only the $D < 0$ set is in agreement with the EPR data. Further refinement of these parameters gives D = -19.6 cm^{-1}, g = 2.38, J = -0.319 cm^{-1} with frequency-space Lorentzian linewidths of η(X-band) = 6 GHz and η(Q-band) = 12 GHz. Given the lack of fine structure in the EPR spectra, it is not possible to further refine the model to estimate the rhombicity of the local ZFS tensors. *Ab initio* CASSCF-SO calculations on single sites of **9** again lend support to these conclusions, predicting D = -12.3 cm^{-1}, E = 2.6 cm^{-1} and g = 2.34; furthermore the trend of D for **9** being greater than for **7** is also verified.

$$\widehat{H}_2 = \sum_{i=1}^{2}[D\left(\hat{S}_{i,z}{}^2 - \frac{1}{3}\hat{S}_i{}^2\right) + E(\hat{S}_{i,+}{}^2 + \hat{S}_{i,-}{}^2) + g\hat{S}_i \cdot B] - 2J\hat{S}_1 \cdot \hat{S}_2 \qquad (2)$$

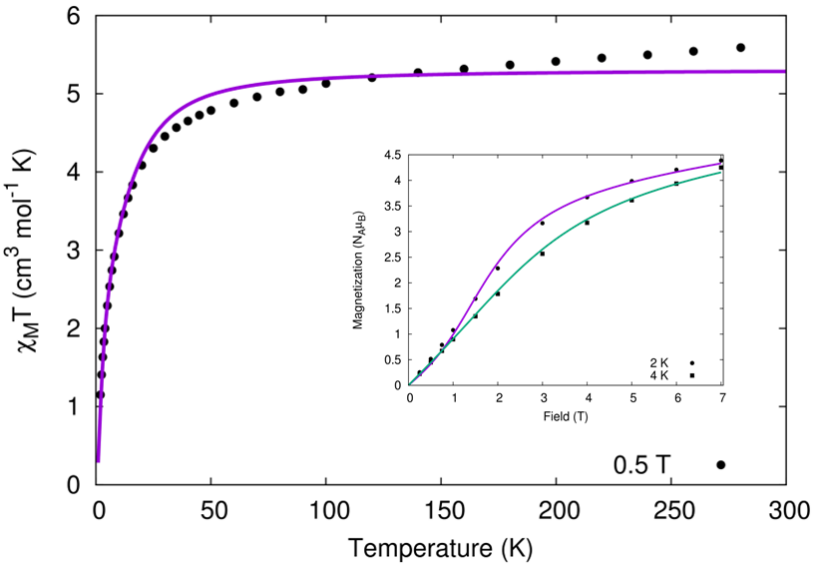

Figure 2.10. Experimental (black circles) and fitted (purple line) $\chi_M T$ for **9** in a 0.5 T field. (inset) Experimental (black circles and squares) and fitted (purple and green lines) magnetization for **9** at 2 and 4 K.

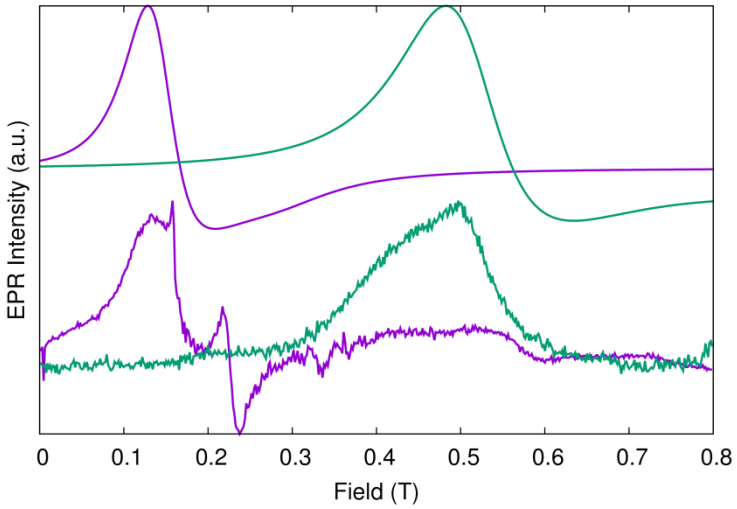

Figure 2.11. Experimental (lower traces) and simulated (upper traces, parameters in text) EPR spectra for a polycrystalline powder of **9** at 9.40040 GHz (purple) and 33.927 GHz (green) at 5 K. Note that the feature at ~ 0.23 in the X-band spectrum is a background signal.

$\chi_M T$ vs. T for compound **4** is similarly temperature independent from 300 K down to 20 K, with a value of 6.04 $cm^3\ mol^{-1}$ K at 300 K, before a small increase to a maximum value of 6.22 $cm^3\ mol^{-1}$ K at 7 K followed by falling to reach 4.95 $cm^3\ mol^{-1}$ K at 2 K (Figure 2.12). Such a rise directly indicates exchange coupling between the Co^{II} ions. The magnetization vs. field data at 2 and 4 K and 7 T are nearly coincident with a value of 5.35 μ_B mol^{-1}, indicating a well isolated ground manifold (Figure 2.12, inset). Owing to the likely presence of significant magnetic exchange in this case and given that the CASSCF-SO calculations have been good estimates for **7** and **9**, such calculations are also used for **4** in order to estimate the local electronic structure of the Co^{II} centres. As the Co sites are related by crystallographic inversion symmetry, both will possess the same local electronic structure; the calculations suggest that the Co^{II} ions are subject to a very large ZFS of D = +48.4 cm^{-1} with E = -8.9 cm^{-1} and g = 2.38 (note that the sign of D is also different to **7** and **9**). The very large ZFS leads to a well-isolated ground Kramers doublet (first excited state at ~ 114 cm^{-1}) with effective g-values of g_1 = 1.8, g_2 = 3.5 and g_3 = 6.5 that are approximately associated with metal-ligand directions in the first coordination sphere; g_1 is associated with the approximate three-fold axis of the trigonal bipyramid (Cl1-Co1-N6), g_2 is associated with the other bridging Cl^- anion (Cl1´-Co1), and g_3 is perpendicular to the Cl1'-Co1-Cl1 plane

(roughly along the Co1-N1 direction). Based on the prediction of a very large ZFS with D > 0, the magnetic data for **4** can be satisfactorily modelled using Equation 2 with D = +10 cm^{-1}, E = -2 cm^{-1}, g = 2.5 and J = +1 cm^{-1}. This model gives effective g-values for the ground Kramers doublet of each Co^{II} ion as g_1 = 2.2, g_2 = 3.4 and g_3 = 6.3, which are in excellent agreement with those suggested by CASSCF-SO calculations. The characteristic rise in $\chi_M T$ at the lowest temperatures can loosely be associated with a ferromagnetic interaction, however this is a poor description when the local ZFS >> J. EPR spectra for **4** are much more featured than for **7** and **9**, and show a general decrease in intensity on increasing temperature, as seen in Figures 2.13 and 2.14. The X-band spectra show a structured resonance at low field, while the Q-band spectra show four clear resonances from 0.16 to 1.2 T. Owing to the large ZFS and small exchange interaction, the EPR experiments only probe the four lowest lying states of the exchange coupled manifold. Therefore, the most appropriate model for these data is the pseudo-spin S = 1/2 model, where the lowest lying Kramers doublet of each Co^{II} ion is treated as a S = 1/2 state with the magnetic anisotropy given by three principal g-values, and the intramolecular interaction modelled with an anisotropic effective exchange term, Hamiltonian Equation 3. Fixing the local orientations of the g-tensors from the CASSCF-SO calculations, and approximating the Cl1´-Co1-Cl1 angle as 90° (it is 84.5° from X-Ray crystallography), the local $\overline{\overline{g_e}}$ matrix of each site is rotated around the z-axis by ±45° and thus the model is constructed according to Figure 2.15. The anisotropic exchange term is approximated by considering a unique value for J_x connecting the Co^{II} ions with fixed J_y = J_z. The best simulation was obtained with g_1 = 1.84, g_2 = 3.61, g_3 = 5.36, J_x = ±0.240 cm^{-1} and J_{yz} = ±0.344 cm^{-1} with anisotropic frequency-space Lorentzian linewidths of η_{xy}(X-band) = 3 GHz, η_z(X-band) = 5 GHz, η_{xz}(Q-band) = 5 GHz and η_y(Q-band) = 10 GHz (Figures 2.13 and 2.14), which is in good agreement with the effective g-values determined both by CASSCF-SO and the magnetometry data. It is noted that the spectra are insensitive to the overall sign of the J terms, however the relative signs of both must be the same (i.e. the product J_xJ_{yz} is positive). While this model is unable to replicate the magnetometry data directly owing to the influence of excited states, simulation of $\chi_M T$ for J_x and J_{yz} positive shows an increase at the lowest temperatures, compared to a decrease with J_x and J_{yz} negative (Figure S7) and hence it is suggested that J_x and J_{yz} are both positive.

$$\hat{H}_3 = \mu_B(\hat{S}_1 \cdot \overline{\overline{g_e}} + \hat{S}_2 \cdot \overline{\overline{g_e'}}) \cdot B - 2(J_x \hat{S}_{1,x}\hat{S}_{2,x} + J_{yz}(\hat{S}_{1,y}\hat{S}_{2,y} + \hat{S}_{1,z}\hat{S}_{2,z})) \quad (3)$$

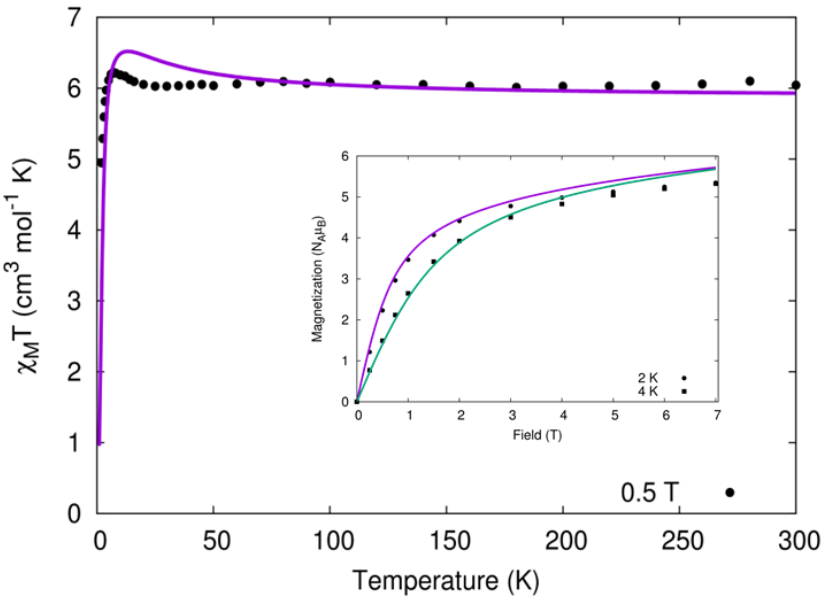

Figure 2.12. Experimental (black circles) and simulated (purple line) $\chi_M T$ for **4** in a 0.5 T field. (inset) Experimental (black circles and squares) and fitted (purple and green lines) magnetization for **4** at 2 and 4 K.

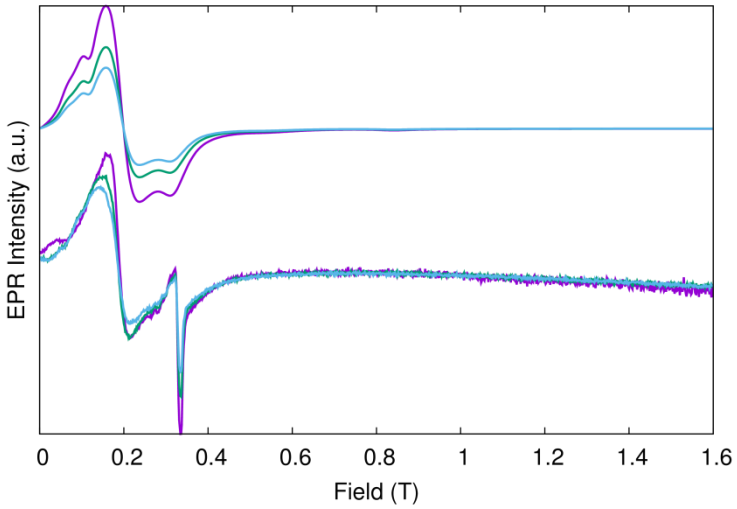

Figure 2.13. Experimental (lower traces) and simulated (upper traces) X-band EPR spectra for **4** at 9.3854 GHz and 5 (purple), 7.5 (green) and 10 (blue) K. Note that the feature at ~ 0.32 T is a background signal.

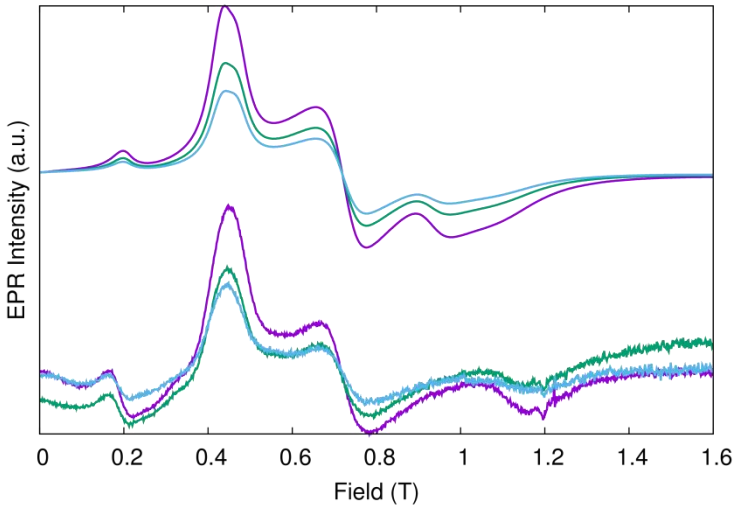

Figure 2.14. Experimental (lower traces) and simulated (upper traces) Q-band EPR spectra for **4** at 33.95 GHz and 5 (purple), 7.5 (green) and 10 (blue) K.

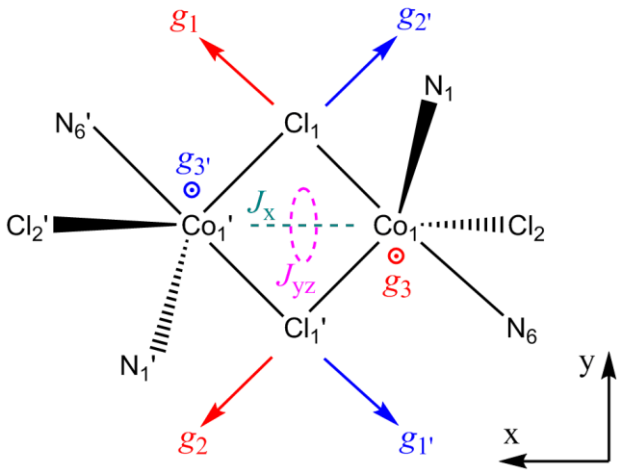

Figure 2.15. Relative orientations of principal *g*-values and exchange coupling terms in Hamiltonian Equation 3 for compound **4**.

2.3. Conclusion

To summarize, the potential versatility of a series of benzotriazole-based semi-rigid ligands in cobalt coordination chemistry has been investigated. The ten compounds derived from this systematic study reveal a large structural variety that is owed on synthetic parameters (ratio, temperature and salt) and flexible ligand selection (various conformations in each ligand dependent on temperature). Tuning of these parameters allows for a greater control and

manipulation of the system towards compounds with desired characteristics, generating a series of 0D dimers, 1D and 2D CPs with various metal geometries. A temperature-induced single-crystal to single-crystal transformation of compound **3** to **4** is additionally reported.

In addition, the magnetic properties of a selection of representative compounds, including the low-dimensional CPs **4** and **7** have been investigated. The relevant results show considerable differences when only minor structural variations take place, suggesting that tetrahedral Co^{II} nodes in CPs could function as sensitive signals of small changes in the local environment.

These findings show that the chosen ligands, particularly $\mathbf{L^2}$ and $\mathbf{L^3}$, are indeed ideal candidates for the generation of low-dimensional CPs, producing dynamic architectures that can be easily manipulated and tuned. The following Chapters will present subsequent investigations dedicated to: i) employing different metals to fully explore the coordination potential of these ligands, ii) exploiting the versatility of this system to generate compounds with potential catalytic properties.

Chapter 3: A copper-benzotriazole based coordination polymer catalyses the efficient one-pot synthesis of (*N′*-substituted)-hydrazo-4-aryl-1,4-dihydropyridines from azines

Abstract: A series of new (*N′*-substituted)-hydrazo-4-aryl-1,4-dihydropyridines (**C3D**) were successfully synthesized via a facile one-pot catalytic pathway utilizing azines (**C3Z**) and propiolate esters (**C3L**) as starting materials. A novel Cu^{II}-based 1D CP, formulated as $[Cu^{II}(\mathbf{L^3})_2(MeCN)_2]\cdot(ClO_4)_2\cdot MeCN$ (**11**) is employed as the catalyst. The proposed method provides good yields, with catalyst loadings as low as 2 mol% and under mild conditions. In the absence of catalyst, formation of the corresponding 5-substituted-4,5-dihydropyrazoles (**C3P**) is instead promoted with moderate to high yields. Compounds $[Cu^{II}(\mathbf{L^3})(NO_3)_2]\cdot MeCN$ (**12**) and $[Zn^{II}(\mathbf{L^3})_2(H_2O)_2]\cdot(ClO_4)_2\cdot 2MeCN$ (**13**) were also synthesized during efforts to optimise the catalytic behaviour, allowing for more insights in regards to the plausible reaction mechanism.

External Contributions: Ioannis N. Lykakis (University of Thessaloniki) was responsible for the design of the synthetic method towards dihydropyridines and the proposing mechanisms. Initial development of catalytic protocols (results in Tables 3.2, 3.3) was performed by Michael Kallitsakis (University of Thessaloniki). Nicholas F. Chilton (University of Manchester) was responsible for the collection and interpretation of magnetic data. Alaa Abdul-Sada (University of Sussex) was responsible for the collection of all ESI-MS data. Graham J. Tizzard and Simon J. Coles (University of Southampton) were responsible for the collection of some crystallographic data (compound **11i**).

3.1. Introduction

In the constant search for efficient activation and optimization of organic reactions with transition metal elements, copper remains one of the most attractive options due to the many advantages it offers. Apart from its abundance and low cost, copper presents an incredibly versatile chemistry and may be easily available in one of multiple (Cu^0, Cu^I, Cu^{II}, Cu^{III}) oxidation states. As a result, its salts and compounds can be powerful catalysts for reactions that involve both one and two-electron (radical and bond-forming) mechanisms.

Furthermore, it can easily coordinate to heteroatoms as well as π-bonds to form organometallic intermediates that are crucial promoters of these transformations[137,176,177]. These reasons made copper an obvious choice for the purposes of this thesis.

In view of the importance of the synthesis of pyridine derivatives, the metal-catalysed access to 1,4-dihydropyridines (1,4-DHPs) has received considerable attention[178,179]. 1,4-DHPs and their derivatives are a significant class of biologically active organic compounds with extensive use in pharmacology; notable examples are the calcium channel blockers amlodipine, nifedipine and felodipine[180–182]. Moreover, symmetrical *N′*-substituted-hydrazo-4-aryl-1,4-DHPs (HA-1,4-DHPs) are new heterocycles in nature with probably wide-ranging biological activity[183,184]. Since the first synthesis (Hantzsch reaction[185], Scheme 3.1) multiple methodologies including multicomponent[178,179,186], cycloaddition[187–189], or C-C coupling reactions[190] have been used for the formation of 1,4-DHPs derivatives (Scheme S3.1, Appendix). A series of organocatalytic procedures have been employed for such purposes[191–194], however these exhibit major drawbacks such as high reagent cost, high temperatures and tedious work up.

This work reports the synthesis and characterization of three novel coordination compounds, $[Cu^{II}(\mathbf{L^3})_2(MeCN)_2]\cdot(ClO_4)_2\cdot MeCN$ (**11**), $[Cu^{II}(\mathbf{L^3})(NO_3)_2]\cdot MeCN$ (**12**) and $[Zn^{II}(\mathbf{L^3})_2(H_2O)_2]\cdot(ClO_4)_2\cdot 2MeCN$ (**13**). **11** presents a 1D polymeric structure and shows significant homogeneous catalytic activity in the one-pot synthesis of a series of HA-1,4-DHPs based on the reaction between symmetrical electron rich aldazines and alkyl propiolate (Scheme 3.2, highlighted in blue). As conjugated dienes, aldazines[195] are a class of compounds with interesting chemical properties that undergo a wide variety of chemical processes (i.e. redox, cycloadditions, criss-cross reactions)[196–198] to yield hydrazones, pyrazoles, purines or pyrimidines (Scheme 3.2). However, an extensive literature search showed that the synthesis of substituted symmetrical HA-1,4-DHPs using aryl aldazines and propiolates as starting materials is a previously unknown chemical transformation. The proposed reaction employs mild conditions and only 2 mol% of **11**, providing good yields. Catalytic and mechanistic aspects are also discussed, as the use of **12** and **13** provides more insights in regards to the plausible reaction mechanism and fine tuning of the catalyst.

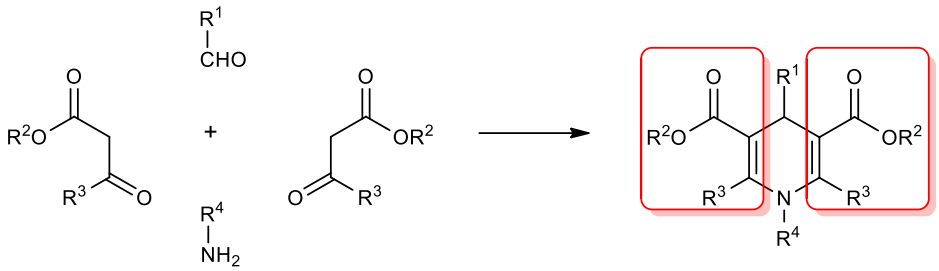

Scheme 3.1. The multicomponent Hantzsch reaction for the synthesis of 1,4-DHPs starting with β-ketoester, an aldehyde and an amine.

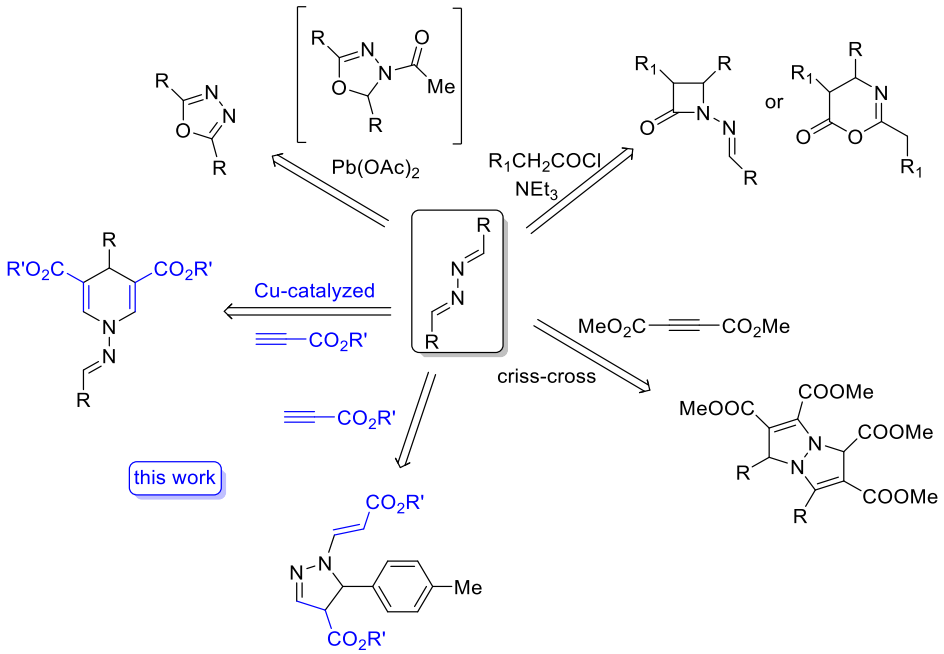

Scheme 3.2. Synthetic scheme for known reactions that aldazines undergo. Highlighted in blue: the synthesis of HA-1,4-DHP derivatives and 5-aryl-pyrazoles as reported in this Chapter.

3.2. Results and Discussion

3.2.1. Crystal Structure Description of Compounds 11 – 13

Compound **11** crystallizes in the triclinic space group $P\bar{1}$ and its asymmetric unit consists of a Cu^{II} centre, one $\mathbf{L^3}$ molecule, a perchlorate lattice anion and two acetonitrile solvent molecules (Figure 3.1, left). One of these solvents acts as a terminal ligand and one is in the

lattice; the latter will not be further discussed. In this conformation of the ligand (Table 3.1, Mode A), the angle between the planes of the benzotriazole molecules is 123.00(5)°. As a result, the structure extends to one dimension along the *a* axis, forming a 1D framework with small voids (Figure 3.1, right). Cu^{II} is coordinated to six nitrogen atoms and possesses a distorted octahedral geometry, in which the axial positions are occupied by acetonitrile nitrogen atoms. The relevant N - Cu - N bond angles range from 87.02(7)° to 92.98(7)°. As for the relevant bond lengths, the mean Cu-N_{ligand} distances are 2.0815(16) and 2.0133(17) Å, significantly shorter than the respective Cu-$N_{acetonitrile}$ distance which was measured at 2.422(2) Å. No strong hydrogen bonds or other supramolecular interactions are observed. Additionally, compound **13** was found to be isostructural to **11**; **13** was synthesized using $Zn(ClO_4)_2 \cdot 6H_2O$ and shows an identical 1D framework, however the two coordinating acetonitrile moieties are replaced by H_2O molecules (Figure 3.2). As a result, its structure will not be described in further detail.

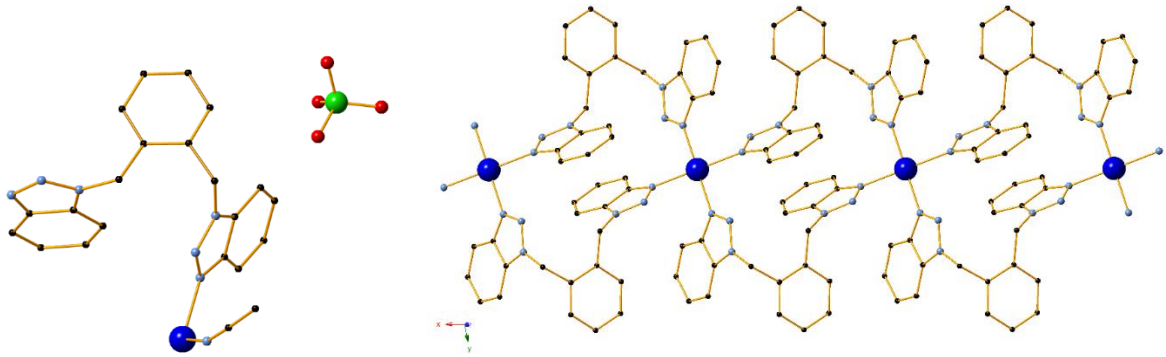

Figure 3.1. (left) The asymmetric unit of **11**. (right) Part of the one-dimensional framework in **11** along the *a* axis. H atoms, certain perchlorate anions and solvent molecules are omitted for clarity. Colour code Cu (blue), C (black), N (light blue), Cl (green), O (red).

In compound **12** the complex crystallizes in the monoclinic $P2_1/n$ space group. A Cu^{II} centre, one $\mathbf{L^3}$ molecule, two coordinating nitrate anions and one acetonitrile lattice solvent molecule are found within the asymmetric unit (Figure 3.3, left). The coordination mode of $\mathbf{L^3}$ is the same as in the mode in **11** (Table 3.1, Mode A). However, in this case the presence of both chelating and bridging nitrate moieties leads to the formation of an unusual dimeric Cu_2 unit as the structure extends in two dimensions along the *b0c* plane (Figure 3.3, right). A search

in the Cambridge Structure Database[199] reveals no other example of such a Cu_2 unit based on nitrates. The metal centre has a coordination environment of $\{N_2O_5\}$ and possesses a pseudo-octahedral geometry; five nitrate oxygen atoms occupy the equatorial positions of the pseudo-octahedron, while two nitrogen atoms from ligand molecules occupy the axial positions. The mean Cu-N distances are 1.9849(6) and 1.9916(6) Å, while the Cu-O distances range from 1.9813(6) to 2.6587(6) Å. The relevant N-Cu-O bond angles range from 85.32(4)° to 95.66(4)°. A summary of all coordination characteristics for compounds **11**-**13** may be found in Table 3.1.

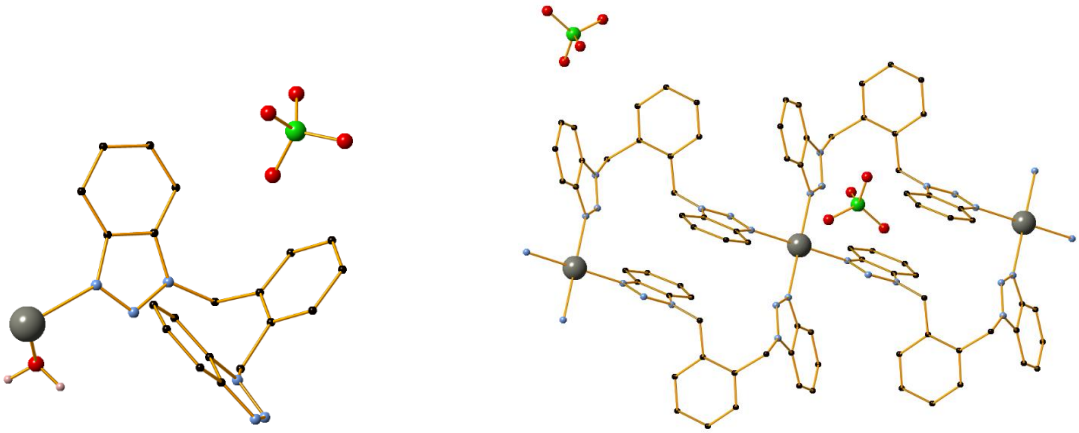

Figure 3.2. (left) The asymmetric unit of compound **13**. (right) Part of the one-dimensional framework of the complex. H atoms, certain perchlorate anions and solvent molecules are omitted for clarity. Colour code Zn (grey), C (black), N (light blue), Cl (green), O (red).

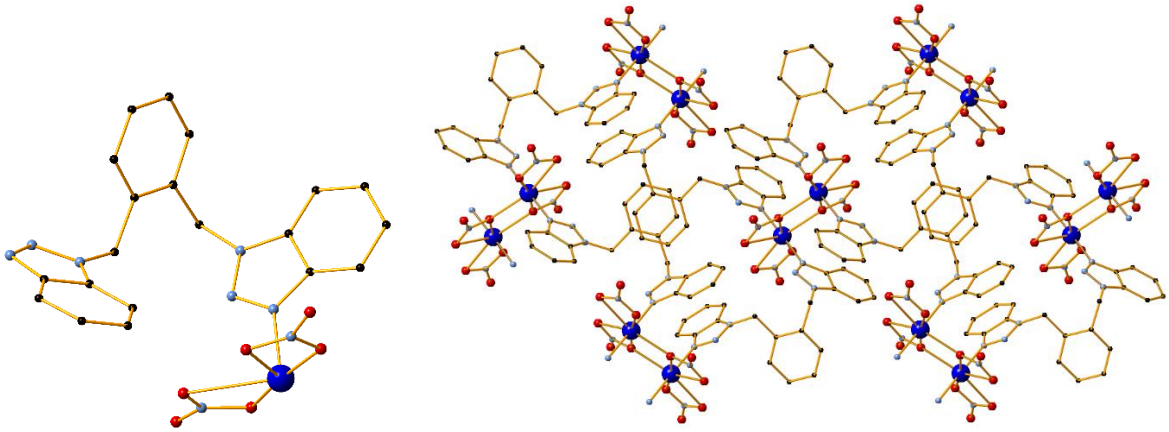

Figure 3.3. (left) The asymmetric unit of compound **12**. (right) Part of the two-dimensional framework of **12**. H atoms and solvent molecules are omitted for clarity. Colour code Cu (blue), C (black), N (light blue), O (red).

Table 3.1. Overview of the coordination characteristics (ligand conformation, coordination geometry of the metal) of the compounds used in this study (S = solvent).

Entry	Compound	Coordination Environment of M^{II}	Coordination Mode	Dimensionality
1	**11**	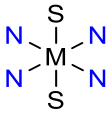	A	1D
2	**12**	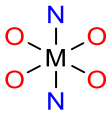	A	2D
3	**13**	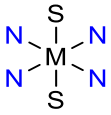	A	1D
		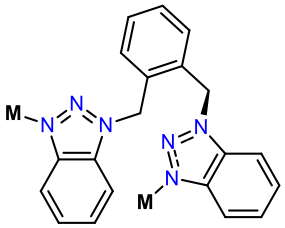 Mode A	M = Cu^{II} or Zn^{II}	

3.2.2. Synthetic Aspects

Similar synthetic concepts to the ones established in Chapter 2 were employed to generate the resulting compounds. As a result, good quality crystals for all complexes were afforded by leaving the samples undisturbed in room temperature or through the liquid diffusion technique. Although the yields in all cases were comparable, the best values were obtained through the former technique for compounds **11** and **13**, and the latter for **12**. The metal:ligand molar ratio does not appear to have a significant effect, as ratios from 2:1 to 1:2 afford the same compound with little change in the resulting yield. In regards to the temperature, solvothermal reactions of copper and zinc perchlorate with $\mathbf{L^3}$ resulted once again in the formation of **11** and **13**; no crystals were formed in the analogous experiments with copper nitrate. These findings indicate that the formation of the resulting frameworks is

heavily favoured especially in the 1D CPs **11** and **13**. As in the case of the Co^{II}-based compounds **1**-**10**, the metal centre (Cu^{II} or Zn^{II}) is only coordinated to the N3 nitrogen atom of the benzotriazole molecules in all complexes. Finally, **11**-**13** are very soluble in DMF and slightly soluble in other common organic solvents (e.g. acetonitrile, methanol, THF); their solubility in these solvents increases greatly when heated. However, they are insoluble in water.

3.2.3. Characterization of Compounds 11 – 13

Solid-state Studies

Magnetic measurements for **11** and **12** in the solid state are consistent with octahedral S = ½ Cu^{II} centres with g ~ 2.2. For **11** there are negligible interactions along the chain (Figure S3.7, Appendix), whilst in **12** a weak short-range ferromagnetic exchange is observed within the dimeric repeat unit of ca. 1 cm^{-1} (Figure S3.8, Appendix). Furthermore, TGA measurements were conducted to examine the thermal stability of all complexes. In all cases (Figures S3.9-S3.11, Appendix), the first mass loss corresponds to the loss of the coordinated and/or lattice solvent molecules, while the remaining frameworks are stable up to ~150-200 °C. Due to the presence of perchlorates, thermal studies for **11** and **13** were conducted only up to 230 °C, as a very large endothermic peak appeared in temperatures above that level (Appendix, Figure S3.9, inset). In **11**, a continuous mass loss occurs from room temperature up to 226 °C, corresponding in good agreement to the loss of the lattice and coordinated acetonitrile molecules (calc.: 11.87%, theor.: 11.57%). The analysis for **12** shows an initial mass loss which begins from room temperature and agrees to one acetonitrile molecule (calc.: 5.73%, theor.: 6.22%). Decomposition to CuO follows immediately, beginning from 217 °C. For **13**, the first mass loss is completed at ~150 °C, attributed to the loss of two water molecules (calc.: 4.23%, theor.: 3.69%). The remaining core is then immediately subjected to a further mass loss.

Solution Studies

ESI-MS (positive-ion mode) in methanolic solution for the Cu^{II} complexes **11** and **12** reveals two main peaks at 403.07 and 743.22 m/z which correspond perfectly to the respective $[Cu(\mathbf{L})]^{1+}$ and $[Cu(\mathbf{L})_2]^{1+}$ fragments. Additional peaks are also observed in each spectrum,

corresponding perfectly to the $[Cu(\mathbf{L})X]^{1+}$, $[Cu(\mathbf{L})_2X]^{1+}$, $[Cu(\mathbf{L})_3X]^{1+}$ (where X is the anion present in each compound) metal-ligand-anion fragments. Similar fragments were obtained for the Zn^{II}-based compound **13**. ESI-MS spectra, along with detailed analysis of the fragments are presented in the Appendix (Figures S3.4-S3.6). These results indicated that the CPs of this study could retain their polymeric structure in the solution. To elaborate on this, the same method was applied in a DMF solution of **11**, given that generally DMF molecules can easily coordinate to the metal centre. Indeed, the mass spectrum showed identical peaks as above, as well as an additional peak at 575.07 m/z, corresponding perfectly to $[Cu(\mathbf{L})(DMF)(ClO_4)]^{1+}$ (Appendix, Figure S3.4, lower). To further clarify on their solution behaviour, the UV-Vis spectra of **11** and **12** were measured in MeOH, showing a broad peak in the region of 750-850 nm which is characteristic of *Jahn Teller* effect and consistent for a Cu^{II} centre with an octahedral geometry (Figure S3.12-S3.14, Appendix).

3.2.4. Catalytic Studies

3.2.4.1. Benchmarking and Optimisation

The present catalytic protocol arose during the study of the title reaction using 1,2-bis ((*E*)-4-methylbenzylidene) hydrazine (**C3Z1**) and ethyl propiolate (**C3L1**), in the presence of various copper sources. Initial experiments with copper salts (2 mol%), 0.1 mmol of **C3Z1**, **C3L1** (2 eq. based on the amount of **C3Z1**) in MeOH under reflux for 24 hours (Table 3.2, entries 1 - 6), showed consumption of **C3Z1** which in most cases was almost quantitative. The corresponding 4-methylbenzaldehyde (**C3A1**) was afforded as the major or only product, along with a mixture of unidentified products. This result was attributed to the oxidation reaction taking place between the starting aldazine and molecular oxygen, forming the corresponding aldehyde through a hydrolysis pathway. Indeed, aldehyde **C3A1** was formed as the only product when oxygen saturated methanolic solution of aldazine **C3Z1** was used under the same catalytic conditions (Table 3.2, entry 13).

Interestingly, an analogous reaction in the absence of catalyst afforded aldehyde **C3A1** in 35% relative yield, as well as a significant amount (30%) of the corresponding pyrazole derivative 5-(*p*-tolyl)-4,5-dihydro-1*H*-pyrazole-4-carboxylate (**C3P1**) (Table 3.2, entry 7). A literature search revealed that this transformation has never been reported before under the

present reaction conditions. However, when compound **11** was incorporated (2 mol%) as the catalyst under similar conditions, the corresponding dihydropyridine **C3D1** was formed in 65% yield, as determined by ^{1}H NMR (Table 3.2, entry 8). On the contrary, the use of **12** gave no conversion (Table 3.2, entry 9), whereas employment of **13** yielded a mix of pyrazole **C3P1** and aldehyde **C3A1** (Table 1, entry 10) in yields comparable to the ones when no catalyst was added. These results clearly indicate that a clean and selective transformation of **C3Z1** to **C3D1** only takes place in the presence of **11**. To further confirm this, **L^3** was then tested as catalyst under the same conditions; in this case, formation of **C3P1** with lower conversion and yield was observed (Table 3.2, entry 11). For comparison, a mixture of $Cu(ClO_4)_2$ (2 mol%) and **L^3** (4 mol%) was found to catalyse the formation of **C3D1** in a lower 14% yield (Table 3.2, entry 12). However, in the absence of **L^3** no formation of **C3D1** was observed (Table 3.2, entry 1). The latter indicates a significant ligand effect that probably plays a crucial role to the catalytic reaction mechanism (see the mechanistic discussion in Section 3.2.4.3).

Table 3.2. Initial experiments of the transformation of aldazine **C3Z1** to the corresponding dihydropyridine (**C3D1**), pyrazole (**C3P1**) and aldehyde (**C3A1**) derivatives using various catalysts.

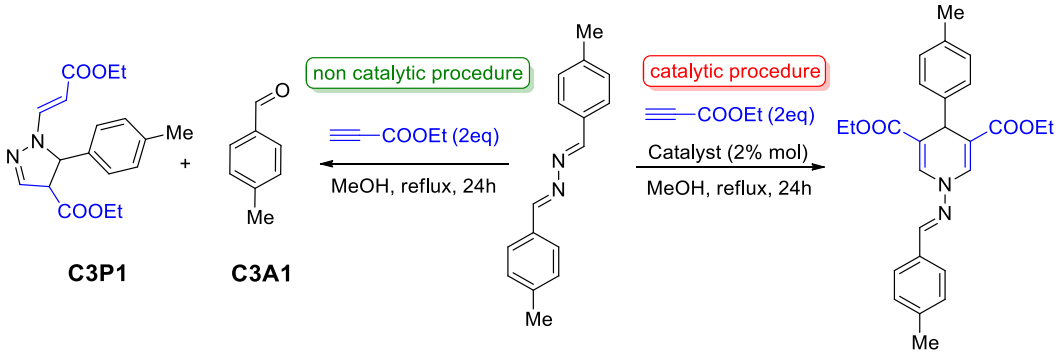

Entry	Catalyst[a]	Conv.[b] (%)	C3D1 [c] (%)	C3P1 [c] (%)	C3A1 [c] (%)
1	$Cu(ClO_4)_2$	>99	-	-	>99
2[d]	$Cu(NO_3)_2$	54	-	-	31
3[d]	$Cu(OAc)_2$	42	-	-	32

4	$CuCl_2$	>99	-	-	>99
5	$CuSO_4$	>99	-	-	>99
6	$Cu(PPh_3)_2(MeCN)_2]ClO_4$	N.r.[e]	-	-	-
7	No catalyst	65	-	30	35
8	**11**	>99	65	13	22
9	**12**	N.r.[e]	-	-	-
10	**13**	52	-	25	27
11	$\mathbf{L^3}$	25	-	12	13
12[d]	$Cu(ClO_4)_2$ + $\mathbf{L^3}$ [f]	99	14	-	-
13	$Cu(OAc)_2$ [g]	100	-	-	100

[a] **C3Z1** (0.1 mmol), ethyl propiolate (0.2 mmol) and 2 mol% of the solid catalysts. [b] Based on the consumption of **C3Z1** as determined by ^{1}H NMR. [c] Relative yields based on ^{1}H NMR analysis from the integration of the corresponding proton shifts. [d] A mixture of unidentified products was observed by ^{1}H NMR. [e] No reaction. [f] 4 mol% of $\mathbf{L^3}$ was added into the reaction mixture. [g] Oxygen saturated methanolic solution was used as solvent.

Among the solvents studied, high conversion of **C3Z1** was observed using methanol while EtOH afforded lesser consumption. The use of non-protic polar solvents, such as DMF, CH_3CN, acetone, DCE or THF resulted in no conversion as only formation of the C-C coupling product, diethyl hexa-2,4-diynedioate, was observed. Subsequently, no formation of **C3D1** was observed when H_2O was employed as reaction solvent or co-solvent. However, no significant increase of the relative yield of **C3D1** was observed when the reaction was performed under dry methanolic solution (over 3 Å molecular sieves). The full results of the solvent screening are presented in Table 3.3.

Having identified methanol as the most suitable solvent, the next step was to optimise the remaining conditions of the catalytic procedure. Table 3.4 contains the results of these experiments. It was found that higher or lower loadings of **11** afforded lower yields of **C3D1**. Additionally, **C3Z1** remains intact when the reaction is performed at room temperature, while heating the mixture at 50^{o}C provided low conversions. However, no dihydropyridine is formed when the reaction takes places under microwave irradiation; instead, the formation

of the corresponding hydroalkoxylation product, ethyl (*Z*)-3-methoxyacrylate as the major product is observed. Finally, no reaction took place in the presence of several other alkyl or aryl alkynes (i.e. DMAD, phenyl acetylene, propargyl bromide, propargyl alcohol and crotyl ester), as the formation of the corresponding dihydropyridine was only observed when methyl or ethyl propiolate were used (Table S3.2, Appendix).

Table 3.3. Evaluation of solvents in the catalytic transformation of **C3Z1** to the corresponding products using **11** (2 mol%) as the catalyst. The remaining reaction parameters were the same as the ones employed for the results of Table 3.2.

Entry	**Solvent**	**C3Z1 (%)**	**C3D1 (%)**	**C3P1 (%)**	**C3A1 (%)**
1	MeOH	-	65	13	22
2	MeOH (dried over mol. sieves 3 Å)	-	69	14	17
3	MeOH/H_2O (99/1)	64	-	-	36
4	MeOH/DCE	35	29	10	26
5	EtOH	28	21	24	48
6	H_2O	>99	-	-	-
7	MeCN	43	-	21	26
8	MeCN/H_2O (99/1)	68	-	-	32
9	Dioxane	86	-	-	14
10	DCE	78	trace	-	21
11	THF	>99	-	-	
12	Toluene	>99	-	-	
13	Acetone	72	-	-	28
14	DMF	>99	-	-	-

Table 3.4. Optimisation of the catalyst loading and temperature conditions in the catalytic transformation of **C3Z1** to the corresponding products using **11** as the catalyst and methanol as solvent. The remaining reaction parameters were the same as the ones employed for the results of Table 3.2.

Entry	Conditions	Catalyst (mol%)	Conv. (%)	C3D1 (%)	C3P1 (%)	C3A1 (%)
1	reflux	-	65	-	30	35
2	reflux	**11** (2)	100	65	13	22
3	reflux	**11** (1)	69	42	10	17
4	reflux	**11** (4)	100	55	18	27
5	r.t.	**11** (2)	0	-	-	-
6	50ºC	**11** (2)	74	36	13	25
7	M.W.[a]	**11** (2)	36	-	-	36
8	reflux [b]	**11** (2)	52	-	10	42
9	reflux [c]	**11** (2)	100	-	-	100

[a] The corresponding hydroalkoxylation product was formed as the major one. [b] Adding 1,2,3-trimethoxybenzene. [c] Oxygen saturated methanolic solution was used as solvent.

3.2.4.2. Scope of Reaction

To study the limitation of the above catalytic procedure, a series of substituted azines were examined. Scheme 3.3 summarizes the results obtained using **11** as catalyst. In all cases the corresponding HA-1,4-DHPs derivatives (Scheme 3.3, entries **C3D1** – **C3D18**) were formed with good isolated yields (ca. 44-68%). It is worth noting that electron rich aromatic azines (X = Me or MeO) are transformed to the corresponding HA-1,4-DHPs derivatives (entries **C3D1 – C3D5**, **C3D11 – C3D14**), with higher yields (44%-68%) within 24 hours, compared to the electron deficient azine (X = CF_3) in which negligible yield (<5%) for the corresponding dihydropyridine **C3D8** was observed within 48 hours. Remarkably, no reaction was observed when the *para*-nitro substituted azine was used as substrate. In addition, the use of methyl propiolate instead of ethyl propiolate gave similar conversions and isolated yields of the corresponding HA-1,4-DHPs derivatives (entries **C3D11 – C3D15**) compared to the respective ethyl propiolate entries. Heterocyclic substituted azines

containing thiophenyl and furyl units were also tested under the present catalytic conditions, giving the corresponding dihydropyridines **C3D16** and **C3D17** in ca.67% and 10% isolated yield, respectively. Subsequently, the analogous naphthyl substituted azine shows lower activity, with the corresponding product formed in negligible yield (<5%). All the products were determined by ^{1}H NMR spectroscopy, whereas **C3D4**, **C3D5**, **C3D6** and **C3D13** were additionally characterized with single X-Ray diffraction (Figure 3.4).

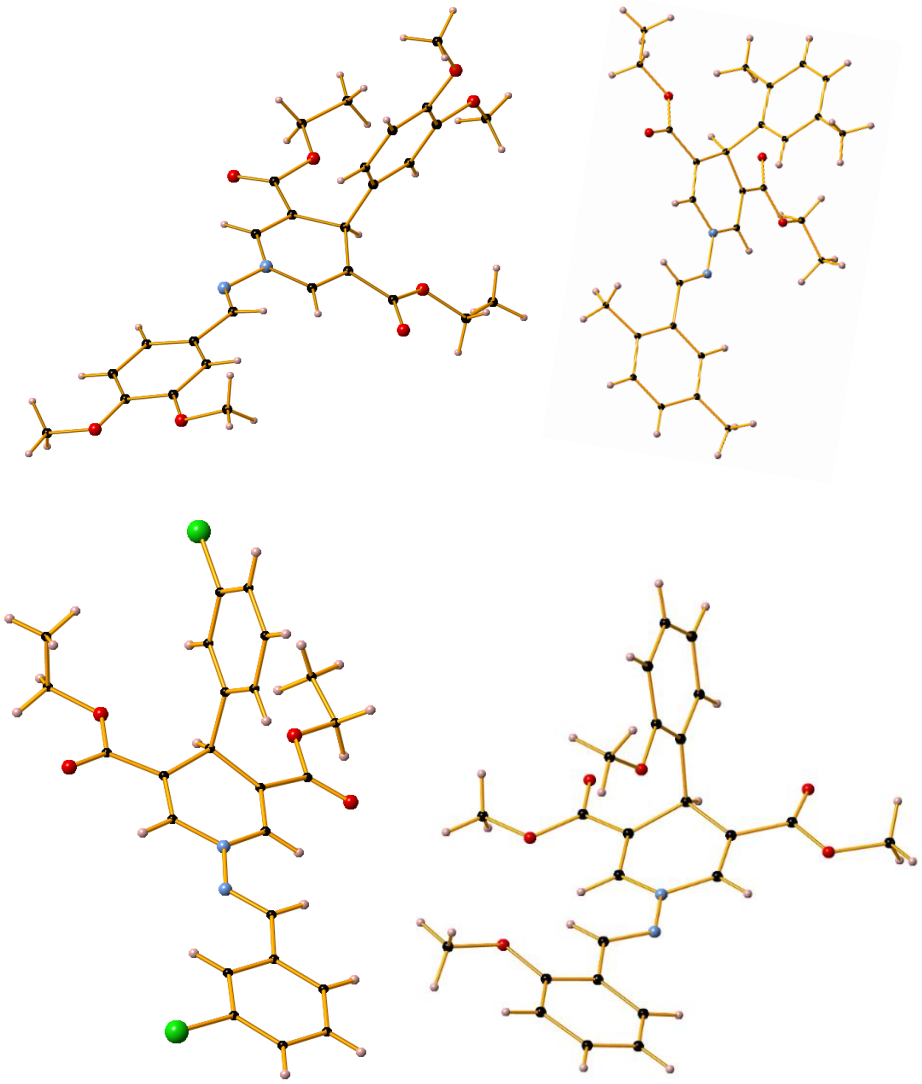

Figure 3.4. Crystal structures of the 1,4-DHPs for entries **C3D4** (upper left), **C3D5** (upper right), **C3D6** (bottom left) and **C3D13** (bottom right). Colour code C (black), H (light pink), N (light blue), Cl (green), O (red).

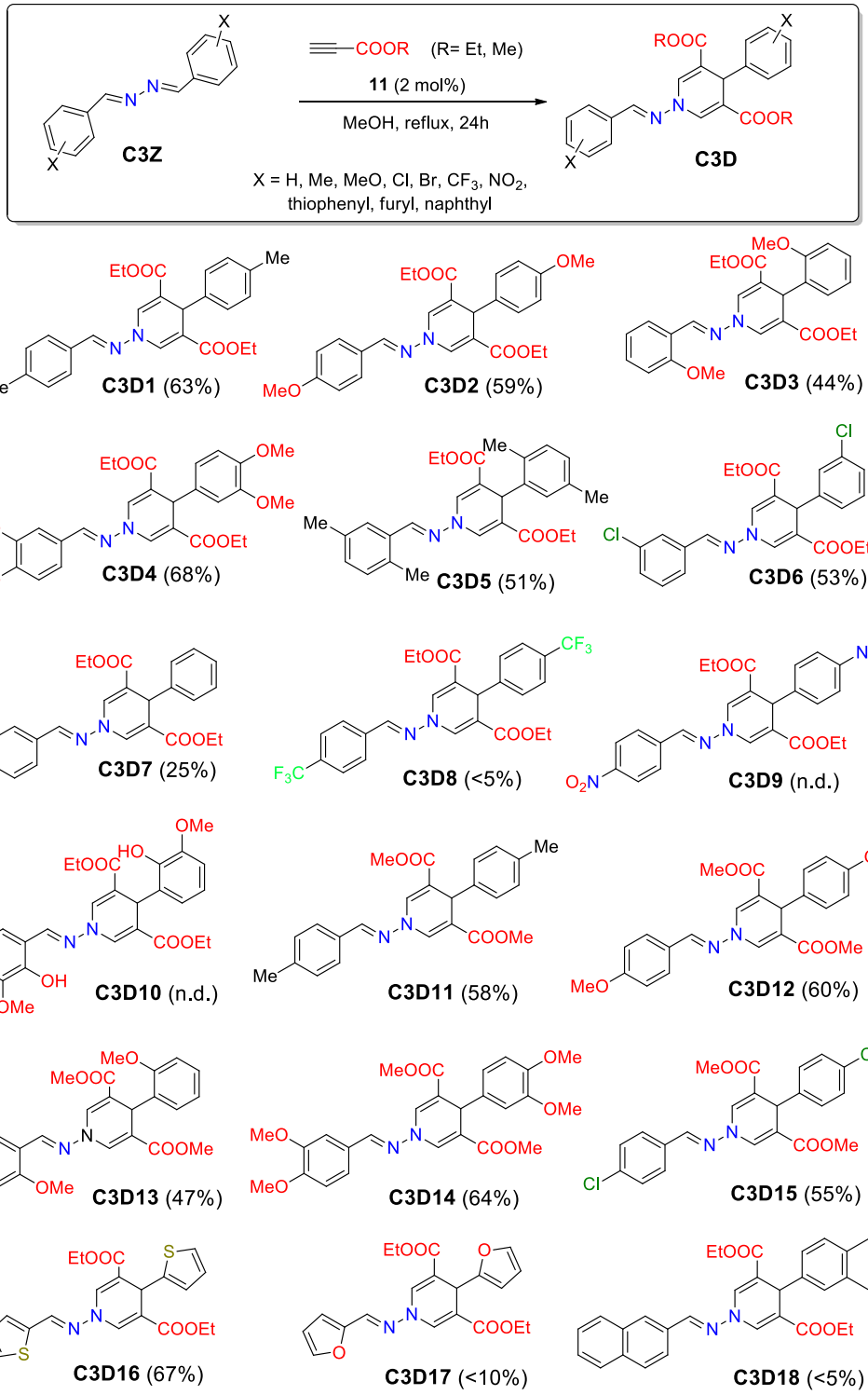

Scheme 3.3. Various (*N´*-substituted)-hydrazo-4-aryl-1,4-dihydropyridines synthesized by Cu-catalysed reaction. The percentages correspond to the yields of isolated products. n.d. = not detected. Relative yields for the catalytic 1,4-DHP products (**C3D**) and non-catalytic pyrazoles products (**C3P**) in each case may be found in Table S3.1, Appendix.

3.2.4.3. Mechanistic Insights

Regarding the mechanism of the title reaction, the following were observed:

a) For azines bearing electron donating groups such as 4-Me, 4-MeO, 3-MeO, 3,4-diMeO and 2,5-diMe a five times faster reaction was observed compared to the corresponding reaction of the azine containing H atoms in the 4-positions (entry **C3D7**). On the other hand, the azine bearing the electron-withdrawing CF_3 substituent in the *para* position reacted with a slower manner, while the respective NO_2-containing azine remained intact and did not react. This observation implies that an initial complex between the azine and the Cu^{II}-catalyst is formed, followed by a single electron transfer (SET)[200] process to form the active species. In the same context, a small amount (10 mol%, based on **C3Z1**) of the electron donor molecule. trimethoxybenzene (TMB) was added, as TMB shows oxidation potential less than that of azines ($E_{1/2}$ox *vs* SCE 1.12 V)[201]. As seen in Table 3.4, entry 8, this addition retards the reaction process.

b) Having in mind the ability of azines to donate electrons via lone pairs of the N atom or the C=N p-orbital electrons[195], it was expected that binding between the Cu^{II} catalyst and the azine would take place in solution. It is already known that azines show versatile properties of coordination in binding to metal centres, such as Cu^{II} or Fe^{II}, especially when the aromatic ring of the azine contains a hydroxyl group in the *ortho* position[202]. Indeed, experiments with the relevant starting material (containing the 2-OH and 3-MeO groups) under the proposed catalytic conditions showed no reactivity towards the synthesis of **C3D10**, probably through the *in-situ* azine-Cu^{II} catalyst coordination effect (a proposed complex is shown in Figure S3.15, Appendix).

c) The reaction of 4-methylbenzaldehyde (**C3A1**), ethyl propiolate and **11** in methanol yielded a mixture of unidentified products as confirmed by ^{1}H NMR (Figure S3.16, Appendix). Furthermore, the hetero-azine (1E,2E)-1-(4-chlorobenzylidene)-2-(4-methoxybenzylidene)hydrazine, which bears two different substituents in the para-positions of the aromatic rings (MeO and Cl), was tested as a substrate. In that case, both HA-1,4-DHP derivatives **C3D19a** and **C3D19b** were formed in a ratio of 2:1, as determined by ^{1}H NMR and LC-MS (Figures S3.17-S3.19, Appendix). These results indicate that the azine does not

dissociate during the current catalytic reactions. Therefore, the present catalytic procedure probably follows a different mechanistic pathway compared to the commonly proposed multi-component reaction (MCR) or Lewis-acid catalysed processes[178,179]. In addition, when (*Z*)-3-methoxyacrylate (a common starting material for the above literature studies) was employed instead of the propiolate ester under the same catalytic conditions, the desired 1,4-dihydropyridine product was not observed (Table S3.2, Appendix).

d) During attempts to recover the catalyst, a yellow solid material formulated as [Cu^{I}(**L**^{3})Cl] (**11i**) was isolated and characterized via single crystal X-Ray crystallography, corresponding to a 1D CP that extends infinitely through chlorine bridging while **L**^{3} retains the same conformation and coordination mode (Figure 3.5). This indicates that ClO_4^- and Cu^{II} convert to Cl^- and Cu^{I} respectively[203]. Therefore, it is envisaged that at a certain point, transformation of perchlorate to chloride occurs, which in turn starts to coordinate to Cu^{I} centres, transforming the catalyst to **11i** (Scheme 3.4, bottom). In addition, **11i** was found to be catalytically inactive when tested under the same conditions. This result indicates a low value of turnover number (TON) of the present catalytic system **11**, with a max number of ca. 55).

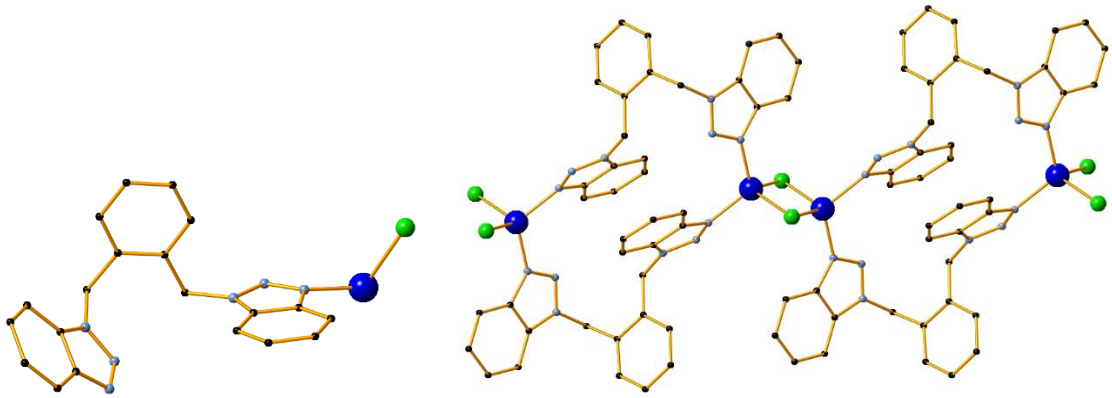

Figure 3.5. (left) The asymmetric unit of compound **11i**. (right) part of the one-dimensional framework of the complex. H atoms are omitted for clarity. Colour code Cu (dark blue), C (black), N (light blue), Cl (green).

Based on the above experimental results and observations, a possible reaction mechanism is proposed in Scheme 3.4. Azine (**Z**) initially coordinates to the catalyst (**$Cu^{II}L_2$**), forming a new catalytic intermediate **$Cu^{II}L_2Z$** (Scheme 3.4, top). ESI-MS and UV-Vis studies in methanolic solutions indicate that Cu^{II} in **11** retains the octahedral geometry and coordinates to four N atoms of four different **L^3** ligands; a similar pattern was observed for the isostructural Zn analogue **13**. In comparison, in the case of the catalytically inactive compound **12** Cu^{II} retains its geometry but coordinates to two N atoms belonging to two **L^3** ligands. Sequentially, a single electron transfer (SET) occurs from the electron rich azine to the **$Cu^{II}L_2Z$**, yielding the active reduced form, **$Cu^{I}L_2Z$**. This active species is responsible for the first catalytic pathway which includes the simultaneously formed propiolate complex and the proton release by the presence of the perchlorate anion forming the corresponding Cu^{I}-acetylide intermediate (**$Cu^{I}L_2Z$'**). Then, **$Cu^{I}L_2Z$'** may undergo a cyclization process, forming the unusual five-membered Cu^{III}-metallacycle intermediate **I** (**path A**, Scheme 3.4). A similar intermediate has been supported by a previous theoretical study on the copper-catalysed synthesis of azoles[204]. This hypothesis has also found support from related literature on the Cu-benzotriazole catalysed electrophilic cyclization of *N*-arylamines[205], as well as the Cu-catalysed synthesis of isoquinoline derivatives or other heteroarenes[206–208].

Subsequently, a reductive single cleavage (ring contraction)[209] leads to the common intermediate **II**, which after proteolysis releases the cyclo-compound dihydroazete **III**; this is followed by simultaneous conrotatory ring opening, yielding the corresponding diene which in turn reacts *in situ* with a second molecule of propiolate via a [4+2], giving the desired dihydropyridine derivative as the final product. This pathway requires a ligand replacement by the azine material that coordinates to a Cu centre[204] (Scheme 3.4). On the other hand, pathway B which contains the cyclization process without any ligand replacement or azine binding effect cannot be excluded (**path B** and intermediate **I'**, Scheme 3.4). However, it is worth noting that during the catalytic process a white powder was formed, that was found to be ligand **L^3** (confirmed by IR and NMR). In addition, a possible reductive elimination pathway from intermediate **I** would lead to the $Cu^{I}L$ which would then react with Cl^- to form the inactive specie $[Cu^{I}LCl]$ (Scheme 3.4, bottom).

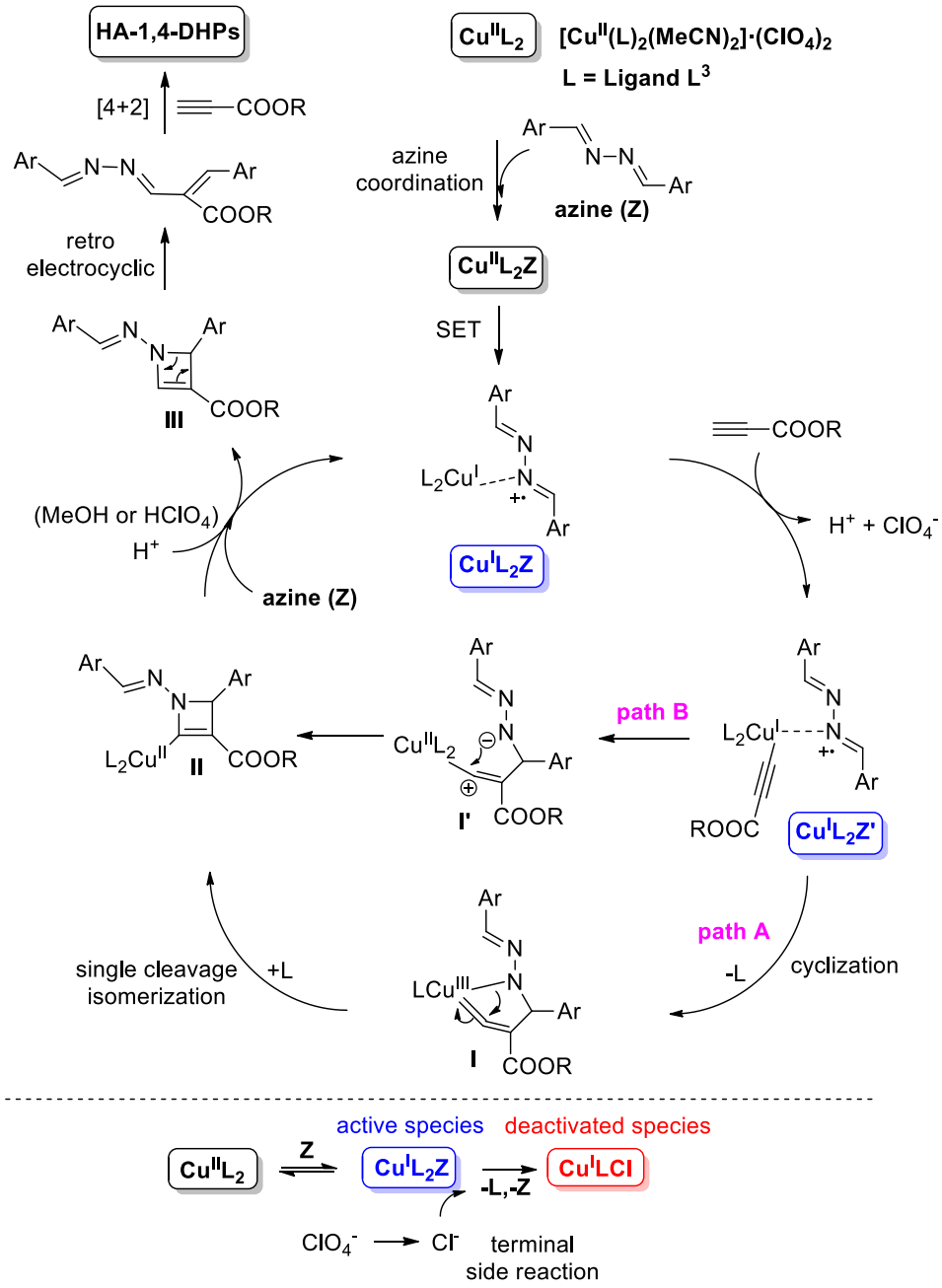

Scheme 3.4. Plausible mechanism for the synthesis of the (*N*'-substituted)-hydrazo-4-aryl-1,4-dihydropyridines through the Cu-catalysed coupling of azine and propiolate.

In parallel and under non-catalytic conditions, the formation of pyrazole products is promoted through a stepwise mechanism which contains a known criss-cross reaction ([3+2] cycloaddition) between the azine and the triple bond of propiolate, at a first step[195,196]. After

that, a nucleophilic addition and hydrolysis take place (with either one preceding the other) resulting to the corresponding 5-substituted-4,5-dihydro pyrazoles, as shown in Scheme 3.5. This is accompanied with an equimolar amount of the corresponding X-substituted benzaldehydes as the product from the hydrolysis pathway. It is worth noting that X-substituted benzaldehydes were also formed through an oxidative pathway from the initial azine; as shown in Table 3.4, entry 9, using molecular oxygen (O_2) saturated methanolic solution and under the present catalytic conditions (**C3Z1**, ethyl propiolate and **11** as catalyst) the corresponding aldehyde **C3A1** was observed as the only product.

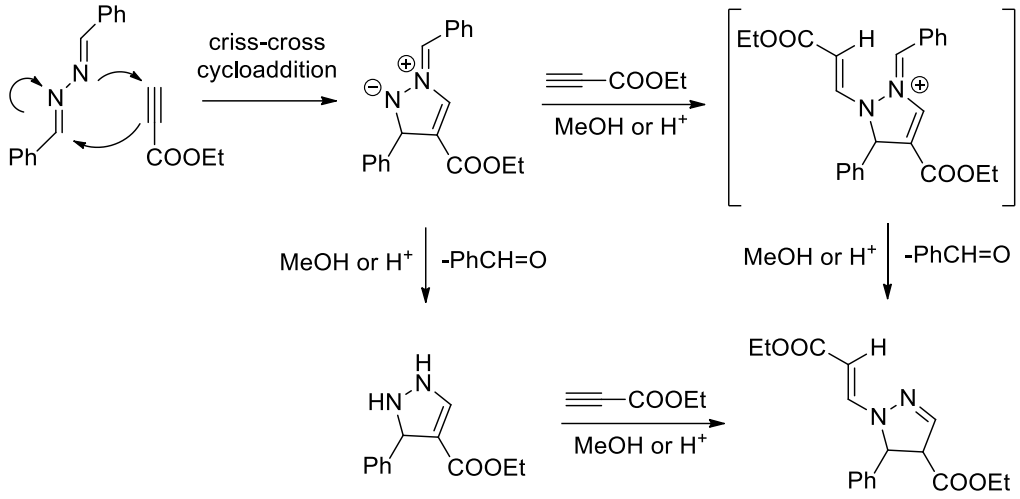

Scheme 3.5. Proposed mechanism for the synthesis of 5-substituted-4,5-dihydropyrazoles.

3.3. Conclusion

In conclusion, the current work exemplifies the unique nature of the Cu^{II} benzotriazole-based 1D CP **11** as a catalyst in the efficient synthesis of HA-1,4-DHPs. **11** may be easily synthesized in very good conversions and promotes the formation of a series of substituted dihydropyridines in good isolated yields, under relatively mild conditions and a low catalyst loading. Useful information about the mechanism of the reaction was obtained through fine tuning of the catalyst and the use of compounds **12** and **13**. From the mechanistic point of view, a metal:azine coordination initial step is followed by a SET pathway and a cyclization process constituting the basic catalytic procedures in the title reaction. The herein Cu-catalysed process is advantageous because of its possible wide use towards the synthesis of different heterocyclic organic molecules and because of its unique mechanistic

understanding. Having identified the potential of this system, Chapters 4 and 5 will document efforts on optimising its catalytic behaviour and its potential application towards other chemical transformations.

Chapter 4: Cu^{II} coordination polymers as vehicles in the A^3 coupling

Abstract: A family of benzotriazole-based coordination compounds, obtained in two steps and good yields from commercially available materials, formulated as $[Cu^{II}(\mathbf{L^3})_2Cl_2]_2$ (**14**), $[Cu^{II}_5(\mathbf{L^3})_2Cl_{10}]$ (**15**), $[Cu^{II}_2(\mathbf{L^3})_4Br_2]\cdot 4MeCN\cdot(Cu^{II}_2Br_6)$ (**16**), $[Cu^{II}(\mathbf{L^3})_2(MeCN)_2]\cdot(BF_4)_2$ (**17**), $[Cu^{II}(\mathbf{L^3})_2(CF_3SO_3)_2]$ (**18**), $[Zn^{II}(\mathbf{L^3})_2(MeCN)_2]\cdot(CF_3SO_3)_2$ (**19**) $[Cu^{II}_2(\mathbf{L^4})_4(H_2O)_2]\cdot(CF_3SO_3)_4\cdot 4Me_2CO$ (**20**) and $[Cu^{II}_2(\mathbf{L^5})_4(CF_3SO_3)_2]\cdot(CF_3SO_3)_2\cdot Me_2CO$ (**21**) are reported. Along with already reported complexes **11-13**, these air stable compounds were tested as homogeneous catalysts for the A^3 coupling synthesis of propargylic amine derivatives (**C4P**) from aldehyde (**C4A**), amine (**C4M**) and alkyne (**C4L**) under a non-inert atmosphere. Fine-tuning of the catalyst resulted in a 1D CP (**18**) with excellent catalytic activity towards a wide range of substrates, avoiding any issues that would inhibit its performance.

External Contributions: Nikolaos Tsoureas (University of Sussex) was responsible for the collection and interpretation of cyclic voltammetry data. Alaa Abdul-Sada (University of Sussex) was responsible for the collection of all ESI-MS data.

4.1. Introduction

The metal catalysed multi-component reaction (MCR) of an aldehyde, an amine and an alkyne, also known as the A^3 coupling (Scheme 4.1), has gathered significant interest[210–218]. This coupling reaction yields propargylic amines, which have been proposed as key intermediates in the synthesis of nitrogen-containing biologically active compounds such as acrylamidines[219], oxazoles[220,221], pyrroles[222], pyrrolidines[223] as well as natural products[224,225]. Due to this importance, a large variety of metal sources have been employed to catalyse this reaction such as Au^I/Au^{III} [226–228], Ag^I [229–232], Cu^I [217,233–236], In^{III} [237] or Rh^{III} [238]. More common transition metals, such as Cu^{II} [239–241], Fe^{III} [242–244], Ni^{II} [245] and Zn^{II} [246] have also been occasionally employed, albeit with higher catalyst loadings and under inert conditions.

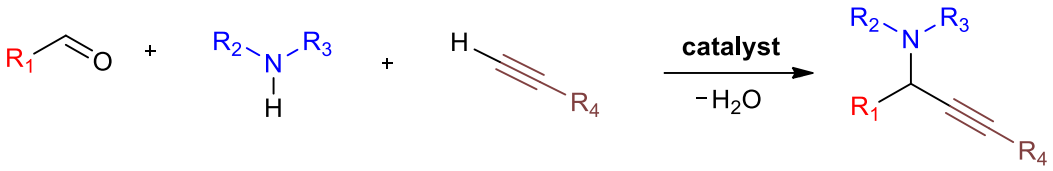

Scheme 4.1. The A^3 coupling reaction towards the formation of propargylic amines.

Chapter 3 demonstrated the catalytic activity of compound **11** in the synthesis of 1,4-dihydropyridines through a proposed mechanism which involved the formation of a Cu^{I}-acetylide intermediate, whereas compounds **12** and **13** were catalytically inactive. This big discrepancy in catalytic activity was attributed to the different coordination environment (**11** against **12**) as well as the different metal centre (**11** against **13**). Moreover, the catalytic performance of **11** was inhibited due to its conversion to the catalytically inactive compound **11i** where ClO_4^- is converted to Cl^-. These results revealed the large catalytic potential of this Cu^{II}/**L**^{3} system in similar transformations of high interest; however, more tests were required in order to further elucidate and tune this behaviour as well as identify more mechanistic aspects.

As a result of all the above, the next step in these efforts was to further explore the coordination capabilities of **L**^{3} with other Cu^{II} salts to characterize new low-dimensional CPs and use them as catalysts towards the well-known A^3 coupling reaction. It is worth noting that no 1D Cu^{II} CPs have been reported as catalysts for this reaction so far. To provide additional insight, analogous ligands **L**^{4} and **L**^{5} (Scheme 4.2), where benzotriazole molecules are replaced by 5-methylbenzotriazole and 5,6-dimethylbenzotriazole respectively, were synthesized and employed in these investigations. Therefore, this Chapter reports the synthesis and characterization of eight new compounds formulated as $[Cu^{II}(\mathbf{L^3})_2Cl_2]_2$ (**14**), $[Cu^{II}_5(\mathbf{L^3})_2Cl_{10}]$ (**15**), $[Cu^{II}_2(\mathbf{L^3})_4Br_2]\cdot 4MeCN\cdot(Cu^{II}_2Br_6)$ (**16**), $[Cu^{II}(\mathbf{L^3})_2(MeCN)_2]\cdot(BF_4)_2$ (**17**), $[Cu^{II}(\mathbf{L^3})_2(CF_3SO_3)_2]$ (**18**), $[Zn^{II}(\mathbf{L^3})_2(MeCN)_2]\cdot(CF_3SO_3)_2$ (**19**) $[Cu^{II}_2(\mathbf{L^4})_4(H_2O)_2]\cdot(CF_3SO_3)_4\cdot 4Me_2CO$ (**20**) and $[Cu^{II}_2(\mathbf{L^5})_4(CF_3SO_3)_2]\cdot(CF_3SO_3)_2\cdot Me_2CO$ (**21**), as well as the catalytic application of **11** – **21** in to the A^3 coupling reaction between aldehydes, alkynes and amines yielding the corresponding propargylamine derivatives.

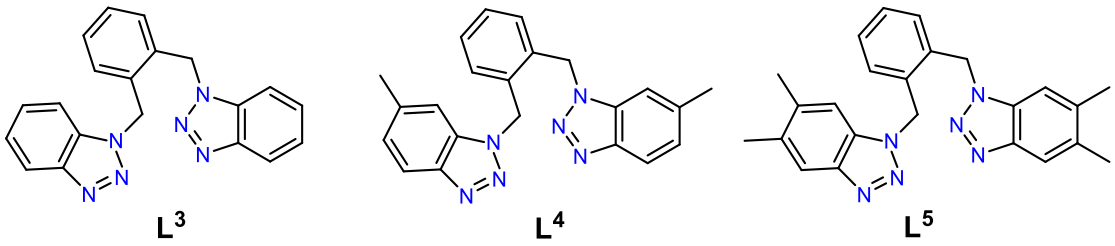

Scheme 4.2. The organic ligands (**L^3-L^5**) used in this study.

4.2. Results and Discussion

4.2.1. Crystal Structure Description of Compounds 14 – 21

The crystal structures of **11** – **13** were described in Chapter 3 and will not be discussed in detail in this Section. In addition, the structures of Cu^{II}-based compound **17** and Zn^{II}-based **19** were also found to be analogous to the one of **11**, with BF_4^- and CF_3SO_3 units instead of ClO_4^- respectively. As a result, they show the same M^{II} coordination environment (Table 4.1, entries 7, 9) and ligand conformation (Table 4.1, Mode A), generating similar 1D polymeric frameworks as seen in Figures 4.3 and 4.5. For this reason, these structures and their crystallographic parameters will also not be discussed further.

Compound **14** crystallizes in the triclinic $P\bar{1}$ space group and consists of two $[Cu_2(\mathbf{L^3})_2Cl_4]$ units. All metal centres in the structure show a distorted trigonal bipyramidal geometry through a coordination environment of $\{N_2Cl_3\}$ ($\tau = 0.46$ for Cu1, 0.40 for Cu2)[247]. The basal plane in the geometries of both metal centres consists of chloride atoms, while ligand nitrogen atoms are in the axial positions. These units are not further linked through intermolecular interactions and each ligand adopts a *syn*-conformation in regards to the position of the benzotriazole groups (Table 4.1, Mode B). This accounts for the eventual formation of zero-dimensional dimeric units (Figure 4.1, left). The mean Cu-N distances are 2.015(4) and 2.028(4) Å. Cl-Cu-Cl bond angles range from 93.65(4)° to 154.33(6)° while the respective values for the N-Cu-N angles are 177.47(17)° and 178.44(17)°.

Compound **15** also crystallizes in the triclinic $P\bar{1}$ space group. However, in this case the asymmetric unit contains two full-occupancy and one half-occupancy Cu^{II} centres, as well as one $\mathbf{L^3}$ molecule and five chlorine atoms. Two of the metal centres (Cu2, Cu3) are coordinated to the ligand and to chlorine atoms, while the third (Cu1) is only coordinated to chlorine atoms and bridges the $[Cu_2(\mathbf{L^3})_2]$ nodes. The ligand adopts the same conformation as in Mode A, but a different coordination mode (Table 4.1, Mode C). All of the above lead to the formation of an unusual two-dimensional coordination polymer which extends along the *a0c* plane, as shown in Figure 4.1 (right). The coordination environment and geometries of the metal centres are also varied. Cu1 is coordinated to five chlorine atoms and exhibits a distorted square pyramidal geometry ($\tau = 0.15$)[247]. The basal plane in this geometry has a mean deviation of 0.129 Å. Cu2 is also coordinated to five atoms and possesses a distorted square pyramidal geometry ($\tau = 0.09$)[247], however in this case the basal plane consists of three chlorine atoms and one ligand nitrogen atom, while the axial position is occupied by another ligand nitrogen atom, resulting in a $\{N_2Cl_3\}$ coordination environment. In this case, the respective plane has a deviation of 0.151 Å. Finally, Cu3 shows a $\{N_2Cl_4\}$ coordination environment consistent with an octahedral geometry, in which the ligand nitrogen atoms occupy the axial positions while chlorine atoms form the basal plane. The mean Cu-Cl bond distances range from 2.2671(12) to 2.6348(10) Å, while the respective Cu-N bond lengths range from 2.016(3) to 2.425(3) Å.

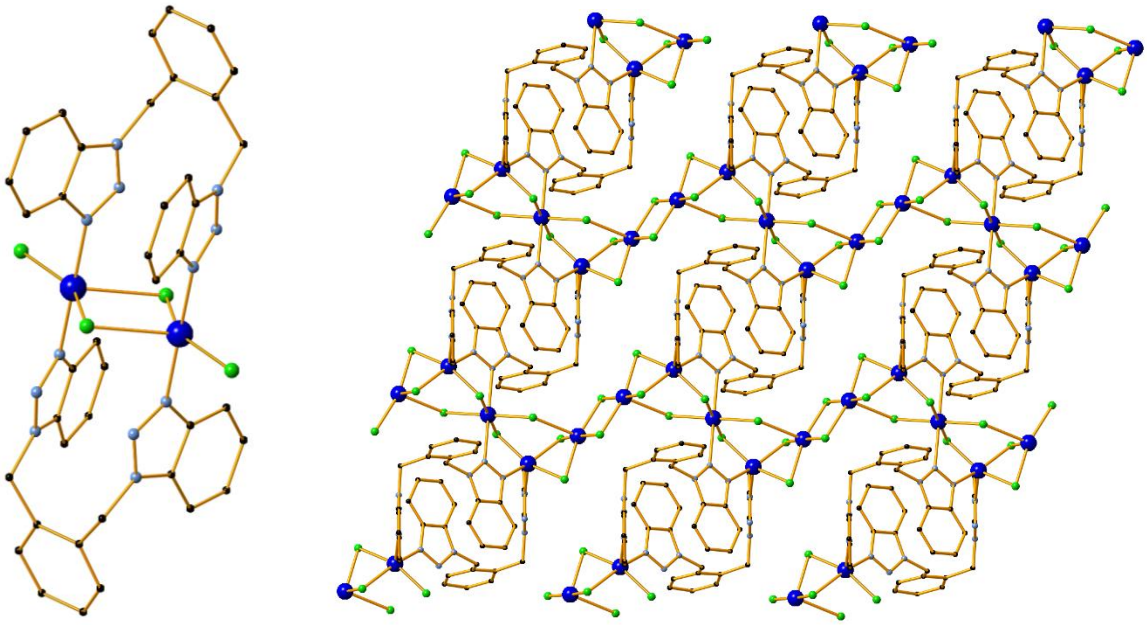

Figure 4.1. The structures of compounds **14** (zero-dimensional dimer, left) and **15** (two-dimensional framework, right). H atoms are omitted for clarity. Colour code Cu (blue), C (black), N (light blue), Cl (green).

Compound **16** was synthesized using $CuBr_2$ and crystallizes in the monoclinic C2/c space group. The main core of the structure consists of a $[Cu_2(\mathbf{L^3})_4Br_2]^{2+}$ dicationic dimer. A dianionic $[Cu_2Br_6]^{2-}$ unit is also present and completes the charge balance for all Cu^{II} centres. In similar fashion to **14**, this dimer does not form any intermolecular interactions and thus the structure is zero-dimensional **(**Figure 4.2). In this case the angle between the planes of the benzotriazole molecules of the ligand was measured at 125.4(4)°, similar to the one in Mode A. However, a concurrent rotation of the non-rigid C-N bond is also observed, leading to a different conformation mode (Table 4.1, Mode D). The metal centre that shows ligand coordination (Cu1) possesses a distorted trigonal bipyramidal ($\tau = 0.65$)[247] geometry through a $\{N_4Br\}$ environment. The bromine atom and two nitrogen atoms from ligand molecules consist of the basal plane, with the relevant angles ranging from 102.2(5)° to 139.0(3)°. The two remaining nitrogen atoms also derive from ligand molecules and occupy the axial positions of the bipyramid.

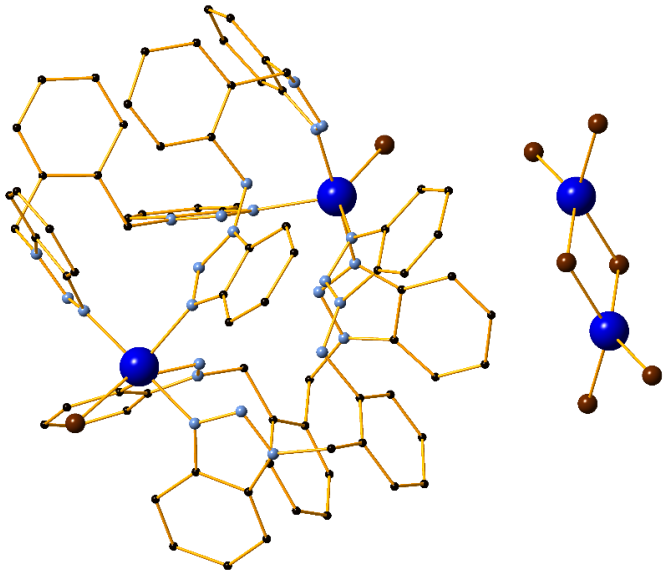

Figure 4.2. The structure of compound **16**. H atoms and solvent molecules are omitted for clarity. Colour code Cu (blue), C (black), N (light blue), Br (brown).

Compound **18** crystallizes in the triclinic $P\bar{1}$ space group and its asymmetric unit contains a Cu^{II} centre, one $\mathbf{L^3}$ molecule and one triflate anion molecule. The metal centre is coordinated to a total of six atoms and possesses an octahedral geometry through a $\{N_4O_2\}$ coordination environment. The complex shows an identical one-dimensional framework to the one found in compounds **11**, **13**, **17** and **19**; the only difference is that the axial positions of the octahedron are now occupied by triflate oxygen atoms instead of acetonitrile nitrogen (Figure 4.4). Consequently, the ligand adopts the same coordination mode as in the aforementioned compounds (Mode A). The mean Cu-O distance was measured at 2.536(4) Å, while the Cu-N bond lengths are 2.009(5) and 2.013(7) Å. No strong hydrogen bonds or other supramolecular interactions are observed.

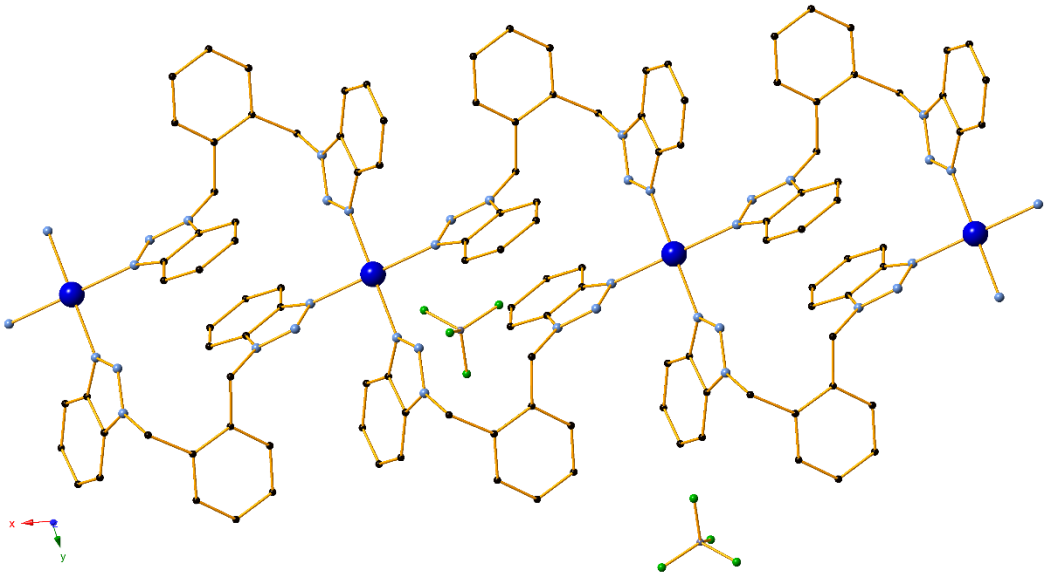

Figure 4.3. Part of the one-dimensional framework of **17** along the *a* axis. H atoms and solvent molecules are omitted for clarity. Colour code Cu (blue), C (black), N (light blue), B (dark grey), F (light green).

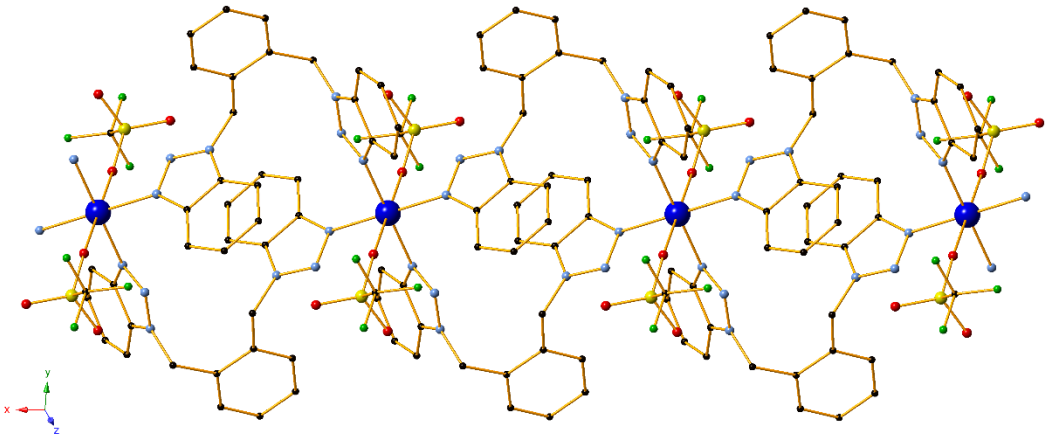

Figure 4.4. Part of the one-dimensional framework of **18** along the *a* axis. H atoms are omitted for clarity. Colour code Cu (blue), C (black), N (light blue), O (red), S (yellow), F (light green).

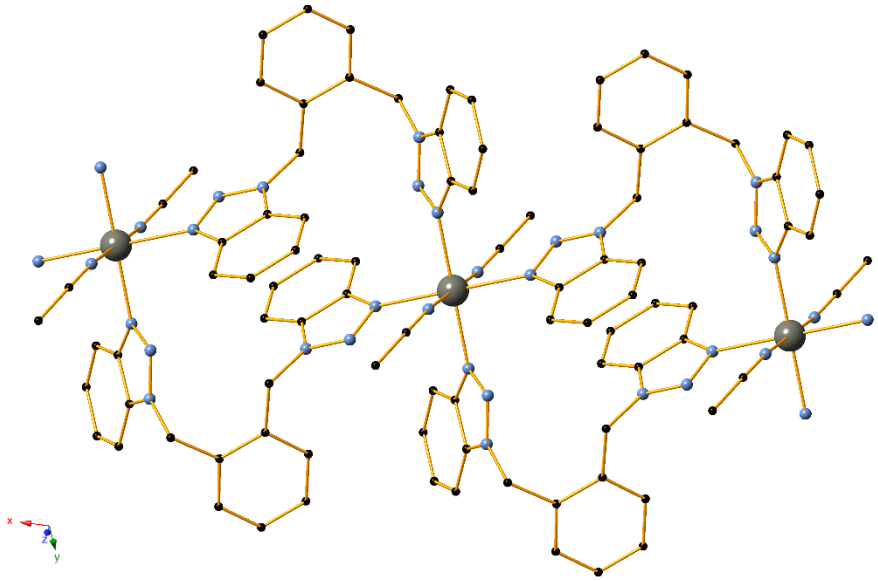

Figure 4.5. Part of the one-dimensional framework of **19** along the *a* axis. H atoms and anion molecules are omitted for clarity. Colour code Zn (grey), C (black), N (light blue).

Compound **20** was prepared using $\mathbf{L^4}$ as the ligand and crystallizes in the monoclinic C2/c space group. The structure is similar to the one of compound **16** as it contains a tetracationic dimer, $[Cu_2(\mathbf{L^4})_4(H_2O)_2]^{4+}$, as the main core. Four triflate anions are present in the lattice to complete the charge balance for all metal centres. As a result, the structure is zero-dimensional **(**Figure 4.6) and the dimer is further stabilized through the formation of two strong O-H···O hydrogen bonds, each formed between a water molecule and a triflate anion. The $\mathbf{L^4}$ ligand behaves similarly to $\mathbf{L^3}$ in the case of compound **16**, adopting the same conformation and coordination mode (Table 4.1, Mode D). Each metal centre shows a $\{N_4O\}$ coordination environment through four ligand nitrogen atoms and one oxygen atom from the water molecule, possessing a distorted square pyramidal ($\tau = 0.29$)[247] geometry. The basal plane of this pyramid consists of three nitrogen atoms and one oxygen and shows a mean deviation of 0.149 Å. Compound **21** may be considered as isoskeletal to **20** as it contains a similar dimeric $[Cu^{II}_2(\mathbf{L^5})_4(CF_3SO_3)_2]$ core; in this case the two coordinating water molecules are replaced by triflate anions while $\mathbf{L^5}$ exhibits the same conformation as $\mathbf{L^4}$ (Figure 4.7). Due to the similarities, the resulting zero-dimensional structure will not be further described.

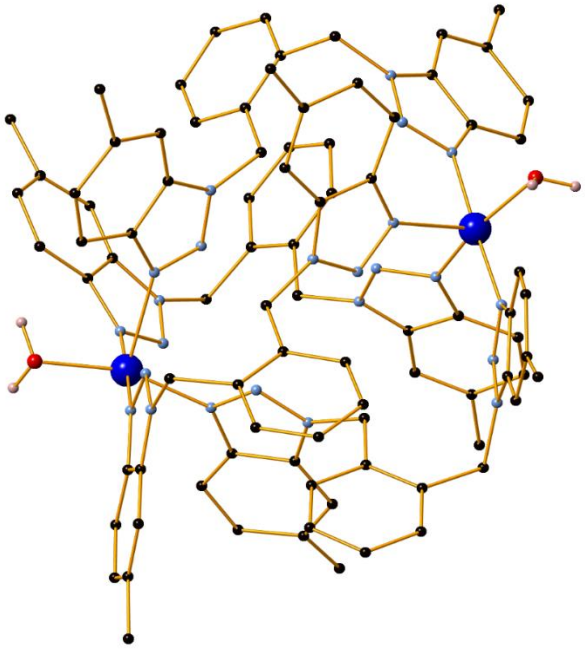

Figure 4.6. The structure of compound **20**. Lattice solvent molecules, lattice anions and certain H atoms are omitted for clarity. Colour code Cu (blue), C (black), N (light blue), O (red), H (light pink).

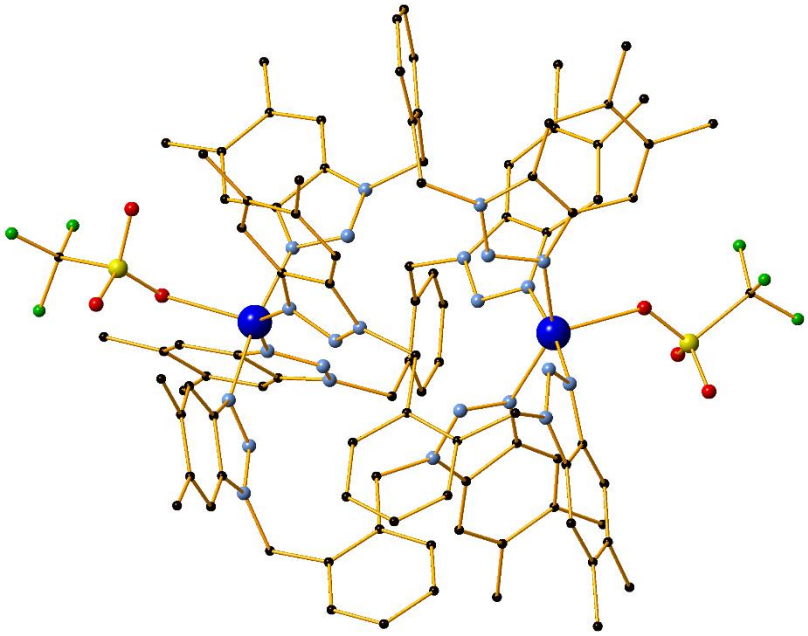

Figure 4.7. The zero-dimensional compound **21**. Lattice solvent molecules, lattice anions and H atoms are omitted for clarity. Colour code Cu (blue), C (black), N (light blue), O (red).

Table 4.1. Overview of the coordination characteristics (ligand conformation, coordination geometry of the metal) of the compounds used in this study (S = solvent).

Entry	Compound	Geometry of M^{II}	Coordination Mode	Dimensionality
1	**11**	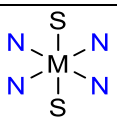	A	1D
2	**12**	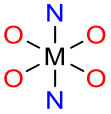	A	2D
3	**13**	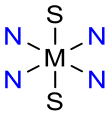	A	1D
4	**14**	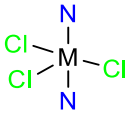	B	0D
5	**15**	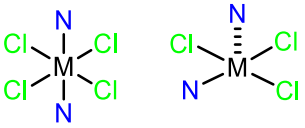	C	2D
6	**16**	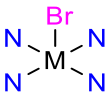	D	0D
7	**17**	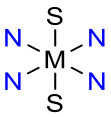	A	1D
8	**18**	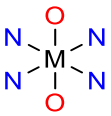	A	1D
9	**19**	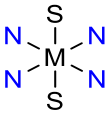	A	1D
10	**20**	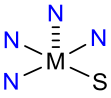	D	0D
11	**21**	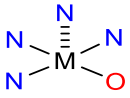	D	0D

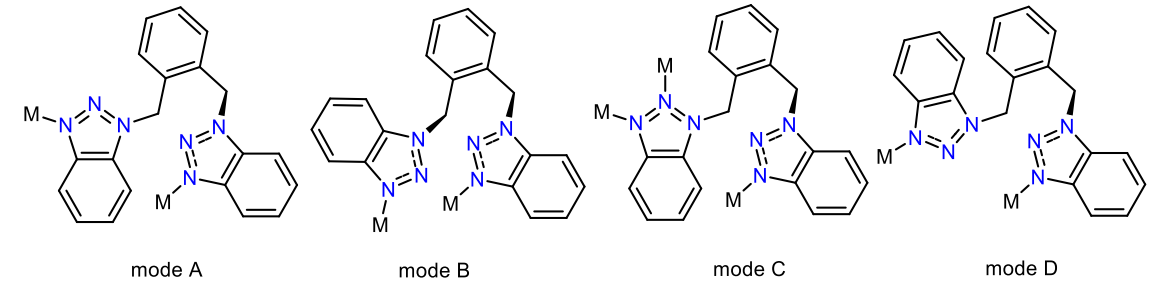

4.2.2. Synthetic Aspects

An efficient synthetic strategy to generate Cu^{II} and Zn^{II}-based compounds using **L³** was discussed in detail in Chapter 3. Therefore, several of the compounds presented in this Chapter employ the same techniques of leaving the sample undisturbed in room temperature (compounds **16**, **17**) and using liquid diffusion (compounds **18** – **19**). In the case of $CuCl_2$-based compounds **14** and **15**, a crystalline material was obtained through the use of solvothermal conditions. Ligands **L⁴** and **L⁵** show similar behaviour to **L³** as they are soluble in DMF, acetonitrile and acetone while they are insoluble in water and alcoholic media. As a result, similar techniques were employed for the synthesis of **20** and **21**, with liquid diffusion providing the better quality of crystals. The same materials were obtained by employing all aforementioned techniques, albeit with worse crystal quality, showing that the formation of 0D dimers over CPs is heavily favoured in the case of **L⁴** and **L⁵**, possibly due to the steric effects caused by the additional methyl groups.

All reactions, with the exception of compounds **14** and **15**, are not sensitive to the M^{II}:L molar ratio; ratios from 3:1 to 1:3 yield the same compound in comparable yields and purity. In the case of **14** and **15**, the final product depends on the appropriate ratio of starting materials (1:1 and 3:1, respectively) and temperature (75° and 95°C, respectively), accompanied by a change in the conformation of the ligand. These effects are consistent with the ones reported in the $CoCl_2$-based compounds in Chapter 2. In this case, efforts to obtain **15** through a crystal transformation of **14** proved unsuccessful. The use of $Cu^{I}Cl$ as the metal source resulted in the synthesis (through liquid diffusion) of the catalytically inactive species **11i** and therefore was not investigated further. As in all previous compounds, the metal centre (Cu^{II} or Zn^{II}) is not coordinated to the middle nitrogen atom of the benzotriazole molecules in any of the compounds. Furthermore, **14**-**21** show no solubility in water, good solubility in DMF and

little solubility in other common organic solvents (such as acetonitrile or alcoholic media), which increases greatly when the mixture is heated.

4.2.3. Characterization of Compounds 14 – 21

TGA Studies

TGA measurements in all compounds showed (Figures S4.10-S4.17, Appendix) that the thermal stability of the frameworks is retained up to the region of ~250-400 °C, where gradual decomposition takes place. Before these temperatures an initial mass loss occurs in certain compounds, corresponding to the loss of any existing solvent molecules or the counter-anions. In detail, compound **14** shows an initial mass loss which occurs at 312 °C and corresponds in good agreement to the loss of all chlorine atoms (calc.: 16.10%, theor.: 15.08%). The complex then undergoes another mass loss due to the gradual decomposition to copper oxide (calc.: 73.81%, theor.: 74.58%). In compound **15**, mass loss begins in the region of ~250 °C due to the loss of all ten chlorine atoms (calc.: 26.40%, theor.: 26.00%) before decomposition takes place (calc.: 70.34%, theor.: 69.13%). In **16**, a continuous mass loss from room temperature up to ~190 °C takes place initially, in reasonable agreement with the loss of four acetonitrile molecules (calc.: 4.47%, theor.: 5.81%). Gradual decomposition of the remaining core occurs almost immediately. A similar procedure (calc.: 6.74%, theor.: 7.21%) is observed in the TGA analysis of **17** with the remaining framework retaining its stability up to ~260 °C. In compound **18** a continuous mass loss up to the region of ~270 °C occurs due to the loss of the triflate anions (calc.: 27.94%, theor.: 28.80%) before the decomposition of the remaining framework to copper oxide. The analysis for **19** shows an initial mass loss from room temperature up to ~250 °C, due to the loss of all acetonitrile molecules (calc.: 8.94%, theor.: 7.29%). The next mass loss occurs immediately and up to ~400 °C (calc.: 25.29%, theor.: 26.50%) and corresponds to the loss of triflates. Decomposition to ZnO follows after that temperature (calc.: 59.16%, theor.: 59.10%). A similar procedure takes place in compound **20**, with the first and second mass loss corresponding to the respective losses of solvent molecules (calc.: 10.29%, theor.: 10.89%) and triflates (calc.: 24.45%, theor.: 24.20%). The remaining framework begins to decompose to CuO (calc. 58.98%, theor.: 58.52%) at the region of 380-400 °C. Finally, compound **21** shows an initial loss up to the region of ~380-400 °C, due to the loss of triflates and acetone

lattice molecules (calc. 29.45%, theor.: 30.56%). The remaining framework then decomposes gradually to the respective oxide (calc. 62.52%, theor.: 61.93%).

Solution Studies

ESI-MS (positive-ion mode) experiments performed in methanolic solution for all Cu^{II} compounds (**14** – **18**, **20** – **21**) once again showed the presence of two main peaks which are attributed to the respective $[Cu(\mathbf{L})]^{1+}$ and $[Cu(\mathbf{L})_2]^{1+}$ fragments with excellent agreement. Each spectrum also contains several additional peaks, with the main peaks corresponding with perfect agreement to metal-ligand-anion fragments; the most common fragments found were $[Cu(\mathbf{L})X]^{1+}$, $[Cu_2(\mathbf{L})X]^{1+}$, $[Cu(\mathbf{L})_2X]^{1+}$, $[Cu(\mathbf{L})_3X]^{1+}$, where X is the anion present in each compound. It is worth noting that many of these peaks in the ESI-MS spectrum of the $CuBF_4$-based compound **17** correspond perfectly to analogous fragments with F^- as the anion present, suggesting a possible conversion of BF_4^- to F^- within the solution. In regards to the Zn^{II} compound **19**, similar peaks were observed corresponding perfectly to the $[Zn(\mathbf{L^3})]^{+1}$, $[Zn(\mathbf{L^3})_2]^{1+}$, $[Zn(\mathbf{L^3})X]^{+1}$, $[Zn(\mathbf{L^3})_2X]^{+1}$, $[Zn(\mathbf{L^3})_3X]^{+1}$ fragments. ESI-MS spectra, along with detailed analysis of the fragments are presented in the Appendix (Figures S4.1-S4.8). Additionally, the UV-Vis spectra of compounds **17**, **18**, **20** and **21** in MeOH show a broad peak (ca. 800 nm) which is characteristic of *Jahn Teller* effect and consistent for a Cu^{II} centre with an octahedral $\{N_4O_2\}$ geometry (Figure S4.9, Appendix).

Cyclic Voltammetry Studies for Compound 18

To investigate its electron donating capabilities, the electrochemistry of **18** was studied by cyclic voltammetry (CV). CV in the cathodic direction over several cycles showed a quasi-reversible reduction process at -0.423 V vs $Fc^{+/0}$ (i_a/i_c = 1.5) (Figure 4.8) vs $FeCp_2^{+/0}$ and a non-reversible reduction process[248] at -1.156 V vs $Fc^{+/0}$. The former may be assigned to the $[Cu^{II}]\leftrightarrow[Cu^{I}]$ couple, further supporting the possible formation of a Cu^{I} intermediate during a catalytic reaction.

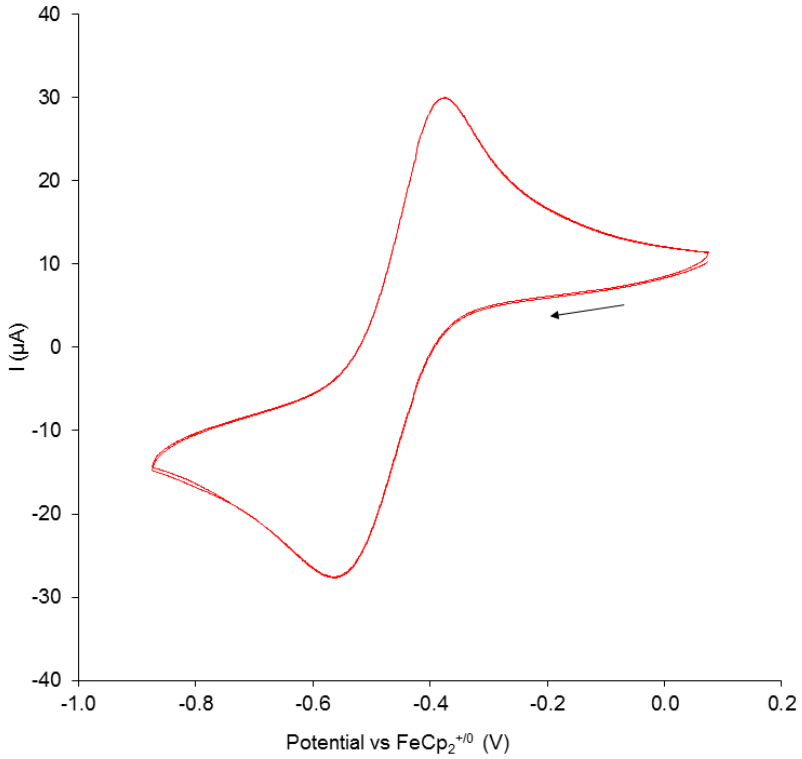

Figure 4.8. Overlaid CV scans (2 cycles) of **18** in 0.05 M [^{n}Bu$_4$N][PF$_6$]/DMSO. Scan rate 300 mVs -1.

4.2.4. Catalytic Studies

4.2.4.1. Benchmarking and Optimisation

In order to test the possible catalytic activity of **11** – **21**, the application of these catalytic systems was first studied in the A^3 coupling of benzaldehyde, pyrrolidine and phenylacetylene. During initial experiments with **11** as catalyst, a yellow crystalline material was isolated after the end of the reaction, as based on TLC. X-Ray crystallography showed that this material corresponds to the same Cu^{I} 1D CP **11i**, which has already been reported in Chapter 3 and found to inhibit the catalytic performance of **11**. To avoid these conversion issues, compound **18** was therefore employed in the following optimization procedures.

After screening a variety of solvents for the title reaction, 2-propanol (iPrOH), an environmentally friendly solvent[249], was found to provide an excellent 89% yield of the corresponding propargylamine when the reaction mixture was heated to 90^{o}C (Table 4.2, entry 6). Additionally, the reaction was found to be catalysed by only 0.02 mmol of the

catalyst (in 1 mmol reaction scale of benzaldehyde), in 12 hours stirring and under air atmosphere; the turn-over number (TON) and turn-over frequency (TOF) for this result were thus calculated at 44.5 and 3.71 hr^{-1} respectively. In contrast, other common organic solvents (such as DMF, acetonitrile, DCM) afforded lower yields. The remaining compounds **11-17**, **19-21** were also tested as catalysts under the same conditions (Table 4.3), showing inferior activity. A thorough discussion on rationalizing this behaviour is included in Section 4.2.4.3.

Table 4.2. Solvent optimization of the multi-component coupling of phenylacetylene, pyrrolidine and benzaldehyde using **18** as the catalyst.

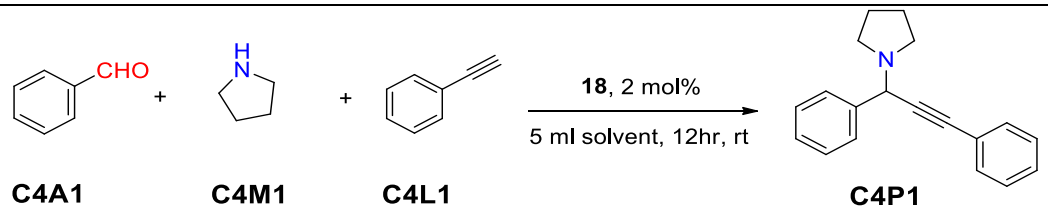

Entry	Solvent	[**product**] %
1	DMF	NR
2	DMSO	NR
3	MeOH	trace
4	EtOH	11
5	i-PrOH	26
6	i-PrOH[a]	89
7	Toluene	24
8	Toluene[a]	76
9	MeCN	13
10	CH_2Cl_2	NR
11	$CHCl_3$	trace

Reaction conditions: Benzaldehyde (102 µL, 1 mmol), pyrrolidine (90µL, 1.1 mmol), phenylacetylene (132 mL, 1.2 mmol), **18** (2% mmol), solvent (5 ml), rt, 12 h. Relative yields based on ^{1}H NMR analysis from the integration of the corresponding proton shifts. NR = no reaction. [a] heated at 90^{o}C.

Table 4.3. Overview of the characteristics and catalytic activity of the coordination compounds in this study (S = Solvent).

Entry	Compound	Geometry of M^{II}	Yield % [a, b]
1	**11**	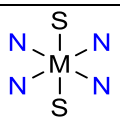	68
2	**12**	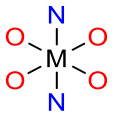	<5
3	**13**	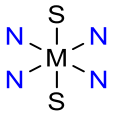	<10
4	**14**	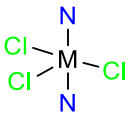	NR[c]
5	**15**	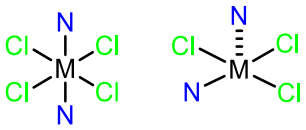	NR[c]
6	**16**	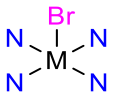	NR[c]
7	**17**	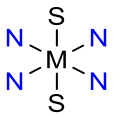	64
8	**18**	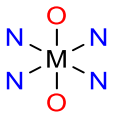	89(85)[d]
9	**19**	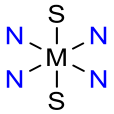	21
10	**20**	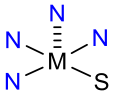	57
11	**21**	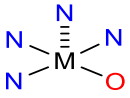	44

[a] Relative yields based on ^{1}H NMR analysis from the integration of the corresponding proton shifts. [b] Reaction conditions: benzaldehyde (102 µL, 1 mmol), pyrrolidine (90µL, 1.1 mmol),

phenylacetylene (132 mL, 1.2 mmol), catalyst (2 mol%), iPrOH (5 ml), T = 90°C, 12 hr stirring. [c] No reaction. [d] The reaction was performed in presence of 10% TEMPO.

To further evaluate the catalytic activity of **18**, several control experiments with common Cu^{II} salts were performed for the same A^3 reaction and the results are summarized in Table 4.4. In all cases, the corresponding Cu^{II} salts afforded significantly lower yields, ranging from 55 to 65%, at a higher catalyst loading of 10 mol% based on the benzaldehyde amount (Table 4.4, entries 1-8). Moreover, the use of Cu^{II} salts as catalysts in the analogous A^3 coupling with other *para*-substituted benzaldehydes (such as the 4-chloro-, 4-trifluoromethyl-, 4-methoxy-) instead of benzaldehyde, yielded the corresponding product in low yields (10-15%) showcasing their limited catalytic efficiency (Table 4.4, entries 9-14). In the absence of catalyst no reaction was observed, a result that supports the catalytic behaviour of the studied multi-component coupling.

Table 4.4. Evaluation of various Cu^{II} salts as catalysts in the multi-component coupling of phenylacetylene, pyrrolidine and benzaldehyde.

Entry	**Catalyst**	[**product** %] [a]
1	$CuCl_2$	64
2	$Cu(NO_3)_2 \cdot 2.5H_2O$	65
3	$Cu(ClO_4)_2 \cdot 6H_2O$	60
4	$CuBr_2$	64
5	$CuBF_2 \cdot 6H_2O$	55
6	$Cu(OAc)_2 \cdot H_2O$	58
7	$Cu(OTf)_2 \cdot H_2O$	53
8	$Cu(OTf)_2 \cdot H_2O$ [b]	59
9	$CuCl_2$ [c]	11
10	$CuCl_2$ [d]	13
11	$CuCl_2$ [e]	11
12	$Cu(NO_3)_2 \cdot 2.5H_2O$ [c]	13
13	$Cu(NO_3)_2 \cdot 2.5H_2O$ [d]	15

14	$Cu(NO_3)_2 \cdot 2.5H_2O$ [e]	10
15	No catalyst	NR[f]

[a] Reaction conditions: Benzaldehyde (102 μL, 1 mmol), pyrrolidine (90μL, 1.1 mmol), phenylacetylene (132 μL, 1.2 mmol), catalyst (10 mol%), iPrOH (5 ml), heated at 90ºC for 12 hr. Relative yields based on ^{1}H NMR analysis from the integration of the corresponding proton shifts. [b] Two equivalents of **L^3** were added to the reaction mixture. [c] 4-chloro-benzaldehyde was used as instead of benzaldehyde. [d] 4-trifluoromethyl-benzaldehyde was used as instead of benzaldehyde. [e] 4-methoxy-benzaldehyde was used as instead of benzaldehyde. [f] No reaction.

4.2.4.2. Scope of Reaction

The scope of the reaction was then explored by employing a variety of aldehydes, amines and alkynes. The results are presented in Scheme 4.3. Using different aldehydes, pyrrolidine as the amine and phenylacetylene under the above described conditions, a variety of alkyl and aryl substituted propargylamines (**C4P1**-**C4P11**) were formed in moderate to high isolated yields. In particular, saturated aliphatic aldehydes react with higher isolated yields (98-100%), compared to the aromatic aldehydes that show slightly lower reactivity with moderate yields in the range of 57 to 89%. Consequently, the results of the amine screening (**C4P12**-**C4P21**) indicate that only secondary amines lead to reaction completion, in contrast to primary amines in which no reaction was observed. In general, cyclic aliphatic and aromatic secondary amines afford the corresponding propargylamine products in excellent yields, ranging from 98 to 100%; acyclic secondary amines were found to be slightly less effective. Finally, the employment of 1-hexyne and 4-trifluoromethylphenylacetylene in the reaction process (**C4P22**-**C4P24**), demonstrated that both alkynes react with the produced imine forming the analogous propargylamine products in good to excellent yields.

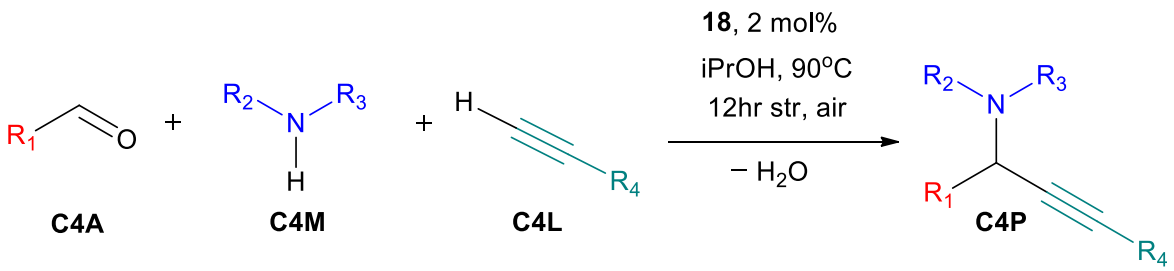

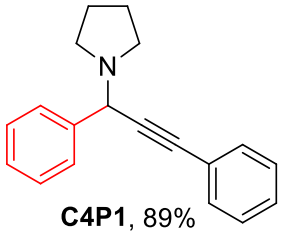

C4P1, 89%

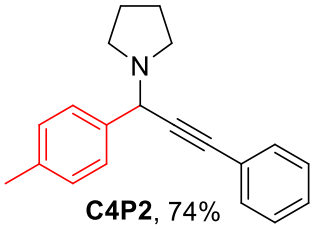

C4P2, 74%

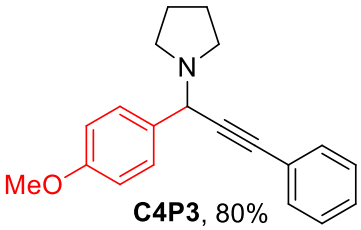

C4P3, 80%

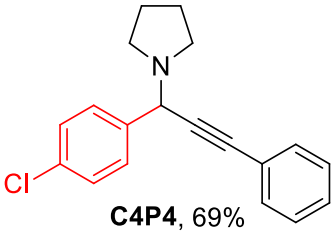

C4P4, 69%

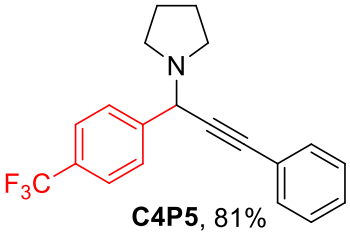

C4P5, 81%

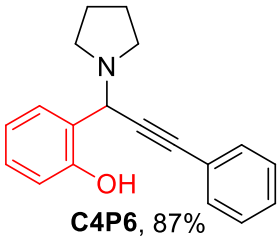

C4P6, 87%

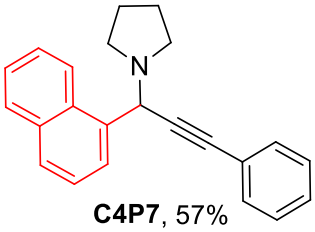

C4P7, 57%

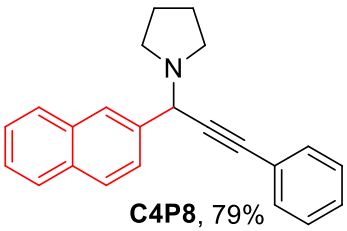

C4P8, 79%
(t=24hr)

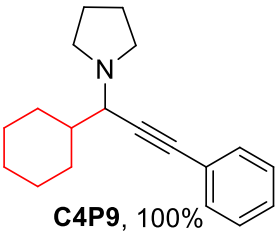

C4P9, 100%

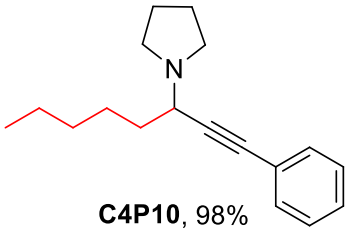

C4P10, 98%

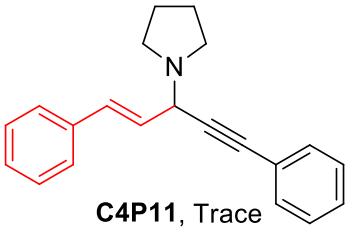

C4P11, Trace

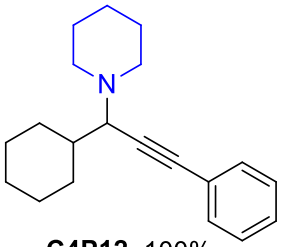

C4P12, 100%

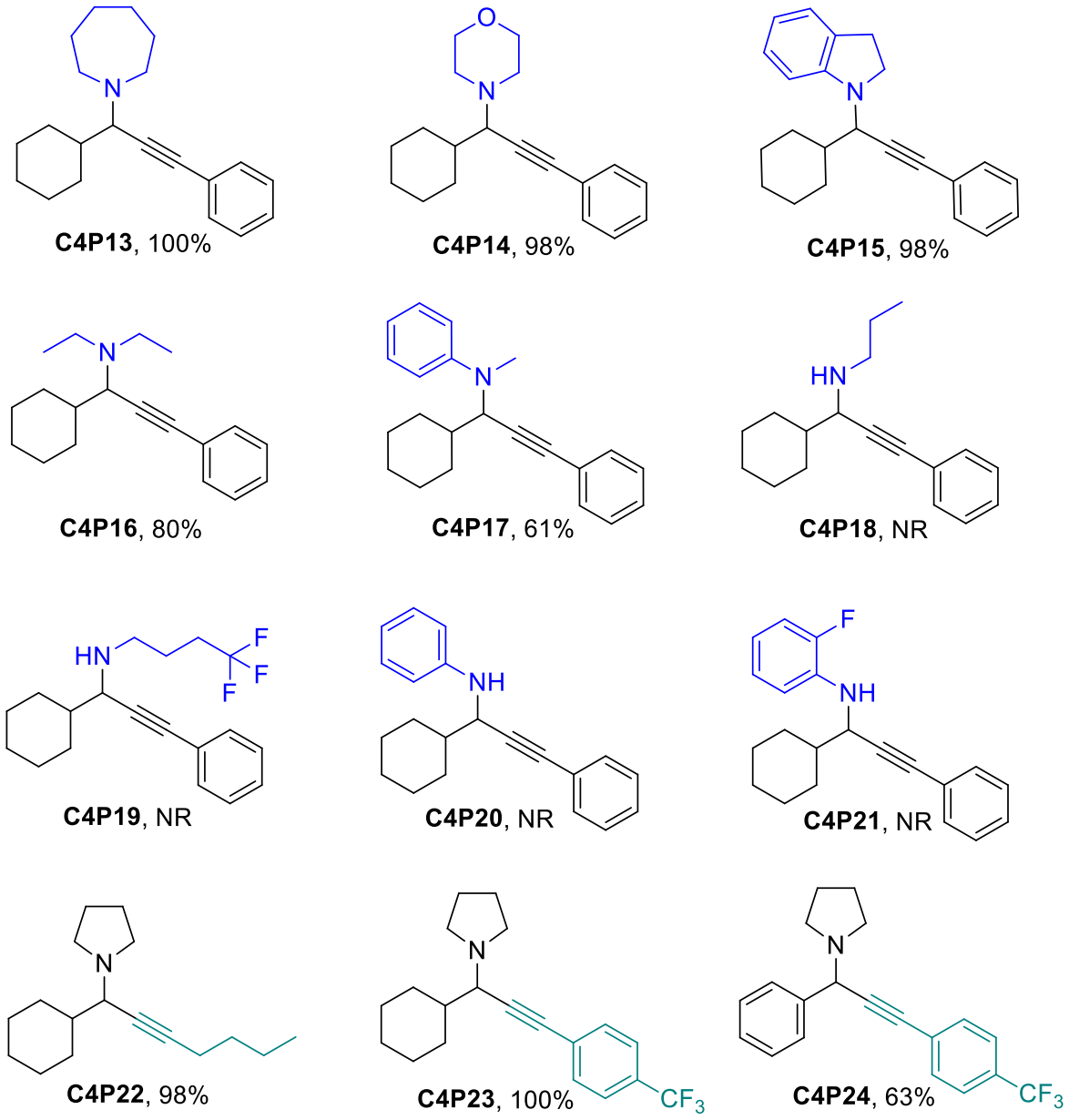

Scheme 4.3. Catalytic activity of **18** in the A^3 coupling between aldehydes, amines and substituted acetylenes towards the synthesis of propargylamine derivatives.

4.2.4.3. Mechanistic Insights

In order to investigate the role of CPs in the reaction and shed light into the respective mechanism, a variety of Cu^{II} CPs with the same ligand were synthesized by fine tuning their composition; these studies would provide significant information on factors such as the metal geometry or the different anion in the compounds and their effect on the catalytic activity, allowing for optimization of their catalytic performance. As a result, compounds which

possess the desired characteristics (as detailed in Tables 4.1 and 4.3) were obtained. **12** was synthesized using $Cu(NO_3)_2 \cdot 2.5H_2O$ and the metal centre has a coordination environment of $\{N_2O_5\}$, possessing a pseudo-octahedral geometry. The resulting 2D CP, however, only accounted for disappointing yields when tested as a catalyst (Table 4.3, entry 2). The employment of halogen copper sources afforded complexes **14**, **15** and **16**, which show considerable differences. The presence of a coordinating anion with bridging capabilities once again affects the resulting coordination environments ($\{N_2Cl_3\}$, $\{N_2Cl_4\}$, $\{N_4Br\}$) and geometries (trigonal bipyramidal, octahedral), which can be found in further detail in Table 4.1 (entries 4, 5, 6). Nevertheless, none of the compounds show any catalytic activity in the tested reaction.

Furthermore, by using Cu^{II} sources with traditionally non-coordinating anions (as in the case of the initial catalyst, **11** which contains perchlorates), the isolation of compounds **17** and **18** was made possible. Both compounds show an identical 1D framework and similar solution behaviour compared to **11** and only the present anion (BF_4^- or OTf) is different. The use of **17** as a catalyst (Table 4.3, entry 7) provided results similar to **11**. This indicated that a similar Cu^I species is generated, possibly through the conversion of BF_4^- to F^- (further supported by the ESI-MS analysis of **17**, in which several peaks containing F^- as the anion were observed) and inhibits the performance of the catalyst. In contrast, **18** showed very good catalytic activity in the tested reaction, with yields superior compared to any of the tested catalysts (Table 4.3, entry 8). Cyclic voltammetry experiments for **18** showed a quasi-reversible reduction process which may be assigned to the $[Cu^{II}] \leftrightarrow [Cu^{I}]$ couple, further supporting the formation of a Cu^I intermediate during the catalytic reaction.

Additional control experiments were then performed to investigate the importance of the redox potential. Given that Zn^{II} has lower potential than Cu^{II}, compounds **13** and **19** were employed; both are 1D Zn^{II} CPs constructed using metal salts with non-coordinating anions and show the same framework as their respective Cu^{II} compounds (**11** and **18**); they also have similar thermal and solution behaviour. In the case of **13**, the corresponding propargylamine was afforded only at 10% yield (Table 4.3, entry 3). Similarly, **19** was found to catalyse the title reaction in only 21% yield, as determined by ^1H NMR (Table 4.3, entry 9).

Further investigations were made using the modified benzotriazole derivatives in position 5 (**L^4**) or positions 5,6 (**L^5**), which yielded the corresponding dimers, **20** and **21** and not the anticipated 1D CPs. These dimers were found to moderately catalyse the reaction (Table 4.3, entries 10 and 11). In both structures, each Cu^{II} centre coordinates to four N atoms (from four different ligands) and one O atom, adopting a distorted square planar geometry. However, the UV-Vis spectra show that the Cu^{II} centres in **20** and **21** adopt an octahedral geometry (4N+2O) and possibly upon solvation four N atoms and two O atoms, from four ligands and two MeOH solvated molecules (catalysis takes place in iPrOH), occupy the equatorial and axial positions, respectively. In this way, the adaption of the symmetrical $\{N_4\}$ plane in solution yields the anticipated 1D CP and this transformation may explain the catalytic activity of **20** and **21**. However, the poorer catalytic performance of **20** and **21** in comparison to **18** may be explained by the following factors or a combination of them: A) The aforementioned "in situ" transformation is required for **20** and **21** to behave as catalysts, B) Substitution in position(s) 5(6) of the benzotriazole moieties may attribute a second coordination sphere effect to Cu centres. C) The presence of different axial ligands H_2O (**20**) or Br (**16**) versus OTf (**18**) may disrupt the aforementioned "in situ" transformation or decrease the reactivity of the catalysts[250,251]. It is also worth noting that the addition of 10 mol % of TEMPO did not affect the reaction yield, showcasing the absence of a clear radical process containing the Cu^{I}-complex species and supporting the plausible *in-situ* formation of the Cu^{I}-acetylide intermediate, that is responsible for the catalytic cycle.

Based on the above observations, the presence of a Cu^{II} centre in the solution featuring an octahedral geometry with four nitrogen atoms occupying the equatorial positions, is important in order to promote catalytic activity. Furthermore, the choice of the proper anion is critical, as the desired catalytically active motif (4N+2O) can only be reproduced through the use of non-coordinating anions. In contrast, the use of other anions results in different coordination geometries and dimensionalities, with zero catalytic activity. These observations are also consistent with the commonly suggested mechanism of the A^3 coupling, which involves the activation of the alkyne by the catalyst (Scheme 4.4). The planar $\{N_4\}$ geometry of Cu^{II} promotes the coordination of the alkyne with concomitant activation of the C–H bond and the formation of the corresponding Cu^{I}-acetylide (the acetylenic hydrogen

might be abstracted from the hydroxyl anions produced from the iminium ion formation). Consequently, the symmetrical {N_4} plane accounts for adequate electron delocalization to ensure the reduction of Cu^{II} to Cu^{I}, which is further promoted by the redox potential of Cu^{II}. Finally, addition of the Cu^{I}-acetylide to the *in situ* generated iminium ion yields the corresponding propargylamine derivative and water, and regeneration of the catalyst. The proposed catalytic pathway can be supported, in part, by the recently reported kinetic studies on the effect of alcoholic solvents to Cu^{II} Schiff base complexes[250], as well as the reported Cu^{II}-catalysed aerobic oxidation of benzylic alcohols in an imidazole containing {N_4} ligand framework[251].

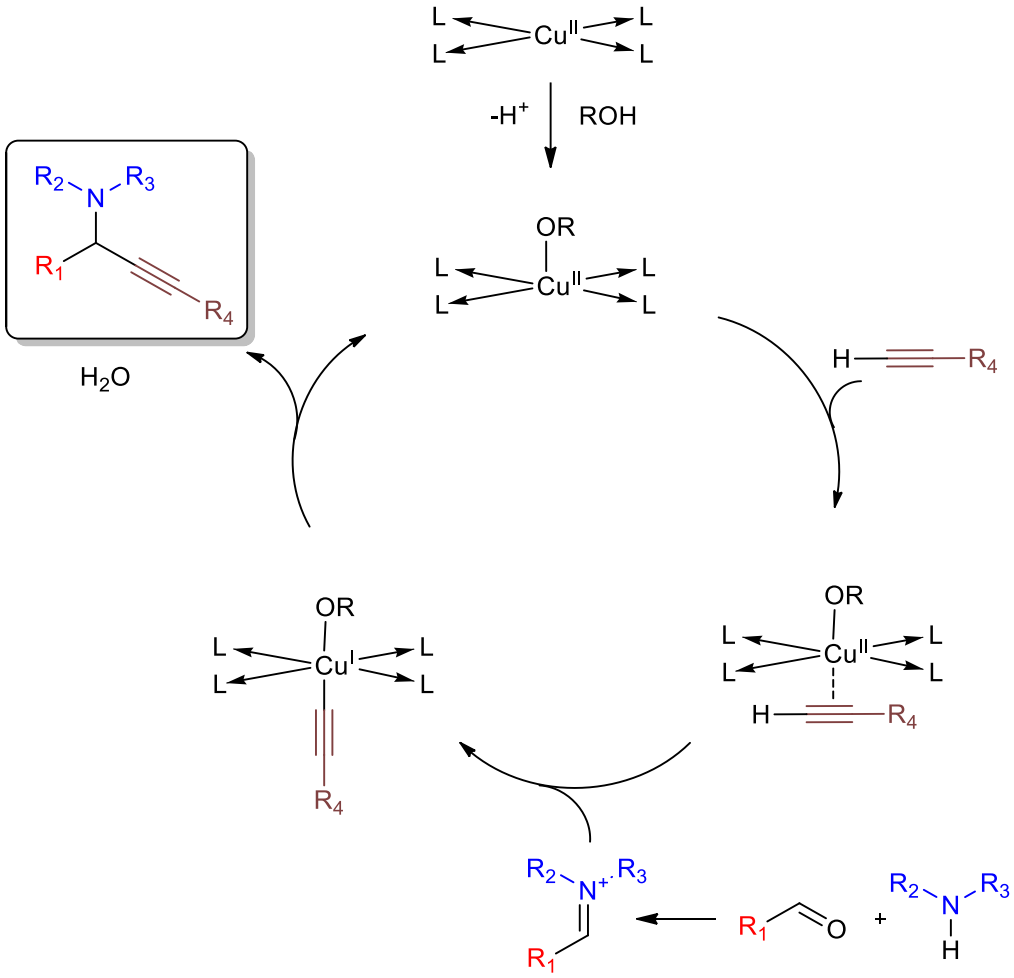

Scheme 4.4. A plausible mechanism of the A^3 reaction catalysed by Cu^{II}-CP **18**.

4.3. Conclusion

In this work, a system of 1D Cu^{II} CPs that can catalyse the multicomponent reaction of aldehydes, amines and alkynes to produce propargylamine derivatives is introduced. In particular, fine-tuning of the catalyst allowed for the generation of a 1D CP with excellent catalytic activity, avoiding any issues that would inhibit its performance. The method uses relatively mild conditions and provides results for a broad range of substrates, especially when aliphatic aldehydes and secondary amines are employed. Furthermore, it eliminates the need for expensive metal salts, inert atmosphere or high loadings. Attempts were also made to shed more light on the mechanism of the reaction, from an inorganic point of view; through a thorough synthesis and study of targeted CPs, factors like coordination geometry, anion, ligand tuning were evaluated for their effect in the catalytic activity. The results are consistent with the suggested mechanism. It is envisioned that this work further demonstrates the catalytic potential of the rarely used 1D CPs, especially when combined with *N*-donor ligands. As such, efforts in Chapters 5 and 6 will be dedicated to a) synthesizing variations of **18** with the use of analogous *N*-donor ligands, in order to further investigate their effect, b) using the present library of catalysts to other chemical transformations and c) employing CPs of other metals in the given A^3 coupling reaction.

Chapter 5: Cu^{II}-benzotriazole coordination compounds in click chemistry: A diagnostic reactivity study

Abstract: This diagnostic study aims to shed light on the catalytic activity of a library of Cu^{II}-based coordination compounds with benzotriazole-based ligands. The synthesis and characterization of five new coordination compounds formulated as $[Cu^{II}(\mathbf{L^2})(MeCN)_2(CF_3SO_3)_2]$ (**22**), $[Cu^{II}(\mathbf{L^6})_2(CF_3SO_3)_2]$ (**23**), $[Cu^{II}(\mathbf{L^7})_2(MeCN)(CF_3SO_3)]\cdot(CF_3SO_3)$ (**24**), $[Cu^{II}(\mathbf{L^7})_2(H_2O)(CF_3SO_3)]\cdot(CF_3SO_3)\cdot 2(Me_2CO)$ (**25**), $[Cu^{I}_4(\mathbf{L^3})_2(\mathbf{L^{3T}})_2(CF_3SO_3)_2]_2\cdot(CF_3SO_3)_4\cdot 8(Me_2CO)$ (**26**), derived from similar nitrogen-based ligands, is herein reported. The homogeneous catalytic activity of these compounds along with selected coordination compounds (**11**, **13**, **11i**, **17** – **21**) from previous chapters, derived from similar ligands, is tested against the well-known Cu^{I}-catalysed azide-alkyne cycloaddition reaction. The optimal catalyst $[Cu^{II}(\mathbf{L^3})_2(CF_3SO_3)_2]$ (**18**) activates the reaction to afford 1,4-disubstituted 1,2,3-triazoles with yields up to 98% and without requiring a reducing agent. Various control experiments are performed to optimize the method as well as examine parameters such as ligand variation, metal coordination geometry and environment, in order to elucidate the behaviour of the catalytic system.

External Contributions: Csilla Kállay and Gizella Csire (University of Debrecen) were collectively responsible for the collection and interpretation of cyclic voltammetry data. Alaa Abdul-Sada (University of Sussex) was responsible for the collection of all ESI-MS data. Adam Brookfield (University of Manchester) was responsible for the collection and interpretation of EPR data. Graham J. Tizzard and Simon J. Coles (University of Southampton) were responsible for the collection of some crystallographic data (Compounds **24-26**).

5.1. Introduction

The Huisgen 1,3-dipolar cycloaddition[252,253] of organic azides and alkynes is a characteristic reaction in the field of copper catalysis. In the absence of a catalyst, the reaction proceeds very slowly and under harsh conditions to produce a mixture of 1,4- and 1,5-disubstituted

1,2,3-triazoles with no regioselectivity (Scheme 5.1, pathway A). However, the introduction of a Cu^{I} source, as found independently by the groups of Meldal[254] and Sharpless[255], greatly improves the rate[256] and regioselectivity of the reaction to produce only the 1,4-disubstituted analogue (Scheme 5.1, pathway B) under favourable conditions. The resulting triazoles have considerable applications in various biological activities, and as a result the Cu-catalysed azide–alkyne cycloaddition (CuAAC) reaction has been employed in the fields of drug discovery[257], biochemistry[258–261] and materials science[262].

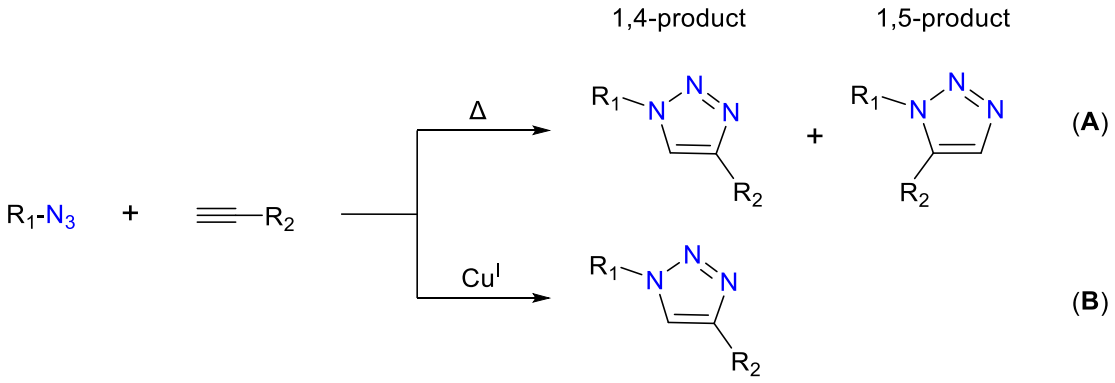

Scheme 5.1. General synthetic scheme of disubstituted 1,2,3-triazoles through azide-alkyne cycloaddition.

Multiple studies have shown that the reaction proceeds using almost any copper source as a catalytic precursor, as long as it generates catalytically active Cu^{I} species in the reaction medium[256,263–265]. The most popular method involves the use of an inexpensive Cu^{II} salt and a reducing agent (e.g sodium ascorbate[255] or hydrazine hydrate[266]) in large excess. The choice of the ligand is also important in the CuAAC reaction; it has been shown that certain nitrogen-containing ligands (e.g. amines[267], histidines[268], triazoles[269], benzimidazoles[270] and other polydentate chelators[261,271,272]) accelerate the transformation and enhance the stability of the Cu^{I} state through coordination, which protects the metal centres from oxidation. Therefore, the formation of unnecessary by-products is avoided.

Chapters 3 and 4 investigated the coordination and catalytic capabilities of Cu^{II} compounds based on the semi-rigid benzotriazole-derived organic ligands **L³** – **L⁵** (Scheme 5.2). These studies showed that the catalytic activity of this system is greatly influenced by factors like

coordination geometry, anion and ligand tuning. In addition, various results from these studies indicated the formation of a Cu^{I} intermediate during the reaction, which acts as the catalytically active species. However, more specific details on the mechanistic nature of the catalyst remained yet elusive.

Having all these in mind, in this work a study of a two-fold character is performed. Firstly, to evaluate the efficacy of the catalysts derived from the benzotriazole-based organic ligand **L^{3}** against other isotypical nitrogen-based ligands **L^{2}**, **L^{4}** – **L^{8}** (Scheme 5.2), which involve the use of substituted benzotriazoles (**L^{2}** – **L^{5}** and **L^{8}**), benzimidazole (**L^{6}**) or imidazole (**L^{7}**), in a given reaction system. Secondly, to shed light on the mechanistic aspects and performance of the present catalytic library in the CuAAC reaction, a well-refined and known transformation that is promoted exclusively by Cu^{I} sources. To perform this diagnostic study, the synthesis and characterization of five new compounds formulated as $[Cu^{II}(\mathbf{L^{2}})(MeCN)_2(CF_3SO_3)_2]$ (**22**), $[Cu^{II}(\mathbf{L^{6}})_2(CF_3SO_3)_2]$ (**23**), $[Cu^{II}(\mathbf{L^{7}})_2(MeCN)(CF_3SO_3)]\cdot(CF_3SO_3)$ (**24**), $[Cu^{II}(\mathbf{L^{7}})_2(H_2O)(CF_3SO_3)]\cdot(CF_3SO_3)\cdot2(Me_2CO)$ (**25**), $[Cu^{I}_4(\mathbf{L^{3}})_2(\mathbf{L^{3T}})_2(CF_3SO_3)_2]_2\cdot(CF_3SO_3)_4\cdot8(Me_2CO)$ (**26**) is herein reported. The catalytic performance of **22**-**26** in the one pot synthesis of 1,4-disubstituted 1,2,3-triazoles (click reaction) is additionally reported. The tested methods employ either organic halides or phenylboronic acid as starting materials, along with sodium azide to generate the organic azides *in situ* and avoid the isolation of potentially unstable intermediates. To provide further comparisons and draw useful conclusions towards these targets, suitable coordination compounds from Chapters 3 and 4, formulated as $[Cu^{II}(\mathbf{L^{3}})_2(MeCN)_2]\cdot(ClO_4)_2\cdot MeCN$ (**11**·MeCN), $[Zn^{II}(\mathbf{L^{3}})_2(H_2O)_2]\cdot(ClO_4)_2\cdot2MeCN$ (**13**·2MeCN), $[Cu^{I}(\mathbf{L^{3}})Cl]$ (**11i**), $[Cu^{II}(\mathbf{L^{3}})_2(MeCN)_2]\cdot(BF_4)_2$ (**17**), $[Cu^{II}(\mathbf{L^{3}})_2(CF_3SO_3)_2]$ (**18**), $[Zn^{II}(\mathbf{L^{3}})_2(MeCN)_2]\cdot(CF_3SO_3)_2$ (**19**) $[Cu^{II}_2(\mathbf{L^{4}})_4(H_2O)_2]\cdot(CF_3SO_3)_4\cdot4Me_2CO$ (**20**) and $[Cu^{II}_2(\mathbf{L^{5}})_4(CF_3SO_3)_2]\cdot(CF_3SO_3)_2\cdot Me_2CO$ (**21**) were selected and their respective catalytic performance was also evaluated.

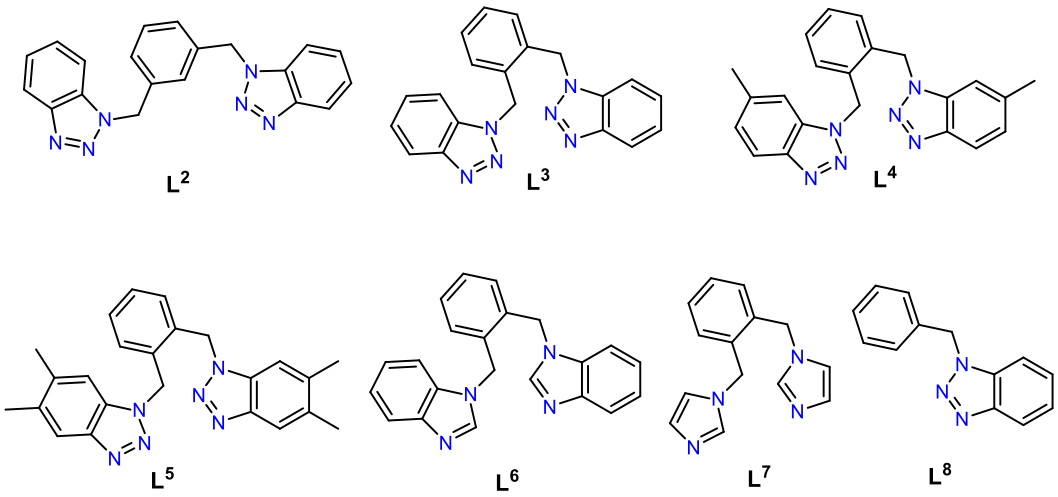

Scheme 5.2. The organic ligands (**L²**-**L⁸**) used in this study.

5.2. Results and Discussion

5.2.1. Crystal Structure Description of Compounds 22 – 26

The crystal structures of compounds **11**, **13**, **11i**, **17** – **21** have already been reported and described in Chapters 3 and 4. Hence, only the structures of **22** – **26** will be discussed in detail in this section. These complexes have been synthesized having in mind the structural characteristics of reference compound **18**; therefore, certain comparisons to this framework will be made in each description. A summarizing table providing structural details for all compounds is given in Table 5.1.

22 was prepared using the **L²** ligand and crystallizes in the triclinic $P\bar{1}$ space group. One Cu^{II} centre, one **L²** molecule, two coordinating triflate anions and two coordinating acetonitrile molecules are contained in the asymmetric unit. The **L²** ligand molecules in the structure adopt a type of *syn*- conformation that promotes the formation of a one-dimensional chain as shown in Figure 5.1. The behaviour of the flexible unit of **L²** is similar to the one of **L³**, with an angle of 123.96(4)° between the planes of the benzotriazole moieties. However, due to the meta-substitution in **L²** the resulting polymer in **22** shows a Cu-Cu distance of 9.3801(5) Å, larger compared to the 9.0095(3) Å measured for **18**. Each Cu^{II} centre possesses a slightly distorted octahedral geometry and a $\{N_4O_2\}$ coordination environment in which the axial

positions of the octahedron are occupied by the triflate oxygen atoms; relevant Cu-O distances were measured at 2.370(4) and 2.401(4) Å. The remaining four nitrogen atoms form a near-perfect square plane, as the mean Cu-N distances range from 1.994(5) to 2.003(4) Å. While similar coordination characteristics were found in the main catalyst **18**, in this case only two of the four nitrogen atoms that form the square plane derive from ligand molecules. The relevant N-Cu-N angles were found to be in the range of 87.82(15) to 91.16(17)°. Finally, no $\pi\cdots\pi$ interactions or strong hydrogen bonds were observed in the compound.

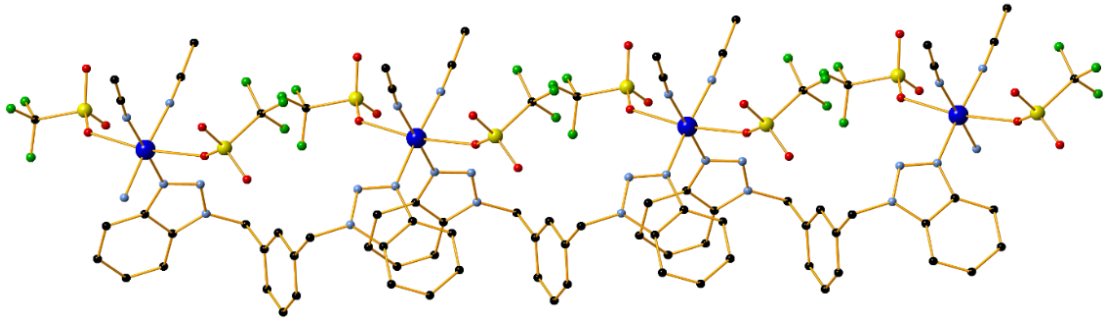

Figure 5.1. Part of the one-dimensional chain in **22**. H atoms are omitted for clarity. Colour code Cu (blue), C (black), N (light blue), O (red), S (yellow), F (light green).

Compound **23** was synthesized using the benzimidazole-based $\mathbf{L^6}$ ligand; the compound crystallizes in the triclinic $P\bar{1}$ space group and its asymmetric unit contains a Cu^{II} centre, one $\mathbf{L^6}$ molecule and one triflate anion molecule. Due to the generated symmetry, the structure propagates into a ribbon-like one-dimensional polymeric framework with small cavities (Figure 5.2). This framework is isoskeletal to the one of reference compound **18** and as a result **23** contains very similar structural characteristics in regards to coordination mode of the ligand and the coordination geometry of the Cu centre. Owed to the flexibility of the $-CH_2$ groups in $\mathbf{L^6}$, the planes of the benzimidazole molecules are found at an angle of 117.21(12)° to each other. Due to this, the metal centres are fairly separated and the corresponding Cu-Cu distance was measured at 9.0686(6) Å. Each Cu^{II} centre possesses an octahedral geometry through a $\{N_4O_2\}$ coordination environment. In this arrangement, the axial positions of the octahedron are occupied by triflate oxygen atoms as the four nitrogen atoms from $\mathbf{L^6}$ molecules in the equatorial positions create a perfect square plane. The mean Cu-O and Cu-N bond lengths were measured at 2.549(3) Å and 2.022(4) Å, respectively.

The imidazole-based **L**^{7} ligand was employed for the construction of compound **24**. The complex crystallizes in the monoclinic C2/c space group and its asymmetric unit contains one Cu^{II} centre, two **L**^{7} molecules, two triflate anion molecules and one acetonitrile molecule. As in the cases of the benzotriazole (**18**) and benzimidazole (**23**) analogues, the Cu^{II} centres possess an octahedral geometry that also includes a $\{N_4\}$ square plane with ligand-deriving nitrogen atoms at distances ranging from 1.996(4) to 2.017(4) Å. As a result, **24** exhibits a similar one-dimensional framework as shown in Figure 5.3 (top). A triflate and an acetonitrile molecule also coordinate through the axial positions in significantly larger distances (Cu-O: 2.513(5) Å, Cu-N: 2.549(6) Å respectively) to complete the octahedron, while a second triflate anion is also present in the crystal lattice to account for the charge balance. In this case the distance between the metal centres was measured at 9.7264(3) Å, which is the highest relevant in the study. This may be attributed to the absence of the bulky phenyl groups which limits potential steric effects and the possible formation of weak C-H···π interactions. As a result of this increased flexibility, the angles between the planes of the imidazole moieties were measured at 100.1(2) and 111.5(3)°, differing significantly compared to the previous compounds.

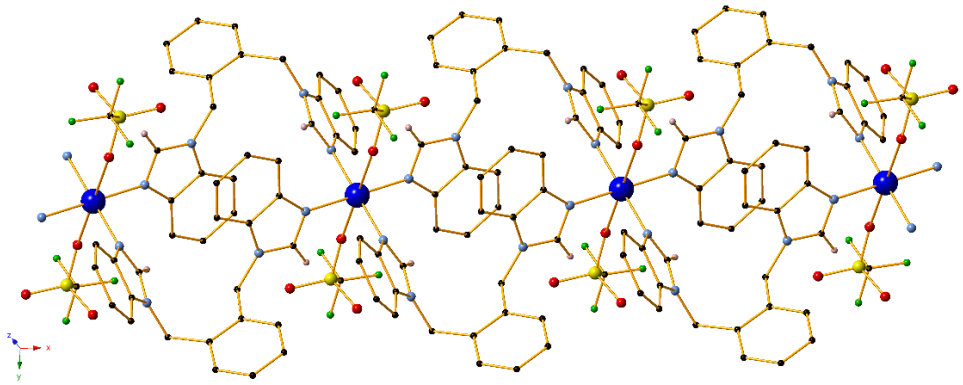

Figure 5.2. Part of the one-dimensional framework in compound **23** along the *a* axis. Certain H atoms are omitted for clarity. Colour code Cu (blue), C (black), H (light pink), N (light blue), O (red), S (yellow), F (light green).

Compound **25** was also synthesized using **L**^{7} and $Cu(OTf)_2 \cdot H_2O$ as the metal salt. Compared to **24**, compound **25** reveals an analogous one-dimensional framework which consists of the

same $[Cu^{II}(\mathbf{L}^{7})_2(solvent)(CF_3SO_3)]$ units, however with some structural differences based on the use of different crystallization solvents (H_2O/Me_2CO instead of MeCN). In this case, the complex crystallizes in the monoclinic $P2_1/n$ space group and a water molecule acts as the coordinating solvent (Figure 5.3, bottom). This accounts for octahedral Cu^{II} centres with $\{N_4O_2\}$ environment, slightly different compared to the case of compound **24**, however the ligand-derived $\{N_4\}$ square plane is present on both occasions. A second triflate anion along with solvent molecules are also found in the crystal lattice. The structure of **25** is further stabilized by the formation of two strong O-H···O hydrogen bonds between the oxygen from the water molecule and an oxygen atom of either a triflate anion or a solvent molecule in each case.

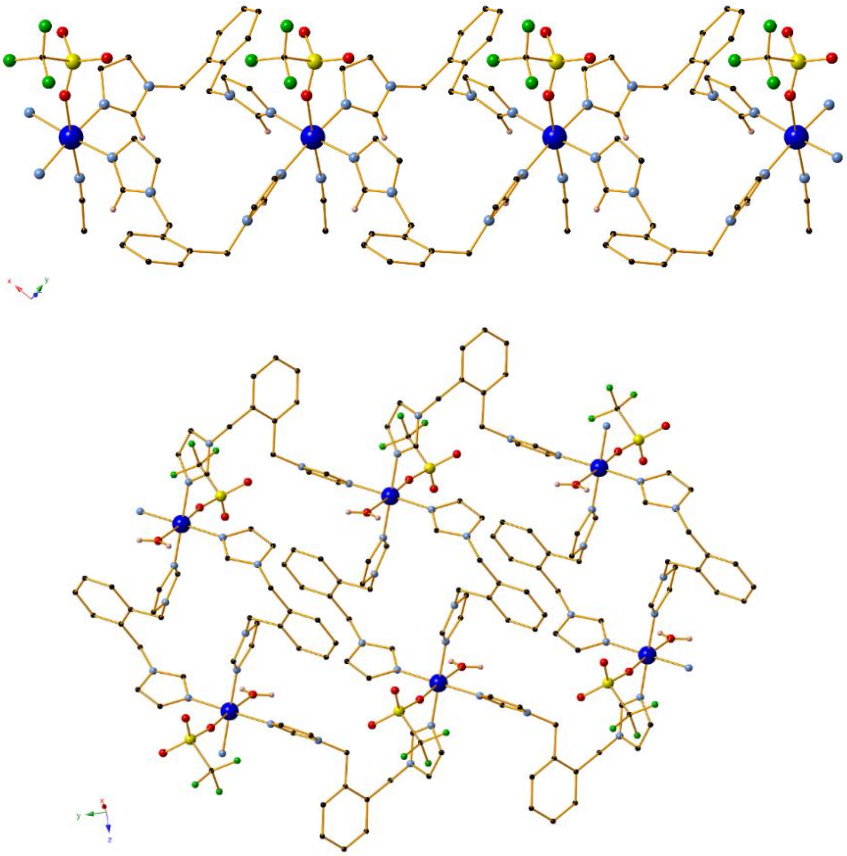

Figure 5.3. The one-dimensional frameworks in **24** (top) and **25** (bottom). Certain H atoms are omitted for clarity. Colour code Cu (blue), C (black), H (light pink), N (light blue), O (red), S (yellow), F (light green).

Determination of the structure of **26** by X-ray crystallography reveals a zero-dimensional Cu^{I} tetramer (Figure 5.4) which crystallizes in the triclinic space group $P\bar{1}$. All of the metal centres in this Cu_4 unit appear aligned in a single plane. Four organic ligands derived from $\mathbf{L^3}$ are also present. An interesting case of ligand isomerism is observed in two of these ligands, as the $-CH_2$ linker is bonded to the central N atom of one of the benzotriazole moieties, generating the 1,2-disubstituted benzotriazole analogue (Scheme 5.3, $\mathbf{L^{3T}}$) despite the fact that pure crystals of $\mathbf{L^3}$ were used during the synthesis. This phenomenon is common in substituted benzotriazole derivatives, as multiple studies by Katritzky's group[273,274] have shown that both the benzotriazol-1-yl and -2-yl adducts exist in solution; the position of this equilibrium has been found to be strongly dependant on parameters such as the polarity of the solvent, the temperature or the bulkiness of the substrate[275–279], however the 1-yl adduct remains predominant, which explains the presence of both species in the structure. A more detailed study on these phenomena will follow in Chapter 6. Two triflate molecules are also present in these tetramer units, each coordinating to one metal centre. All Cu^{I} centres exhibit tetrahedral geometry; the two external centres have a $\{N_3O\}$ coordination environment which involves nitrogen atoms from three different ligand molecules (two as $\mathbf{L^3}$ and one as $\mathbf{L^{3T}}$). Respective Cu-N distances for these atoms were measured from 1.981(3) to 2.010(3) Å. The remaining metal centres in-between are coordinated to nitrogen atoms from two as $\mathbf{L^3}$ and two $\mathbf{L^{3T}}$ ligands, possessing an $\{N_4\}$ environment. In this case, the measured Cu-N distances were found to be slightly larger, ranging from 2.037(3) to 2.080(3) Å. In regards to the triflate coordination, the analogous Cu-O distance was calculated at 2.173(3) Å. Finally, the relevant angles for all tetrahedra were found to be in the range of 99.47(12) and 112.74(12)°.

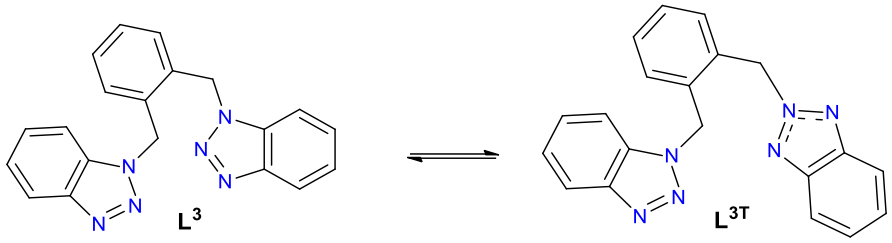

Scheme 5.3. The ligand isomerization observed in compound **26**.

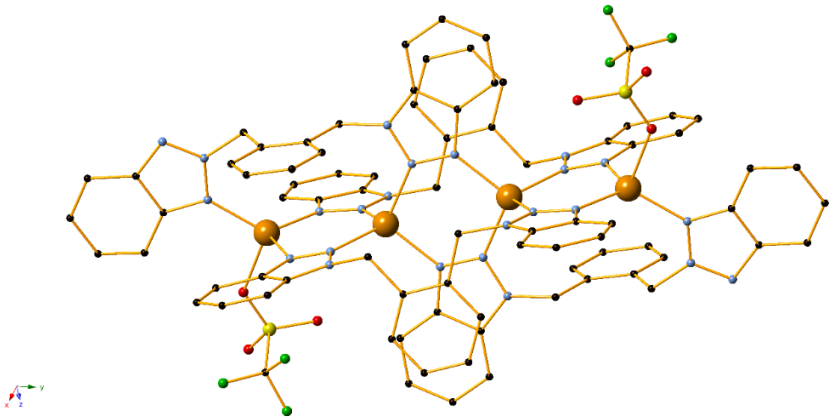

Figure 5.4. The structure of the tetrameric units in compound **26**. Lattice solvent and anion molecules, as well as H atoms are omitted for clarity. Colour code Cu (orange), C (black), N (light blue), O (red), S (yellow), F (light green).

Table 5.1. Structural summary of all compounds used in this study (S = Solvent).

Entry	Compound	Ligand	Coordination Environment (M = Cu/Zn)	M source	Dimensionality
1	**11**	**L^3**	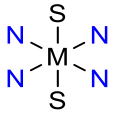	$Cu(ClO_4)_2 \cdot 6H_2O$	1D
2	**13**	**L^3**	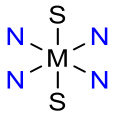	$Zn(ClO_4)_2 \cdot 6H_2O$	1D
3	**11i**	**L^3**	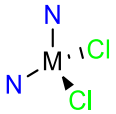	$Cu(ClO_4)_2 \cdot 6H_2O$	1D
4	**17**	**L^3**	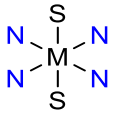	$Cu(BF_4)_2 \cdot 6H_2O$	1D
5	**18**	**L^3**	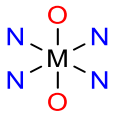	$Cu^{II}(OTf)_2 \cdot H_2O$	1D
6	**19**	**L^3**	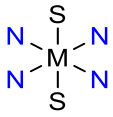	$Zn(OTf)_2$	1D

7	**20**	**L^{4}**	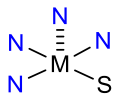	$Cu^{II}(OTf)_2 \cdot H_2O$	0D (dimer)
8	**21**	**L^{5}**	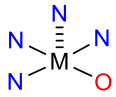	$Cu^{II}(OTf)_2 \cdot H_2O$	0D (dimer)
9	**22**	**L^{2}**	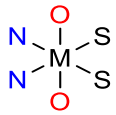	$Cu^{II}(OTf)_2 \cdot H_2O$	1D
10	**23**	**L^{6}**	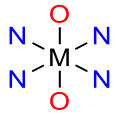	$Cu^{II}(OTf)_2 \cdot H_2O$	1D
11	**24**	**L^{7}**	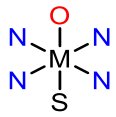	$Cu^{II}(OTf)_2 \cdot H_2O$	1D
12	**25**	**L^{7}**	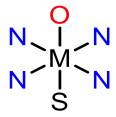	$Cu^{II}(OTf)_2 \cdot H_2O$	1D
13	**26**	**L^{3} , L$^{3T'}$**	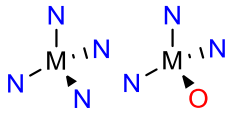	$Cu^{I}(OTf)(MeCN)_4$	0D (tetramer)

5.2.2. Synthetic Aspects

Due to the similar chemical nature and behaviour of ligands **L^{2}**, **L^{4}** – **L^{8}** compared to the prototype **L^{3}**, similar methods and techniques were employed to generate frameworks that resemble the coordination geometry and environment of the main catalyst **18**. As a result, all newly reported compounds were synthesized under aerobic conditions and analogous concentrations. The experiments were mainly conducted using acetonitrile or acetone as the main solvent, in order to i) provide satisfying solubility for all ligands and metal salts, ii) maintain the same synthetic method that was used during experiments with **L^{3}**, iii) efficiently engineer the resulting coordination environment through the coordinating (MeCN) or non-coordinating (Me_2CO) capabilities of the solvents. The main crystallization technique that was used for all compounds in order to provide high diffraction quality crystals was liquid or vapour diffusion. In regards to the secondary crystallization solvent, the non-coordinating solvents Et_2O and n-hexane proved to be the best choices; nevertheless H_2O (a coordinating solvent) also provided some success during the synthesis of **25** and allowed for a slight

manipulation in the coordination environment of Cu^{II}. Room temperature conditions were employed in almost all compounds, with the exception of **22**; it has been reported in Chapter 2 that the temperature effect on $\mathbf{L^2}$ further promotes the formation and dimensionality of coordination polymers. For this reason, the mixture in this case was initially heated at 95 °C. Despite several efforts, a crystalline material could not be obtained during experiments with $Cu(OTf)_2$ and $\mathbf{L^8}$ in order to generate a compound with analogous coordination characteristics to the ones in **18** (for purposes explained in Section 5.2.4.3). As a result, the targeted material was synthesized *in situ*; indicated peaks in the corresponding ESI-MS spectra, as reported in the Appendix (Figure S5.16), gave conclusive proof of successful coordination and thus the material was used in this way during catalytic experiments. All compounds are soluble in DMF, less soluble in other common organic solvents (eg. acetonitrile, THF, alcoholic media) and insoluble in water.

5.2.3. Characterization of Compounds 22 – 26

TGA Studies

Thermogravimetric analysis experiments of **22-26** up to a temperature of 1000°C revealed that the polymeric compounds **22-25** are slightly more stable than the zero-dimensional tetrameric complex **26**; the former retain their main metal-ligand core until the region of 260-300°C after which gradual decomposition to copper oxide begins. In complex **26**, the same procedure occurs at a slightly lower temperature region (~240°C).

In more detail, compound **22** undergoes an initial mass loss (calcd: 4.68%, theor: 5.01%) in the 100-125°C range due to the loss of any remaining acetonitrile solvent, while the second mass loss occurs at approximately 285°C as the existing core begins to decompose to the resulting oxide (calcd: 86.28%, theor.: 84.31%). Compound **23** completely retains its stability up to the region of 260°C, where removal of the triflate anions occurs (calcd: 28.77%, theor.: 28.70%). The remaining polymeric core loses its stability at approximately 375°C towards gradual decomposition to CuO (calcd: 63.93%, theor.: 63.64%). In the case of **24**, there is an immediate mass loss which concludes at 163°C, owed to the loss of the coordinated acetonitrile molecule with satisfactory agreement (calcd: 5.997%, theor.: 4.02%). The remaining residue remains stable until approximately 300°C before it begins to decompose.

The TGA analysis of compound **25** is in agreement with the elemental analysis measurements which suggest that the acetone molecules in the lattice are removed under room temperature. As such, the first mass loss in the range of 85-100°C is attributed to the removal of the coordinated water solvent from the framework. The remaining core is stable until it begins decomposing in the region of 300-325°C to the eventual oxide residue. The total mass loss for these processes (92.84%) is in very good agreement to the theoretical value (91.71%). Finally, in compound **26** there is a continuous mass loss which occurs immediately, until approximately 217°C. This corresponds to the loss of the remaining four acetone solvent molecules that are present in the lattice (calcd: 9.54%, theor: 9.50%). An immediate second mass loss occurs after this, as the remaining framework is decomposed. The TGA graphs are presented in the Appendix (Figures S5.11-S5.15).

Mass Spectometry Studies

ESI-MS (positive-ion mode) in methanolic solution for complexes **22**-**26** shows a variety of peaks depending on their behaviour in solution as well as the ligand used. The most common peaks can be found in all or almost all compounds and correspond perfectly to the respective $[Cu(\mathbf{L})]^+$, $[Cu(\mathbf{L})_2]^+$, $[Cu(\mathbf{L})(CF_3SO_3)]^+$ and $[Cu(\mathbf{L})_2(CF_3SO_3)]^+$ fragments. Additional peaks are also observed in each spectrum, which are consistent to various metal–ligand-anion fragments. For example, **22** and **23** also contain peaks that correspond to the respective $[Cu_2(\mathbf{L})_2(CF_3SO_3)_3]^+$ and $[Cu_2(\mathbf{L})_3(CF_3SO_3)_3]^+$ fragments. Imidazole-based compounds **24** and **25** present additional peaks that match the theoretical values for the $[Cu(\mathbf{L^7})_3]^+$ and $[Cu(\mathbf{L^7})_3(CF_3SO_3)]^+$ fragments. Finally, the ESI-MS spectrum of **26** reveals five main peaks which are attributed to the corresponding $[Cu(\mathbf{L^3})]^+$, $[Cu(\mathbf{L^3})_2]^+$, $[Cu(\mathbf{L^3})_2(CF_3SO_3)]^+$, $[Cu_2(\mathbf{L^3})_2(CF_3SO_3)]^+$ and $[Cu_2(\mathbf{L^3})_3(CF_3SO_3)]^+$ fragments. Overall, **22-26** appear to behave in solution similarly to the already reported compounds **11**, **13**, **17-21** which were also employed in this catalytic study. All ESI-MS spectra, along with a detailed analysis of the fragments, are presented in the Appendix (Figures S5.6–S5.10).

Cyclic Voltammetry studies

As a first step, cyclic voltammetric studies of selected ligands $\mathbf{L^3}$, $\mathbf{L^4}$, $\mathbf{L^6}$, $\mathbf{L^7}$ were performed. During these experiments, no processes were observed in either the negative or positive

potential range and only the CV of the TBAP was measurable. Therefore, it can be established that the ligands are stable in DMSO and in DMF, and they are not oxidized. CV studies were then performed for the Cu based compounds (Figures 5.5 and 5.6). Compounds **18**, **20** and **23** were selected for these purposes due to their structural characteristics and catalytic performance. **18** and **23** can be reduced in the first step and can be then oxidized back in the second step in the positive potential range. The I_a/I_c is ~1 and the $v^{1/2}$-|Ic| function is not linear whereas the potential difference of the anodic and cathodic peak potential is more than 59 mV indicating a structural change. This can be rationalized to the different coordination preference of the Copper element in different oxidation states (I or II), therefore the intra-conversion (II to I to II) takes place in a slower manner, or the electron crossing may be slower on the electrode surface. These results show that these processes are quasi-reversible. The redox potentials are positive in both cases and substantially different when compared with the redox potential of $Cu(NO_3)_2$, thus supporting that the measured potential values correspond to Cu^{II} complexes. The CV of compound **20** complex is similar to the $Cu(NO_3)_2$ cyclic voltammogram in both solvents, indicating that compound **20**, despite having similar structural characteristics with **18** and **23**, is not stable in DMF and in DMSO.

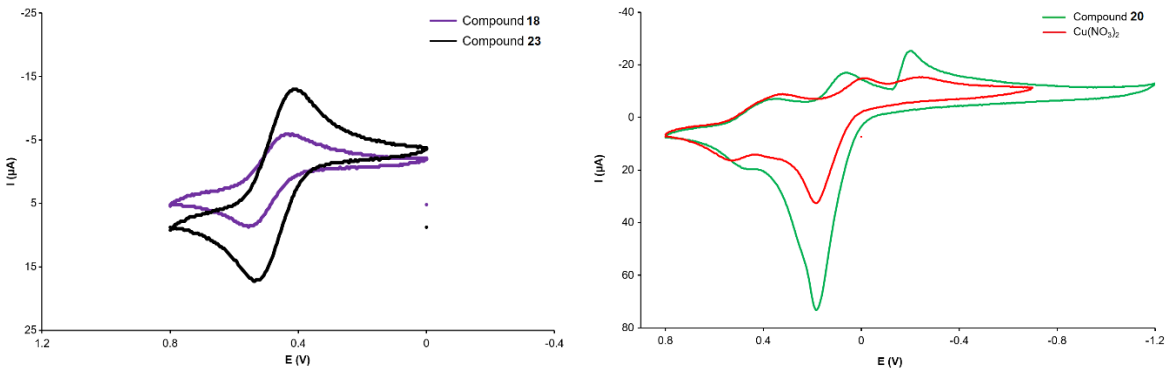

Figure 5.5. Voltammograms of **18** (purple) and **23** (black) in 0.1 M TBAP/DMF (Potential range: 800-0 mV. Scan rate 100 mV/s). (right) Voltammograms of **20** (green) and $Cu(NO_3)_2$ (red) in 0.1 M TBAP/DMF (Potential range: 800-(-1200) mV for **20**, 800-(-700) mV for $Cu(NO_3)_2$. Scan rate 100 mV/s).

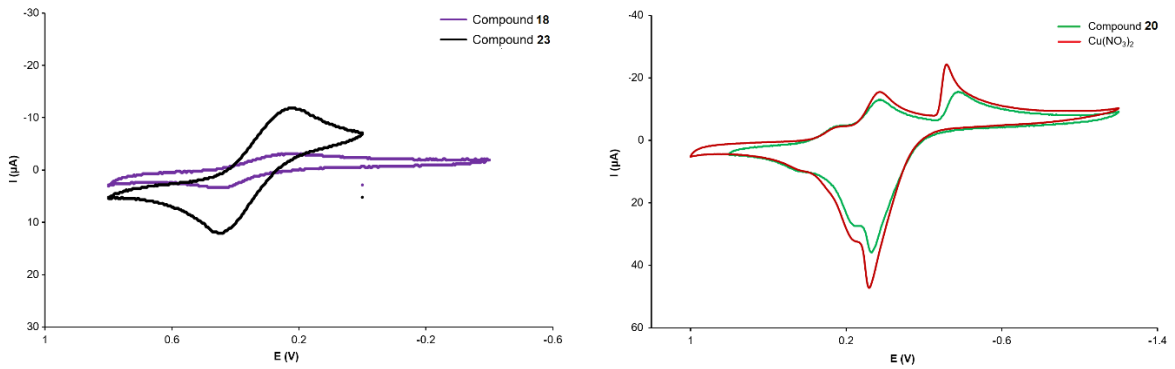

Figure 5.6. (left) Voltammograms of **18** (purple) and **23** (black) in 0.1 M TBAP/DMSO (Potential range: 800-(-400) mV for **18**, 800-0 mV for **23**. Scan rate 100 mV/s). (right) Voltammograms of **20** (green) and $Cu(NO_3)_2$ (red) in 0.1 M TBAP/DMSO (Potential range: 800-(-1200) mV for **20**, 1000-(-1200) mV for $Cu(NO_3)_2$. Scan rate 100 mV/s).

EPR Studies

To gain further structural insights, X-band EPR studies of characteristic compounds **18**, **20**, **23** were performed. The spectra of polycrystalline samples in solid-state or in frozen alcoholic solution were recorded at a temperature of 5 K. Initial investigations took place for **23**, followed by **18** and **20**. For compound **23**, a comparison between the spectra of the solid-state sample and the one in frozen methanol (Appendix, Figure S5.17, right) shows similar signals in both case, however fewer hyperfine lines are observed in the former. A closer look at the crystallographic parameters of the compound reveals severe axial distortion in the octahedron due to Jahn-Teller effects, with the Cu-N and Cu-O distances at 2.022(3) and 2.549(3) Å respectively. Furthermore, a series of weak intramolecular interactions (C–H···π, C–H···O_{OTf}) involving the –CH group of the imidazole moiety is observed. Both these phenomena contribute to weaker magnetic coupling between neighbouring cations and eventually a narrowing of the hyperfine lines. The best simulation (Appendix, Figure S5.17, left) was obtained with (g_x, g_y, g_z) = (1.92, 1.99, 2.3) ± 0.01 and A = 200 ± 30 MHz (where A = hyperfine) which is in agreement with the above observations. In contrast, the EPR signal of **23** in methanolic solution provides much more defined hyperfine lines which are consistent to a Cu^{II} (S=1/2) interaction with four ^{14}N nuclei from $\mathbf{L^6}$ ligands in a square planar environment, pointing to an eventual $\{N_4O_2\}$ octahedral geometry. A plausible hypothesis for the difference in the clarity of the two spectra could be that, in solution, methanol

molecules replace the triflate anions and coordinate to the Cu^{II} centres, removing any potential formation of C–H···O interactions[250,251].

Similar studies for compound **18**, as can be seen in Figure S5.18, Appendix, show that Cu^{II} retains the $\{N_4O_2\}$ octahedral geometry in alcoholic solution, and the structure remains polymeric. This result is consistent with the UV-Vis studies reported in Chapter 4 which showed that the compound retains a similar coordination environment in solution. It is worth noting that the spectrum in this case is very well defined compared to the one of compound **23**, as no weak C–H···O interactions are formed in the absence of the imidazolic moiety. A comparison of the hyperfine lines shows slight changes in the coordination environment upon solvation but does not alter, indicating once again potential replacement of the triflate anions with ethanol molecules. A simulation with very good agreement for the polycrystalline sample at room temperature provided the fitting parameters (g_x, g_y, g_z) = (2.08852, 2.03142, 2.29635) ± 0.01 and A = 520 ± 30 MHz, indicating that the unpaired electron is localized in the $d_{x^2-y^2}$ orbital. Furthermore, they are in accordance to the corresponding values of similar Cu^{II} complexes with a $\{N_4O_2\}$ coordination environment[280–282].

While the crystallographic data for **20** could not be optimally refined, the Cu^{II} centres clearly exhibited a square pyramidal geometry in the crystal structure, with a $\{N_3O\}$ environment in the equatorial plane. The X-band EPR studies (Figure S5.19, Appendix) of the polycrystalline sample at 5 K further confirm this behaviour. Reasonable fits are obtained for (g_x, g_y, g_z) = (1.96, 2.04, 2.28) ± 0.01 and A = 350 ± 30 MHz; these values are in satisfying agreement to the ones of related Cu^{II} complexes with a $\{N_4O\}$ coordination sphere[283,284]. Once again, a narrowing of the hyperfine lines is also observed, possibly due to the formation of weak π···π and C–H···π interactions within the structure.

5.2.4. Catalytic Studies

5.2.4.1. Benchmarking and Optimisation

In order to provide an ideal scheme for the reaction, attention was paid towards establishing a catalytic protocol which would avoid the isolation of the potentially unstable organic azides (especially azides with low molecular weights[263]). For these reasons, the multicomponent

reaction between organic halides (**C5H**), alkynes (**C5L**) and sodium azide (**C5Z**) was adopted as the initial reaction scheme, in which the respective organic azide is generated *in situ*. The initial catalytic protocol included the use of benzyl chloride, sodium azide and phenylacetylene, as well as reference compound **18** as the homogeneous catalyst. After several catalytic tests (Table 5.2), it was found that optimal results were obtained when the reaction takes place in ethanol for 24 hrs, under reflux and 5 mol% of the catalyst (Table 5.2, entry 2). Under these conditions, the starting material is consumed and the reaction leads to the corresponding triazole **C5T1** in an excellent 93% yield. Notably, this result was obtained in the absence of any external reducing agent, providing substantial evidence towards the formation of a Cu^{I} intermediate during the reaction.

Encouraged by this result, the performance of various Cu^{I} and Cu^{II} salts was then tested under the same reaction conditions (Table 5.3), demonstrating the superior performance of **18**. In addition; in some of these cases, the starting material was not even entirely consumed.

Table 5.2. Optimization of the synthesis of triazole **C5T1** using **18** as the catalyst.

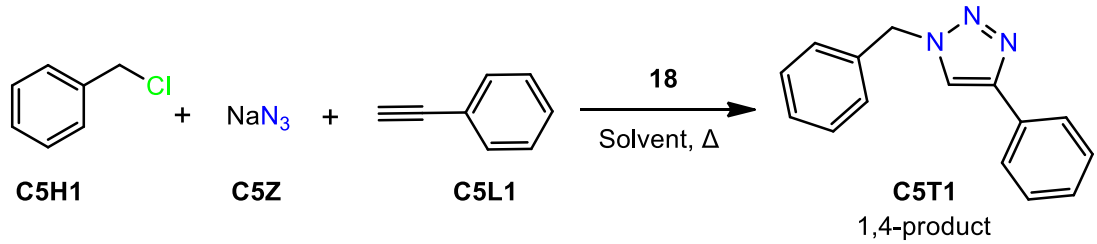

Entry	Solvent	Temperature (°C)	Time (h)	Loading (mol %)	Conversion (%)[a]	Yield (%)[b]	Regioselectivity 1,4/1,5-product	TON/TOF (hr^{-1})
1	MeOH	64	24	5	76	62	83:17	12.4/0.52
2	EtOH	78	24	5	100	93	99:1	18.6/0.78
3	iPrOH	82	24	5	94	76	98:2	15.2/0.63
4	MeCN	82	24	5	65	43	99:1	8.6/0.36
5	Toluene	110	24	5	NR	-	-	-
6	DMF	120	24	5	96	46	98:2	9.2/0.38

7	1,4-Dioxane	101	24	5	NR	-	-	-
8	H_2O	100	24	5	NR	-	-	-
9	EtOH	78	24	2.5	83	47	99:1	18.8/0.78
10	EtOH	78	1	5	45	22	98:2	4.4/4.4
11[c]	EtOH	78	24	5	93	82	97:3	16.4/0.68
12[d]	EtOH	78	24	5	87	87	99:1	17.4/0.73
13[e]	EtOH	78	24	5	100	93	99:1	18.6/0.78
14[e]	EtOH	78	1	5	99	92	99:1	18.4/18.4
15	EtOH	rt	24	5	NR	-	-	-

Reaction conditions: benzyl chloride (0.5 mmol), sodium azide (0.5 mmol), phenylacetylene (0.5 mmol), **10**, solvent (3 mL). [a]: based on benzyl chloride. Differences between the conversion and yield percentages are due to the unreacted benzyl azide. [b]: calculated from the crude mixture by ^{1}H NMR. [c]: with 0.5 ml solvent. [d] with the addition of 15% $P(Ph)_3$. [e] with the addition of 15% Sodium Ascorbate. NR = no reaction. The reported[285] ^{1}HNMR peaks of the 1,5-analogue were employed to determine regioselectivity.

Table 5.3. Evaluation of various Cu^I and Cu^{II} salts in the synthesis of triazole **C5T1**.

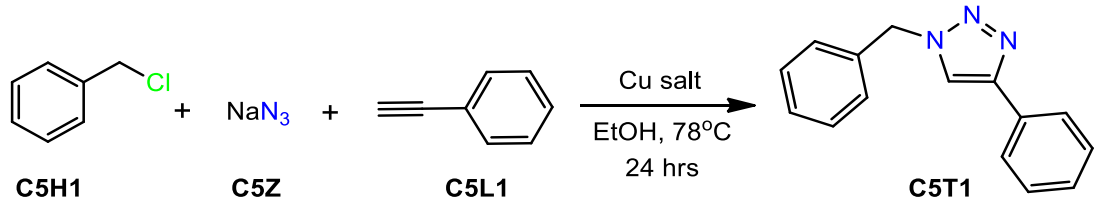

Entry	Catalyst	Conversion (%)[a]	Yield (%)[b]	Regioselectivity	TON/TOF (hr^{-1})
1	Cu^ICl	100	72	99:1	14.4/0.6
2	$Cu^I(BF_4)(MeCN)_4$	93	80	99:1	16/0.67
3	$Cu^I(OTf)(MeCN)_4$	100	78	99:1	15.6/0.65
4	$Cu^{II}Cl_2$	79	35	99:1	7/0.29
5	$Cu^{II}Br_2$	77	32	98:2	6.4/0.27

6	$Cu^{II}(OTf)_2 \cdot H_2O$	99	78	99:1	15.6/0.65
7	$Cu^{II}(OAc)_2 \cdot H_2O$	92	40	99:1	8/0.33
8	$Cu^{II}(ClO_4)_2 \cdot 6H_2O$	99	76	97:3	15.2/0.63
9	$Cu^{II}(BF_4)_2 \cdot 6H_2O$	99	71	96:4	14.2/0.59
10	$Cu^{II}(NO_3)_2 \cdot 2.5H_2O$	93	62	96:4	12.4/0.52

Reaction conditions: benzyl chloride (0.5 mmol), sodium azide (0.5 mmol), phenylacetylene (0.5 mmol), catalyst (5% mol), EtOH (3 mL), heated at 78°C for 24 h. [a]: based on benzyl chloride. Differences between the conversion and yield percentages are due to the unreacted benzyl azide. [b]: Relative yields based on ^{1}H NMR analysis from the integration of the corresponding proton shifts. The reported[285] ^{1}HNMR peaks of the 1,5-analogue were employed to determine regioselectivity.

5.2.4.2. Scope of Reaction

Having obtained the optimal conditions for the system, a number of substrates were then tested in order to study the catalytic scope and limitations of **18**. Initial substrate screening included the use of organic halides as starting materials as well as a variety of terminal alkynes (e.g. aromatic, alkyl, linear, containing hydroxyl or carboxylate groups). The results are presented in Scheme 5.4. The reaction affords triazoles in excellent (88 - 99%) yields when aromatic or substituted aliphatic alkynes are used. In regards to the organic halide, increasing the strength of the leaving group from Cl^- (entries **C5T1** – **C5T6**) to Br^- (entries **C5T7** – **C5T11**) led to improved results as expected. It is also worth noting that the triazoles derived from benzyl halide proved to be very easy to crystallize. As such, X-Ray crystallography structures of representative triazoles **C5T1** – **C5T4** are additionally included. Iodobenzene was also tested as a possible substrate during attempts to generate the relevant aryl triazole analogues, however these efforts were unsuccessful. This was not surprising as the azidonation of aryl halides[269,286,287] is generally a slow process that requires very harsh or tedious conditions. For this reason, the inexpensive and readily available benzeneboronic acid was employed in order to obtain the corresponding product[288]. As a result, the resulting triazole **C5T12** was generated in a very good 80% yield, as seen in Scheme 5.5. Additional screening of the arylboronic acid with other alkynes led to the formation of triazoles **C5T13** – **C5T15** in poorer yields, whereas reactions with 2-hydroxyphenylboronic acid did not yield

any product (**C5T16** – **C5T17**). Nevertheless, these results provided another potential pathway for catalyst **18** which avoids the isolation of unstable organic azide intermediates.

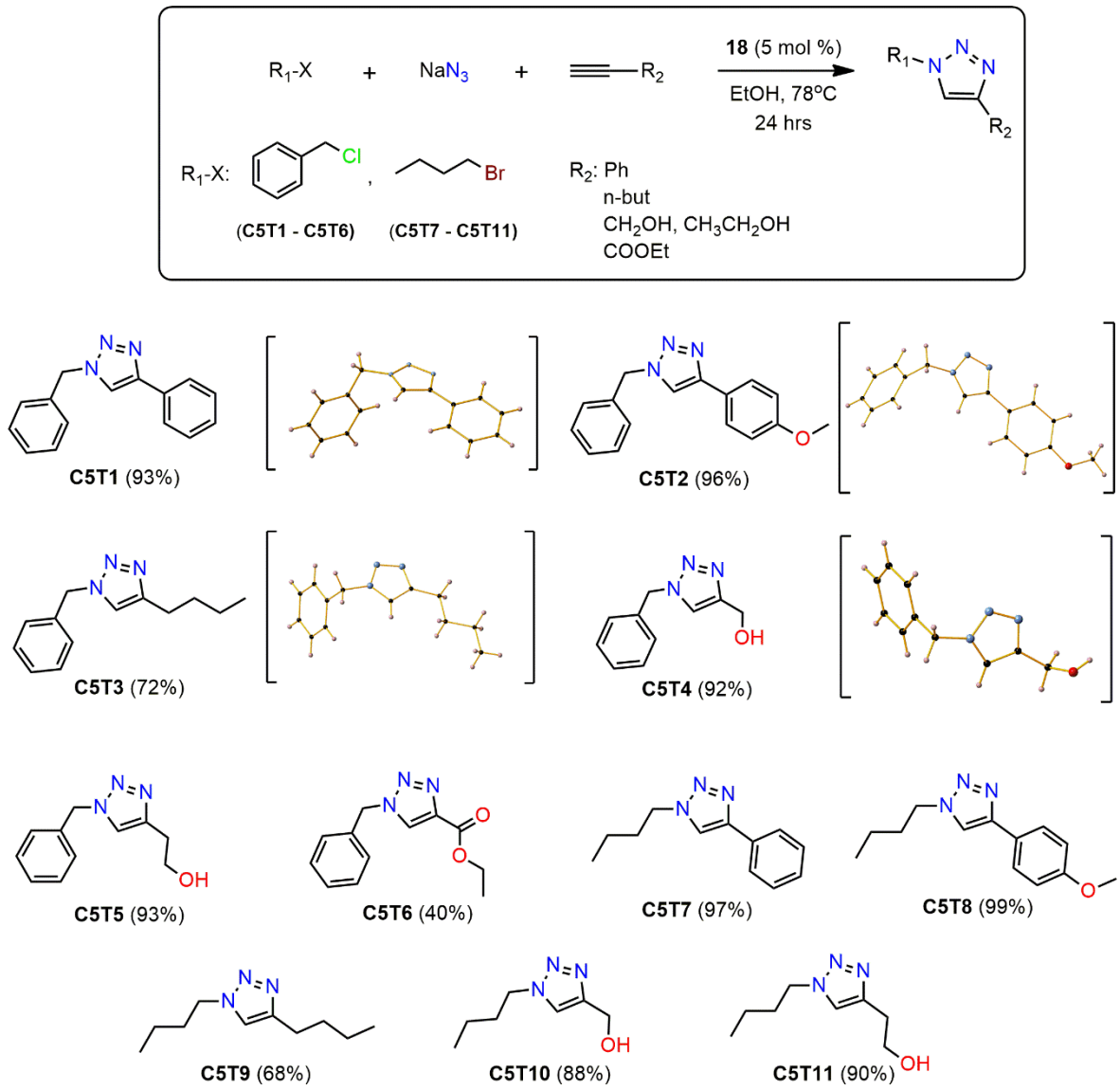

Scheme 5.4. Catalytic activity of **18** in the multicomponent synthesis of 1,4-disubstituted 1,2,3-triazoles from organic halides.

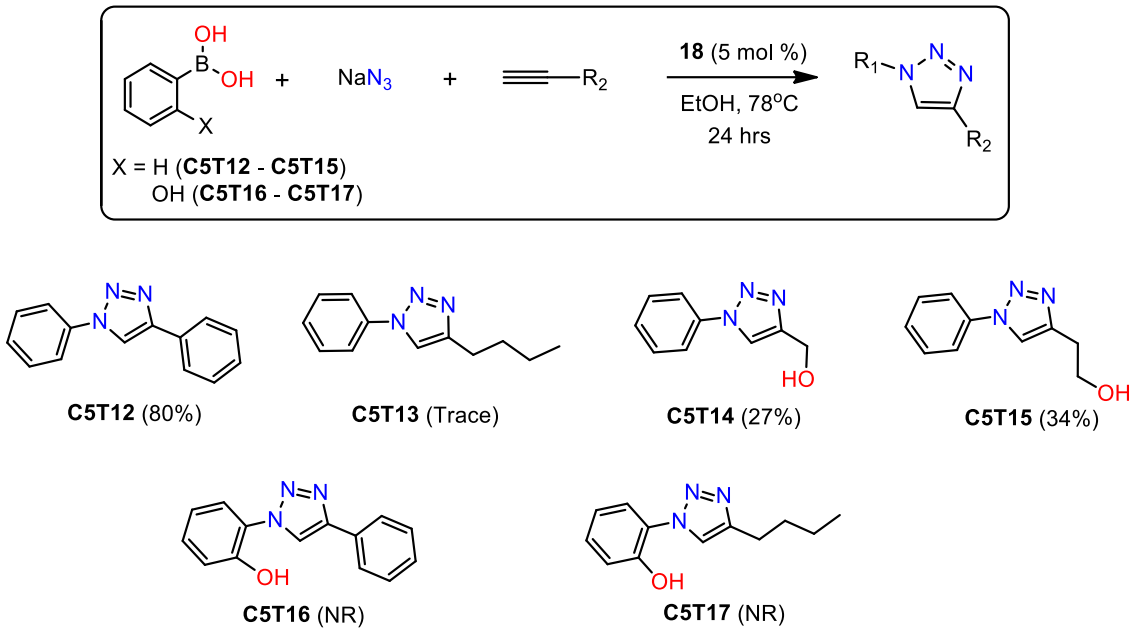

Scheme 5.5. Catalytic activity of **18** in the one-pot synthesis of 1-aryl-1,2,3-triazoles from boronic acid derivatives.

5.2.4.3. Mechanistic Insights

The homogeneous catalytic performance of **18** in the azide-alkyne cycloaddition provides yet another organic transformation in which this library of 1D Cu^{II} CP catalysts may be applied. More importantly, the presence of a Cu^{I} source is necessitated for this specific reaction to occur; this serves as an excellent blueprint, which could shed light into the mechanistic function of the catalysts. Up to this point, it has been established that these polymeric Cu^{II} compounds retain their nature in alcoholic solution, and can generate Cu^{I} species when tested as pre-cursor catalysts in organic reactions under alcoholic media which involve the formation of the important Cu^{I}-acetylide intermediate. Within these concepts, an extensive set of control experiments and techniques was performed in order to: i) diagnose the exact nature of the generated Cu^{I} species, ii) find the limits of the present catalytic system, iii) identify the importance of the Cu^{II} pre-cursor in the catalytic activity, iv) further examine the effect of parameters such as ligand variation, metal effect, polymeric nature, dimensionality, geometry and coordination sphere. The results of these experiments are shown in Table 5.4.

Firstly, the importance of metal selection in the construction of the catalysts was evaluated. Zn^{II}-based compounds **13** and **19** were tested as catalysts for the synthesis of **C5T1**, as they are isostructural to **18**, containing the same one-dimensional framework; they also behave similarly in solid and solution state. Recent investigations[289,290] on the feasibility of a ZnAAC system have shown that the reaction is indeed possible. However, it requires the presence of a reducing agent (when none is present in the proposed system in this Chapter) and is highly sensitive to steric effects in regards to the choice of alkyne. Nevertheless, no product was formed in both cases (Table 5.4, entries 2 and 6). Given the inactivity of Zn centres towards the AAC reaction, this experiment excludes the possibility that the reaction is promoted by the ligand.

The next step was to assess the performance of all Cu^{I} complexes from the library of related obtained structures presented so far in this thesis. Relevant compounds **11i** and **26** were employed for these purposes, accounting for average yields as seen in Table 5.4, entries 3 and 13. As a consequence, the remaining fine-tuning efforts were narrowed down to Cu^{II} compounds. Therefore, the next step was to study the effect of the choice of metal salt during the catalytic process. The comparison tests in this case involved the isoskeletal 1D catalysts **11**, **17** and **18** (Table 5.4, entries 1, 4, 5) that differ in the counter anion (ClO_4^-, BF_4^-, OTf^- respectively). The results show significant differences in the afforded yield, with the OTf^- analogue exhibiting superior behaviour and the BF_4^- analogue accounting for the lowest activity. In addition, lower conversion (90%) of the starting material was observed in both ClO_4^- and BF_4^- analogues. These results indicate that $Cu(OTf)_2$ is the ideal choice of metal salt for the construction of catalysts in this system. Having also in mind that the triflate analogues provided the most encouraging results during the evaluation of Cu^{I} compounds and Cu^{I}/Cu^{II} salts (Table 5.3, entries 3 and 6), it is envisioned that this performance is established as either the reaction requires the presence of a weak base to get a proton or the triflate unit has better resistance to the oxidation/reduction reaction, compared to ClO_4^- or BF_4^-. Moreover, any anion conversion issues that would inhibit the catalytic activity, such as the ones reported in Chapters 3 and 4 for the ClO_4^- and BF_4^- analogues (respectively converted to Cl^- and F^-), are avoided.

The influence of the nitrogen-based ligand was then examined. Employment of organic ligands **L^4** and **L^5** in which the benzotriazole moieties contain –CH_3 groups in positions 5 and 5,6 respectively resulted in the isolation of coordination compounds **20** and **21**. Both of these compounds show important structural differences compared to the reference catalyst **18** which derived from the parent ligand **L^3**. More specifically, the Cu^{II} centres possess different coordination geometry and the complexes have no polymeric nature, forming dicopper dimers instead. As seen in Table 5.4, entries 7 and 8, the catalytic tests for **20** and **21** showed average behaviour compared to **18**. This may be attributed to the aforementioned structural differences as well as a possible second sphere coordination effect to the Cu^{II} centres, due to the presence of the –CH_3 groups. The ligand **L^2** was also employed to determine the effect of the position of the substituted benzotriazole molecules. Compared to the *ortho*-substitution in parent ligand **L^3**, the *meta*-substitution in **L^2** provides increased flexibility to account for any potential steric effects. For this reason, the resulting 1D polymer **22** reveals larger Cu-Cu distances compared to **18** as well as larger angles between the benzotriazole molecules. **22** also provides increased space for substrate accommodation, as the four nitrogen atoms which comprise the square plane of the {N_4O_2} coordination environment are derived from two **L^2** and two MeCN molecules. However, its catalytic activity proved to be lower (Table 5.4, entry 9); it can be thus concluded that this lack of ligand molecules leads to different and less active species during the catalysis, making **22** a less effective catalytic precursor. Having this result in mind, the next efforts focused exclusively on nitrogen-based ligands with *ortho*-substitution. The use of benzimidazole (compound **23**) or imidazole (compounds **24**, **25**) instead of benzotriazole generates topologically equivalent Cu^{II}-based 1D frameworks; however, their use as catalysts reveals a considerable decrease in the product yield (Table 5.4, entries 10 - 12). As CV studies show that the benzimidazole-based analogue **23** behaves similarly to **18**, the yield difference can be attributed to electronic factors / second coordination sphere effect, while the absence of the bulky phenyl group might be a factor in the case of the imidazole-based compounds. The possibility that more drastic species are formed with the benzotriazole ligand should also be considered. It is worth noting that both compounds **24** and **25** present the ligand-derived {N_4} square plane that is required for the catalytic activity, however they have slight differences in the species that occupy the axial positions of the octahedron (OTf^-/MeCN versus OTf^-

/H_2O). The latter parameter appears to have no effect in the catalytic performance, based on the similar yields measured in each case (69 and 70% respectively). Furthermore, to determine the importance of the polymeric nature on the catalysts, the ligand 1-benzyl-1H-1,2,3-benzotriazole, **L^8**, was employed as the mono-substituted version of **L^3** in order to guarantee the generation of 0D coordination compounds. The *in situ* reaction of $Cu(OTf)_2$ and **L^8** yields the corresponding product in poorer yields (Table 5.4, entry 14) indicating the necessity of a bis-substituted ligand. Finally, the *in situ* reaction of $Cu(OTf)_2$ and **L^3** also resulted in significantly lower yield (Table 5.4, entry 15), showcasing that other, non-catalytically active species are formed during this process. From these results, it can be concluded that higher catalytic efficacy is achieved using the well-characterized, polymeric precursors.

In regards to the use of additives, it was found that the presence of sodium L-ascorbate enhances the Cu^I to Cu^{II} conversion (Table 5.2, entries 13 and 14), therefore improving the catalytic affinity. However, after 24 hours the catalytic conversion is similar to that without any additive. Triphenylphosphine (PPh_3) was also tested as an additive in the reaction; apart from its role as a reducing agent, PPh_3 may potentially react with the organic azide to eventually produce the corresponding amine through the Staudinger reaction[291], thus deactivating the CuAAC transformation. However, no significant effect in the yield was observed in the analogous catalytic tests (Table 5.2, entry 12), indicating that PPh_3 is not involved in the catalytic cycle.

Additionally, a series of EPR experiments was performed monitoring the synthesis of triazole **C5T1** using **18** as the catalyst, in order to investigate the nature of the copper-based compound during the reaction. A comparison of the afforded spectra during the first 120 minutes of the reaction (Appendix, Figure S5.20, left) confirms the constant presence of Cu^{II} species in the solution, albeit with a continuous decrease in the intensity, which could indicate the change into EPR silent Cu^I. In comparison, similar studies were performed with the addition of the reducing agent sodium-L-ascorbate in the reaction mixture (Appendix, Figure S5.20, right). While the intensity decrease is higher in the first 60 minutes of the reaction, the

signals after 120 minutes are eventually similar to the ones without the presence of the additive, which is consistent to the similar catalytic results as previously mentioned.

Considering all these parameters and taking into account the above CV and EPR studies, a possible mechanistic pathway as depicted in Scheme 5.6 is proposed. CV studies showed reversible transition $Cu^{II}(L)_2$ (**A**) to $Cu^{I}(L)_2$ (**B**) for compounds **18** and **23** but not for **20**, therefore $Cu^{I}(L)_2$ (**B**) is considered to be the possible catalytic active species. However, the comparison of the TOF values 4.4 (after 1 hour reaction time) and 0.8 (after 24 hours) (Table 5.2, entries 2 and 10) indicates structural change of the catalyst. The crystallographic characterization (as reported in Chapter 3) of the 1D compound $[Cu^{I}(\mathbf{L^3})Cl]$ (**11i**) as the deactivated catalytic species, confirms the partial dissociation of the ligand yielding the $Cu^{I}(L)$ (**C**) species. The structure of **C** can be a 1D $[Cu^{I}N_2]$ compound, or due to the flexibility of the organic ligand it may consist of dimeric species. In these cases, the transition of **C** to the corresponding $Cu^{II}(L)$ species (**D**) cannot be excluded. EPR studies during the first 120 minutes of the reaction confirm the presence of Cu^{II} species in the solution, thus excluding the possibility that the Cu^{II} has converted in full to Cu^{I} at the beginning of the reaction. As the reaction proceeds, the excess of the produced 1,4-triazoles, that have similar coordination abilities to $\mathbf{L^3}$, yields in further dissociation of $\mathbf{L^3}$ and formation of the species $[CuN_4]$ (**E**) and termination of the catalytic cycle. The two Cu^{I} units in the crystallographically characterized analogue of **C** are at an approximate distance of 8.74 Å, thus any chance that the reaction is promoted from a species involving neighbouring copper centres[256,265] should be excluded for this catalytic system. Therefore, both active species **B** and **C** could catalyse the present 1,3-dipolar cycloaddition, as shown in Scheme 5.6. Consequently, a coordination of copper to the acetylene takes place forming the corresponding Cu^{I}-acetylide intermediate, that in the presence of the azide undergoes a cyclization process through an unusual six-membered copper metallacycle intermediate. This pathway is supported by theoretical studies on copper-catalyzed 1,3-dipolar cycloaddition process and synthesis of azoles[204,292]. Finally, the ring contraction to a triazolyl-copper derivative is followed by protonolysis that delivers the triazole product and closes the catalytic cycle.

Table 5.4. Catalytic evaluation of all coordination compounds tested in the synthesis of triazole **C5T1**.

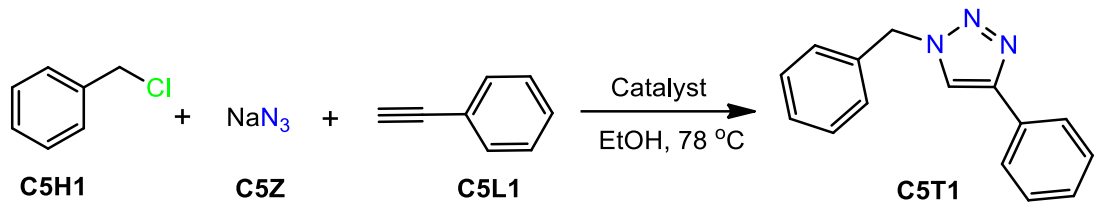

Entry	Catalyst	Conversion (%)[a]	Yield (%)[b]	Regioselectivity of **C5T1**[c]
1	**11**	90	56	99
2	**13**	NR	-	-
3	**11i**	100	58	98
4	**17**	90	47	99
5	**18**	100	93	99
6	**19**	NR	-	-
7	**20**	97	78	98
8	**21**	94	76	98
9	**22**	99	74	99
10	**23**	99	84	99
11	**24**	100	69	99
12	**25**	100	70	99
13	**26**	99	77	99
14	$Cu(OTf)_2 \cdot H_2O$ + **L**[8]	87	28	99
15	$Cu(OTf)_2 \cdot H_2O$ + **L**[3]	99	57	99

Reaction conditions: benzyl chloride (57.5 µL, 0.5 mmol), sodium azide (32.5 mg, 0.5 mmol), phenylacetylene (55 µL, 0.5 mmol), catalyst (5 mol %), EtOH (3 mL), heated at 78°C for 24 h. [a]: based on benzyl chloride. Differences between the conversion and yield percentages are due to the unreacted benzyl azide. [b]: Relative yields based on ^{1}H NMR analysis from the integration of the corresponding proton shifts. [c]: calculated from regioisomers 1,4-product : 1,5-product.

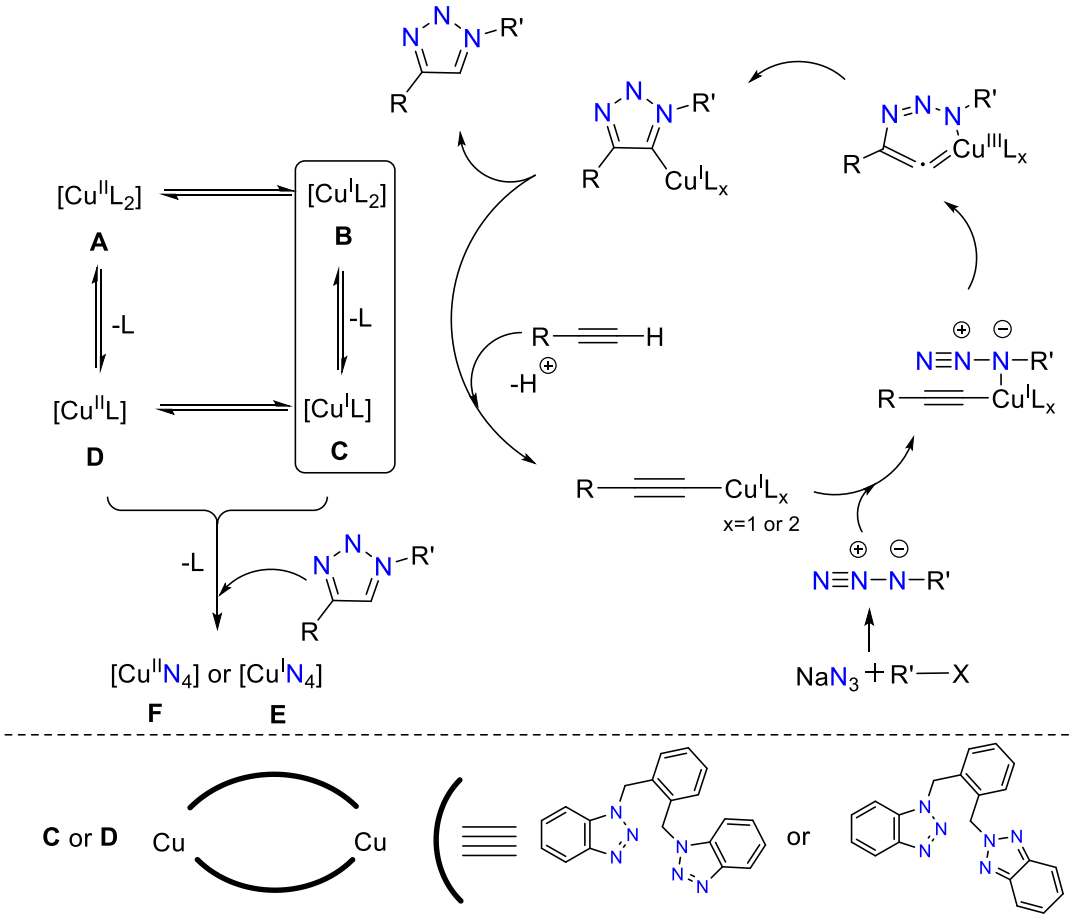

Scheme 5.6. A plausible mechanism of the AAC reaction catalysed by **18**.

5.3. Conclusion

This work has afforded a series of Cu coordination compounds with nitrogen-containing ligands which have been added in the pre-existing library of analogous catalysts introduced in the previous Chapters. Attempts have been made to understand their homogeneous catalytic performance and mechanistic nature through their activity in the well-known Cu^{I}-promoted AAC reaction. In particular, compound $[Cu^{II}(\mathbf{L^3})_2(CF_3SO_3)_2]$ (**18**) is the optimal catalyst affording 1,4-disubstituted 1,2,3-triazoles with moderate to excellent (27-99%) yields without requiring a reducing agent. Furthermore, the proposed method avoids the isolation of potentially unstable organic azides, using either organic halides or benzeneboronic acid as starting materials.

CV studies of selected samples showed that fine-tuning the organic ligand has a significant effect on the electrochemical properties (**20** differs to **18** and **23**). The coordination sphere of **18** and **23** is rather similar which is proved by the similar formal potential values. The measured formal potential values are more negative in DMSO than in DMF, which supports that it is much more difficult to reduce the complexes in stronger donor solvents. This fact may help in choosing the right solvent for a more effective catalysed reaction.

The catalytic system has also been optimized and fine-tuned using an extensive set of control experiments and techniques throughout Chapters 3, 4 and 5. These studies confirm that **18** can act as an excellent precursor in a number of organic reactions under alcoholic media, providing Cu^{I} active species. Initiating the catalysis from a polymeric Cu^{II} compound appears essential for the system, since the efforts to obtain the corresponding Cu^{I} derivatives or improve the catalytic performance with monomeric analogues were not successful. Through this diagnostic study, the benzotriazole-based ligand is identified as the most suitable for this catalytic system. The findings also confirm the optimal metal geometry and coordination environment for the precursor. Furthermore, the semi-flexibility of the ligand through the introduction of the $–CH_2$ groups appears to be crucial, allowing for the formation and fine-tuning of the initial polymeric compounds, as well as the transformation to the various species during the catalytic cycle.

Having established a good understanding of the catalytic activity of this system using Cu sources, the following chapter will focus on analogous efforts while exploring the catalytic potential of other metals.

Chapter 6: Structural diversity and catalytic properties in a family of Ag^{I}-benzotriazole based coordination compounds

Abstract: In this work the coordination chemistry of benzotriazole based ligands **L^1-L^3** is studied using the low coordination number but versatile Ag^{I} ions. This has led to nine new coordination compounds formulated as $[Ag(\mathbf{L^1})(CF_3CO_2)]$ (**27**), $[Ag_2(\mathbf{L^{1T}})_2(CF_3SO_3)_2]\cdot 2Me_2CO$ (**28**), $[Ag(\mathbf{L^{2T}})(ClO_4)(Me_2CO)]$ (**29**), $[Ag(\mathbf{L^{2T}})(BF_4)(Et_2O)]$ (**30**), $[Ag_2(\mathbf{L^{3T}})_2(ClO_4)_2]_2$ (**31**), $[Ag(\mathbf{L^3})(NO_3)]$ (**32**), $[Ag_2(\mathbf{L^{3T}})_2(CF_3CO_2)_2]$ (**33**), $[Ag_2(\mathbf{L^{3T}})(CF_3SO_3)_2]$ (**34**) and $[Ag_2(\mathbf{L^{3T}})_2(CF_3CF_2CO_2)_2]\cdot 2Me_2CO$ (**35**). These compounds show structural diversity including dimers (**31**, **33**, **35**), 1D (**29**, **30**, **32**) and 2D (**27**, **28**, **34**) CPs. The presence of the two $-CH_2-$ units between the three rigid backbones, benzotriazole/-C_6H_4-/benzotriazole, provides a limited but significant, flexibility in **L^1-L^3**, influencing their varying coordination abilities. Interestingly, certain structures exhibit an isomerism effect (**L^{1T}-L^{3T}**) in the benzotriazole unit when in solid state; a series of studies are indicative of the 1,1- form being generally dominant in solution even in cases where the crystal structure does not contain this tautomer. The homogeneous catalytic efficacy of all compounds against the well-known multi component A^3 coupling reaction and the hydration of alkynes are investigated. Compound **30** was identified as the optimal catalyst for both reactions, promoting the multicomponent coupling as well as the alkyne hydration reaction under low loadings (0.5 and 3 mol%, respectively) and in high yields (up to 99 and 93% in each case).

External Contributions: Iain Day (University of Sussex) was responsible for the interpretation of the ^{15}N NMR studies. Alaa Abdul-Sada (University of Sussex) was responsible for the collection of all ESI-MS data.

6.1. Introduction

The use of silver for the construction of coordination architectures has been receiving increasing attention due to its rich and unique chemistry. Compared to other metals, Ag^{I} provides a wide range of coordination environments, with multiple possibilities in coordination number (from 2 to 6) and geometries (e.g. linear, trigonal, tetrahedral, trigonal bipyramidal, square pyramidal, octahedral)[293]. This versatility and adaptability of Ag^{I}

systems, along with the potential formation of argentophilic (Ag^I – Ag^I) interactions, has contributed significantly to the formation of peculiar structural topologies[294–303] with various dimensionalities, as well as uncommon supramolecular architectures[304]. These exploits have also been crucial towards the development of Ag^I CPs with structural interest and potential applications, which include luminescence[305–307], anion exchange[307–309], antibacterial[310–316] and catalytic activity[231,317–322]. Focusing on the latter, several Ag CPs and MOFs have been especially used as catalysts in organic transformations that involve alkyne activation[138,323] due to the supreme capability of the metal to form organometallic intermediates through π-coordination with the carbon–carbon triple bond.

The cobalt and copper chemistry of ligands **L^1-L^3** (Scheme 6.1) was investigated extensively in Chapters 2-5. The results demonstrated the structural diversity and flexibility of these *N*-containing ligands, leading to multiple coordination compounds with interesting magnetic and catalytic properties. The next step in these studies was to combine this rewarding and flexible system with the rich chemistry and unique coordination variety of Ag^I ions, exploring the resulting structural aspects as well as potential catalytic applications to add to the existing findings.

Having the superior alkynophilicity of Ag^I in mind, the A^3 multicomponent coupling and the hydration of terminal alkynes were identified as two potential reactions to test any afforded compounds. The former reaction and its importance have been already discussed in Chapter 4; as mentioned, the key mechanistic step during this coupling requires the formation of a metal acetylide intermediate which is then added to the iminium ion to generate the resulting propargylamine. For this reason, a variety of Ag^I sources has been utilized in this reaction[324], including simple salts[230], coordination compounds[325–328] and CPs[231,320,329]. The second reaction involves treatment of alkynes with water, resulting to the synthesis of ketones that follow Markonikov's rule. As the classic method for this reaction requires the addition of toxic mercury under harsh acidic conditions, multiple systems involving other transition metal elements (e.g Cu[330], Fe[331], Ru[332], Au[333]) have also been explored. Another common[334–336] strategy involves incorporation of silver as a co-catalyst with gold to activate this reaction; on the other hand, only a few reports using solely silver sources as catalysts can be found.

The first example dates back to 2012, when Wagner and co-workers[337] employed $AgSbF_6$ for the selective hydration of terminal alkynes. In the following years $AgBF_4$[338], AgOTf[339] and a silver exchanged silicotungstic acid (STA) catalyst[340] were also tested successfully. However considerable disadvantages in these procedures, such as the high loadings (up to 10 mol% in most cases) or temperatures, the use of expensive salts (such as $AgSbF_6$) or the lengthy workup for the preparation of the catalyst (in the case of AgSTA) reveal the need for further optimization in this area. In addition, a literature search showed that no silver coordination compounds have been reported to catalyse this reaction up to this date.

As a result of all the above, this Chapter reports i) the synthesis and characterization of compounds $[Ag(\mathbf{L^1})(CF_3CO_2)]$ (**27**), $[Ag_2(\mathbf{L^{1T}})_2(CF_3SO_3)_2]\cdot 2Me_2CO$ (**28**), $[Ag(\mathbf{L^{2T}})(ClO_4)(Me_2CO)]$ (**29**), $[Ag(\mathbf{L^{2T}})(BF_4)(Et_2O)]$ (**30**), $[Ag_2(\mathbf{L^{3T}})_2(ClO_4)_2]_2$ (**31**), $[Ag(\mathbf{L^3})(NO_3)]$ (**32**), $[Ag_2(\mathbf{L^{3T}})_2(CF_3CO_2)_2]$ (**33**), $[Ag_2(\mathbf{L^{3T}})(CF_3SO_3)_2]$ (**34**) and $[Ag_2(\mathbf{L^{3T}})_2(CF_3CF_2CO_2)_2]\cdot 2Me_2CO$ (**35**) and ii) the demonstration of their catalytic activity in the A^3 coupling and alkyne hydration reactions.

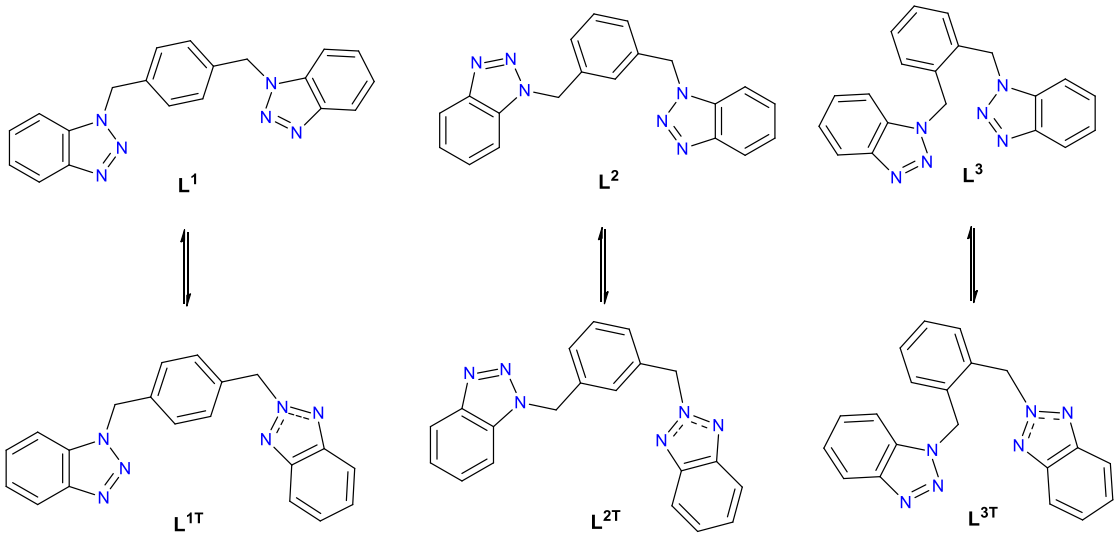

Scheme 6.1. The organic ligands $\mathbf{L^1}$, $\mathbf{L^2}$, and $\mathbf{L^3}$ used in this study and their potential isomer forms $\mathbf{L^{1T}}$, $\mathbf{L^{2T}}$, and $\mathbf{L^{3T}}$.

6.2. Results and Discussion

6.2.1. Crystal Structure Description of Compounds 27 – 35

Compound **27** was synthesized using silver trifluoroacetate and the *para*-substituted **L^{1}** ligand. The structure crystallizes in the triclinic $P\bar{1}$ space group and its asymmetric unit consists of one Ag^{I} centre, one **L^{1}** molecule and one trifluoroacetate anion. In this coordination mode, **L^{1}** adopts a chair conformation, with the benzotriazole units being parallel to each other. Each ligand molecule coordinates to a total of two Ag^{I} centres as seen in Scheme 6.2, mode A. The trifluoroacetate anions also act as bridging ligands, generating $[Ag_2(L^1)_4(CF_3CO_2)_2]$ nodes which expand to a two-dimensional architecture. As a result, **27** may be described as a 2D coordination polymer that propagates along the *a0c* plane (Figure 6.1, upper). Each of the metal centres possesses a tetrahedral geometry and a $\{N_2O_2\}$ coordination environment. This tetrahedron is rather distorted, with the relevant angles ranging from 97.18(18) to 140.94(19)°. The related Ag-N and Ag-O bond distances are surprisingly similar, ranging from 2.304(5) to 2.340(5) Å. No hydrogen bonds or other supramolecular interactions were observed.

Compound **28** was synthesized through the use of silver triflate as the metal salt and the resulting structure crystallizes in the monoclinic $P2_1$ space group. In this case, an isomerism phenomenon is observed in the benzotriazole moieties of all **L^{1}** molecules, as one of the two $–CH_2$ linkers connects to the middle N atom of the benzotriazole. Consequently, the disubstituted 1,2-yl analogue (**L^{1T}**) is obtained, instead of the 1,1-yl. As a result the asymmetric unit of **28** contains two Ag^{I} centres, two **L^{1T}** molecules, two triflate anion molecules that act as terminal ligands and two acetone lattice solvents. The latter will not be further mentioned in this description. The coordination mode for the two crystallographically independent **L^{1T}** molecules (Scheme 6.2, Modes B and C) is similar, as each of the ligands coordinates to three different Ag^{I} centres. More specifically, the benzotriazol-1-yl unit coordinates to one Ag^{I} centre through the single far nitrogen atom, while the 2-yl moiety coordinates to two metal centres through its two far nitrogen atoms. The two **L^{1T}** molecules however differ slightly in orientation as the angle between their benzotriazole entities are 49.27(3) and 43.47(3)° respectively. This conformation accounts for the formation of

$[Ag_2(\mathbf{L^{1T}})_2(CF_3SO_3)_2]$ nodes which are connected to each other through Ag-N bonding to generate the resulting two-dimensional coordination polymer along the *b0c* plane (Figure 6.1, lower). Each Ag^I centre possesses a $\{N_3O\}$ coordination environment and a slightly distorted tetrahedral geometry. The Ag-N bonds range from 2.266(10) to 2.349(10) Å, while the Ag-O are slightly larger at 2.323(15) and 2.366(9) Å. The angles of the tetrahedra range from 97.2(3) to 135.0(3)°. While no strong H-bonds are formed, π···π interactions form between the benzene and the benzotriazole moieties of ligand molecules to further stabilize the two-dimensional architecture. The parameters for these interactions are detailed in the Appendix (Table S6.1).

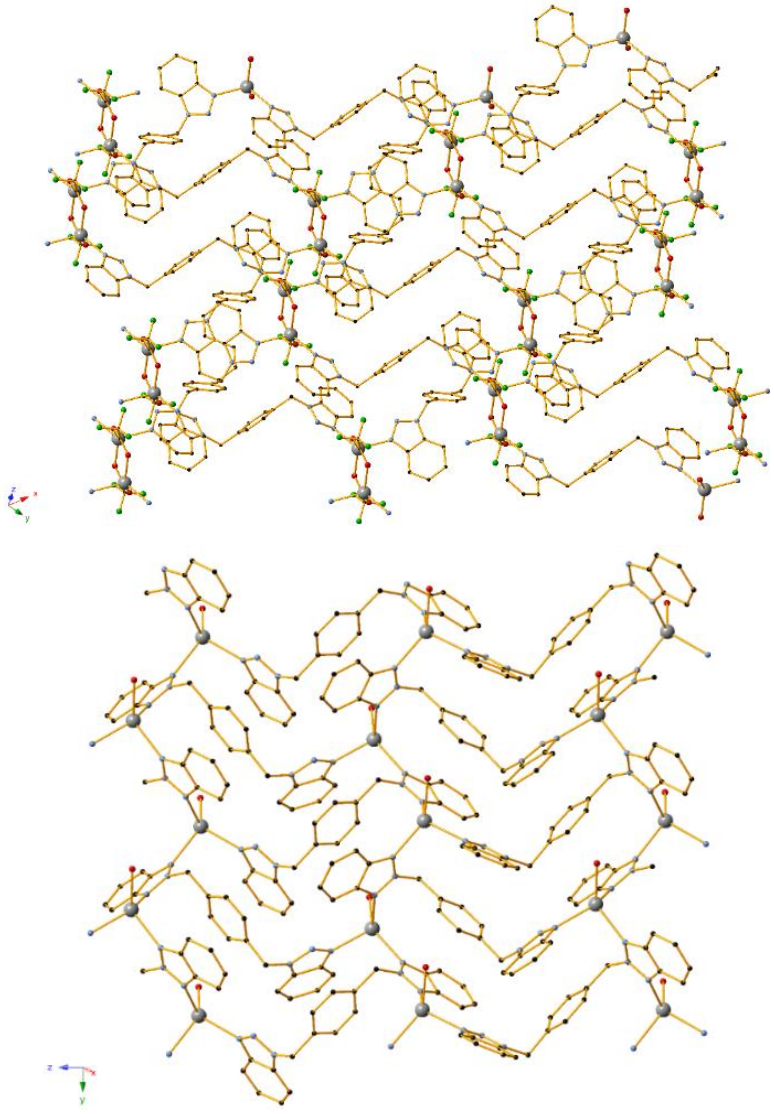

Figure 6.1. (upper) Part of the two-dimensional framework along the *a0c* plane in compound **27**. H atoms are omitted for clarity. Colour code Ag (grey), C (black), N (light blue), O (red),

F (light green). (lower) Part of the two-dimensional framework along the *b0c* plane in compound **28**. For clarity, H atoms, solvent molecules and part of the triflate anions have been omitted. Colour code Ag (grey), C (black), N (light blue), O (red).

For the construction of compound **29** the *meta*-substituted ligand $\mathbf{L^2}$ was utilized along with silver perchlorate. The complex crystallizes in the monoclinic $P2_1/n$ space group and contains one Ag^I centre, a ligand molecule, a perchlorate anion as well as one acetone molecule in the asymmetric unit. Interestingly, another case of ligand isomerism is observed as the ligand molecule appears as the 1,2-disubstituted benzotriazole analogue ($\mathbf{L^{2T}}$). Each of these $\mathbf{L^{2T}}$ ligands coordinates to two different Ag^I centres through the far N atom of each benzotriazole moiety. Due to the increased flexibility of the $–CH_2$ linkers, in this conformation mode (Scheme 6.2, Mode D) the planes of the two benzotriazole moieties are found at an angle of 54.56(19)°. As a result of these features, the structure of **29** consists of a one-dimensional polymeric chain which propagates along the *b* axis (Figure 6.2, upper). The perchlorate and acetone molecules also coordinate to the Ag^I centre, which exhibits a heavily distorted tetrahedral geometry in a $\{N_2O_2\}$ coordination environment. As expected, the Ag-O bond distances, ranging from 2.47520(8) to 2.52007(9) Å, are significantly larger than the analogous Ag-N values which were calculated at 2.15565(8) and 2.18819(7) Å respectively.

Compound **30** was found to crystallize in the monoclinic $P2_1/n$ space group. Determination of the structure through X-Ray crystallography reveals a similar case of isomerization of $\mathbf{L^2}$ to $\mathbf{L^{2T}}$ as seen in **29**. However, in this case the ligand shows a different conformation (Scheme 6.2, Mode E), as the two benzotriazole moieties are almost parallel to each other at an angle of only 3.70(11)°. Due to this, the compound propagates in one direction, forming 1D helix-like chains along the *b* axis as shown in Figure 6.2, lower. This difference in the conformation of $\mathbf{L^{2T}}$ also accounts for significant variance in Ag-Ag distance; this value was measured at 8.9893(4) Å in **29** and 10.3143(9) Å in **30**. Each Ag^I centre is coordinated to four atoms in a distorted tetrahedral geometry. The coordination environment consists of two N atoms from two $\mathbf{L^{2T}}$ molecules, one F atom from tetrafluoroborate anions and one O atom from a coordinating diethyl ether solvent molecule. The largest bond in this coordination sphere is the Ag-F distance which was measured at 2.615(4) Å. In contrast, the Ag-N bond values were

the smallest at 2.224(5) and 2.250(4) Å. The arrangement of the framework also promotes the formation of inter-molecular π···π interactions[341] which account for further stability. These weak interactions occur between certain benzotriazole aromatic rings, as detailed in the Appendix (Table S6.2).

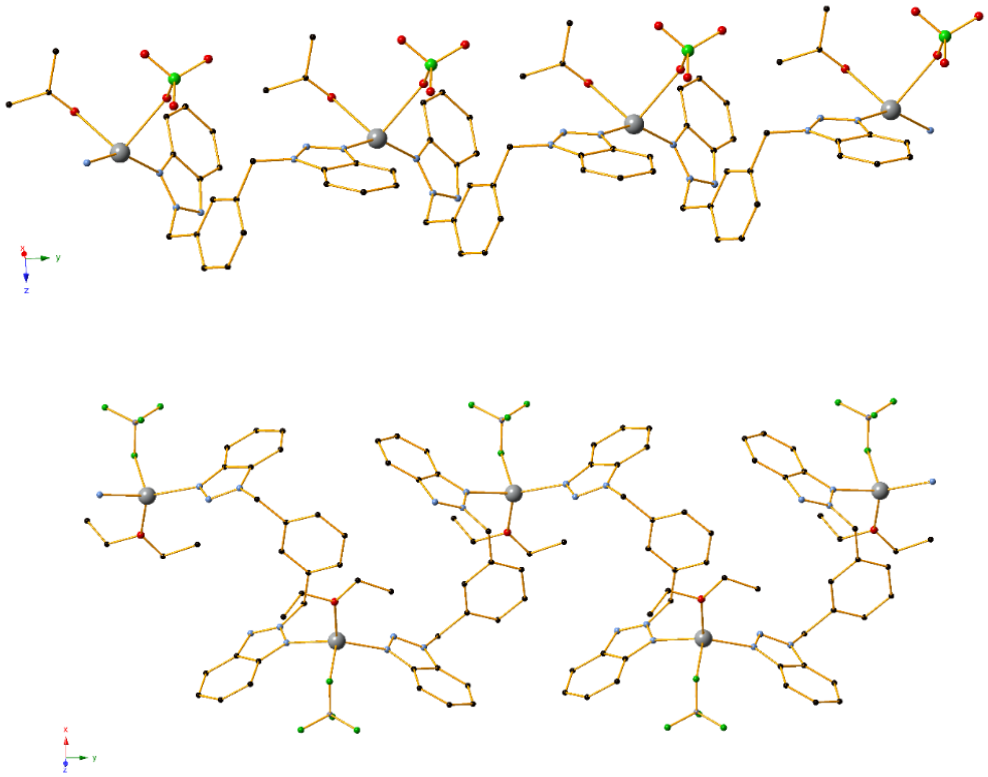

Figure 6.2. (upper) Part of the one-dimensional framework in **29**. H atoms are omitted for clarity. Colour code Ag (grey), C (black), N (light blue), O (red), Cl (light green). (lower) Part of the one-dimensional framework in **30** along the *b* axis. H atoms are omitted for clarity. Colour code Ag (grey), C (black), N (light blue), B (dark grey), F (light green).

Compound **31** crystallizes in the triclinic $P\bar{1}$ space group and its structure consists of two crystallographically independent dimeric $[Ag_2(\mathbf{L^{3T}})_2(ClO_4)_2]$ units as shown in Figure 6.3. Similarly to the *para*- and *meta*- analogues, the *ortho*-substituted ligand also appears here as the $\mathbf{L^{3T}}$ isomer. The presence of two different types of dimeric units within the structure are due to the coordination modes and conformations of $\mathbf{L^{3T}}$ (Scheme 6.2, Modes F and G). In the first unit the benzotriazol-1-yl moiety coordinates to both Ag^{I} centres through the

respective middle and far nitrogen atoms; the related atoms appear aligned in a single plane. The 2-yl moiety is found at an angle of 63.31(9)° to this plane and coordinates to only one metal centre. As a result, the relevant Ag^{I} centres possess a distorted tetrahedral $\{N_3O\}$ environment. In contrast, the second dimer consists of $\mathbf{L}^{\mathbf{3T}}$ ligands in which the benzotriazole entities are almost parallel (6.02(8)° angle between the two planes). This dimeric component is further stabilized by a weak Ag···π interaction which is formed as the phenyl group of the ligand backbone faces towards the silver atom with a slight slippage of 1.717 Å, as depicted in Figure S6.1, Appendix. The centroid-metal distance in this case was measured at 3.177(2) Å. A series of relevant Ag···C distances from 2.737(5) to 3.317(5) further support the formation of this interaction. Each of these units coordinate to one Ag^{I} centre through their respective far nitrogen atoms and therefore the metal ions show a distorted trigonal geometry and a $\{N_2O\}$ coordination environment. The formation of several intermolecular π···π interactions (Appendix, Table S6.3) further stabilizes the packing arrangement of these dimeric units.

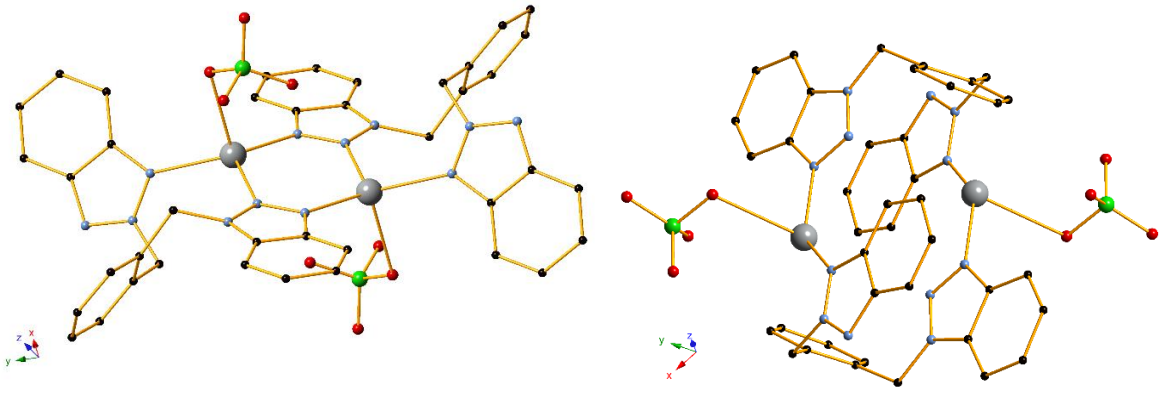

Figure 6.3. The two crystallographically independent dimeric units in **31**. H atoms are omitted for clarity. Colour code Ag (grey), C (black), N (light blue), O (red), Cl (light green).

Crystallographic analysis for compound **32** reveals a one-dimensional polymeric structure which extends along the *b* axis to form a ribbon-like 1D framework with small voids (Figure 6.4, left). The compound crystallizes in the triclinic $P\bar{1}$ space group and its asymmetric unit contains an Ag^{I} centre, one $\mathbf{L}^{\mathbf{3}}$ ligand molecule and one nitrate anion which acts as a bridging ligand. Interestingly, no isomerization of the ligand is observed: each of the benzotriazol-1-yl moieties coordinate to one Ag^{I} ion through the far nitrogen atom (Scheme 6.2, Mode H), with the respective Ag-Ag distance at 10.749(3) Å. In regards to the ligated nitrate anion,

one oxygen atom coordinates to the metal ion, while another oxygen coordinates to the same Ag^{I} centre as well as a symmetry related one. As a result, two zig-zag 1D architectures are bridged by the nitrate anions to form the resulting ribbon-like framework. The resulting $\{N_2O_3\}$ coordination environment of the metal ion provides a distorted square pyramidal geometry ($\tau = 0.05$[164]). As expected, the mean Ag-N distances (2.242(7) and 2.243(6) Å) are significantly shorter than the respective Ag-O distances (ranging from 2.512(6) to 2.720(6) Å).

Compounds **33** and **35** contain isoskeletal cores and as such only the former will be described in detail. The structure of **33** consists of a wheel-like $[Ag_2(\mathbf{L^{3T}})_2(CF_3CO_2)_2]$ dimeric unit in which the ligand appears as the $\mathbf{L^{3T}}$ isomer (Figure 6.4, right). Similarly to one of the dimers in compound **31**, the benzotriazole moieties in the ligand are found almost parallel to each other at an angle of 7.97(8)° and coordinate to a total of two Ag^{I} ions through their respective far nitrogen atoms (Scheme 6.2, Mode I). This Ag-Ag distance was measured at 3.9108(7) Å. A trifluoroacetate anion also coordinates to the metal centre through one oxygen atom to complete its $\{N_2O\}$ coordination sphere. The relevant angles in this trigonal geometry range from 105.18(13)° to 127.82(11)°. Intermolecular $\pi\cdots\pi$ interactions provide extended stability to this architecture. The parameters for these interactions may be found at the Appendix (Table S6.4).

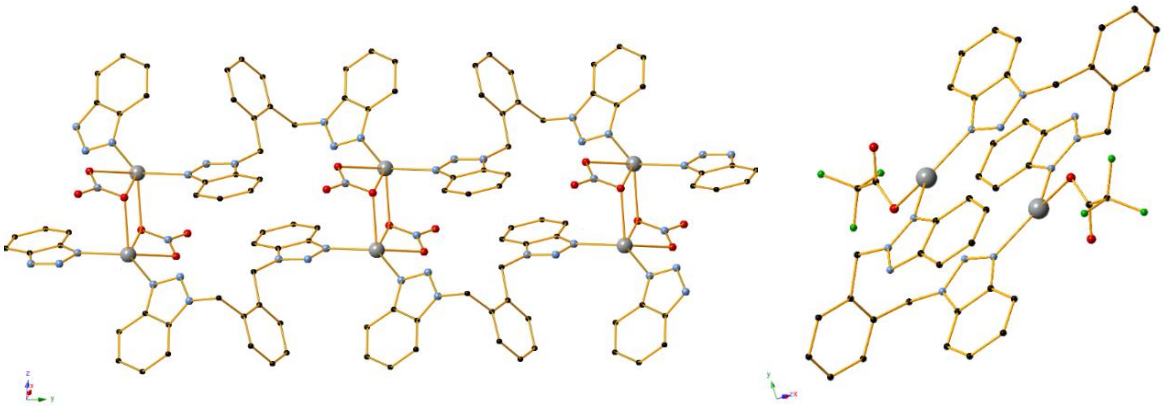

Figure 6.4. (left) Part of the one-dimensional framework in **32** along the *b* axis. H atoms are omitted for clarity. Colour code Ag (grey), C (black), N (light blue), O (red). (right) The structure of compound **33**. H atoms are omitted for clarity. Colour code Ag (grey), C (black), N (light blue), O (red), F (green).

Finally, compound **34** crystallizes in the monoclinic $P2_1/n$ space group and its asymmetric unit contains two Ag^I centres, two triflate anion molecules and one organic ligand as the $\mathbf{L^{3T}}$ isomer. The conformation of the latter is similar to other compounds mentioned in this study, with the planes of the benzotriazole entities forming a very small angle of 12.18(12)°. However, the coordination mode varies in this case, as the benzotriazol-2-yl unit utilize both far nitrogen atoms to coordinate to two metal centres (Scheme 6.2, Mode J). The ligated triflates also play an important role in the resulting architecture as they bridge symmetry related $[Ag_2(\mathbf{L^{3T}})_2]$ nodes. This bridging leads to the formation of a two-dimensional sheet along the *b0c* plane (Figure 6.5) which is supported by argentophilic interactions between two symmetry-related Ag^I centres which are found at a distance of 3.1794(11) Å. Further support is provided by the formation of weak π···π interactions between aromatic rings as detailed in Table S6.5, Appendix. It is worth noting that each of the triflate units bridge the aforementioned nodes in a different way (Scheme 6.2, bottom middle and right). For the first triflate, each of the three oxygen atoms coordinate to different Ag^I ions, while the second anion employs only one oxygen atom for coordination, binding concurrently to the two Ag^I centres which participate in the argentophilic interaction. As a result of all the above, the two crystallographically independent metal centres of this compound possess a distorted trigonal bipyramidal ($\tau = 0.68$[164]) coordination geometry, respectively.

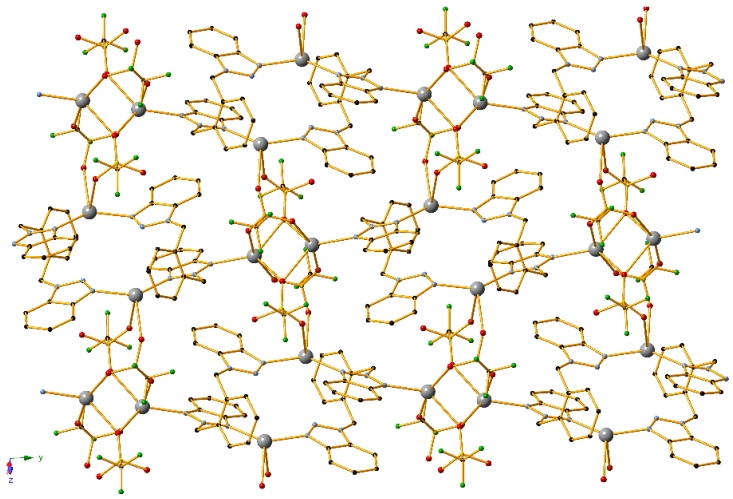

Figure 6.5. Part of the two-dimensional framework along the *b0c* plane in compound **34**. H atoms are omitted for clarity. Color code Ag (grey), C (black), N (light blue), O (red), F (green), S (yellow).

Table 6.1. Structural summary of compounds **27-35** (M = Ag).

Entry	Compound	Ligand in Crystal Structure	Coordination Environment of Ag^{I}	Solvent Used	Metal salt	Dimensionality
1	**27**	**L^{1}**		MeCN	$AgCF_3CO_2$	2D
2	**28**	**L^{1T}**	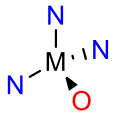	Me_2CO	$AgCF_3SO_3$	2D
3	**29**	**L^{2T}**		Me_2CO	$AgClO_4$	1D
4	**30**	**L^{2T}**	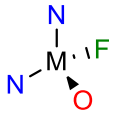	Me_2CO	$AgBF_4$	1D
5	**31**	**L^{3T}**	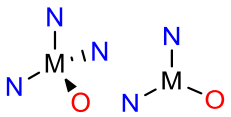	Me_2CO	$AgClO_4$	0D
6	**32**	**L^{3}**	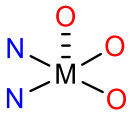	MeCN	$AgNO_3$	1D
7	**33**	**L^{3T}**	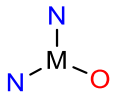	Me_2CO	$AgCF_3CO_2$	0D
8	**34**	**L^{3T}**	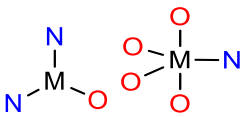	Me_2CO	$AgCF_3SO_3$	2D
9	**35**	**L^{3T}**	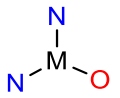	Me_2CO	$AgCF_3CF_2CO_2$	0D

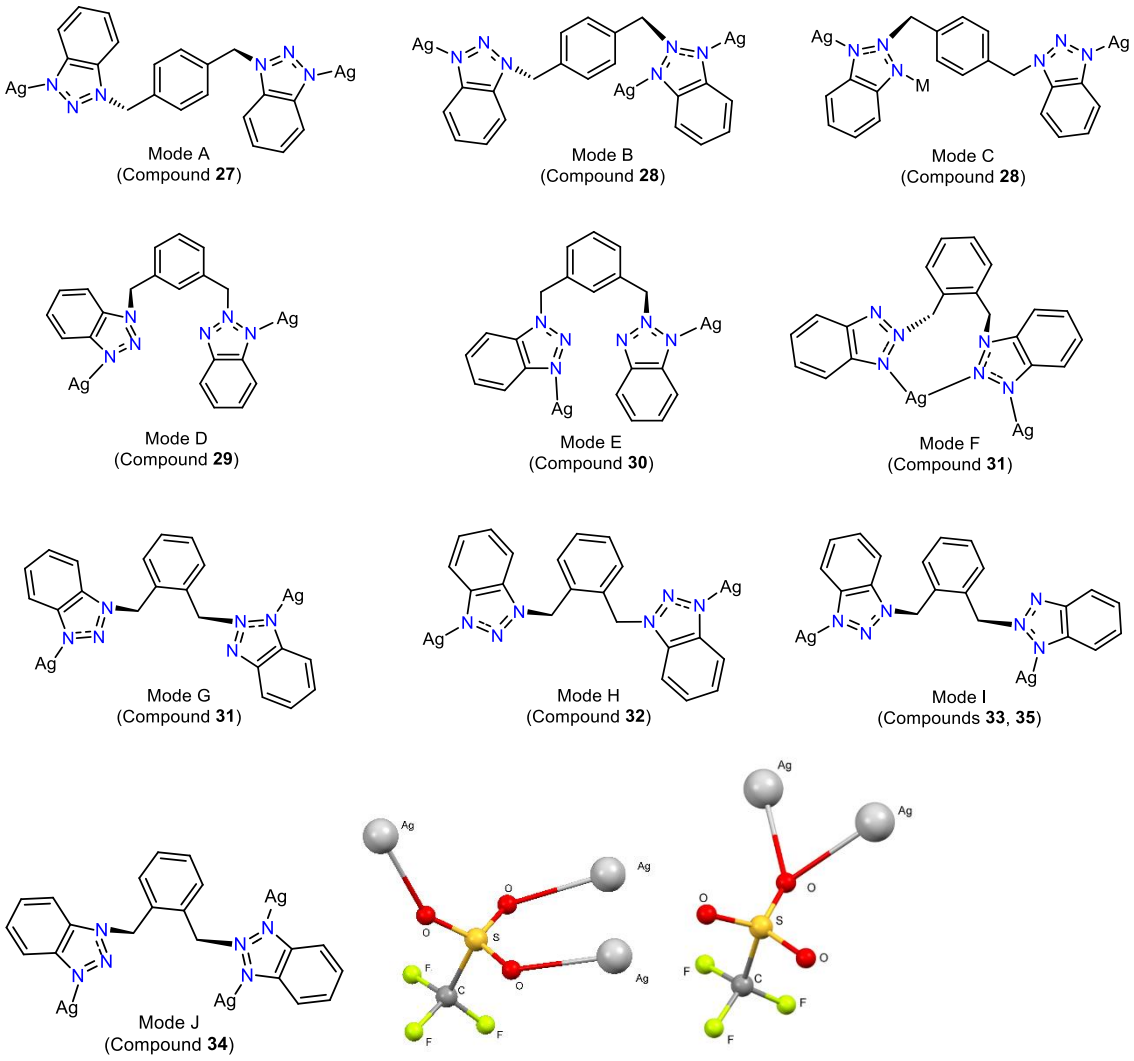

Scheme 6.2. (Modes A-J) The coordination modes for all ligands that appear in compounds **27-35**. (bottom middle and right) The coordination modes of the triflate anions[342] in compound **34**.

6.2.2. Synthetic aspects

The chemistry used to afford **27-35** was similar to the one mentioned in the synthetic aspects of Chapters 2-5. The compounds were generated under the use of various metal:ligand ratios ranging from 2:1 to 1:2, in either acetone or acetonitrile and with diffusion or slow evaporation as the crystallization technique. In this case, no crystalline material was afforded through the use of higher temperatures. All synthetic experiments were performed in the absence of light (vials were covered with tin foil, then stored in a closed cupboard), although the resulting silver compounds do not appear to be light sensitive.

6.2.3. Characterization of Compounds 27 – 35

TGA Studies

TGA experiments to determine the thermal stability of **27**-**35** revealed similar outcomes, as in all cases the main (polymeric or dimeric) core retains its stability up to the region of ~220-300°C, where gradual decomposition begins to take place. Complex **27** shows a gradual mass loss in the 50-250°C range which is due to the removal of trifluoroacetate entities (calcd.: 20.45%, theor.: 20.18%). Almost immediately, the core is subjected to further gradual decomposition towards the final oxide (calcd.: 58.77%, theor.: 59.30%). In the case of complex **28**, the first mass loss (9.59%) occurs from 50 to 114°C and corresponds to the loss of the acetone lattice molecule in good agreement (theoretical value: 8.87%). The remaining core is stable until 291°C, where it collapses towards gradual decomposition. In compound **29**, the main core retains its stability until 297°C where it is decomposed to Ag_2O (calcd.: 79.24%, theor.: 78.96%). Compound **30** remains relatively stable until the region of 285°C (as the Et_2O molecule is lost before the TGA measurement begins) and the first mass loss corresponds to the collapse of the entire framework until decomposition (calcd.: 82.94%, theor.: 81.14%). Complex **31** shows very similar thermal stability, retaining its main core up to 285°C before eventual collapse. In compound **32**, an initial mass loss of 11.60% occurs at approximately 273°C and finishes at 286°C, attributed to the loss of the nitrate anion (theor.: 12.15%). Decomposition of the remaining framework takes place almost immediately (calcd.: 65.65%, theor.: 65.33%). The structure of **33** remains relatively stable up to the region of 215°C, where a large mass loss occurs (81.73%), attributed to the collapse of the framework with reasonable agreement (theor: 79.48%). In complex **34**, there is initially a removal of the triflate anions (28.11% mass loss) from the framework which begins at 275°C and concludes at 310°C. Shortly after this point, the remaining structure collapses to eventual decomposition to silver oxide (calcd.: 54.58%, theor.: 55.59%). Finally, in compound **35** the first mass loss occurs until approximately 218°C and corresponds to the loss of the acetone lattice solvent molecule (calcd: 4.54%, theor: 5.96%). The second mass loss begins almost immediately (at the region of 220°C) and is owed to the collapse of the remaining compound up to decomposition (82.16% mass loss) with satisfactory agreement to the theoretical value (84.26%). The respective TGA graphs are presented in the Appendix (Figures S6.13-S6.21).

Solution Studies

Electrospray ionization mass spectrometry (ESI-MS) in methanolic solution was also performed for compounds **27**-**35**. As in the case of the cobalt and copper compounds in this thesis, the resulting spectra are very similar for all complexes, with two peaks at 447.05 and 789.20 m/z which correspond to the relevant $[Ag(\mathbf{L})]^+$ and $[Ag(\mathbf{L})_2]^+$ fragments. These are the main peaks of all compounds with the exception of complex **32**; in this case, the main peaks correspond to ligand-based fragments and the aforementioned Ag-containing peaks are found in very low intensity, indicating that the polymer may not be so stable in solution. Several of the remaining compounds present additional peaks and the most common fragment is $[Ag_2(\mathbf{L})_2X]^+$, where X is the relevant anion in each case. Other peaks that are present in some compounds correspond perfectly to the $[Ag(\mathbf{L})_3]^+$, $[Ag_2(\mathbf{L})_3X]^+$, $[Ag_3(\mathbf{L})_2X_2]^+$ and $[Ag(\mathbf{L})_3X_2]^+$ fragments. All spectra are presented in the Appendix (Figures S6.22-S6.30) along with a detailed analysis of the fragments.

Isomerism effect and NMR studies

The tautomerism of heterocycles[343,344] is a very common phenomenon that has been extensively studied for several decades. Related reports[345–349] focusing specifically on benzotriazole and its derivatives began surfacing especially after the 1980s, including studies on relevant metal complexes[279,350–353]. Multiple efforts have documented that several types of substituted benzotriazole derivatives exist in solution as an equilibrium mixture of the corresponding 1- and 2-isomers[273,274,354,355]. Some of these cases include *N*-arylmethyl-[275], *N*-(aminomethyl)-[276,278], *N*-(alkoxyalkyl)-[356] and *N*-(alkylthioalkyl)- or *N*-(arylthioalkyl)-benzotriazoles[357]. It has been shown[343,346,354] that the main parameters that affect the position of this equilibrium are i) solvent polarity, as a more polar solvent shifts the equilibrium towards the more polar 1-isomer, ii) temperature, as benzotriazole has been found to be stable as the 2-isomer in gas phase, and iii) the nature of the substituent, as the ratio of the 2-isomer increases in equilibrium when the bulkiness of the substituent is also increased.

Interestingly, a search in the literature reveals no similar investigations for bis-benzotriazole substituted compounds. The first example of such phenomena was observed in the Cu^I-based compound **26**, presented in Chapter 5. Moreover, the current Chapter contains several

compounds with both isomer forms in three different bis-benzotriazole ligands, while the presence of Ag^{I} allows for possible NMR studies. Therefore, this provided an excellent opportunity to shed more light into this isomerism effect. The sole reported Ag^{I} compound with these ligands in the literature is a dimeric $[Ag_2(\mathbf{L^2})_3]\cdot(NO_3)_2\cdot(MeCN)$ compound as described by O'Keefe and Steel[151], in which only the 1,1-isomer form of $\mathbf{L^2}$ is present in the crystal structure; unfortunately, no NMR studies were performed for the compound in that report.

To initiate these investigations, purity during the synthesis was established by employing crystals of the 1,1-isomer form for ligands $\mathbf{L^1}$-$\mathbf{L^3}$. Crystals of compounds **27**-**35** were then characterized with ^{1}HNMR in deuterated DMSO, as none of the complexes was soluble in $CDCl_3$. The obtained ppm shifts reveal interesting results: In general, the 1,1-isomer form exists almost solely (>99:1 ratio) in solution for compounds **27** and **32**; this result is consistent with that determined in the crystal structure. Surprisingly, the corresponding 1,1-isomers were also obtained for compounds **28**-**30**, despite the exclusive presence of the 1,2-isomers in their crystal structures. On the other hand, both 1,1- and 1,2- isomers are present in the solution form for complexes **31**, **33**, **34** and **35** with various ratios (1:1, 1:1, 2:1 and 1:1 respectively). These results demonstrate that the 1,1- form is generally dominant in solution even in cases where the crystal structure does not contain this tautomer; however, the equilibrium may still move towards the 1,2-form in some cases. Having in mind that all NMR studies were performed under the same solvent and temperature conditions, it can be proposed that the main reason for the presence of the 1,2-isomer is the nature of the substitution. This hypothesis is consistent with the findings for compounds **31**, **33**-**35** where the used substituent is increasing its bulky effect and the benzotriazole units are found in the *ortho*-position. From the crystal structure of these compounds it is evident that the *ortho*-substitution accounts for larger steric effects compared to the *para*- and *meta*-substituted structures. Additional intermolecular $\pi\cdots\pi$ and argentophilic interactions are also present in these complexes, possibly hindering the equilibrium shift to the 1,1-form even further. ^{15}N HMBC studies (Figures S6.40-S6.41, Appendix) were also performed for selected compounds **30** and **32**. Both spectra show only a single resonance, originating from the -CH_2 linker, showing a 2JNH correlation to the pyrrole-like nitrogen of the triazole. The respective

^{15}N chemical shifts (referenced to CH_3NO_2) at -155.99 (for **30**) and -154.37 (for **32**) ppm are also consistent with a pyrrole-like nitrogen, suggesting the existence of 1,1-isomer in both compounds.

On the other hand, less clear conclusions may be drawn in regards to the parameters which promote the presence of the 1,2-isomer in the solid state. Synthetic conditions such as the temperature, metal:ligand ratio or crystallization method do not seem to have any noticeable effect. However, a correlation with the solvent choice and polarity during the initial synthesis may be observed, as all 1,1-based compounds were afforded in acetonitrile (μ = 3.92 D), while the use of the slightly less polar acetone (μ = 2.88 D) resulted only in 1,2-based compounds. Interestingly, this pattern is additionally supported by two more compounds synthesized during these experiments, which are not presented in detail due to very weak crystallographic data. Both of these compounds, formulated as $[Ag(\mathbf{L^2})(CF_3CF_2CO_2)]$ and $[Ag_2(\mathbf{L^2})_3](ClO_4)_2$ (Figures S6.2-S6.3, Appendix), were synthesized in acetonitrile and contain only the 1,1-isomer of the ligand. A comparison between the latter complex and compound $[Ag(\mathbf{L^{2T}})(ClO_4)(Me_2CO)]$ (**29**) show that the choice of solvent could indeed play an important role. Moreover, the $[Ag_2(\mathbf{L^2})_3]\cdot(NO_3)_2\cdot(MeCN)$ compound[151] was also prepared through recrystallization in acetonitrile. However, this phenomenon is only consistent for Ag^I complexes, as several Cu^{II} and Co^{II} compounds presented in previous Chapters did not exhibit similar behaviour. As such, more studies are required to fully comprehend this effect.

6.2.4. Catalytic Studies in the A^3 Coupling

6.2.4.1. Benchmarking and Optimisation

Initial investigations for the catalytic potential of **27-35** involved the employment of compounds in the multicomponent A^3 coupling of benzaldehyde, pyrrolidine and phenylacetylene, performing an extensive screening of all related parameters as seen in Table 6.2. All compounds proved to be ineffective in solvents such as water, DMF and DMSO (Table 6.2, entries 7 – 9, 23 – 25), however they provided low yields in the homogeneous catalysis of the reaction when other common organic solvents were used such as Toluene, THF, CH_3CN, CH_2Cl_2 and $CHCl_3$ (Table 6.2, entries 6, 10 – 13, 22, 26 – 29). In general, the highest yields were achieved through the use of polar alcoholic solvents and especially with

the environmentally friendly solvent[249] 2-propanol (iPrOH) when the reaction mixture was heated to 90°C for 12 hours. All compounds were found to catalyse the reaction under these conditions (Table 6.2, entries 4-5, 14-15, 19-21, 32-36); amongst these, the 1D CP **30** afforded the corresponding product at excellent yields of 94%, with very low loadings of 0.5 mol% used (TON = 188 and TOF = 15.7 hr^{-1}, calculated with the ratio of product mol/catalyst mol).

Table 6.2. Optimization of the conditions for the synthesis of propargylamines.

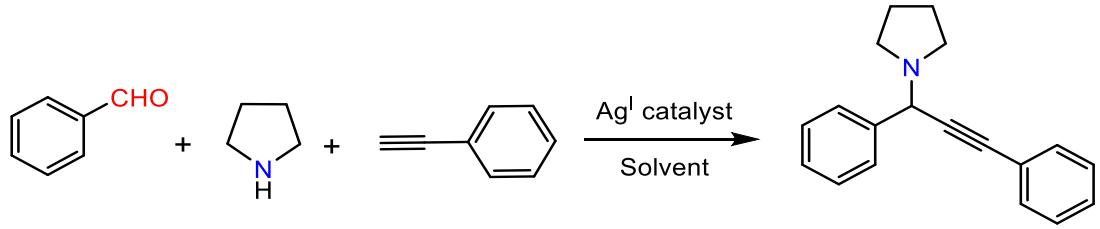

Entry	Catalyst (mol%)[a]	Solvent	Yield (%)[b]	TON	TOF (hr^{-1})
1	**27** (2)	MeOH	trace	-	-
2	**27** (2)	EtOH	18	9	0.8
3	**27** (2)	iPrOH	28	14	1.2
4	**27** (2)	iPrOH[c]	85	43	3.6
5	**27** (0.5)	iPrOH[c]	83	166	13.8
6	**27** (2)	Toluene	14	7	0.6
7	**27** (2)	H_2O	NR[d]	-	-
8	**27** (2)	DMF	NR[d]	-	-
9	**27** (2)	DMSO	NR[d]	-	-
10	**27** (2)	THF	10	5	0.4
11	**27** (2)	MeCN	13	7	0.6
12	**27** (2)	CH_2Cl_2	11	6	0.5
13	**27** (2)	$CHCl_3$	14	7	0.6
14	**28** (0.5)	iPrOH[c]	81	162	13.5
15	**29** (0.5)	iPrOH[c]	88	176	14.7
16	**30** (2)	MeOH	<10	-	-

17	**30** (2)	EtOH	16	8	0.7
18	**30** (2)	iPrOH	29	15	1.3
19	**30** (2)	iPrOH[c]	95	48	4
20	**30** (1)	iPrOH[c]	94	94	7.8
21	**30** (0.5)	iPrOH[c]	94	188	15.7
22	**30** (2)	Toluene	18	9	0.8
23	**30** (2)	H_2O	NR[d]	-	-
24	**30** (2)	DMF	NR[d]	-	-
25	**30** (2)	DMSO	NR[d]	-	-
26	**30** (2)	THF	<10	-	-
27	**30** (2)	MeCN	11	6	0.5
28	**30** (2)	CH_2Cl_2	15	8	0.7
29	**30** (2)	$CHCl_3$	16	8	0.7
30	**30** (0.5)[e]	iPrOH[c]	63	126	21
31	**30** (0.5)[f]	iPrOH[c]	94	188	7.8
32	**31** (0.5)	iPrOH[c]	70	140	11.7
33	**32** (0.5)	iPrOH[c]	81	162	13.5
34	**33** (0.5)	iPrOH[c]	66	132	11
35	**34** (0.5)	iPrOH[c]	71	142	11.8
36	**35** (0.5)	iPrOH[c]	74	148	12.3
37	No catalyst	iPrOH[c]	NR[d]	-	-

[a] Reaction conditions: benzaldehyde (25 μL, 0.25 mmol), pyrrolidine (22 μL, 0.275 mmol), phenylacetylene (43 μL, 0.4 mmol), catalyst (mol% based on aldehyde amount), solvent (3 ml), 12 hr stirring, air. [b] Relative yields based on ^{1}H NMR analysis from the integration of the corresponding proton shifts. [c] T = 90^{o}C. [d] No reaction. [e] under 6 hrs stirring. [f] under 24 hrs stirring.

To further evaluate the efficiency of **30**, its performance was compared to the ones of all reported Ag^I sources that have been tested in the model reaction within the literature. This

search included simple salts, coordination polymers and coordination compounds (Table 6.3). Notably, **30** emerges as a highly advantageous catalyst in many aspects, due to the resulting excellent yield and TOF value which outperforms many of the reported Ag sources (Table 6.3, entries 1-8). On the other hand, the stirring times in the case of **30** appear to be longer than those usually reported[230,231,320,325,328,358]. Despite this, the conditions of the proposed reaction system appear to be less harsh or tedious (e.g. no N_2 atmosphere or environmentally unfriendly solvent is needed). Various Ag^I salts were also tested under the same conditions (Table 6.3, entries 10-15) showing slightly inferior performance, further indicating the superiority of **30**.

Table 6.3. Comparison of the performances of all reported Ag^I sources for the A^3 coupling of benzaldehyde, pyrrolidine and phenylacetylene.

Entry	Catalyst (mol%)	Conditions	Yield (%)	TON	TOF (hr^{-1})	Reference
1	AgI (3)	H_2O, 100°C, N_2, 2 h	95	31.7	15.8	[230]
2	(NHC)Ag(OAc) (3)	MeOH, 25°C, 3 h, air	88	29.3	9.8	[358]
3	[Ag(bpa)(NO_3)CH_3CN] (2)	DCM, 5h, 60°C, N_2	96	48	9.6	[325]
4	[Ag(bpa)NO_3] (0.5)	DCM, 5h, 60°C, N_2	95	190	38	[325]
5	[Ag(psmb)NO_3] (2)	DMSO, 3h, 60°C, air	93	46.5	15.5	[320]
6	[Ag(psemb)NO_3] (2)	DMSO, 3h, 60°C, air	94	47	15.7	[320]
7	[Ag(Pc-L)]·OTf^- (3)	Toluene, 150°C, mW, 10 min	96	32	192	[328]
8	[Ag(bdob)(NO_3)] (1.9)	$CHCl_3$, 12 h, air, rt	68	35.8	3.0	[231]
9	**30** (0.5)	iPrOH, 90°C, air, 12 hr	94	188	15.7	This work
10	$AgClO_4$ (0.5)	iPrOH, 90°C, air, 12 hr	88	176	14.7	This work
11	AgOTf (0.5)	iPrOH, 90°C, air, 12 hr	84	168	14	This work
12	$AgNO_3$ (0.5)	iPrOH, 90°C, air, 12 hr	91	182	15.2	This work
13	$AgCF_3CO_2$ (0.5)	iPrOH, 90°C, air, 12 hr	89	178	14.8	This work
14	$AgBF_4$ (0.5)	iPrOH, 90°C, air, 12 hr	85	170	14.2	This work
15	$AgCF_3CF_2CO_2$ (0.5)	iPrOH, 90°C, air, 12 hr	83	166	13.8	This work

bpa = 4,5-bis(phenylthiomethyl)acridine, psmb = 1-phenylsulfanylmethyl-1*H*-benzotriazole, psemb = 1-phenylselenylmethyl-1*H*-benzotriazole, Pc-L = 6-(Naphthalen-1-ylmethyl)-3,9-ditosyl-3,6,9,15-tetraazabicyclo[9,3,1]pentadeca-1(15),11,13-triene, bdob = 1,4-bis(4,5-dihydro-2-oxazolyl)benzene.

6.2.4.2. Scope of Reaction

Having determined the optimal efficiency, various aldehydes, amines and alkynes were coupled under the proposed conditions in order to explore the substrate scope of the system. The results are shown in Scheme 6.3. The effect of the aldehyde was first investigated, retaining pyrrolidine and phenylacetylene as the model substrates. In all cases the corresponding A^3 products **C6P1**-**C6P9** were formed in good to high isolated yields, however the substituted aromatic aldehydes show lower reactivity, allowing for more moderate (64-89%) yields and sometimes requiring higher catalyst loading. In contrast, saturated aliphatic aldehydes display excellent reactivity and provide very high (98-99%) yields, irrespective of whether the tested substrate is cyclic or linear. Having this in mind, amine screening proceeded by employing cyclohexylcarboxaldehyde and phenylacetylene as the remaining two model substrates. These tests showed that the proposed reaction system is ideal for secondary amines, as the resulting products are afforded in excellent yields of 93 to 99% (**C6P9**-**C6P15**). There are seemingly no restrictions in the choice of secondary amine, as similar results were obtained for cyclic or linear aliphatic and aromatic substrates. However, this behaviour seems to be limited as no reaction was observed when primary amines were used (entries **C6P16** and **C6P17**). Finally, in regards to the alkyne selection, the use of either phenylacetylene or 1-hexyne resulted to the corresponding propargylamines in excellent yields, **C6P9** and **C6P18** in 99% and 98%, respectively.

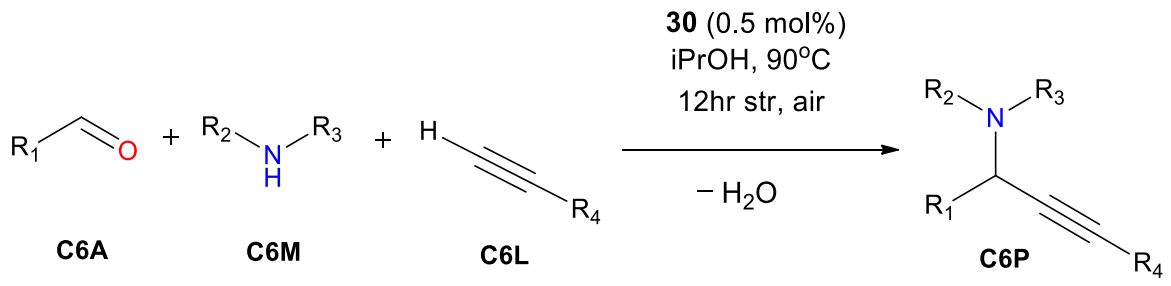

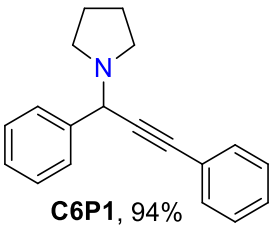

C6P1, 94%

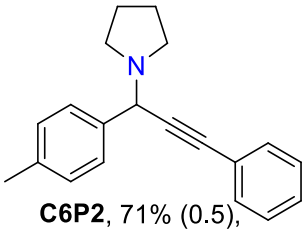

C6P2, 71% (0.5), 89% (1)

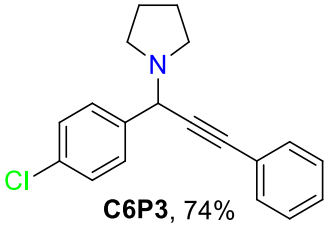

C6P3, 74%

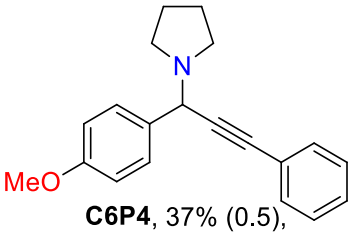

C6P4, 37% (0.5), 64% (1)

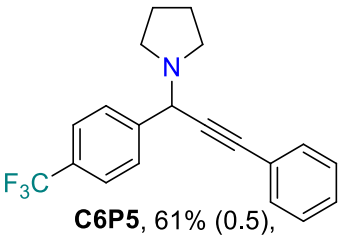

C6P5, 61% (0.5), 86% (1)

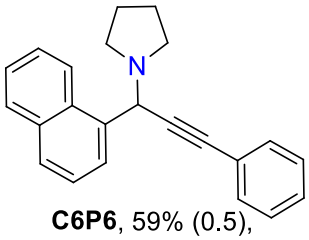

C6P6, 59% (0.5), 83% (1)

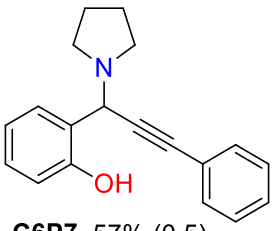

C6P7, 57% (0.5), 80% (1)

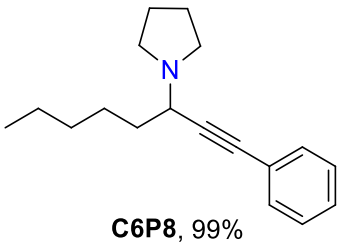

C6P8, 99%

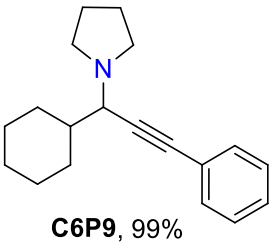

C6P9, 99%

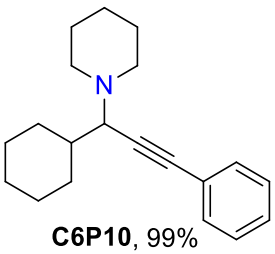

C6P10, 99%

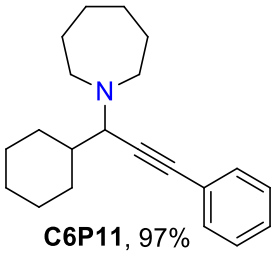

C6P11, 97%

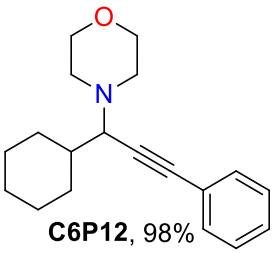

C6P12, 98%

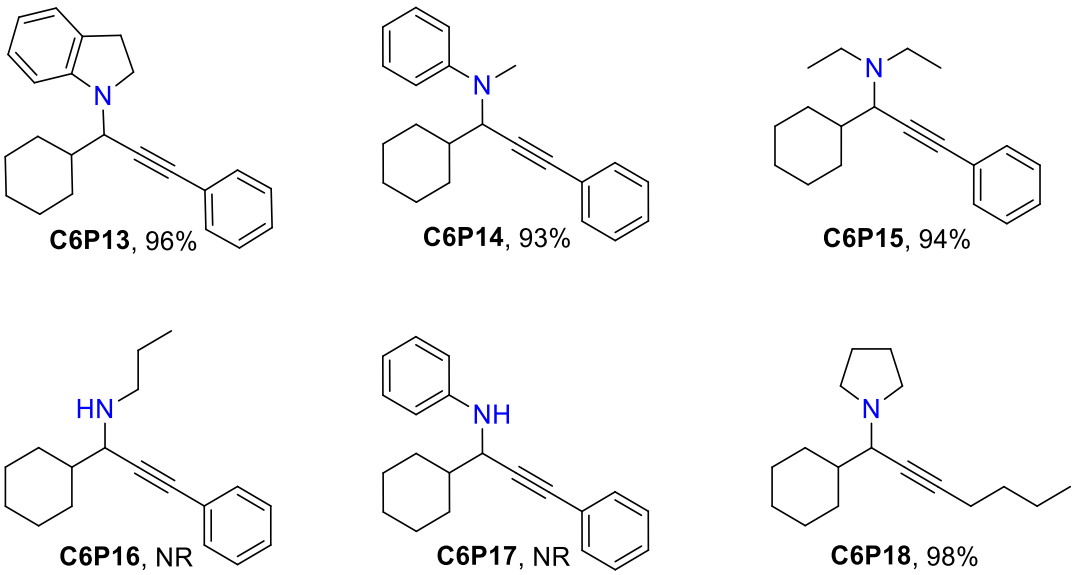

Scheme 6.3. Catalytic activity of **30** in the A^3 coupling between various aldehydes, amines and alkynes towards propargylamine synthesis.

6.2.4.3. Mechanistic Insights

A possible mechanism for this multicomponent coupling on the basis of many reported proposals (including the findings in Chapter 4) is presented in Scheme 6.4. It involves the activation of the alkyne by the silver catalyst to form a metal-acetylide π-complex intermediate. Concurrently, the addition of aldehyde and amine results to the generation of an iminium ion *in situ*; the hydroxyl anions produced during the formation of this species might also assist in the abstraction of the acetylenic proton. In the last step of the catalytic cycle the Ag^I-acetylide is added to this iminium ion to produce the corresponding propargylamine derivative and water, as the catalyst is regenerated. It is envisioned that the formation of the metal-acetylide intermediate could also be influenced by the coordination and geometric characteristics of the catalytic precursors; both compounds **29** and **30**, which resulted in the highest yields in the control experiments, possess a trigonal $\{N_2X\}$ environment (CHN and TGA studies show that all other coordinating solvents contained are removed from the frameworks at slightly above room temperature) that provides adequate space and possibly promotes the coordination of the alkyne. The helix-like chain in **30**, owed to the flexibility of the $–CH_2$ linkers which leads to almost parallel conformation of the benzotriazole planes, accounts for further space between the Ag^I centres, with the Ag-Ag

distance measured at 10.3143(9) Å, the largest between these two complexes. It is also worth noting that the dimeric core compounds (**31**, **33** and **35**) of the study resulted in lower yields in all cases. It can be therefore suggested that the use of polymeric precursors leads to the formation of the most catalytically active species and is essential for optimal efficiency in the reaction.

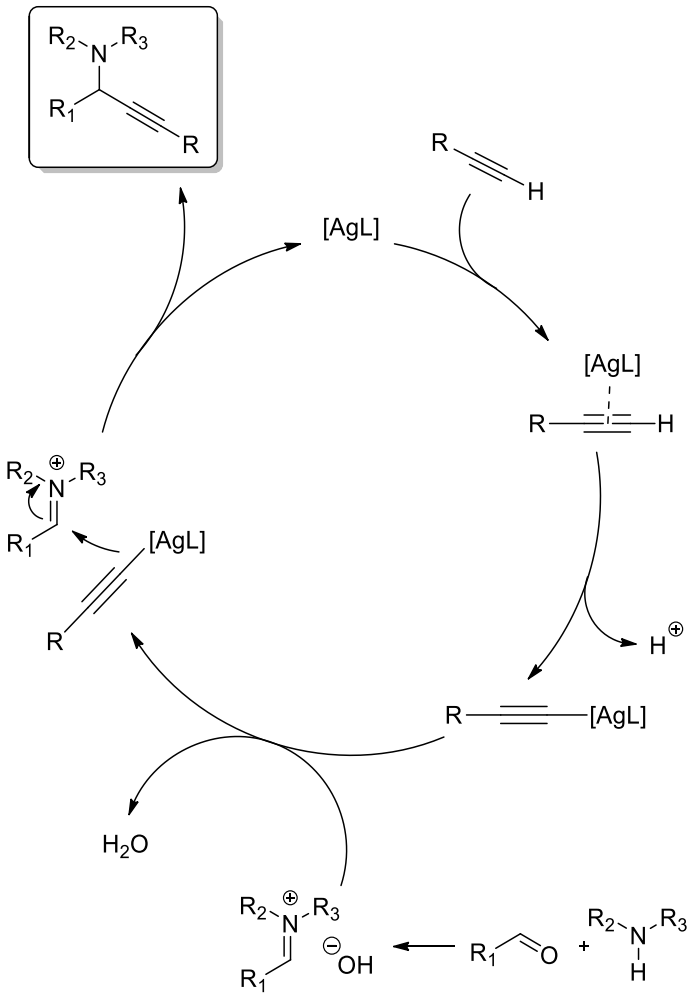

Scheme 6.4. A plausible mechanism of the A^3 coupling catalysed by **30**.

6.2.5. Catalytic Studies in the Hydration of Alkynes

6.2.5.1. Benchmarking and Optimisation

The selective hydration of alkynes is an important transformation in organic chemistry. When Markovnikov's rule is followed, the reaction leads to the formation of ketones, which are very important due to their abundance in natural products and their extensive use as building

blocks in organic synthesis. For the initial experiments, **30** was used towards the hydration of phenylacetylene in various solvent/water systems in a 10/1 ratio. The outcomes of these screenings are shown in Table 6.4. Notably, this procedure selectively affords the resulting acetophenone (**C6K1**) in an excellent 93% yield, when MeOH/H_2O is used as the solvent system, under 90°C for 24 hours and 3 mol% catalyst loading, with TON = 31.0 and TOF = 1.32 hr^{-1} (Table 6.4, entry 3). The presence of alcoholic media and temperature appears to be essential for the system (Table 6.4, entries 3, 5 and 8), as no product was afforded when the reaction took place at room temperature or in other solvents such as CH_3CN and EtOAc (Table 6.4, entries 6 and 7). The other catalytic compounds **27**-**29** and **31**-**35** of this study were also examined in the reaction (Table 6.4, entries 9-16), providing lower yields. Compound **29** shows the best catalytic activity compared to the others, catalysing the reaction in an excellent 86% yield. This result further supports the above suggestions that the coordination characteristics of **29** and **30** promote the formation of the silver-acetylide intermediate. Interestingly, none of the dimeric compounds of the study afforded the corresponding ketone, as the only remaining compounds that promoted the reaction were the 2D CPs **27**, **28** and **34** with moderate to good yields (Table 6.4, entries 9, 10 and 15 respectively).

Table 6.4. Optimization experiments for the hydration of phenylacetylene to acetophenone.

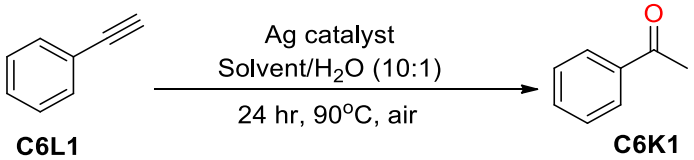

Entry	Catalyst (mol%)	Solvent	Yield(%)[a, b]	TON	TOF (hr^{-1})
1	**30** (0.5)	MeOH	66	22.0	0.92
2	**30** (1)	MeOH	74	24.7	1.03
3	**30** (3)	MeOH	93	31.0	1.32
4	**30** (3)	MeOH	NR[c,d]	-	-
5	**30** (3)	EtOH	77	25.7	1.07
6	**30** (3)	MeCN	NR[c]	-	-
7	**30** (3)	EtOAc	NR[c]	-	-

8	**30** (3)	iPrOH	65	21.7	0.90
9	**27** (3)	MeOH	44	14.7	0.61
10	**28** (3)	MeOH	60	20.0	0.83
11	**29** (3)	MeOH	86	28.7	1.20
12	**31** (3)	MeOH	NR[c]	-	-
13	**32** (3)	MeOH	NR[c]	-	-
14	**33** (3)	MeOH	NR[c]	-	-
15	**34** (3)	MeOH	66	22.0	0.92
16	**35** (3)	MeOH	NR[c]	-	-

[a] Relative yields based on ^{1}H NMR analysis from the integration of the corresponding proton shifts. [b] Reaction conditions: phenylacetylene (121 μL, 1 mmol), catalyst, solvent (1.5 ml), H_2O (150 μl), 90°C, 24 hr stirring, air. [c] No reaction. [d] At room temperature.

6.2.5.2. Scope of Reaction

The hydration of other terminal alkynes using **30** was also tested successfully (Scheme 6.5) under the optimal conditions. The presence of a methoxy- substituent in the initial alkyne does not appear to affect the reaction as the corresponding 4-methoxyacetophenone (**C6K2**) was produced in 94% yield. Furthermore, to evaluate the catalytic ability of this system with aliphatic alkynes the linear 1-hexyne was employed under the same conditions, forming the corresponding ketone in good conversions (**C6K3**, in 66% yield).

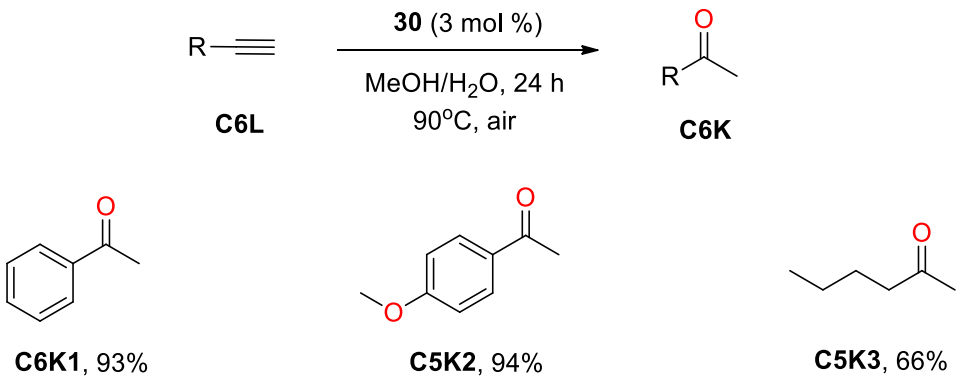

Scheme 6.5. Catalytic activity of **30** in the hydration of alkynes to ketones.

6.2.5.3. Mechanistic Insights

It is envisioned that the mechanism proceeds in a commonly proposed pathway (Scheme 6.6) in which the silver-acetylide species (**A**) is formed in the first step, possibly promoted by the coordination environment of the catalyst as well as the use of the protic solvent methanol. It is highly likely, by analogy with Belanzoni and Zuccaccia's mechanistic studies on gold catalyzed hydration reactions[359], that the ligand is facilitating the reaction through electrostatic interaction between water and the ligand(s) *via* hydrogen bonding to one of the Brønsted-basic nitrogens. This chelation directs H_2O during the addition reaction to generate the enol intermediate (**B**) and the ligand can subsequently assist with the proton transfer from the newly formed oxonium. **B** then undergoes keto–enol tautomerism to produce (**C**) which subsequently undergoes proto-demetalation to generate the resulting ketone (**D**). Importantly, the best results are of great eco-friendly impact, with low catalyst loading and acid-free conditions, and requiring environmentally-benign methanol as solvent.

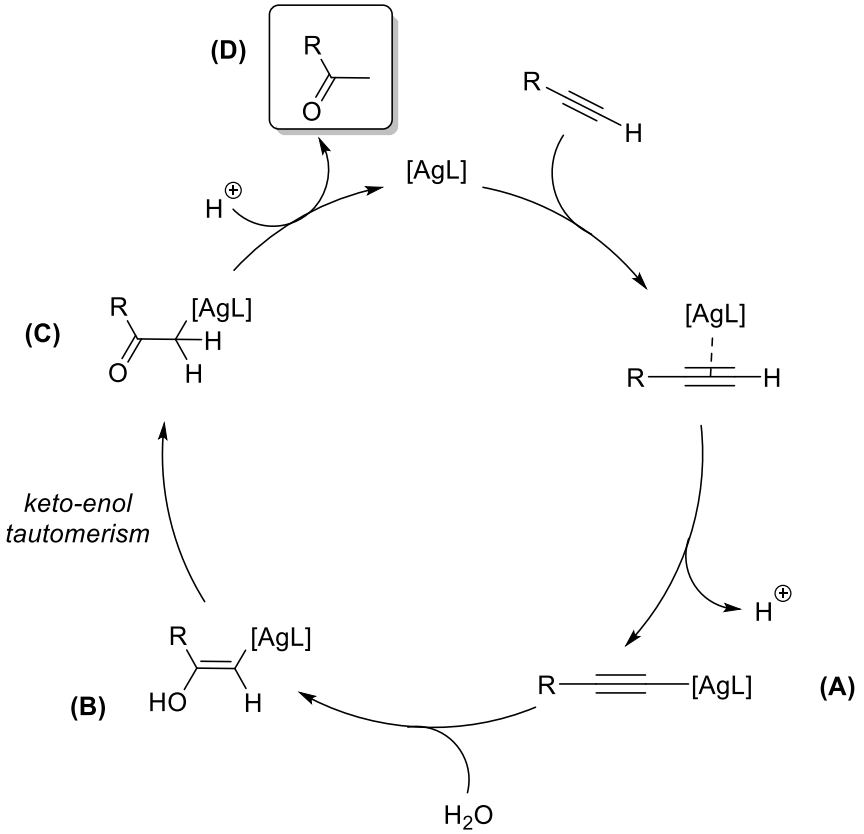

Scheme 6.6. A plausible mechanism of the hydration of alkynes catalysed by **30**.

6.3. Conclusion

In this study, attempts have been made to combine the rich chemistry and coordination capabilities of Ag^{I} ions with a series of semi-rigid benzotriazole-based ligands **L^1-L^3**. The resulting compounds **27-35** exhibit a large structural diversity that includes a range of 0D dimers and 1D / 2D coordination polymers with interesting topological features and architectures as well as peculiar isomerism effects observed. An important factor for the variety in these coordination networks is owed to the flexibility of the ligands, which accounts for multiple coordination modes. The complexes have also been investigated for their potential catalytic applications. Due to its structural nature and coordination characteristics, compound **30** serves as homogeneous catalyst in A^3 coupling and alkyne hydration reactions, providing the respective propargylamines and ketones in generally excellent yields (up to 99 and 93% in each case) that are comparable or superior to the ones of other reported Ag^{I}-based catalysts. Both proposed reaction schemes include easy synthetic conditions and avoid the use of inert atmosphere or environmentally harsh solvents. Furthermore, the superior alkynophilicity of Ag^{I} compared to Cu^{II} makes **30** a favourable option against the relevant Cu^{II}-based coordination polymers with reported catalytic performance, as high yields are achieved with much lower catalyst loadings (0.5 mol% compared to 2 mol%). Encouraged by these results, future work will focus on using this structural information to expand the scope to additional *N*-containing flexible ligands with Ag^{I} sources and tune their coordination environment to optimize their application potential.

Chapter 7: Conclusions and Future Work

7.1. Concluding Remarks

The purpose of this Chapter is to summarize the results presented in Chapters 2-6 and contextualize them in regards to the aims of the thesis. The impact and limitations of this work, as well as future potential directions will also be discussed to bring the dissertation to a conclusion.

Summary

The main target of this thesis as outlined in Chapter 1 was the development of a system that generates low-dimensional CPs in order to study their potential properties in magnetism and catalysis. Most results were produced using the benzotriazole-based semi-rigid ligands **L^{1}-L^{3}**; *N*-based ligands **L^{4}-L^{8}**, based on other heterocyclic units, were also employed to yield the corresponding isostructural compounds, providing very useful structural information and allowing for the optimization of the system's catalytic behaviour. In total, 35 main compounds were synthesized and characterized in detail across Chapters 2-6. All compounds presented low to no dimensionality, ranging from dimers and tetramers, to 1D and 2D CPs.

Chapter 2 reported the initial efforts of determining the potential of **L^{1}-L^{3}** in such purposes using Co^{II} sources and served as an introduction to the ligands' coordination capabilities. The ten novel compounds presented (**1-10**) revealed the diversity of this system, showing that manipulation of the resulting product and its dimensionality is possible through careful ratio (e.g. compounds **7** - **9**) or temperature (e.g. **1** and **2**, **3** and **4**) adjustments. These findings demonstrated the suitability of this ligand system, especially **L^{2}** and **L^{3}**, for the generation of low-dimensional CPs in high yields and through easy synthetic methods. Apart from these structural studies, the magnetic properties of selected compounds **4**, **7** and **9**, show considerable differences despite only minor variations in the coordination environment and the metal geometry.

Chapters 3-5 embarked on the development of a system of catalysts mainly based on the *ortho*-substituted **L^{3}** linker and Cu^{II} salts. This system was then optimized and evaluated from

an inorganic chemistry approach. Several new compounds (**11**-**26**) were synthesized and characterized after extensive investigations and fine tuning. It was established that the use of $\mathbf{L^3}$ with Cu^{II} sources that contain traditionally non-coordinating anions generates isoskeletal 1D CPs with a ribbon-like framework (**11**, **17**, **18**) in high yields, using an easy two step method and room temperature conditions. These compounds have a general formula of $[Cu^{II}(\mathbf{L^3})_2(X)_2]$ (where X = anion or solvent) and exhibit octahedral Cu^{II} centres that contain a symmetrical $\{N_4\}$ square plane with the nitrogen atoms belonging to $\mathbf{L^3}$ molecules. Additionally, Cu^{II} in these compounds can be quasireversibly reduced to Cu^{I}. Owed to these characteristics, **11** was found to homogeneously catalyse the one-pot synthesis of symmetrical 1,4-dihydropyridines using a previously unreported synthetic method. Good yields (up to 68%) of the resulting products are afforded in a protocol that employs mild conditions (methanol, reflux, air atmosphere) and low (2 mol%) catalyst loadings. Further fine-tuning of the catalyst led to compound **18**, which was found to be an excellent homogeneous catalytic precursor for the multicomponent A^3 coupling and the azide-alkyne "click" reaction to produce propargylamines and 1,2,3-triazoles respectively. Both reactions take place in alcoholic media do not require harsh conditions or tedious work-ups and generate excellent yields of the resulting products (almost quantitative in both reaction schemes). Additional diagnostic experiments using ligands $\mathbf{L^4}$-$\mathbf{L^8}$ showcased the superiority of the benzotriazole-based polymeric precursors in regards to the catalytic efficacy, while providing useful mechanistic evidences for the functionality of the system.

Finally, Chapter 6 showcased attempts to explore the coordination potential of $\mathbf{L^1}$-$\mathbf{L^3}$ combined with the diverse chemistry of Ag^{I} ions. The nine resulting compounds (**27**-**35**) show a large structural variety with diverse motifs, ligand conformations and coordination networks. An isomerism effect ($\mathbf{L^{1T}}$-$\mathbf{L^{3T}}$) is also observed in the benzotriazole unit when in solid state, however investigations showed that the 1,1-form is generally dominant in solution. The homogeneous catalytic activity of all compounds was also examined in the A^3 coupling reaction and the hydration of alkynes. In both of these transformations, compound **30** was found to be the best catalytic precursor, providing excellent yields (up to 99 and 93% in each case) under relatively mild conditions and using low loadings (0.5 and 3 mol%).

Synthetic Aspects

The development of a system with ease of chemistry was an especially important target in this thesis. It is felt that the efforts towards this direction were very successful, as all 35 compounds were afforded using straightforward methods in air atmosphere and under non-harsh conditions. The crystallization techniques involved liquid and vapour diffusion, slow evaporation or storage of the sample under room temperature, as well as heating of the sample; the harshest synthetic method involved solvothermal treatment of the mixture up to only 95 ^{o}C for less than a day. In general, the compounds are easily reproducible in a range of metal:ligand ratios (from 2:1 to 1:2) and bulk materials are afforded in good to excellent yields.

Main ligands **L^{1}-L^{3}** appear to be ideal for the generation of low-dimensional materials: during experiments in this work, multiple synthetic conditions using cobalt, copper or silver sources were tested, however the synthesis of 3D compounds could not be performed. Nevertheless, the formation of such networks under harsh solvothermal conditions or by using different solvents and/or bridging anions cannot be excluded, considering that there do not seem to be any steric effects from preventing this. The use of a secondary ligand could also be another method to induce dimensionality; the initial compounds, especially the ones forming dimeric and tetrameric 0D frameworks, could be then used as building blocks similarly to the examples mentioned in Chapter 1. Nevertheless, since this thesis only investigated the potential of **L^{1}-L^{3}** as primary ligands, the resulting complexes clearly show that certain ligand conformations and topologies are promoted under most applied conditions, leading to 0D, 1D and, under the presence of bridging anions, 2D structures. In addition, these architectures are further stabilized in some cases by various weak interactions.

Additional *N*-containing ligands **L^{4}-L^{8}** were also tested for comparison and diagnostic purposes. These linkers maintain the *ortho*-substitution of **L^{3}** and allow for studying the influence of phenomena such as second coordination sphere and steric effects, or enforce the generation of analogous non-polymeric structures. The results showed that the added steric effects in **L^{4}** and **L^{5}** promote the synthesis of dimeric structures which are unstable in solution (as shown by UV-Vis and CV studies), making these ligands unsuitable for generation of

stable CPs. On the other hand, ligands **L^6**-**L^7** behave much more similar to **L^3**, providing similar 1D polymeric frameworks. However, due to second coordination sphere effect these compounds showed inferior activity compared to the benzotriazole analogue. In addition, **L^6** and **L^7** have been extensively used in the literature with cobalt, copper and silver sources and therefore do not show much novelty. For these reasons, their use was limited to tuning and optimization purposes.

The above remarks confirm that **L^1**-**L^3** were an excellent choice for the synthesis of the targeted materials for this thesis. Despite this, the potential isomerization phenomena make their behaviour more unpredictable; this could also explain why bis(benzotriazole) ligands have been seldom used in the literature compared to their imidazole/benzimidazole counterparts. Chapter 6 detailed initial efforts to understand these effects during the synthesis of coordination compounds, however more studies should ensue to provide more accurate conclusions.

Characterisation

A range of characterisation techniques were employed to fully determine the nature of the synthesized materials in solid state and in solution. In regards to the solid state methods, large efforts were made to generate crystalline material for all related ligands and compounds wherever that was possible. Apart from establishing purity, this process was essential since the study and optimization of magnetic and catalytic properties of the compounds was often dependant on specific coordination characteristics such as geometry and environment. As a result, the use of single-crystal X-Ray diffraction proved critical in the determination of these features. Other characterisation methods (powder diffraction, elemental analysis and FT-IR) were also used to confirm the structure of the bulk material, while the thermal stability of the compounds was identified through TGA measurements.

Determining the behaviour of the compounds in the solution was a more complex task. The ESI-MS spectra of **1**-**35** displayed several peaks that corresponded to various metal-ligand and metal-ligand-anion fragments. This indicated that the compounds may retain their identity in solution, although more investigations were required to provide conclusive proof,

especially for the coordination polymers that were used in the subsequent catalytic studies. For this reason, EPR and UV-Vis studies on selected Cu^{II} based CPs were additionally performed, providing the required information. On the other hand, the nature of the Ag^{I} compounds was examined through ^{1}H NMR studies, which also allowed for the investigation of the ligand isomerization phenomena. Finally, CV studies were also performed on selected Cu^{II} compounds to determine their suitability as catalysts in reactions that involve redox processes.

Impact and System Limitations

Apart from meeting the aims of this thesis, it is felt that several of the results have notably contributed to the scientific literature. In regards to the originality of the ligand system, the chosen linkers **L^{1}-L^{3}** based on benzotriazole had been largely untested in coordination chemistry up to this point, in contrast to their benzimidazole and imidazole counterparts. As shown in Chapter 1, the existing literature on bis(benzotriazole) ligands only included the use of alkyl chain spacer groups between the benzotriazole units, while the resulting compounds were mostly examined for their structural features. Instead, the current ligand system introduced the semi-rigid -CH_2-C_6H_4-CH_2- backbone which proved to be crucial to the control and manipulation of the resulting compounds, as well as the formation of various weak interactions which stabilized the afforded architectures. In addition, while several studies have focused on the isomerization phenomena of benzotriazole derivatives, this thesis presents the first relevant results in the topic of bis(benzotriazole) molecules. Finally, the novelty factor was also evident for ligands **L^{4}** and **L^{5}**, with compounds **20** and **21** being the first reported examples of using these linkers in coordination chemistry.

The crystal engineering and structural studies in the afforded compounds provided an interesting insight on the capabilities of this system. However, the biggest impact was undoubtedly made during the inspection of their potential properties. The results in Chapter 2 presented a systematic investigation of carefully selected compounds, showcasing the importance of structure dimensionality, coordination environment and metal geometry in the ensuing magnetic properties. This study was also reported in the journal *Crystal Growth and Design*.

The studies detailed in Chapters 3-6 successfully demonstrated the use of various 1D CPs as catalysts in a series of organic transformations; the catalytic system was developed, optimized and evaluated through an "inorganic approach" that involved tuning of several coordination parameters in order to obtain important mechanistic information. It is felt that these results add an extensive amount of novel scientific input in the currently underutilized (as discussed in Chapter 1) field of 1D CPs in catalysis. In addition to the diagnostic research and novel approaches presented in these Chapters, the catalytic results and protocols in each case provide further scientific contribution of importance: Chapter 3 introduces a previously unreported method in the synthesis of 1,4-DHPs, molecules with extensive use in biology and pharmacology, under a protocol that includes low catalyst loadings and non-harsh conditions. Chapter 4 contains the first report of 1D Cu^{II} CPs as catalysts in the A^3 coupling to generate propargylamines in excellent yields. Chapter 5 reports the use of a Cu^{II} 1D polymeric precursor with very good activity in the Cu^{I}-catalysed click reaction; the 1,2,3-triazole products are afforded without the need of a reducing agent and are molecules of great importance in biological applications. Finally, Chapter 6 includes the first case of a Ag^{I} coordination compound used as a catalyst in the hydration of alkynes. It is worth noting that, in all these cases, the catalytic behaviour of the CPs was found to be superior to the one of the relevant metal salts under the same conditions. These studies were also reported in the journals *Advanced Synthesis and Catalysis*, *Inorganic Chemistry*, *Dalton Transactions* and *Crystal Growth and Design*, respectively.

While these results are certainly encouraging, the system presents some notable limitations which will need to be overcome in the future. The isomerization observed in benzotriazole-based ligand systems present additional difficulties in regards to ease of chemistry and determination of behaviour in solution. These phenomena are more extensive in bis(benzotriazole) linkers and created eventual hindrances in the determination of the active species during catalytic studies with copper and silver. Further limitations may also be identified in the catalytic system; while the relevant results in this thesis were very promising, all active CPs required increased temperatures, did not operate under the presence of aqueous media and only showed homogeneous catalytic behaviour.

Nevertheless, it is hoped that the contributions of this thesis will encourage efforts towards a more systematic design and study of low-dimensional materials beyond the realms of structural reports, in order to exploit their unique features and untap their potential in other interesting fields. In particular, the catalytic studies of 1D CPs in this thesis revealed an intriguing system which provided invaluable information while bridging the fields of Inorganic Chemistry, Organic Chemistry and Catalysis. It is therefore felt that this is a research topic that should definitely be more explored in the future.

7.2. Future Work

The following work on CPs with these *N*-containing ligands may be expanded into several directions. Since the magnetic properties of the Co^{II}-based compounds were explored in detail, focus may be instead shifted on their possible catalytic activity. Such efforts could result in the addition of more compounds to the existing library of catalysts, while increasing the scope and knowledge on this system. An important characteristic of the respective Cu^{II} catalysts in Chapters 3-5 was the $\{N_4O_2\}$ octahedral geometry in the metal centres, which contained a symmetrical square plane consisting of ligand nitrogen atoms. Looking back at the results of Chapter 2, it can be observed that such a coordination environment is promoted through the use of cobalt nitrate; notably, the $\mathbf{L^3}$-based complex **10** (Figure 7.1, upper) shows the same 1D framework seen in the main copper catalysts of this work. Preliminary synthetic efforts with the imidazole-based analogue $\mathbf{L^7}$ revealed that the same framework is once again promoted, generating a compound formulated as $[Co(\mathbf{L^7})_2(H_2O)_2]\cdot(NO_3)_2$ (**36**, Figure 7.1, middle). As such, initial future efforts could involve CV voltammetry studies of **10** and **36**, to determine the feasibility of a reversible redox process, and their employment as catalysts in relevant transformations. Other metals could also be employed in a similar fashion and provide the desired coordination characteristics; Mn^{II}-based compound $[Mn(\mathbf{L^3})_2(NO_3)_2]$ (**37**, Figure 7.1, lower), also synthesized during these preliminary efforts, could be another candidate for these purposes.

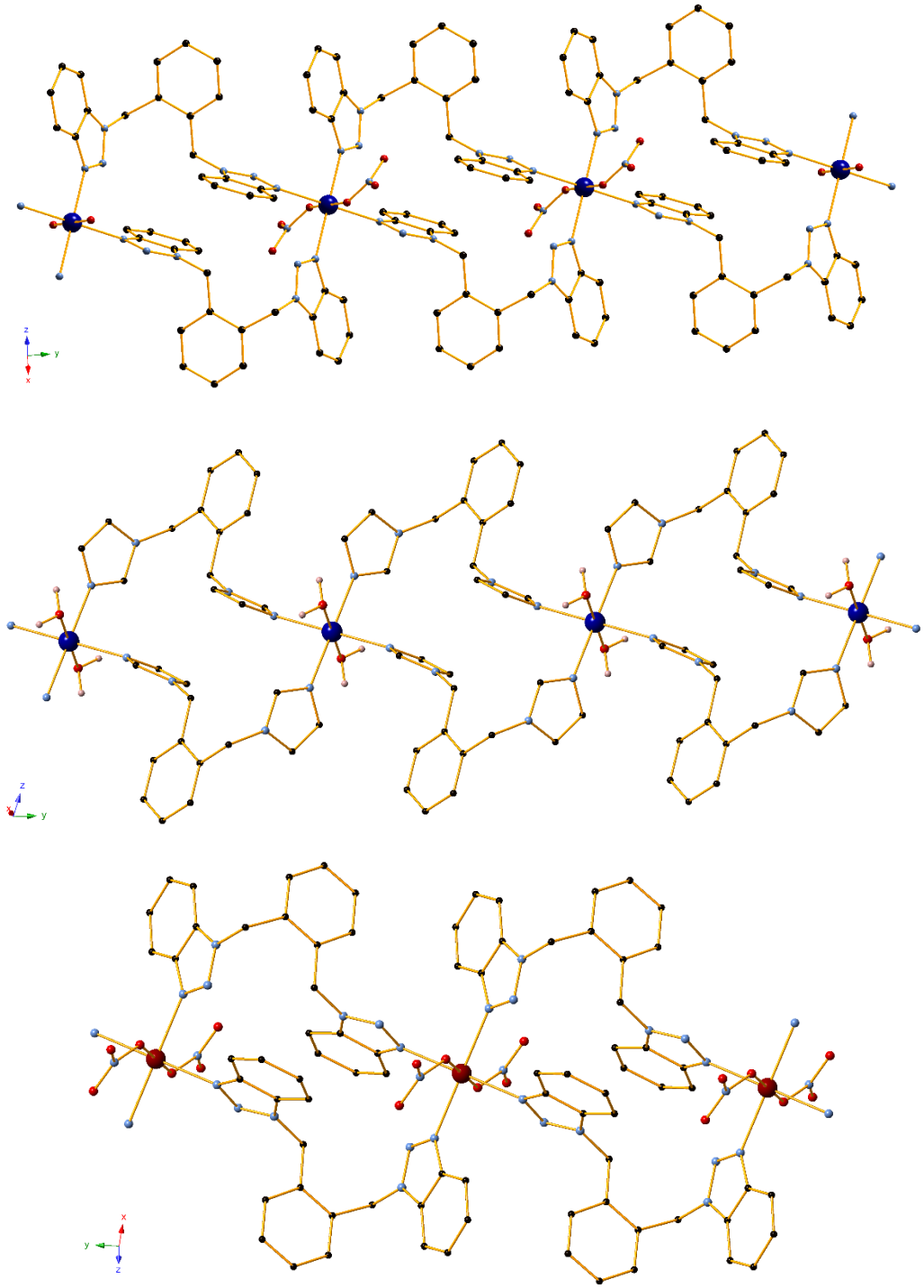

Figure 7.1. The architectures in 1D CPs **10** (upper) **36** (middle) and **37** (lower). Certain anion molecules and H atoms have been omitted for clarity. Colour code: Co (dark blue), Mn (maroon), C (black), H (light pink), N (light blue), O (red).

In regards to the copper catalysts of this study, an important aspect of future research should be the heterogenization of the catalyst, which would allow for its collection and reuse. Such a process would make this library of catalysts much more attractive for industrial purposes. Furthermore, the catalytic activity of these compounds could be tested in additional organic transformations which would broaden the scope of the system and reveal further mechanistic details. C-C coupling reactions that involve the formation of a Cu^{I}-acetylide intermediate could be explored, such as the Sonogashira reaction (Scheme 7.1) or the Glaser homocoupling (Scheme 7.2).

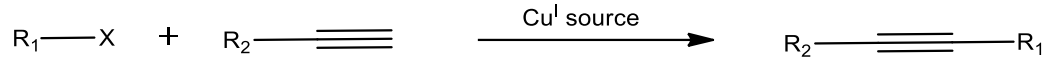

R_1-X: aryl / vinyl halide

Scheme 7.1. A general overview of the Sonogashira coupling reaction.

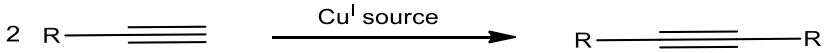

Scheme 7.2. A general overview of the Glaser coupling reaction.

Another direction where future efforts could be concentrated would be the introduction of enantioselectivity into the system. The behaviour of Cu^{II} compound **18** showed that the axial components (triflate oxygen atoms) of the octahedral centres may be easily replaced; similar observations were made for the Ag^{I} compound **30**. Therefore, an enantioselective catalyst may be developed in the solid state or *in situ* with the addition of various aminoacids such as L-Alanine or L-Tyrosine.

Finally, upcoming investigations could also expand on the *N*-based ligand design (Scheme 7.3). Having determined the novelty and superiority of bis(benzotriazole) ligands over analogous linkers with other heterocyclic molecules, future research could further explore the effect of the backbone moiety. Various units, such as phthaloyl (**L**[12]), pyridine (**L**[13]), 2,6-dimethylpyridine (**L**[14]), 4,4-biphenyl (**L**[15]), 9,10-dimethylanthracene (**L**[16]), 1,3,5-triethyl-2,4,6-trimethylbenzene (**L**[17]) could drastically affect the resulting coordination compounds through parameters such as steric effects, potential interactions or additional coordination

sites. In turn, this could lead to entirely different behaviour and properties. Additionally, a more systematic study on the topic of benzotriazole-based ligands could also involve molecules not used in this thesis, such as benzotriazole-5-carboxylic acid, 5-chlorobenzotriazole or the simpler 1,2,4-triazole (example ligands **L^{9}-L^{11}**)

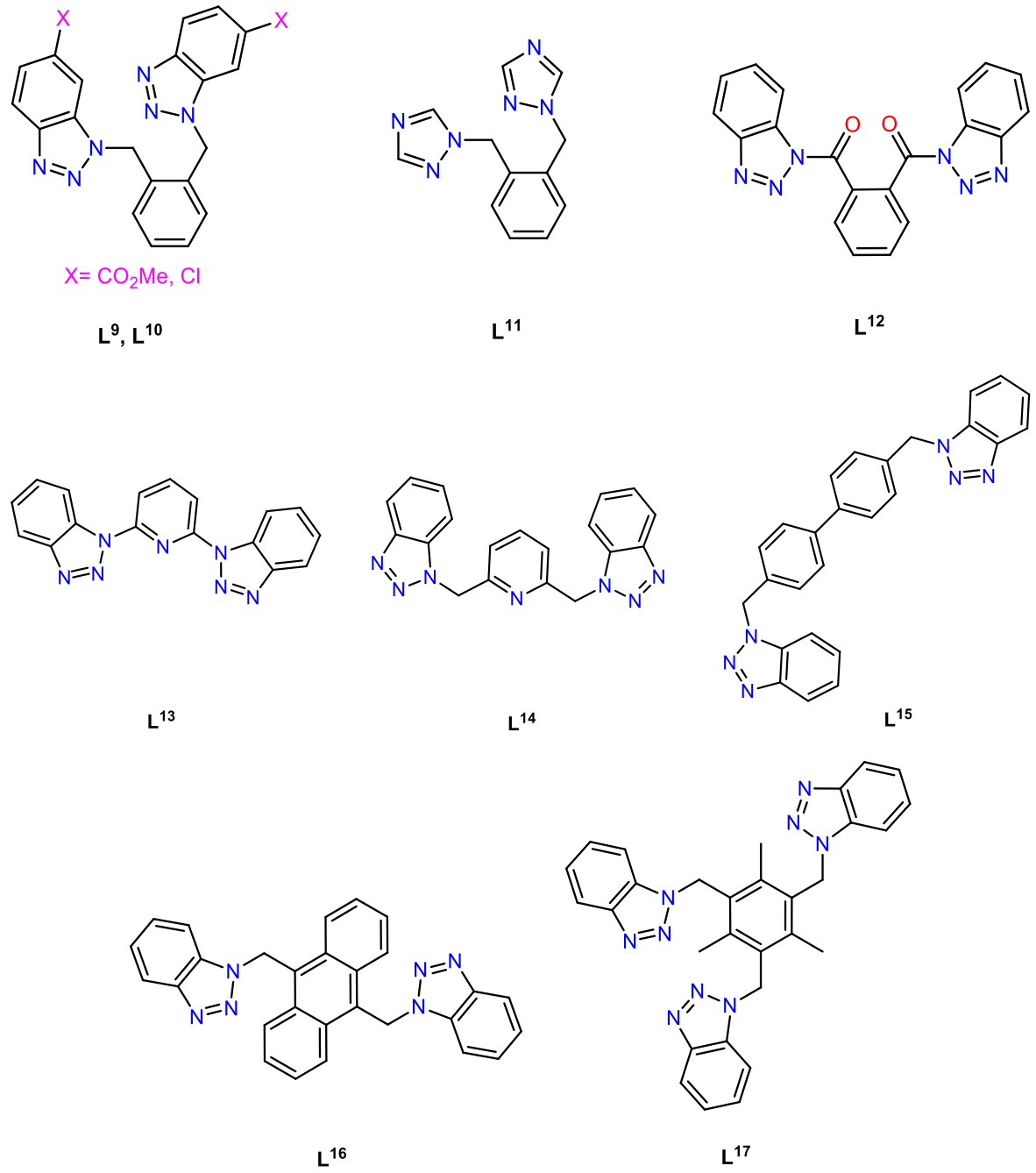

Scheme 7.3. Potential *N*-containing ligands to expand the scope of the current system.

Chapter 8: Experimental and Synthetic Details

8.1. General Methods

Materials

Chemicals (reagent grade) were purchased from Sigma Aldrich, Acros Organics and Alfa Aesar. All experiments were performed under aerobic conditions using materials and solvents as received. Unless stated in their chemical formula, the metal salts used were anhydrous. *Safety notes*: Perchlorate salts and azides are potentially explosive; such compounds should be used in small quantities and handled with caution using the appropriate protection measures at all times.

Instrumentation

FT-IR. IR spectra of the samples were recorded over the range of 4000-650 or 600 cm^{-1} on a Perkin Elmer Spectrum One FT-IR spectrometer fitted with a UATR polarization accessory.

ESI-MS. ESI-MS was performed on a VG Autospec Fissions instrument (EI at 70 eV).

NMR. NMR spectra were measured on a Varian VNMRS solution-state spectrometer (at 400, 500 or 600 MHz) at 30°C using residual isotopic solvent (DMSO-d_5, δ_H= 2.50 ppm or $CDCl_3$, δ_H= 7.26 ppm) as internal reference. Chemical shifts are quoted in parts per million (ppm). Coupling constants (J) are recorded in Hertz (Hz).

TGA. TGA analysis was performed on a TA Instruments Q-50 model (TA, Surrey, UK) under nitrogen and at a scan rate of 10 °C/min.

Powder diffraction. X-ray powder diffraction patterns were recorded at the University of Cyprus.

UV-Vis. UV-Vis measurements were performed on a Thermo Scientific Evolution 300 UV-Vis Spectrophotometer as indicated with quartz cuvettes and the collected data were processed using the Vision Pro software.

Cyclic Voltammetry. *Chapter 4:* Cyclic voltammetry studies were performed using a BASi-Epsilon potentiostat under computer control. IR drop was compensated using the feedback method. Cyclic voltammetry experiments were performed using a three-electrode configuration with glassy carbon disc (7.0 mm^2) as the working electrode, a Pt wire as the

counter electrode and Ag wire as the pseudoreference electrode. Sample solutions were prepared by dissolving the analyte (ca. 5 mM) in DMSO (1 ml) followed by addition of 0.05 M of the supporting electrolyte [$^{n}Bu_4N$][PF_6]. The reported half potentials are referenced to the $FeCp_2^{+/0}$ redox couple, which was measured by adding ferrocene (ca. 1 mg) to the sample solution.

Chapter 5: The cyclic voltammograms of the Cu^{II} complexes were obtained by means of a Metrohm VA 746 Trace Analyzer equipped with a 747 VA Stand driven by a common PC. All the measurements were carried out in DMF and DMSO (0.10 M TBAP was used as the supporting electrolyte). Argon gas was bubbled through the complex solutions again to ensure the absence of oxygen. In each case, the voltammogram of the ligand was registered and no peaks were found. The systems were analysed at 25°C with a three electrode assembly. During the experiments, the working electrode was glassy carbon (glassy carbon electrode: CHI104). The reference electrode was a Vycor tip Ag/AgCl electrode stored in 3 M NaCl (BASI Instr. RE-5B, MF-2079), while the counter electrode was a platinum electrode (distributed by ALS Co., Japan). The concentration of the complexes was $1 \cdot 10^{-3}$ M and the volume of the sample was 1 mL. Before each scan, the working electrode was treated with alumina paste (0.1 micron ordered from Buehler Company) and the surface was cleaned with the help of sandpaper. The electrochemical measuring system was calibrated with the $[Fe(CN)_6]^{3-}/[Fe(CN)_6]^{4-}$ redox system. The redox potential was 0.462 V, which is in good agreement with the published redox potential (0.458 V[360]). The potential range was changed between +800 and –1200 mV. The voltammograms were recorded at 25, 100, 1000 mV/s sweep rates. For the analysis of the voltammograms, the CACYVO program was used which was provided by the distributor of the instrument. The half-wave potential ($E_{1/2}$) values were calculated based on the following equation:

$E_{1/2} = \frac{E_{pc} + E_{pa}}{2}$, where E_{pc} and E_{pa} are the cathodic and anodic peak potentials, respectively.

Considering that $E_{1/2} = E^0$, the E^0 values throughout this work are referred to Normal Hydrogen Electrode (NHE), taking into account that $E^0_{Ag/AgCl}$ versus $E^0_{NHE\ (water)}$ is +209 mV at 25 °C.

$E^0 = E_{1/2} + E^0_{Ag/AgCl}$

Magnetic studies. Magnetization data were measured on a Quantum Design MPMS-XL7 SQUID magnetometer. Ground polycrystalline samples were restrained with eicosane in a gelatin capsule at the center of a straw and fixed to the sample rod. Susceptibility measurements were conducted upon cooling the sample in a magnetic field.

Electron paramagnetic resonance. *Chapter 2:* EPR spectra were collected with a Bruker EMX spectrometer at X-band and Q-band, using liquid helium with an Oxford Instruments temperature controller. *Chapter 5:* 9 GHz continuous-wave X-band electron paramagnetic resonance (EPR) spectra were recorded on a Bruker Biospin EMX spectrometer with a Bruker ER4119HS resonator. The spectra were obtained with 2.2 mW microwave power and 2G modulation under non-saturating conditions at 5K. Low temperature measurements were achieved using an Oxford Instruments ESR900 cryostat. The Easyspin[361] software package was used for all simulations.

X-Ray Crystallography. Data for **L^1**, **L^4**, **L^5**, **L^7**, **L^8**, compounds **1**, **3-15**, **19**, **22**, **23**, **27-31** and **34** , dihydropyridine products **C3D5** and **C3D6** and triazole products **C5T1** – **C5T4** were collected (ω-scans) at the University of Sussex, using either a Rigaku 007HF rotating anode generator with CCD plate detector (for **L^1**, **27**, **28**) or an Agilent Xcalibur Eos Gemini Ultra diffractometer with CCD plate detector (for the remaining molecules). Collection took place under a flow of nitrogen gas at 173(2) K for all compounds except **4** which was measured at 293(2) K. Mo Kα (λ = 0.71073 Å) or Cu Kα radiation (λ = 1.54184 Å) were used. CRYSALIS CCD and RED software was used respectively for data collection and processing. Reflection intensities were corrected for absorption by the multi-scan method. Data for **L^3**, compounds **2**, **16-18**, **20**, **24-26**, **32**, **33** and **35**, and dihydropyridine products **C3D4** and **C3D13** were collected at the National Crystallography Service, University of Southampton.[362] All structures were determined using Olex2[363], solved using SHELXT[364,365] and refined with SHELXL-2014[366]. All non-H atoms were refined with anisotropic thermal parameters, and H-atoms were introduced at calculated positions and allowed to ride on their carrier atoms. Compound **19** is isostructural to **18** (unit cell comparison) and its formula was confirmed by ESI-MS, TGA and CHN analysis, however the lattice OTf molecules were not possible to be refined with anisotropic parameters, therefore the SQUEEZE method was applied to remove them. Crystal data and structure refinement parameters are given in Chapter 9. For compound **21**, three different crystallographic datasets (University of Sussex, National Crystallography

Service, University of Southampton, Diamond Source) confirmed the synthesis of the proposed formula, also suggested from ESI-MS, TGA and CHN analysis. However, despite producing large block shaped green crystals, none of these datasets fulfilled the publication criteria, therefore the crystallographic parameters will not be reported. Geometric/crystallographic calculations were performed using PLATON[367], Olex2[363], and WINGX[366] packages; graphics were prepared with Crystal Maker and MERCURY[368].

8.2. Ligand Synthesis

Supporting Figures for ^{1}H NMR, ^{13}CNMR, FT-IR and ESI-MS may be found in the Appendix.

Synthesis of 1,4-bis((1H-benzo[d][1,2,3]triazol-1-yl)methyl)benzene (L^{1})

Benzotriazole (5.0 g, 42.0 mmol) was dissolved in acetone (50 mL) and then potassium carbonate (12.0 g, 86.2 mmol) and potassium iodide (0.50 g, 3.01 mmol) were added. After stirring for 30 min, solid α,α'-dichloro-p-xylene (3.5 g, 20.0 mmol) was added slowly. The mixture was refluxed for 1 h. After cooling, the solution was filtered and the filtrate evaporated to dryness to give a white solid product. The residue was recrystallized in methanol/water (1:1) to give a white crystalline material. NMR of the pure crystals revealed a mix of isomer forms; the peaks given here correspond to the main (1,1-) isomer. Yield: 63%. Selected IR peaks (cm^{-1}): 3065 (w), 3033 (w), 1940 (w), 1615 (m), 1564 (m), 1495 (m), 1455 (m), 1410 (m), 1322 (m), 1312 (m), 1272 (m), 1222 (m), 1150 (m), 1085 (w), 1050 (w), 1000 (m), 981 (w), 966 (m), 944 (m), 906 (m), 837 (m), 787 (m), 762 (m), 740 (s), 733 (s), 696 (m), 667 (m). ^{1}H NMR (500 MHz, DMSO-d$_6$) δ 8.01 (d, *J* = 8.5 Hz, 2H), 7.80 (d, *J* = 8.9 Hz, 2H), 7.52 – 7.48 (m, 2H), 7.44 – 7.31 (m, 6H), 5.94 (s, 4H). ^{13}C NMR (126 MHz, DMSO-d$_6$) δ 145.8, 144.3, 136.4, 135.5, 129.2, 129.1, 128.6, 128.5, 127.8, 126.9, 124.4, 119.6, 118.2, 111.0, 59.5, 51.0. The results are in agreement to those in the literature[369]. HRMS for $C_{20}H_{17}N_6$ [M + H]: theor. 341.1514 m/z, found 341.1503 m/z.

Synthesis of 1,3-bis((1H-benzo[d][1,2,3]triazol-1-yl)methyl)benzene (L^2)

L^2 was prepared by the same method and ratio as **L^1**, using α,α'-dichloro-m-xylene (3.5 g, 20.0 mmol) after stirring, then refluxing the mixture for 3 h. Yield: 74%. NMR of the pure crystals revealed a mix of isomer forms; the peaks given here correspond to the main (1,1-) isomer. Selected IR peaks (cm^{-1}): 3067 (w), 3034 (w), 1940 (w), 1614 (m), 1588 (w), 1565 (m), 1496 (m), 1453 (m), 1342 (w), 1310 (m), 1274 (m), 1226 (m), 1157 (m), 1105 (w), 1080 (w), 1050 (w), 1000 (m), 981 (w), 954 (m), 850 (m), 780 (m), 739 (s), 702 (m), 665 (m). ^{1}H NMR (500 MHz, DMSO-d_6) δ 8.01 (d, *J* = 8.3 Hz, 2H), 7.70 (d, *J* = 9.1 Hz, 2H), 7.44 (t, *J* = 7.6 Hz, 2H), 7.40 – 7.23 (m, 6H), 5.92 (s, 4H). ^{13}C NMR (126 MHz, DMSO-d_6) δ 145.4, 136.5, 132.7, 129.4, 127.6, 127.4, 127.3, 124.1, 119.3, 110.6, 50.8. The results are in agreement to those in the literature[370]. HRMS for $C_{20}H_{16}N_6K$ [M + K]: theor. 379.1073 m/z, found 379.1063 m/z.

Synthesis of 1,4-bis((1H-benzo[d][1,2,3]triazol-1-yl)methyl)benzene (L^3)

L^3 was prepared by the same method and ratio as **L^1**, using α,α'-dichloro-o-xylene (3.5 g, 20.0 mmol) after stirring, then refluxing the mixture for 2 h. Yield: 78%. NMR of the pure crystals revealed a mix of isomer forms; the peaks given here correspond to the main (1,1-) isomer. Selected IR peaks (cm^{-1}): 3059 (w), 1961 (w), 1616 (m), 1563 (m), 1497 (m), 1451 (m), 1389 (m), 1319 (m), 1297 (m), 1272 (m), 1227 (m), 1145 (m), 1098 (w), 1065 (w), 1001 (m), 969 (m), 946 (m), 907 (m), 846 (m), 787 (m), 765 (m), 736 (s), 692 (m), 669 (m).^{1}H NMR (DMSO-d_6, 500 MHz, ppm): δ 5.98 – 5.90 (m, 4H), 7.44 – 7.28 (m, 7H), 7.54 – 7.45 (m, 1H), 7.85 – 7.70 (m, 1H), 7.88 (m, 2H), 8.03 (d, *J* = 8.3 Hz, 1H). ^{13}C NMR (126 MHz, DMSO-d_6): δ 134.4, 129.1, 129.0, 128.1, 128.0, 127.1, 124.6, 124.6, 119.8, 118.3, 111.1, 48.8. HRMS for $C_{20}H_{17}N_6$ [M + H]: theor. 341.1514 m/z, found 341.1506 m/z.

Synthesis of 1-(2-((5-methyl-1H-benzo[d][1,2,3]triazol-1-yl)methyl)benzyl)-5-methyl-1H-benzo[d][1,2,3]triazole (L^4)

5-methyl-1H-benzotriazole (2.796 g, 21.0 mmol) was dissolved in acetone (40 mL) and then potassium carbonate (6 g, 43 mmol) and potassium iodide (0.50 g, 3.01 mmol) were added. After stirring for 30 min, solid α,α'-dichloro-o-xylene (1.75 g, 10.0 mmol) was added slowly. The mixture was refluxed for 5 hrs. After cooling, the solution was filtered and the filtrate

was evaporated to dryness. The resulting colourless syrup was then dissolved in 20 ml methanol after which a white microcrystalline precipitate was formed. This was subsequently recrystallized in acetonitrile/water (1:1). Yield: 33% (1.2 g). Selected IR peaks (cm^{-1}): 2972 (w), 1624 (w), 1501 (m), 1455 (m), 1311 (w), 1278 (m), 1265 (w), 1222 (s), 1163 (w), 1135 (w), 1117 (m), 1103 (m), 1075 (m), 1039 (w), 951 (m), 930 (m), 860 (m), 801 (s), 757 (s), 740 (s), 722 (s), 693 (m), 664 (w), 616 (m). NMR of single crystals revealed a complicated spectrum due to the presence of multiple isomers. HRMS for $C_{22}H_{21}N_6$ [M + H]: theor. 369.1826 m/z, calcd. 369.1822 m/z.

Synthesis of 1-(2-((5,6-dimethyl-1H-benzo[d][1,2,3]triazol-1-yl)methyl)benzyl)-5,6-dimethyl-1H-benzo[d][1,2,3]triazole (L^5)

5,6-dimethyl-1H-benzotriazole monohydrate (1.3 g, 8 mmol) was dissolved in acetone (30 mL) and then potassium carbonate (2.2 g, 16 mmol) and potassium iodide (0.50 g, 3.01 mmol) were added. After stirring for 30 min, solid α,α'-dichloro-o-xylene (0.65 g, 3.75 mmol) was added slowly. The mixture was refluxed for 5 hrs. After cooling, the solution was filtered and the filtrate was evaporated to dryness after which a brown microcrystalline precipitate was formed. This precipitate was then was recrystallized in acetonitrile/water (1:1) to produce light brown crystals which were identified as [**L^5**]·2H_2O. Yield: 93% (1.38 g). Selected IR peaks (cm^{-1}): 2974 (w), 1630 (w), 1493 (m), 1449 (m), 1372 (w), 1314 (w), 1284 (m), 1259 (w), 1222 (s), 1158 (w), 1117 (m), 1102 (m), 1070 (m), 1049 (w), 1023 (w), 999 (m), 934 (m), 846 (s), 784 (w), 746 (s), 718 (s), 685 (m), 664 (w), 606 (m). NMR of single crystals revealed a complicated spectrum due to the presence of multiple isomers. HRMS for $C_{24}H_{25}N_6$ [M + H]: theor. 397.2141 m/z, calcd. 397.2135 m/z.

Synthesis of 1-(2-((1H-benzo[d]imidazol-1-yl)methyl)benzyl)-1H-benzo[d]imidazole (L^6)

L^6 was synthesized according to the literature method[371] with slight modifications: To a solution of benzimidazole (3.0 g, 25 mmol) in DMF (50 ml) was added a solution of KOH (1.6 g, 25 mmol) in 20 ml H_2O. After 20 minutes of stirring, a,a'-dichloro-o-xylene (2.19 g, 12.5 mmol), was added slowly and the mixture was stirred under room temperature for 4 hrs. Then H_2O (30 mL) was added to the reaction mixture, and stirring was continued for another

1 hr. The mixture was then filtered to provide **L^6** as a pale brown solid. Yield: 71% (2.98 g). ^{1}H NMR (500 MHz, $CDCl_3$) δ 7.84 (d, *J* = 8.0 Hz, 2H), 7.77 (s, 2H), 7.35 – 7.21 (m, 6H), 7.12 (d, *J* = 8.0 Hz, 2H), 7.06 – 7.03 (m, 2H), 5.28 (s, 4H). ^{13}C NMR (126 MHz, $CDCl_3$) δ 143.8, 142.8, 133.7, 132.9, 129.4, 129.0, 123.5, 122.7, 120.7, 109.7, 46.3. Selected IR peaks (cm^{-1}): 3087 (w), 1615 (w), 1496 (m), 1458 (w), 1428 (w), 1402 (w), 1393 (w), 1385 (w), 1366 (w), 1317 (w), 1287 (m) 1265 (m), 1230 (w), 1201 (s), 1006 (w), 963 (w), 937 (w), 891 (m), 866 (w), 849 (w), 771 (m), 733 (s), 645 (w), 631 (w), 619 (m). HRMS for $C_{22}H_{19}N_4$ [M + H]: theor. 339.1604 m/z, found 339.1611 m/z.

Synthesis of 1-(2-((1H-imidazol-1-yl)methyl)benzyl)-1H-imidazole (L^7)

L^7 was synthesized according to the literature method[372] with slight modifications: a solution containing imidazole (3.16 g, 46.4 mmol) and α,α′-dichloro-o-xylene (0.78 g, 4.46 mmol) in methanol (50 mL) was heated under reflux for 20 hrs. After cooling, the solvent was evaporated to give a yellow syrup, which was then dissolved in 80 ml aqueous potassium carbonate (6.13 g). The resulting solution was left undisturbed to produce large crystals which were identified as [**L^7**]·$2H_2O$. Yield: 1.0 g (82%). ^{1}H NMR (500 MHz, $CDCl_3$) δ 7.43 (s, 2H), 7.36 (dd, *J* = 5.7, 3.4 Hz, 2H), 7.09 (s, 2H), 7.07 (dd, *J* = 5.7, 3.4 Hz, 2H), 6.78 (s, 2H), 5.01 (s, 4H). ^{13}C NMR (126 MHz, $CDCl_3$) δ 137.3, 133.7, 130.1, 129.4, 119.2, 117.7, 48.1. HRMS for $C_{14}H_{15}N_4$ [M + H]: theor. 239.1291 m/z, found 239.1290 m/z.

Synthesis of 1-benzyl-1H-benzo[d][1,2,3]triazole (L^8)

Benzotriazole (2.4 g, 20.0 mmol) was dissolved in acetone (50 mL) and then potassium carbonate (6.0 g, 43.0 mmol) and potassium iodide (0.25 g, 1.5 mmol) were added. After stirring for 30 min, benzyl chloride (2.3 ml, 20.0 mmol) was added slowly. The mixture was refluxed for 1 h. After cooling, the solution was filtered and the filtrate evaporated to dryness to give a colourless crystalline material. Yield: 71%. Selected IR peaks (cm^{-1}): 3362 (br), 1615 (w), 1582 (w), 1497 (w), 1449 (w), 1274 (m), 1222 (s), 1170 (s), 1025 (s), 931 (w), 791 (m), 747 (m), 698 (w), 632 (m). ^{1}H NMR (600 MHz, $CDCl_3$) δ 8.08 (d, J = 8.3 Hz, 1H), 7.42 – 7.26 (m, 8H), 5.85 (s, 2H). ^{13}C NMR (151 MHz, $CDCl_3$) δ 145.9, 134.7, 129.0, 128.4, 127.6, 127.4, 123.9, 120.1, 109.7, 77.2, 77.0, 76.8, 52.3. The results are in agreement to those

in the literature[373]. HRMS for $C_{13}H_{11}N_3K$ [M + K]: theor. 248.0590 m/z, found 248.0584 m/z.

8.3. Synthesis of Coordination Compounds 1-35

Synthesis of $[Co_2(\mathbf{L^1})_2Cl_4]\cdot 2MeCN$ (**1**).

Method 1: 0.12 mmol (0.041 g) of $\mathbf{L^1}$ were dissolved in 10 ml MeCN while stirring to produce a colourless solution. A solution containing 0.12 mmol (0.016 g) of anhydrous $CoCl_2$ in MeCN (7.5 ml) was slowly added. The resulting dark blue solution was filtrated, then layered over 10 ml of Et_2O. Blue prismatic crystals were obtained after 2 days. Selected IR peaks (cm^{-1}): 2996 (w), 1595 (w), 1493 (w), 1456 (m), 1439 (w), 1315 (m), 1278 (w), 1226 (m), 1167 (w), 1142 (w), 1104 (w), 1003 (w), 954 (w), 850 (w), 782 (m), 749 (s), 669 (m). Yield: 20% (based on Co). Elemental analysis (%) for $C_{44}H_{38}Cl_4Co_2N_{14}$: C 51.69, H 3.75, N 19.17; found C 51.70, H 3.82, N 19.13. *Alternative Methods*: **1** may also be prepared by the same method as above but using either a 2:1 or 1:2 metal:ligand (M:L) ratio.

Synthesis of $Co_2(\mathbf{L^1})_2Br_4$ (**2**).

Method 1: 0.12 mmol (0.041 g) of $\mathbf{L^1}$ were dissolved in 10 ml Me_2CO while stirring to produce a colourless solution. A solution containing 0.12 mmol (0.027 g) of anhydrous $CoBr_2$ in Me_2CO (7.5 ml) was slowly added. The resulting blue solution was stirred for 45 minutes, while heated to 50°C. After the solution was left to cool, it was filtrated and then carefully layered over 10 ml of Et_2O. Blue needles were obtained after 2 days. Selected IR peaks (cm^{-1}): 3033 (w), 1591 (w), 1495 (w), 1455 (m), 1430 (w), 1313 (m), 1283 (w), 1225 (m), 1180 (w), 1139 (w), 1109 (w), 1002 (w), 963 (w), 836 (w), 772 (m), 734 (s), 669 (m). Yield: 14% (based on Co). Elemental analysis (%) for $C_{40}H_{32}Br_4Co_2N_{12}$: C 42.97, H 2.88, N 15.03; found C 42.99, H 2.92, N 14.93. *Alternative Methods*: **2** is also obtained by performing the same reaction in a 2:1 M:L ratio. It may also be prepared in a similar fashion using MeCN instead of Me_2CO.

Synthesis of [Co(**L²**)Cl_2]·MeCN (**3**). *Method 1*: 0.12 mmol (0.041 g) of **L²** were dissolved in 10 ml MeCN while stirring to produce a colourless solution. A solution containing 0.24 mmol (0.032 g) of anhydrous $CoCl_2$ in MeCN (7.5 ml) was slowly added. The resulting dark blue solution was filtrated, then subjected to slow evaporation. Blue block crystals were obtained 1 day later. Selected IR peaks (cm^{-1}): 2986 (w), 1592 (w), 1492 (w), 1454 (m), 1315 (m), 1279 (w), 1227 (m), 1167 (w), 1122 (m), 1004 (w), 982 (w), 849 (w), 768 (m), 743 (s), 700 (m). Yield: 52% (based on Co). Elemental analysis (%) for $C_{22}H_{19}Cl_2CoN_7$: C 51.69, H 3.75, N 19.17; found C 51.57, H 3.73, N 19.25. *Method 2*: The product may also be obtained performing a similar reaction in a 1:1 M:L ratio.

Synthesis of [Co(**L²**)Cl_2] (**4**). *Method 1*: 0.12 mmol (0.041 g) of **L²** and 0.24 mmol (0.032 g) of anhydrous $CoCl_2$ were dissolved in 12 ml MeCN while stirring to produce a blue solution. After a further 15 minutes of stirring, the solution was stored in a glass vessel and heated at 75 °C for 18 hours to produce large blue block crystals. *Method 2*: **4** may also be obtained by a similar solvothermal reaction in a 1:1 M:L ratio, heating the solution at 100 °C for 3 days. Selected IR peaks (cm^{-1}): 2990 (w), 1594 (w), 1493 (w), 1457 (m), 1314 (m), 1287 (w), 1229 (m), 1167 (w), 1139 (w), 1124 (m), 1093 (w), 1003 (w), 982 (w), 851 (w), 823 (w), 768 (m), 750 (s), 739 (s), 702 (m). Yield: 69% (based on Co). Elemental analysis (%) for $C_{20}H_{16}Cl_2CoN_6$: C 51.09, H 3.43, N 17.87; found C 50.97, H 3.53, N 17.75.

Synthesis of [Co_2(**L₂**)$_2Br_4$]·2MeCN (**5**). **5** was prepared in the same solvent and crystallizing method as **3** (*Methods 1, 2*), using $CoBr_2$ as the metal salt. Selected IR peaks (cm^{-1}): 3055 (w), 1594 (w), 1493 (w), 1456 (m), 1324 (m), 1283 (w), 1224 (m), 1170 (w), 1148 (m), 1002 (w), 972 (w), 779 (m), 765 (m), 747 (s), 702 (m), 672 (m). Yield: 49% (based on Co). Elemental analysis (%) for $C_{44}H_{38}Br_4Co_2N_{14}$: C 44.03, H 3.19, N 16.33; found C 43.90, H 3.12, N 16.20.

Synthesis of [Co(**L²**)$_2$(NO_3)$_2$]·2MeCN (**6**). 0.12 mmol (0.041 g) of **L²** and 0.36 mmol (0.105 g) of Co(NO_3)$_2$·$6H_2O$ were dissolved in 8 ml MeCN while stirring to produce a pink solution. After a further 15 minutes of stirring, the solution was filtrated, then stored in a glass vessel and heated at 100 °C for 3 days to produce pink block crystals. Selected IR peaks (cm^{-1}):

3038 (w), 1978 (w), 1612 (m), 1596 (m), 1497 (m), 1445 (m), 1370 (m), 1321 (m), 1298 (s), 1226 (m), 1168 (m), 1145 (w), 1128 (m), 1028 (m), 1011 (w), 959 (m), 935 (w), 857 (m), 817 (m), 760 (s), 743 (s), 701 (m), 670 (m). Yield: 22% (based on Co). Elemental analysis (%) for $C_{44}H_{38}CoN_{16}O_6$: C 55.88, H 4.05, N 23.69; found C 55.68, H 3.63, N 22.74.

Synthesis of $[Co_2(\mathbf{L^3})_2Cl_4]\cdot 2MeCN$ (**7**). *Method 1*: **7** was prepared in the same method, ratios and crystallization technique as **1**, using $\mathbf{L^3}$ instead of $\mathbf{L^1}$. Blue prismatic crystals were obtained after 2 days. *Method 2*: **7** was also prepared using the same method and solvothermal conditions as **4** (*Method 1*), in a 1:1, 2:1 or 1:2 ratio, employing $\mathbf{L^3}$ instead of $\mathbf{L^2}$. Selected IR peaks (cm^{-1}): 2974 (w), 2861 (w), 1593 (w), 1491 (w), 1455 (m), 1319 (m), 1285 (w), 1228 (m), 1167 (w), 1151 (w), 1116 (m), 1094 (w), 1002 (w), 959 (w), 846 (w), 814 (w), 790 (w), 765(m), 746 (s), 733 (s), 668 (m). Yield: 64% (based on Co). Elemental analysis (%) for $C_{22}H_{19}Cl_2CoN_7$: C 51.69, H 3.75, N 19.17; found C 49.70, H 3.64, N 17.07. This result corresponds to the loss of one acetonitrile molecule and the presence of one water molecule: $C_{20}H_{16}CoN_6(H_2O)$: C 49.20, H 3.72, N 17.19.

Synthesis of $Co_2(\mathbf{L^3})_2Cl_4$ (**8**). 0.12 mmol (0.041 g) of $\mathbf{L^3}$ and 0.36 mmol (0.048 g) of anhydrous $CoCl_2$ were dissolved in 8 ml MeCN while stirring to produce a blue solution. After a further 15 minutes of stirring, the solution was filtrated, then stored in a glass vessel and heated at 75 °C for 18 hours to produce single crystal X-ray quality blue block crystals. Selected IR peaks (cm^{-1}): 2983 (w), 1595 (w), 1497 (w), 1458 (m), 1433 (w), 1323 (m), 1282 (w), 1226 (m), 1171 (w), 1151 (w), 1005 (w), 973 (w), 957 (w), 845 (w), 793 (m), 774 (m), 742 (s), 705 (m), 667 (m). Yield: 60% (based on Co). Elemental analysis (%) for $C_{40}H_{32}Cl_4Co_2N_{12}$: calcd. C 51.09, H 3.43, N 17.87; found C 51.19, H 3.46, N 17.99.

Synthesis of $Co_2(\mathbf{L^3})_2Br_4$ (**9**). **9** was prepared in the same method, ratios and crystallization technique as **1**, using anhydrous $CoBr_2$ as the metal salt and $\mathbf{L^3}$ instead of $\mathbf{L^1}$. Blue prismatic crystals were obtained after 3 days. Selected IR peaks (cm^{-1}): 3097 (w), 1591 (w), 1493 (w), 1456 (m), 1329 (m), 1281 (w), 1230 (m), 1168 (w), 1143 (m), 1002 (w), 967 (w), 841 (w), 792 (w), 780 (m), 767 (m), 742 (s), 712 (m), 669 (m). Yield: 60% (based on Co). Elemental

analysis (%) for $C_{40}H_{32}Br_4Co_2N_{12}$: calcd. C 42.97, H 2.88, N 15.03; found C 42.89, H 2.82, N 14.95.

Synthesis of $Co(\mathbf{L^3})_2(NO_3)_2$ (**10**). **10** was prepared in the same method and ratios as **1**, using $Co(NO_3)_2 \cdot 6H_2O$ as the metal salt and $\mathbf{L^3}$ instead of $\mathbf{L^1}$. The resulting light red solution was filtrated, then kept at a stored vial in room temperature. Pink needle-like crystals were obtained after 3 days. Selected IR peaks (cm^{-1}): 3105 (w), 3081 (w), 1978 (w), 1611 (m), 1592 (m), 1497 (m), 1436 (m), 1374 (m), 1320 (m), 1300 (m), 1279 (m), 1232 (m), 1167 (m), 1145 (m), 1088 (w), 1028 (w), 1003 (m), 970 (m), 953 (m), 930 (w), 857 (m), 814 (m), 755 (s), 741 (s), 711 (m), 669 (m). Yield: 42% (based on Co). Elemental analysis (%) for $C_{40}H_{32}CoN_{14}O_6$: C 55.63, H 3.73, N 22.70; found C 55.62, H 3.64, N 22.79.

Synthesis of $[Cu^{II}(\mathbf{L^3})_2(MeCN)_2] \cdot (ClO_4)_2 \cdot MeCN$ (**11**). 0.24 mmol (0.082 g) of $\mathbf{L^3}$ were dissolved in 10 ml MeCN while stirring to produce a colourless solution. A solution containing 0.48 mmol (0.178 g) of $Cu(ClO_4)_2 \cdot 6H_2O$in MeCN (7.5 ml) was slowly added. The resulting green solution was filtrated, then kept stored in room temperature. High quality green crystals were obtained after 1 day. Selected IR peaks (cm^{-1}): 3464 (br), 1646 (w), 1592 (w), 1495 (w), 1457 (m), 1393 (w), 1319 (m), 1279 (m), 1230 (m), 1171 (m), 1073 (m), 1039 (m), 969 (w), 851 (w), 778 (m), 739 (s), 671 (w), 623 (s). Yield: 49% (based on Cu). Elemental analysis (%) for $C_{46}H_{41}Cl_2CuN_{15}O_8$: theor. C 51.82, H 3.88, N 19.70; found C 52.02, H 3.88, N 19.78.

Synthesis of $[Cu^{II}(\mathbf{L^3})(NO_3)_2] \cdot MeCN$ (**12**). 0.12 mmol (0.041 g) of $\mathbf{L^3}$ were dissolved in 10 ml MeCN while stirring to produce a colourless solution. A solution containing 0.12 mmol (0.027 g) of $Cu(NO_3)_2 \cdot 2.5H_2O$in MeCN (7.5 ml) was slowly added. The resulting blue solution was filtrated, then layered over Et_2O in a 1:2 ratio. Blue crystals were obtained after 1 day. Selected IR peaks (cm^{-1}): 3120 (w), 1594 (w), 1484 (s), 1454 (m), 1436 (w), 1367 (w), 1320 (w), 1279 (s), 1236 (m), 1181 (w), 1166 (m), 1006 (m), 962 (w), 839 (w), 798 (w), 768 (m), 757 (s), 741 (s), 669 (w). Yield: 14% (based on Cu). Elemental analysis (%) for $C_{22}H_{19}CuN_9O_6$: theor. C 46.45, H 3.37, N 22.15; found C 44.04, H 2.65, N 21.08. This result

corresponds to the loss of one acetonitrile molecule and the presence of one water molecule: $C_{20}H_{16}CuN_{8}\cdot(H_2O)$: C 44.03, H 3.32, N 20.55.

Synthesis of $[Zn^{II}(\mathbf{L^3})_2(H_2O)_2]\cdot(ClO_4)_2\cdot 2MeCN$ (**13**). 0.12 mmol (0.041 g) of $\mathbf{L^3}$ and 0.48 mmol (0.180 g) of $Zn(ClO_4)_2\cdot 6H_2O$ were dissolved in 7.5 ml MeCN while stirring to produce a colourless solution. After filtration, the solution was then kept stored in room temperature. White crystals were obtained after 1 week. Selected IR peaks (cm^{-1}): 3402 (br), 1645 (w), 1589 (w), 1494 (w), 1453 (m), 1436 (w), 1317 (m), 1276 (m), 1231 (m), 1170 (m), 1100 (m), 1046 (m), 959 (w), 850 (w), 739 (s), 712 (m), 670 (w), 624 (s). Yield: 19% (based on Zn). Elemental analysis (%) for $C_{40}H_{36}Cl_2N_{12}O_{10}Zn$: theor. C 48.97, H 3.70, N 17.13; found C 48.87, H 3.74, N 17.24.

Synthesis of $[Cu^{II}(\mathbf{L^3})_2Cl_2]_2$ (**14**). 0.12 mmol (0.041 g) of $\mathbf{L^3}$ and 0.12 mmol (0.016 g) of anhydrous $CuCl_2$ were dissolved in 8 ml MeCN while stirring to produce a yellow solution. After a further 15 minutes of stirring, the solution was filtrated, stored in a glass vessel and heated at 75 °C for 18 hours to produce large green block crystals. Selected IR peaks (cm^{-1}): 1590 (w), 1492 (w), 1455 (m), 1315 (m), 1290 (w), 1235 (w), 1145 (w), 1015 (w), 1006 (w), 952 (m), 900 (w), 778 (m), 770 (m), 729 (s), 661 (m). Yield: 18% (based on Cu). Elemental analysis (%) for $C_{40}H_{32}Cl_4Cu_2N_{12}$: calcd. C 50.74, H 3.41, N 17.76; found C 50.79, H 3.46, N 17.89.

Synthesis of $[Cu^{II}_5(\mathbf{L^3})_2Cl_{10}]$ (**15**). 0.12 mmol (0.041 g) of $\mathbf{L^3}$ and 0.36 mmol (0.048 g) of anhydrous $CuCl_2$ were dissolved in 8 ml MeCN while stirring to produce a yellow solution. After a further 15 minutes of stirring, the solution was filtrated, stored in a glass vessel and heated at 95 °C for 18 hours to produce good quality brown block crystals. Selected IR peaks (cm^{-1}): 1589 (w), 1492 (w), 1452 (m), 1370 (w), 1331 (m), 1313 (w), 1278 (w), 1231 (m), 1165 (w), 1144 (w), 1002 (w), 970 (w), 961 (w), 841(w), 792 (w), 779 (w), 752 (m), 738 (s), 711 (m), 668 (m). Yield: 33% (based on Cu). Elemental analysis (%) for $C_{40}H_{32}Cl_{10}Cu_5N_{12}$: calcd. C 35.70, H 2.40, N 12.50; found C 35.59, H 2.46, N 12.43.

Synthesis of $[Cu^{II}_2(\mathbf{L^3})_4Br_2]\cdot 4MeCN\cdot(Cu^{II}_2Br_6)$ (**16**). Anhydrous $CuBr_2$ was used as the metal salt in a procedure similar to the synthesis of **14**. The resultant dark green solution was stored in a vial at room temperature. Small green crystals were obtained after 3 days. Selected IR peaks (cm^{-1}): 1594 (w), 1494 (s), 1456 (m), 1321 (w), 1283 (w), 1233 (m), 1167 (m), 1144 (m), 1002 (w), 966 (w), 843 (w), 789 (m), 736 (s), 670 (w), 628 (m). Yield: 11% (based on Cu). Elemental analysis (%) for $C_{88}H_{76}Br_8Cu_4N_{28}$: theor. C 43.69, H 3.17, N 16.21; found C 43.81, H 3.13, N 16.11.

Synthesis of $[Cu^{II}(\mathbf{L^3})_2(MeCN)_2]\cdot(BF_4)_2$ (**17**). 0.24 mmol (0.082 g) of $\mathbf{L^3}$ were dissolved in 10 ml MeCN while stirring to produce a colourless solution. A solution containing 0.48 mmol (0.170 g) of $Cu(BF_4)_2\cdot 6H_2O$ in MeCN (7.5 ml) was slowly added. The resulting green solution was filtrated and kept stored at room temperature. Green block crystals were obtained after 1 day. Selected IR peaks (cm^{-1}): 3468 (w), 3508 (w), 1651 (w), 1592 (w), 1495 (w), 1454 (m), 1320 (m), 1282 (m), 1234 (m), 1172 (m), 1159 (w), 1060 (s), 1017 (s), 969 (m), 953 (w), 853 (w), 793 (w), 780 (m), 757 (s), 748 (s), 739 (s), 672 (w). Yield: 49% (based on Cu). Elemental analysis (%) for $C_{44}H_{38}B_2CuF_8N_{14}$: theor. C 52.84, H 3.83, N 19.62; found C 52.92, H 3.86, N 19.70.

Synthesis of $[Cu^{II}(\mathbf{L^3})_2(CF_3SO_3)_2]$ (**18**). 0.24 mmol (0.082 g) of $\mathbf{L^3}$ and 0.48 mmol (0.180 g) of $Cu(OTf)_2\cdot H_2O$ were dissolved in 15 ml Me_2CO while stirring to produce a dark green solution. After stirring for 1 hr, the solution was filtrated, then layered over n-hexane in a 1:2 ratio to produce large blue block crystals after 7 days. Selected IR peaks (cm^{-1}): 1589 (w), 1492 (w), 1457 (m), 1320 (m), 1275 (m), 1244 (m), 1163 (w), 1140 (m), 1023 (s), 952 (w), 848 (w), 779 (m), 746 (s), 669 (m). Yield: 11% (based on Cu). Elemental analysis (%) for $C_{42}H_{32}CuF_6N_{12}O_6S_2$: calcd. C 48.41, H 3.10, N 16.14; found C 48.53, H 3.04, N 16.07.

Synthesis of $[Zn^{II}(\mathbf{L^3})_2(MeCN)_2]\cdot(CF_3SO_3)_2$ (**19**). 0.24 mmol (0.082 g) of $\mathbf{L^3}$ were dissolved in 15 ml MeCN while stirring to produce a colourless solution. 0.12 mmol (0.044 g) of $Zn(OTf)_2$ were then added. After stirring for a further 30 min., the resulting colourless solution was filtrated, then layered over Et_2O in a 1:2 ratio. Large colourless block crystals were obtained after 2 weeks. Selected IR peaks (cm^{-1}): 3434 (br), 1654(w), 1592 (w), 1494

(w), 1456 (m), 1372 (w), 1319 (m), 1269 (m), 1226 (s), 1153 (m), 1094 (w), 1025 (s), 951 (w), 880 (w), 843 (w), 766 (w), 740 (s), 714 (w), 669 (m). Yield: 38% (based on Zn). Elemental analysis (%) for $C_{46}H_{38}F_6N_{14}O_6S_2Zn$: C 49.04, H 3.40, N 17.42; found C 49.11, H 3.53, N 17.38.

Synthesis of $[Cu^{II}_2(\mathbf{L^4})_4(H_2O)_2]\cdot(CF_3SO_3)_4\cdot 4Me_2CO$ (**20**). 0.1 mmol (0.036 g) of $\mathbf{L^4}$ and 0.1 mmol (0.037 g) of $Cu(OTf)_2\cdot H_2O$ were dissolved in 15 ml acetone while stirring to produce a turquoise solution. The solution was filtrated, then layered over n-hexane in a 1:2 ratio to produce green needle-like crystals after a few hours. Selected IR peaks (cm^{-1}): 1592 (w), 1504 (w), 1457 (m), 1279 (m), 1223 (s), 1158 (m), 1027 (s), 868 (w), 805 (m), 758 (w), 721 (w), 636 (s). Yield: 23% (based on Cu). Elemental analysis (%) for $C_{104}H_{108}Cu_2F_{12}N_{24}O_{18}S_4$: C 50.65, H 4.42, N 13.64; found C 50.73, H 4.36, N 13.63.

Synthesis of $[Cu^{II}_2(\mathbf{L^5})_4(CF_3SO_3)_2]\cdot(CF_3SO_3)_2\cdot Me_2CO$ (**21**). 0.12 mmol (0.048 g) of $\mathbf{L^5}$ and 0.24 mmol (0.089 g) of $Cu(OTf)_2\cdot H_2O$ were dissolved in 15 ml acetone while stirring to produce a dark green solution. The solution was filtrated, then layered over n-hexane in a 1:2 ratio to produce small green block crystals after 10 days. Selected IR peaks (cm^{-1}): 3436 (br), 1707 (w), 1631 (w), 1590 (w), 1559 (w), 1494 (w), 1456 (m), 1252 (m), 1235 (s), 1221 (s), 1153 (m), 1026 (s), 1003 (m), 965 (w), 901 (w), 845 (m), 785 (w), 748 (m). Yield: 10% (based on Cu). Elemental analysis (%) for $C_{103}H_{102}Cu_2F_{12}N_{24}O_{13}S_4$: C 52.25, H 4.35, N 14.21; found C 52.33, H 4.41, N 14.34.

Synthesis of $[Cu^{II}(\mathbf{L^2})(MeCN)_2(CF_3SO_3)_2]$ (**22**). 0.05 mmol (0.017 g) of $\mathbf{L^2}$ and 0.10 mmol (0.036 g) of $Cu(OTf)_2\cdot H_2O$ were dissolved in 10 mL of MeCN while stirring to produce a green solution. After 10 min of stirring, the solution was stored in a glass vessel and heated at 95 °C for 18 h. After cooling down, the solution was subjected to Et_2O using the vapour diffusion technique. Green block crystals were produced after 3 days. Selected IR peaks (cm^{-1}): 3564 (w), 3512 (w), 1651 (w), 1455 (m), 1321 (m), 1283 (m), 1234 (w), 1172 (w), 1059 (s), 1020 (s), 954 (w), 880 (w), 794 (w), 758 (s), 748 (s), 672 w), 626 (w). Yield: 26% (based on Cu). Elemental analysis (%) for $C_{26}H_{22}CuF_6N_8O_6S_2$: C 39.81, H 2.83, N 14.29; found C 39.96, H 2.82, N 14.38.

Synthesis of $[Cu^{II}(\mathbf{L^6})_2(CF_3SO_3)_2]$ (**23**). 0.06 mmol (0.022 g) of $\mathbf{L^6}$ and 0.12 mmol (0.044 g) of $Cu(OTf)_2 \cdot H_2O$ were dissolved in 15 ml acetone while stirring to produce a dark green solution. Then the solution was filtrated and layered over n-hexane in a 1:2 ratio to produce small blue block crystals after 3 weeks. Selected IR peaks (cm^{-1}): 3351 (br), 3125 (w), 1616 (w), 1558 (w), 1519 (m), 1484 (w), 1465 (m), 1397 (w), 1241 (s), 1224 (s), 1175 (m), 1028 (s), 928 (w), 849 (w), 740 (s), 669 (m). Yield: 19% (based on Cu). Elemental analysis (%) for $C_{46}H_{36}CuF_6N_8O_6S_2$: C 53.22, H 3.50, N 10.80; found C 53.36, H 3.42, N 10.83.

Synthesis of $[Cu^{II}(\mathbf{L^7})_2(MeCN)(CF_3SO_3)] \cdot (CF_3SO_3)$ (**24**). A 10 ml solution of $Cu(OTf)_2 \cdot H_2O$ (0.072 g, 0.2 mmol) in MeCN was dropwise added to a 10 ml solution of $\mathbf{L^7}$ (0.068 g, 0.2 mmol) in methanol. The resulting blue solution was filtered, then carefully layered over Et_2O in a 1:2 ratio to produce blue block crystals after 1 week. Selected IR peaks (cm^{-1}): 3462 (br), 3145 (m), 1659 (w), 1522 (m), 1459 (m), 1445 (w), 1258 (s), 1244 (m), 1226 (s), 1174 (w), 1109 (m), 1089 (m), 1032 (s), 947 (w), 868 (w), 857 (w), 838 (w), 774 (m), 759 (m), 729 (s), 687 (w), 661 (s), 634 (m), 625 (m). Yield: 24% (based on Cu). Elemental analysis (%) for $C_{32}H_{31}CuF_6N_9O_6S_2$: C 43.73, H 3.56, N 14.35; found C 43.70, H 3.72, N 14.43.

Synthesis of $[Cu^{II}(\mathbf{L^7})_2(H_2O)(CF_3SO_3)] \cdot (CF_3SO_3) \cdot 2(Me_2CO)$ (**25**). A 5 ml solution of $\mathbf{L^7}$ (0.038 mg, 0.16 mmol) in acetone was layered on a 8 ml solution of $Cu(OTf)_2 \cdot H_2O$ (0.029 g, 0.08 mmol) in H_2O. Purple needles were obtained after 5 days. Selected IR peaks (cm^{-1}): 3516 (w), 3444 (w), 3135 (w), 1611 (w), 1523 (m), 1461 (m), 1441 (w), 1277 (m), 1263 (m), 1244 (s), 1224 (s), 1155 (m), 1108 (m), 1090 (m), 1026 (s), 950 (m), 842 (w), 827 (w), 773 (w), 758 (w), 734 (s), 667 (m), 655 (m), 634 (s). Yield: 31% (based on Cu). Elemental analysis (%) for $C_{36}H_{42}CuF_6N_8O_9S_2$: C 44.46, H 4.35, N 11.52; found C 42.00, H 3.35, N 12.91. This result corresponds to the loss of two Me_2CO molecules (calcd. C 42.08, H 3.43, N 13.08).

Synthesis of $[Cu^{I}_4(\mathbf{L^3})_2(\mathbf{L^{3T}})_2(CF_3SO_3)_2]_2 \cdot (CF_3SO_3)_4 \cdot 8(Me_2CO)$ (**26**). 0.06 mmol (0.022 g) of $\mathbf{L^3}$ and 0.12 mmol (0.045 g) of $Cu^{I}(MeCN)_4 \cdot CF_3SO_3$ were dissolved in 17.5 ml acetone

while stirring to produce a light yellow solution. Then the solution was filtrated and layered over Et_2O in a 1:2 ratio to produce small yellow block crystals after 2 days. Selected IR peaks (cm^{-1}): 3395 (br), 1608 (w), 1597 (w), 1499 (w), 1522 (m), 1457 (m), 1275 (m), 1223 (s), 1165 (m), 1026 (s), 869 (w), 743 (m), 634 (s). Yield: 41% (based on Cu). Elemental analysis (%) for $C_{96}H_{88}Cu_4F_{12}N_{24}O_{16}S_4$: C 47.17, H 3.63, N 13.75; found C 46.89, H 3.08, N 14.71. This result corresponds to the loss of four acetone molecules (calcd. C 46.77, H 2.85, N 14.87).

Synthesis of [Ag(**L**$^{\mathbf{1}}$)(CF_3CO_2)] (**27**). 0.06 mmol (0.020 g) of **L**$^{\mathbf{1}}$ were dissolved in 17.5 ml MeCN while stirring to produce a colourless solution. 0.12 mmol (0.027 g) of $AgCF_3CO_2$ were then added and the resulting white solution was filtrated and left undisturbed under room temperature to produce white needles after 12 days. Selected IR peaks (cm^{-1}): 3098 (w), 1691 (w), 1593 (w), 1497 (w), 1454 (w), 1310 (w), 1278 (w), 1226 (m), 1162 (w), 1114 (m), 1033 (m), 825 (w), 780 (m), 738 (s), 621 (w). Yield: 36% (based on Ag).^{1}H NMR (600 MHz, DMSO-d_6) δ 8.02 (d, J = 8.3 Hz, 2H), 7.78 (d, J = 8.4 Hz, 2H), 7.49 (t, J = 7.7 Hz, 2H), 7.37 (d, J = 7.8 Hz, 2H), 7.29 (s, 4H), 5.93 (s, 4H). Elemental Analysis (%) for $C_{22}H_{16}AgF_3N_6O_2$: C 47.08, H 2.87, N 14.97; found C 47.01, H 2.81, N 15.08.

Synthesis of [Ag_2(**L**$^{\mathbf{1T}}$)$_2$(CF_3SO_3)$_2$]·2Me_2CO (**28**). 0.06 mmol (0.020 g) of **L**$^{\mathbf{1}}$ were dissolved in 17.5 ml Me_2CO while stirring to produce a colourless solution. 0.12 mmol (0.031 g) of AgOTf were then added. The resulting white solution was filtrated, then layered over n-hexane in a 1:2 ratio. White needles were obtained after 8 days. Selected IR peaks (cm^{-1}): 3404 (w), 1705 (w), 1574 (m), 1517 (w), 1421 (w), 1285 (m), 1234 (m), 1160 (m), 1026 (s), 866 (w), 795 (w), 747 (s), 635 (s). Yield: 32% (based on Ag).^{1}H NMR (600 MHz, DMSO-d_6) δ 8.03 (d, *J* = 8.0 Hz, 2H), 7.80 (d, *J* = 8.3 Hz, 2H), 7.50 (t, *J* = 7.2 Hz, 2H), 7.38 (t, *J* = 7.0 Hz, 2H), 7.30 (s, 4H), 5.94 (s, 4H). Elemental Analysis (%) for $C_{48}H_{44}Ag_2F_6N_{12}O_8S_2$: C 43.98, H 3.38, N 12.82; found C 44.11, H 3.30, N 12.85.

Synthesis of [Ag(**L**$^{\mathbf{2T}}$)(ClO_4)(Me_2CO)] (**29**). 0.12 mmol (0.041 g) of **L**$^{\mathbf{2}}$ were dissolved in 10 ml Me_2CO while stirring to produce a colourless solution. A solution containing 0.12 mmol (0.027 g) of $AgClO_4$ in Me_2CO (10 ml) was slowly added. The resulting white solution was

filtrated, then layered over Et_2O in a 1:2 ratio. White needles were obtained after 4 days. Selected IR peaks (cm^{-1}): 1689 (m), 1594 (w), 1496 (w), 1455 (m), 1318 (m), 1286 (m), 1226 (m), 1159 (w), 1084 (s), 818 (w), 780 (m), 750 (s), 622 (s). Yield: 81% (based on Ag).^{1}H NMR (600 MHz, DMSO-d_6) δ 8.02 (d, J = 8.4 Hz, 2H), 7.72 (d, J = 8.2 Hz, 2H), 7.46 (t, J = 7.5 Hz, 2H), 7.37 (dd, J = 16.6, 9.5 Hz, 3H), 7.31 (t, J = 7.6 Hz, 1H), 7.24 (d, J = 7.7 Hz, 2H), 5.94 (s, 4H). Elemental Analysis (%) for $C_{23}H_{22}AgClN_6O_5$: C 44.60, H 3.86, N 13.87; found C 44.44, H 3.65, N 14.05.

Synthesis of [Ag(**L**$^{\mathbf{2T}}$)(BF_4)(Et_2O)] (**30**). **30** was synthesized using the same method and ratios as **29**, with $AgBF_4$ (0.023 g) as the metal salt. White needles were obtained after 3 days. Selected IR peaks (cm^{-1}): 3098 (w), 1593 (w), 1497 (w), 1456 (w), 1310 (w), 1287 (w), 1226 (m), 1157 (w), 1055 (s), 1034 (s), 818 (w), 779 (m), 751 (s), 741 (s), 698 (w), 640 (w), 618 (w). Yield: 79% (based on Ag). ^{1}H NMR (600 MHz, DMSO-d_6) δ 8.04 (d, J = 8.3 Hz, 2H), 7.73 (d, J = 8.3 Hz, 2H), 7.47 (t, J = 7.6 Hz, 2H), 7.38 (dd, J = 16.0, 8.9 Hz, 3H), 7.33 (t, J = 7.6 Hz, 1H), 7.25 (d, J = 7.5 Hz, 2H), 5.95 (s, 4H). ^{15}N NMR (40 MHz, DMSO-d_6) δ -155.99. Elemental Analysis (%) for $C_{24}H_{26}AgBF_4N_6O$: C 47.32, H 4.30, N 13.80; found C 44.59, H 3.70, N 12.87. This result corresponds to the presence of two water molecules. Elemental Analysis (%) for $(C_{24}H_{26}AgBF_4N_6O)(H_2O)_2$: C 44.68, H 3.69, N 13.03.

Synthesis of $[Ag_2(\mathbf{L}^{\mathbf{3T}})_2(ClO_4)_2]_2$ (**31**). 0.12 mmol (0.041 g) of **L**$^{\mathbf{3}}$ were dissolved in 10 ml Me_2CO while stirring to produce a colourless solution. A solution containing 0.12 mmol (0.027 g) of $AgClO_4$ in Me_2CO (10 ml) was slowly added. The resulting white solution was filtrated, then left undisturbed under room temperature to produce white needles after 2 days. Selected IR peaks (cm^{-1}): 1705 (w), 1594 (w), 1497 (w), 1457 (m), 1226 (m), 1153 (m), 1087 (s), 1025 (m), 953 (w), 856 (w), 780 (m), 765 (m), 741 (s), 622 (s). Yield: 88% (based on Ag).^{1}H NMR (500 MHz, DMSO-d_6) δ 8.04 (d, J = 8.3 Hz, 2H), 7.88 (dd, J = 6.6, 3.2 Hz, 4H), 7.71 (d, J = 8.4 Hz, 2H), 7.50 (t, J = 7.7 Hz, 2H), 7.45 – 7.37 (m, 6H), 7.36 – 7.20 (m, 6H), 6.98 (d, J = 7.3 Hz, 2H), 6.24 (d, J = 4.8 Hz, 8H). These shifts indicate the presence of both isomer forms (1,1 and 1,2) in a 1:1 ratio. Elemental Analysis (%) for $C_{40}H_{32}Ag_2Cl_2N_{12}O_8$: C 43.86, H 2.94, N 13.34; found C 43.78, H 2.85, N 13.37.

Synthesis of [Ag(**L**^{3})(NO_3)] (**32**). 0.06 mmol (0.020 g) of **L**^{3} were dissolved in 10 ml MeCN while stirring to produce a colourless solution. After five minutes a solution containing 0.12 mmol (0.020 g) of $AgNO_3$ in MeCN (10 ml) was slowly added. The resulting white solution was filtrated, then layered over Et_2O in a 1:2 ratio. Colourless blocks were obtained after 1 day. Selected IR peaks (cm^{-1}): 1592 (w), 1495 (w), 1455 (m), 1413 (m), 1290 (m), 1228 (m), 1161 (m), 1135 (w), 1113 (w), 1087 (w), 1033 (w), 1001 (w), 958 (w), 885 (w), 842 (w), 818 (w), 767 (m), 759 (m), 748 (s), 708 (w), 667 (w), 625 (w). Yield: 82% (based on Ag).^{1}H NMR (399 MHz, DMSO-d_6) δ 8.09 (d, J = 8.4 Hz, 2H), 7.78 (d, J = 8.3 Hz, 2H), 7.54 (t, J = 7.6 Hz, 2H), 7.44 (t, J = 7.5 Hz, 2H), 7.28 – 7.21 (m, 2H), 6.96 – 6.89 (m, 2H), 6.27 (s, 4H). ^{15}N NMR (40 MHz, DMSO-d_6) δ -154.37. Elemental Analysis (%) for $C_{20}H_{16}AgN_7O_3$: C 47.08, H 3.16, N 19.22; found C 47.18, H 3.25, N 19.33.

Synthesis of [Ag_2(**L**^{3T})$_2$(CF_3CO_2)$_2$] (**33**). 0.06 mmol (0.020 g) of **L**^{3} were dissolved in 10 ml Me_2CO while stirring to produce a colourless solution. A solution containing 0.12 mmol (0.027 g) of $AgCF_3CO_2$ in Me_2CO (10 ml) was slowly added. The resulting white solution was filtrated, then layered over n-hexane in a 1:2 ratio. White needles were obtained after 2 days. Selected IR peaks (cm^{-1}): 1665 (w), 1595 (w), 1499 (w), 1457 (m), 1222 (s), 1147 (s), 1025 (s), 952 (w), 837 (w), 780 (m), 746 (s), 633 (s). Yield: 52% (based on Ag).^{1}H NMR (600 MHz, DMSO-d_6) δ 8.09 (d, J = 8.5 Hz, 1H), 8.06 (d, J = 8.6 Hz, 1H), 7.92 – 7.86 (m, 2H), 7.79 (d, J = 8.4 Hz, 1H), 7.75 (d, J = 8.4 Hz, 1H), 7.57 – 7.48 (m, 3H), 7.46 – 7.37 (m, 5H), 7.34 – 7.21 (m, 5H), 6.97 (d, J = 7.5 Hz, 1H), 6.94 – 6.89 (m, 2H), 6.28 –6.26 (m, 8H). These shifts indicate the presence of both isomer forms (1,1 and 1,2) in a 1:1 ratio. Elemental Analysis (%) for $C_{44}H_{32}Ag_2F_6N_{12}O_4$: C 47.08, H 2.87, N 14.97; found C 47.00, H 2.84, N 15.06.

Synthesis of [Ag_2(**L**^{3T})(CF_3SO_3)$_2$] (**34**). A procedure similar to the synthesis of **33** was followed, using AgOTf (0.12 mmol, 0.031 g) as the metal salt. White needles were obtained after 1 day. Selected IR peaks (cm^{-1}): 1594 (w), 1498 (w), 1458 (m), 1265 (s), 1241 (s), 1223 (s), 1166 (m), 1023 (s), 956 (w), 861 (w), 766 (w), 751 (s), 740 (s), 629 (s), 606 (w). Yield: 58% (based on Ag).^{1}H NMR (600 MHz, DMSO-d_6) δ 8.08 (d, J = 8.4 Hz, 2H), 8.05 (d, J = 8.4 Hz, 1H), 7.90 – 7.85 (m, 2H), 7.79 (d, J = 8.4 Hz, 2H), 7.76 (d, J = 8.4 Hz, 1H), 7.58 –

7.49 (m, 3H), 7.46 – 7.38 (m, 3H), 7.34 – 7.21 (m, 3H), 6.99 (d, J = 7.5 Hz, 1H), 6.94 (dd, J = 5.6, 3.5 Hz, 2H), 6.27 (s, 6H). These shifts indicate the presence of both isomer forms (1,1 and 1,2) in a 2:1 ratio. Elemental Analysis (%) for $C_{22}H_{16}Ag_2F_6N_6O_6S_2$: C 30.93, H 1.89, N 9.84; found C 31.10, H 2.01, N 9.86.

Synthesis of $[Ag_2(\mathbf{L^{3T}})_2(CF_3CF_2CO_2)_2]\cdot 2Me_2CO$ (**35**). A procedure similar to the synthesis of **33** was followed, using $AgCF_3CF_2CO_2$ (0.12 mmol, 0.033 g) as the metal salt. White needles were obtained after 3 days. Selected IR peaks (cm^{-1}):1661 (m), 1499 (w), 1455 (w), 1319 (m), 1277 (w), 1212 (m), 1166 (m), 1147 (m), 1022 (m), 852 (w), 815 (w), 771 (w), 747 (s), 728 (s), 628 (w). Yield: 64% (based on Ag).^{1}H NMR (600 MHz, DMSO-d_6) δ 8.05 (d, J = 8.4 Hz, 2H), 7.90 (dd, J = 6.6, 3.1 Hz, 4H), 7.74 (d, J = 8.4 Hz, 2H), 7.50 (t, J = 7.7 Hz, 2H), 7.43 (dd, J = 6.6, 3.0 Hz, 4H), 7.39 (t, J = 7.7 Hz, 2H), 7.34 – 7.20 (m, 6H), 6.95 (d, J = 7.5 Hz, 2H), 6.28 (s, 4H), 6.26 (s, 4H). These shifts indicate the presence of both isomer forms (1,1 and 1,2) in a 1:1 ratio. Elemental Analysis (%) for $C_{49}H_{38}Ag_2F_{10}N_{12}O_5$: C 45.96, H 2.99, N 13.12; found C 45.97, H 3.06, N 13.20.

8.4. Catalytic Protocols

Chapter 3

General Catalytic Protocol for the synthesis of 1,4-DHPs (dihydropyridine products **C3D1**-**C3D18**): Into a sealed tube containing the azine (0.2 mmol) and methanol (1 mL), 0.4 mmol of ethyl propiolate and 3 mg of the corresponding Cu catalyst (2 mol%, based on azine amount) were added. The reaction mixture was vigorously stirred at 70 ^{o}C for selected time and the reaction process was monitored by thin layer chromatography (TLC). After completion, the mixture was filtered under reduced pressure through a short pad of Celite and silica gel to withhold any solid material using CH_2Cl_2 (~5 mL) as an eluent. The filtrate was then evaporated under vacuum to give a mixture containing the corresponding dihydropyridine derivative (1,4-DHP). Further purification with column chromatography (solvent mixture with increasing the polarity from hexane to ethyl acetate) afford the 1,4-DHPs in pure form. Supporting Figures for ^{1}H NMR, ^{13}CNMR and ESI-MS may be found in the Appendix.

Diethyl 1-((4-methylbenzylidene)amino)-4-(p-tolyl)-1,4-dihydropyridine-3,5-Dicarboxylate (C3D1)

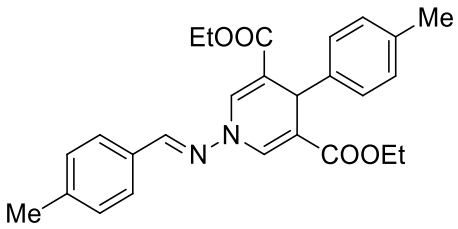

^{1}H-NMR (500 MHz, $CDCl_3$): 8.11 (s, 1H), 7.86 (s, 2H), 7.64 (d, *J* = 8.4 Hz, 2H), 7.26-7.19 (m, 4H), 7.06 (d, *J* = 8.1 Hz, 2H), 4.96 (s, 1H), 4.15 (q, *J* = 7.1 Hz, 4H), 2.41 (s, 3H), 2.28 (s, 3H), 1.25 (t, *J* = 7.1 Hz, 6H). ^{13}C-NMR (125 MHz, $CDCl_3$): 166.5, 143.9, 142.1, 141.1, 136.3, 133.6, 130.6, 129.7, 129.0, 128.0, 127.5, 110.8, 60.5, 37.8, 21.6, 21.1, 14.3. HRMS calcd.: 432.2048 m/z, found: 431.1965 [M-H^{+}].

Diethyl 1-((4-methoxybenzylidene)amino)-4-(4-methoxyphenyl)-1,4-dihydropyridine-3,5-dicarboxylate (C3D2)

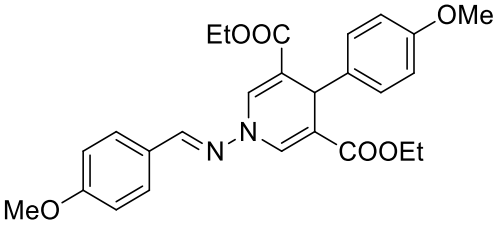

^{1}H-NMR (500 MHz, $CDCl_3$): 8.09 (s, 1H), 7.84 (s, 2H), 7.68 (d, *J* = 8.8 Hz, 2H), 7.23 (d, *J* = 8.6 Hz, 5H), 6.96 (d, *J* = 8.8 Hz, 2H), 6.78 (d, *J* = 8.6 Hz, 2H), 4.94 (s, 1H), 4.16 (q, *J* = 7.1 Hz, 4H), 3.87 (s, 3H), 3.75 (s, 3H), 1.24 (t, *J* = 7.1 Hz, 6H). ^{13}C NMR (125 MHz, $CDCl_3$): 166.6, 161.7, 158.4, 143.9, 137.5, 133.5, 129.2, 129.1, 126.0, 114.5, 113.6, 110.6, 60.5, 55.5, 55.2, 37.4, 14.3. HRMS calcd.: 464.1947 m/z, HRMS found: 463.1864 [M-H^{+}].

Diethyl 1-((2-methoxybenzylidene)amino)-4-(2-methoxyphenyl)-1,4-dihydropyridine-3,5-dicarboxylate (C3D3)

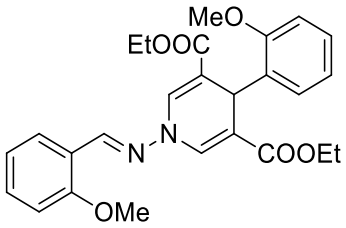

^{1}H-NMR (500 MHz, $CDCl_3$): 8.57 (s, 1H), 7.97 (dd, *J* = 7.8, 1.6 Hz, 1H), 7.87 (s, 1H), 7.44-7.35 (m, 1H), 7.29 (dd, *J* = 7.8, 1.6 Hz, 1H), 7.18-7.13 (m, 1H), 7.01 (t, *J* = 7.8 Hz, 1H), 6.95 (d, *J* = 8.3 Hz, 1H), 6.88-6.84 (m, 2H), 6.81 (d, *J* = 8.3 Hz, 2H), 5.22 (s, 1H), 4.17-4.04 (m, 4H), 3.91 (s, 3H), 3.75 (s, 3H), 1.21 (t, *J* = 7.1 Hz, 6H). ^{13}C-NMR (125 MHz, $CDCl_3$): 166.9, 158.2, 158.0, 138.9, 134.3, 132.4, 131.7, 131.3, 130.9, 128.0, 126.3, 122.0, 121.0, 120.3, 111.1, 109.4, 60.3, 55.6, 55.4, 34.9, 14.2. HRMScalcd: 464.1947 m/z, HRMS found: 463.1864 [M-H^{+}].

Diethyl 1-((3,4-dimethoxybenzylidene)amino)-4-(3,4-dimethoxyphenyl)-1,4-dihydropyridine-3,5-dicarboxylate (C3D4)

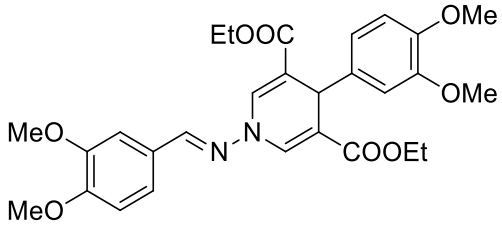

^{1}H NMR (500 MHz, $CDCl_3$): 8.07 (s, 1H), 7.86 (s, 2H), 7.41 (dd, *J* = 8.2, 1.8 Hz, 1H), 7.18 (dd, *J* = 8.2, 1.8 Hz, 1H), 6.96-6.90 (m, 2H), 6.82 (dd, *J* = 8.2, 1.8 Hz, 1H), 6.75 (d, *J* = 8.2 Hz, 1H), 4.95 (s, 1H), 4.24-4.10 (m, 4H), 4.00 (s, 3H), 3.97 (s, 3H), 3.96 (s, 3H), 3.94 (s, 3H), 1.26 (t, *J* = 7.1 Hz, 3H). ^{13}C NMR (125 MHz, $CDCl_3$): 166.6, 151.6, 149.6, 148.5, 147.9, 144.0, 137.9, 133.5, 126.2, 122.8, 120.0, 111.8, 110.9, 110.8, 110.5, 108.0, 60.5, 56.3, 56.1, 55.9, 55.8, 37.7, 14.4. HRMS calcd.: 524.2158 m/z, HRMS found: 523.2075 [M-H^{+}].

Diethyl 1-((2,5-dimethylbenzylidene)amino)-4-(2,5-dimethylphenyl)-1,4-dihydropyridine-3,5-dicarboxylate (C3D5)

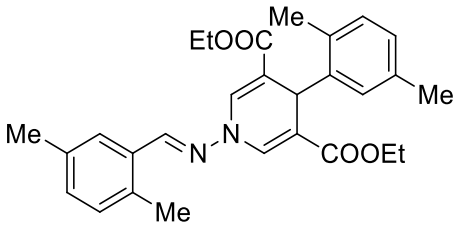

^{1}H NMR (500 MHz, $CDCl_3$): 8.38 (s, 1H), 7.90 (s, 2H), 7.71 (s, 1H), 7.17-7.11 (m, 2H), 6.98-6.93 (m, 2H), 6.86 (d, *J* = 7.6 Hz, 1H), 5.14 (s, 1H), 4.16-4.07 (m, 4H), 2.63 (s, 3H), 2.51 (s, 3H), 2.38 (s, 3H), 2.21 (s, 3H), 1.23 (t, *J* = 7.0 Hz, 6H). ^{13}C NMR (125 MHz, $CDCl_3$): 166.7, 144.1, 142.1, 136.0, 135.4, 134.4, 133.5 (2), 132.9, 131.2, 131.1, 130.8, 129.8, 127.5, 127.4, 111.9, 60.5, 39.0, 21.2, 21.1, 19.4, 19.1, 14.3. HRMS calcd.: 460.2361 m/z, HRMS found: 459.2278 [M-H^{+}].

Diethyl (E)-1-((3-chlorobenzylidene)amino)-4-(3-chlorophenyl)-1,4-dihydropyridine-3,5-dicarboxylate (C3D6)

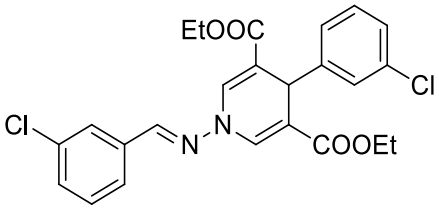

^{1}H NMR (500 MHz, $CDCl_3$): 8.08 (s, 1H), 7.88 (s, 2H), 7.78 (s, 1H), 7.59 (d, *J* = 7.4 Hz, 1H), 7.42-7.33 (m, 2H), 7.27 (s, 1H) 7.25-7.22 (m, 1H), 7.21-7.12 (m, 2H), 4.99 (s, 1H), 4.25-4.09 (m, 4H), 1.25 (t, *J* = 7.3 Hz, 6H). ^{13}C NMR (125 MHz, $CDCl_3$):166.1, 146.6, 141.7, 135.0, 134.1, 133.5, 130.6, 130.3, 130.2, 129.4, 128.4, 127.1 (2), 126.6, 126.0, 110.7, 60.8, 38.3, 14.3. HRMS calcd.: 472.0956 m/z, HRMS found: 495.0848 [M+Na].

Dimethyl 1-((4-methylbenzylidene)amino)-4-(p-tolyl)-1,4-dihydropyridine-3,5-Dicarboxylate (C3D11)

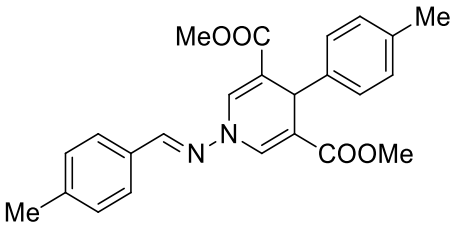

^{1}H-NMR (500 MHz, $CDCl_3$): 8.10 (s, 1H), 7.87 (s, 2H), 7.63 (d, *J* = 8.3 Hz, 2H), 7.26-7-22 (m, 2H), 7.07 (d, *J* = 8.1 Hz, 2H), 4.97 (s, 1H), 3.70 (s, 6H), 2.41 (s, 3H), 2.28 (s, 3H). ^{13}C-NMR (125 MHz, $CDCl_3$):166.9, 144.1, 141.9, 141.2, 136.4, 133.8, 130.5, 129.7, 129.1, 127.9, 127.5, 110.4, 51.7, 37.7, 21.6, 21.1. HRMS calcd.: 404.1735 m/z, HRMS found: 403.1652 [M-H^{+}].

Dimethyl 1-((4-methoxybenzylidene)amino)-4-(4-methoxyphenyl)-1,4-dihydropyridine-3,5-dicarboxylate (C3D12)

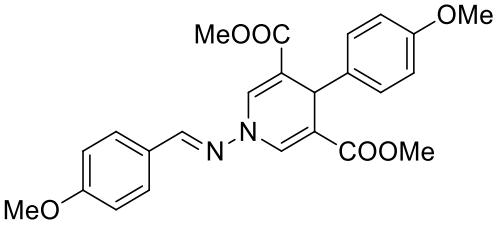

^{1}H NMR (500 MHz, $CDCl_3$): 8.08 (s, 1H), 7.84 (s, 1H), 7.68 (d, *J* = 8.7 Hz, 1H), 7.24 (d, *J* = 8.6 Hz, 1H), 6.96 (d, *J* = 8.7 Hz, 1H), 6.79 (d, *J* = 8.6 Hz, 1H), 4.95 (s, 1H), 3.87 (s, 3H), 3.76 (s, 3H), 3.70 (s, 6H). ^{13}C-NMR (125 MHz, $CDCl_3$):167.0, 161.8, 158.5, 144.1, 137.3, 133.8, 129.2, 129.0, 125.9, 114.3, 113.7, 110.3, 55.5, 55.2, 51.6, 37.3. HRMS calcd.: 436.1634 m/z. HRMS found: 435.1551 [M-H^{+}].

Dimethyl 1-((2-methoxybenzylidene)amino)-4-(2-methoxyphenyl)-1,4-dihydropyridine-3,5-dicarboxylate (C3D13)

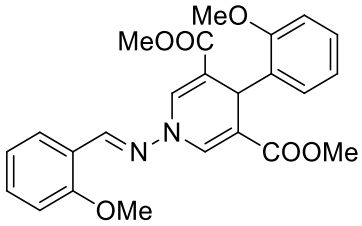

^{1}H NMR (500 MHz, $CDCl_3$):8.57 (s, 1H), 7.96 (d, *J* = 7.8 Hz, 1H), 7.87 (s, 2H), 7.40 (t, *J* = 8.2 Hz, 1H), 7.30 (d, *J* = 7.8 Hz, 1H), 7.16 (t, *J* = 8.2 Hz, 1H), 7.02 (t, *J* = 7.8 Hz, 1H), 6.95 (d, *J* = 8.2 Hz, 1H), 6.88 (d, *J* = 7.8 Hz, 1H) 6.83 (d, *J* = 8.2 Hz, 1H), 5.22 (s, 1H), 3.92 (s, 3H), 3.76 (s, 3H), 3.66 (d,6H). ^{13}C-NMR (125 MHz, $CDCl_3$):167.2, 158.2 (2), 139.1, 134.4, 132.3, 131.8, 131.1, 128.1, 126.3, 122.0, 121.0, 120.5, 111.5, 111.1, 109.0, 55.7, 55.6, 51.5, 34.9. HRMS calcd.: 436.1634 m/z, HRMS found: 435.1551.

Dimethyl 1-((3,4-dimethoxybenzylidene)amino)-4-(3,4-dimethoxyphenyl)-1,4-dihydropyridine-3,5-dicarboxylate (C3D14)

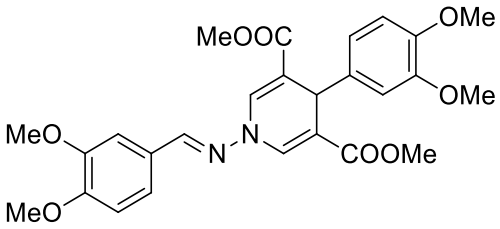

^{1}H-NMR (500 MHz, $CDCl_3$): 8.06 (s, 1H), 7.86 (s, 2H), 7.40 (d, *J*= 1.5 Hz, 1H), 7.17 (d, *J* = 8.2 Hz, 1H), 6.93 (d, *J* = 1.5 Hz, 1H), 6.91 (d, *J* = 8.2 Hz, 1H), 6.82 (dd, *J* = 8.2, 1.5, 1H), 6.75 (d, *J* = 8.2 Hz, 1H), 4.96 (s, 1H), 3.96 (s, 3H), 3.94 (s, 3H), 3.85 (s, 3H), 3.82 (s, 3H), 3.72 (s, 6H). ^{13}C-NMR (125 MHz, $CDCl_3$):166.9, 151.6, 149.6, 148.7, 148.0, 144.2, 137.6, 133.7, 126.2, 122.9, 119.8, 111.7, 111.1, 110.8, 110.2, 108.0, 56.1, 56.0, 55.9, 55.8, 51.7, 37.6. HRMS calcd.: 496.1845 m/z, HRMS found: 495.1762 [M-H^{+}].

Dimethyl 1-((4-chlorobenzylidene)amino)-4-(4-chlorophenyl)-1,4-dihydropyridine-3,5-dicarboxylate (C3D15)

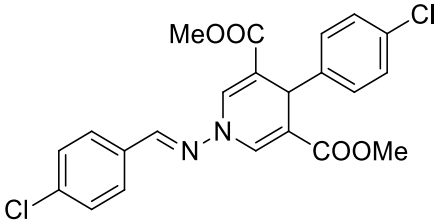

^{1}H NMR (500 MHz, $CDCl_3$): 8.08 (s, 1H), 7.87 (s, 2H), 7.67 (d, *J* = 8.5 Hz, 2H), 7.42 (d, *J* = 8.5 Hz, 2H), 7.26-7.23 (m, 4H), 4.98 (s, 1H), 3.70 (s, 6H). ^{13}C NMR (125 MHz, $CDCl_3$): 166.5, 143.0, 142.3, 136.7, 133.6, 132.7, 131.6, 129.4, 129.3, 128.7, 128.5, 110.4, 51.8, 37.8. HRMS calcd.: 444.0643 m/z, HRMS found: 443.0560 [M-H^{+}]

Diethyl 4-(thiophen-2-yl)-1-((thiophen-2-ylmethylene)amino)-1,4-dihydropyridine-3,5-dicarboxylate (C3D16)

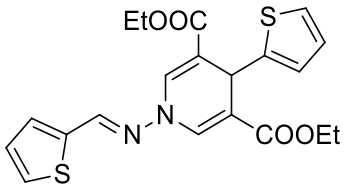

^{1}H NMR (500 MHz, $CDCl_3$): 8.29 (s, 1H), 7.80 (s, 2H), 7.43 (d, *J* = 5.1 Hz, 1H), 7.36 (d, *J* = 3.6 Hz, 1H), 7.12-7.08 (m, 2H) 6.89-6.85 (m, 2H), 5.32 (s, 1H), 4.29-4.19 (m, 4H), 1.29 (t, *J* = 7.1 Hz, 6H). ^{13}C NMR (126 MHz, $CDCl_3$): 166.2, 139.5, 137.9, 137.2, 133.7, 131.1, 129.2, 127.8, 126.8, 124.4, 124.1, 110.1, 60.7, 32.8, 14.4. HRMS calcd.: 416.0912 m/z, HRMS found: 415.0830 [M-H^{+}].

Chapter 4

General Catalytic Protocol for A^3 coupling (propargylamine products **C4P1-C4P23**): A mixture of aldehyde (1 mmol), amine (1.1 mmol), alkyne (1.2 mmol), Cu catalyst (2 mol%, based on aldehyde amount) and 2-propanol (5 ml) was added into a sealed tube and stirred at 90 °C for selected time. After completion, the mixture was filtered upon a short pad of silica (to withhold any solid material) and the filtrate was evaporated under vacuum. The resulting residue was then loaded to a flash column chromatography and the product propargyl amine was isolated through silica gel using a mixture of hexane/EtOAc in a ratio of 10/1, as the eluent. The characterization data of the products matched well with those reported in the literature[374]. Supporting Figures for ^{1}H NMR, ^{13}CNMR and ESI-MS may be found in the Appendix.

1-(1,3-diphenylprop-2-ynyl)pyrrolidine (C4P1)

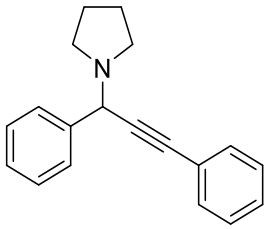

Yellow oil; ^{1}H NMR (500 MHz, $CDCl_3$) δ 7.66 – 7.60 (m, 2H), 7.54 – 7.46 (m, 2H), 7.41 – 7.27 (m, 6H), 4.95 (s, 1H), 2.78 – 2.70 (m, 4H), 1.86 – 1.78 (m, 4H). ^{13}C NMR (126 MHz,

$CDCl_3$) δ 136.41, 131.77, 128.30, 128.23, 128.07, 127.59, 88.81, 85.80, 59.06, 50.20, 23.52. HRMS for $C_{19}H_{20}N$ [M + 1]: calc: 262.1595, found: 262.1590.

1-(3-phenyl-1-(p-tolyl)prop-2-yn-1-yl)pyrrolidine (C4P2)

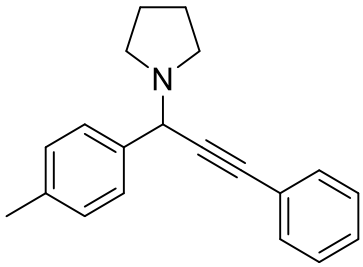

Yellow oil; ^{1}H NMR (500 MHz, $CDCl_3$) δ 7.52 – 7.46 (m, 4H), 7.33 – 7.30 (m, 3H), 7.19 – 7.16 (m, 2H), 4.84 (s, 1H), 2.71 – 2.67 (m, 4H), 2.36 (s, 3H), 1.83 – 1.77 (m, 4H). ^{13}C NMR (126 MHz, $CDCl_3$) δ 134.0, 133.7, 131.8, 129.0, 128.4, 128.3, 128.3, 128.2, 118.6, 88.3, 58.8, 50.2, 23.5, 21.1. HRMS for $C_{20}H_{21}N$ [M]: calc: 274.1595, found: 274.1590.

1-(1-(4-methoxyphenyl)-3-phenylprop-2-yn-1-yl)pyrrolidine (C4P3)

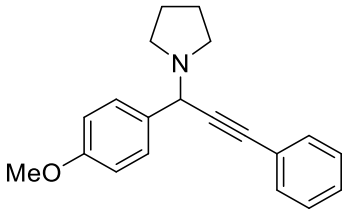

Yellow oil; ^{1}H NMR (500 MHz, $CDCl_3$) δ 7.56 – 7.45 (m, 4H), 7.35 – 7.28 (m, 3H), 6.93 – 6.87 (m, 2H), 4.83 (s, 1H), 3.82 (s, 3H), 2.70 – 2.66 (m, 4H), 1.82 – 1.79 (m, 4H). ^{13}C NMR (126 MHz, $CDCl_3$) δ 159.0, 131.7, 129.3, 128.2, 128.0, 124.2, 113.6, 88.3, 86.6, 58.5, 55.3, 50.2, 23.9, 23.5. EI for $C_{20}H_{21}NO$: 291 [M].

1-(1-(4-chlorophenyl)-3-phenylprop-2-yn-1-yl)pyrrolidine (C4P4)

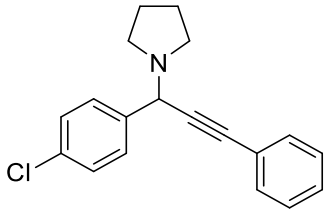

Yellow oil; ^{1}H NMR (500 MHz, $CDCl_3$) δ 7.59 – 7.56 (m, 2H), 7.52 – 7.38 (m, 4H), 7.35 – 7.33 (m, 3H), 4.99 (s, 1H), 2.81 – 2.70 (m, 4H), 1.87 – 1.78 (m, 4H). ^{13}C NMR (126 MHz,

$CDCl_3$) δ 137.8, 131.8, 129.7, 128.4, 128.3, 127.9, 127.6, 120.7, 88.3, 50.1, 23.5. HRMS for $C_{19}H_{19}ClN$ [M + 1]: calc: 296.1205, found: 296.1201.

1-(3-phenyl-1-(4-(trifluoromethyl)phenyl)prop-2-ynyl)pyrrolidine (C4P5)

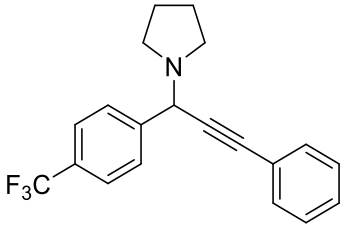

Pale yellow oil; ^{1}H NMR (500 MHz, $CDCl_3$) δ 7.79 – 7.73 (m, 2H), 7.66 – 7.60 (m, 2H), 7.53 – 7.47 (m, 2H), 7.37 – 7.32 (m, 3H), 4.97 (s, 1H), 2.75 – 2.64 (m, 4H), 1.86 – 1.77 (m, 4H). ^{13}C NMR (126 MHz, $CDCl_3$) δ 143.7, 131.8, 129.9, 128.5, 128.3, 125.2, 125.2, 125.2, 125.1, 124.0, 122.9, 110.9, 102.6, 87.6, 85.6, 58.6, 50.1, 31.6, 23.6. HRMS for $C_{20}H_{19}F_3N$ [M + 1]: calc: 330.1469, found: 330.1464.

2-(3-phenyl-1-(pyrrolidin-1-yl)prop-2-yn-1-yl)phenol (C4P6)

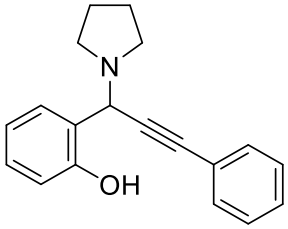

Yellow oil; ^{1}H NMR (500 MHz, $CDCl_3$) δ 7.58 – 7.51 (m, 3H), 7.40 – 7.33 (m, 3H), 7.26 – 7.18 (m, 1H), 6.89 – 6.83 (m, 2H), 5.29 (s, 1H), 2.95 – 2.77 (m, 4H), 1.93 – 1.85 (m, 4H). ^{13}C NMR (126 MHz, $CDCl_3$) δ 157.6, 131.9, 129.3, 128.5, 128.4, 127.8, 122.6, 122.2, 118.9, 116.2, 89.0, 83.0, 57.1, 48.9, 23.9. HRMS for $C_{19}H_{20}NO$ [M + 1]: calc: 278.1544, found: 278.1539.

1-(1-(naphthalen-1-yl)-3-phenylprop-2-yn-1-yl)pyrrolidine (C4P7)

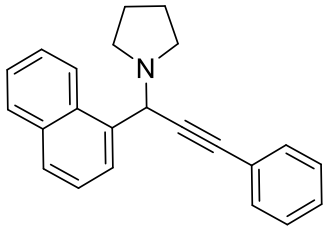

Yellow oil; ^{1}H NMR (500 MHz, $CDCl_3$) δ 8.44 (d, J = 8.5 Hz, 1H), 7.96 – 7.85 (m, 3H), 7.57 – 7.44 (m, 5H), 7.36 – 7.30 (m, 3H), 5.59 (s, 1H), 2.86 – 2.64 (m, 3H), 1.84 – 1.73 (m, 4H). ^{13}C NMR (126 MHz, $CDCl_3$) δ 136.5, 133.9, 131.8, 131.5, 129.0, 128.4, 128.2, 127.9, 126.9, 125.9, 125.8, 125.5, 124.9, 124.8, 124.8, 124.4, 123.4, 87.4, 86.8, 56.7, 50.2, 23.7, 11.4. EI for $C_{23}H_{21}N$: 311 [M].

1-(1-(naphthalen-2-yl)-3-phenylprop-2-yn-1-yl)pyrrolidine (C4P8)

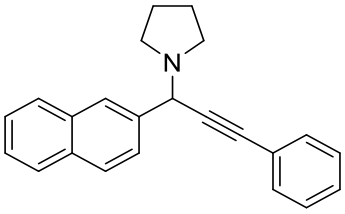

Yellow oil; ^{1}H NMR (500 MHz, $CDCl_3$) δ 8.06 (s, 1H), 7.88 – 7.83 (m, 3H), 7.78 – 7.75 (m, 1H), 7.55 – 7.52 (m, 2H), 7.49 – 7.47 (m, 2H), 7.37 – 7.31 (m, 3H), 5.04 (s, 1H), 2.78 – 2.71 (m, 4H), 1.86 – 1.80 (m, 4H). ^{13}C NMR (126 MHz, $CDCl_3$) δ 137.2, 133.0, 131.8, 128.2, 128.1, 127.9, 127.6, 126.8, 126.5, 125.9, 125.8, 123.3, 88.3, 87.6, 59.3, 50.4, 23.6, 21.0. EI for $C_{23}H_{21}N$: 311 [M].

1-(1-cyclohexyl-3-phenylprop-2-ynyl)pyrrolidine (C4P9)

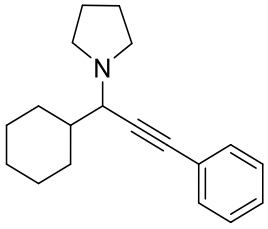

Yellow oil; ^{1}H NMR (500 MHz, $CDCl_3$) δ 7.48 – 7.40 (m, 2H), 7.34 – 7.26 (m, 3H), 3.37 (d, *J* = 8.4 Hz, 1H), 2.79 – 2.71 (m, 2H), 2.69 – 2.64 (m, 2H), 2.15 – 2.07 (m, 1H), 2.00 – 1.95 (m, 1H), 1.84 – 1.77 (m, 6H), 1.73 – 1.66 (m, 1H), 1.65 – 1.54 (m, 1H), 1.34 – 1.06 (m, 5H).

^{13}C NMR (126 MHz, $CDCl_3$) δ 131.7, 128.1, 127.6, 123.7, 85.8, 61.2, 50.0, 41.4, 30.7, 30.3, 26.7, 26.2, 26.2, 23.6. HRMS for $C_{19}H_{26}N$ [M + 1]: calc: 268.2065, found: 268.2060.

1-(1-phenyloct-1-yn-3-yl)pyrrolidine (C4P10)

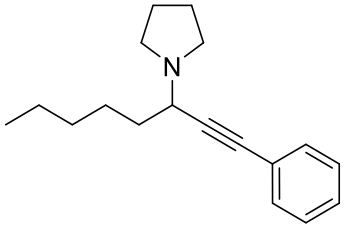

Yellow oil; ^{1}H NMR (500 MHz, $CDCl_3$) δ 7.45 – 7.42 (m, 2H), 7.31 – 7.29 (m, 3H), 3.70 (dd, *J* = 7.5 Hz, 1H), 2.81 – 2.69 (m, 4H), 1.85 – 1.80 (m, 4H), 1.77 – 1.70 (m, 1H), 1.52 – 1.48 (m, 1H), 1.38 – 1.26 (m, 6H), 0.92 (t, *J* = 6.5 Hz, 3H). ^{13}C NMR (126 MHz, $CDCl_3$) δ 138.0, 136.6, 131.7, 128.2, 92.1, 84.0, 51.3, 48.6, 31.6, 26.4, 23.5, 22.6, 22.6, 14.1. HRMS for $C_{18}H_{26}N$ [M + 1]: calc: 256.2065, found: 256.2060.

1-(1-cyclohexyl-3-phenylprop-2-ynyl)piperidine (C4P12)

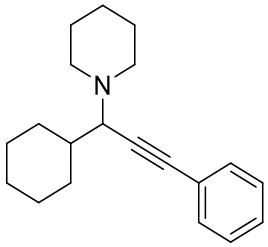

Yellow oil; ^{1}H NMR (500 MHz, $CDCl_3$) δ 7.50 – 7.44 (m, 2H), 7.33 – 7.28 (m, 3H), 3.14 (d, *J* = 9.9 Hz, 1H), 2.69 – 2.64 (m, 2H), 2.47 – 2.41 (m, 2H), 2.18 – 2.04 (m, 2H), 1.84 – 1.76 (m, 2H), 1.75 – 1.54 (m, 6H), 1.50 – 1.44 (m, 2H), 1.35 – 1.17 (m, 3H), 1.10 – 0.92 (m, 2H). ^{13}C NMR (126 MHz, $CDCl_3$) δ 131.7, 128.1, 127.6, 123.9, 87.8, 86.2, 64.4, 39.6, 31.3, 30.5, 26.8, 26.3, 26.3, 26.1, 24.8. HRMS for $C_{20}H_{28}N$ [M + 1]: calc: 282.2221, found: 282.2216.

1-[1-Cyclohexyl-3-(4-methylphenyl)-2-propynyl]hexamethylamine (C4P13)

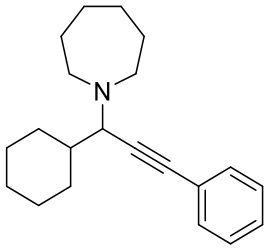

Yellow oil; ^{1}H NMR (500 MHz, $CDCl_3$) δ 7.45 – 7.42 (m, 2H), 7.31 – 7.26 (m, 3H), 3.17 (d, *J* = 10.1 Hz, 1H), 2.85 – 2.78 (m, 2H), 2.62 – 2.55 (m, 2H), 2.20 – 2.08 (m, 2H), 1.81 – 1.75 (m, 2H), 1.72 – 1.62 (m, 8H), 1.56 – 1.48 (m, 1H), 1.37 – 1.17 (m, 3H), 1.06 – 0.88 (m, 2H). ^{13}C NMR (126 MHz, $CDCl_3$) δ 131.7, 128.1, 127.5, 124.0, 90.5, 84.9, 65.2, 52.7, 40.8, 31.1, 30.7, 29.3, 27.1, 26.8, 26.2, 26.1. HRMS for $C_{21}H_{30}N$ [M + 1]: calc: 296.2378, found: 296.2373.

4-(1-cyclohexyl-3-phenylprop-2-ynyl)morpholine (C4P14)

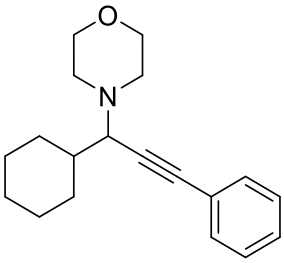

Yellow oil; ^{1}H NMR (500 MHz, $CDCl_3$) δ 7.48 – 7.42 (m, 2H), 7.33 – 7.27 (m, 3H), 3.81 – 3.69 (m, 4H), 3.15 (d, *J* = 9.8 Hz, 1H), 2.75 – 2.68 (m, 2H), 2.57 – 2.49 (m, 2H), 2.16 – 2.02 (m, 2H), 1.83 – 1.58 (m, 4H), 1.36 – 0.94 (m, 5H). ^{13}C NMR (126 MHz, $cdcl_3$) δ 131.7, 128.2, 127.8, 123.4, 86.8, 86.6, 67.2, 64.0, 50.0, 39.1, 31.0, 30.4, 26.7, 26.2, 26.0. HRMS for $C_{19}H_{26}NO$ [M + 1]: calc: 284.2014, found: 284.2011.

1-(1-cyclohexyl-3-phenylprop-2-ynyl)indoline (C4P15)

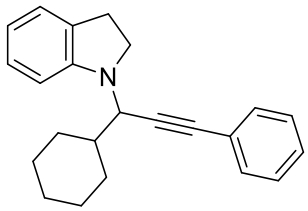

Yellow oil; ^{1}H NMR (500 MHz, $CDCl_3$) δ 7.39 – 7.32 (m, 2H), 7.29 – 7.24 (m, 3H), 7.11 (t, *J* = 7.0 Hz, 2H), 6.70 (t, *J* = 7.3 Hz, 1H), 6.60 (d, *J* = 7.6 Hz, 1H), 4.17 (d, *J* = 10.0 Hz, 1H), 3.57 – 3.43 (m, 2H), 3.07 – 2.98 (m, 2H), 2.24 (d, *J* = 12.4 Hz, 1H), 2.13 (d, *J* = 12.0 Hz, 1H), 1.91 – 1.72 (m, 4H), 1.42 – 1.12 (m, 4H), 1.11 – 1.00 (m, 1H). ^{13}C NMR (126 MHz, $CDCl_3$) δ 151.6, 131.8, 130.1, 128.1, 127.8, 127.1, 124.4, 123.3, 117.8, 107.6, 87.0, 85.2, 55.3, 48.3, 41.1, 31.5, 31.0, 30.2, 28.4, 26.6, 26.1, 26.0. HRMS for $C_{23}H_{26}N$ [M + 1]: calc: 316.2065, found: 316.2060.

1-cyclohexyl-N,N-diethyl-3-phenylprop-2-yn-1-amine (C4P16)

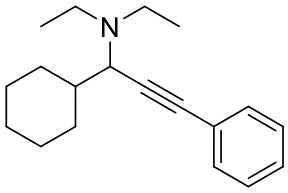

Yellow oil; ^{1}H NMR (500 MHz, $CDCl_3$) δ 7.45 – 7.39 (m, 2H), 7.31 – 7.26 (m, 3H), 3.31 (d, J = 9.9 Hz, 1H), 2.72 – 2.64 (m, 2H), 2.48 – 2.40 (m, 2H), 2.15 – 2.07 (m, 2H), 1.82 – 1.65 (m, 4H), 1.29 – 1.12 (m, 4H), 1.07 (t, J = 7.2 Hz, 6H), 0.94 – 0.85 (m, 1H). ^{13}C NMR (126 MHz, $CDCl_3$) δ 132.5, 131.6, 129.2, 128.4, 128.1, 127.5, 121.8, 81.5, 77.3, 77.0, 76.7, 59.4, 44.9, 40.3, 31.4, 30.9, 30.7, 26.8, 26.2, 26.0, 13.7. HRMS for $C_{19}H_{28}N$ [M + 1]: calc: 270.2221, found: 270.2216

N-(1-cyclohexyl-3-phenylprop-2-yn-1-yl)-N-methylaniline (C4P17)

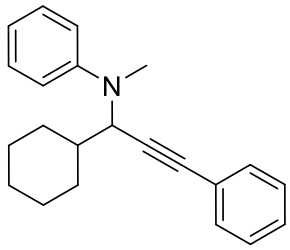

Yellow oil; ^{1}H NMR (500 MHz, $CDCl_3$) δ 7.44 – 7.32 (m, 3H), 7.32 – 7.23 (m, 4H), 6.92 – 6.86 (m, 2H), 6.81 – 6.73 (m, 1H), 4.36 (d, J = 9.6 Hz, 1H), 2.93 (s, 3H), 2.22 – 2.14 (m, 1H), 1.95 – 1.67 (m, 7H), 1.21 – 0.95 (m, 3H). ^{13}C NMR (126 MHz, $CDCl_3$) δ 150.6, 132.5, 131.7, 129.1, 129.0, 128.4, 128.1, 127.9, 123.4, 117.6, 114.4, 88.3, 87.5, 58.8, 41.4, 33.4, 30.7, 30.2, 26.5, 26.1, 25.9. EI for $C_{22}H_{25}N$: 303 [M]

1-(1-cyclohexylhept-2-yn-1-yl)pyrrolidine (C4P22)

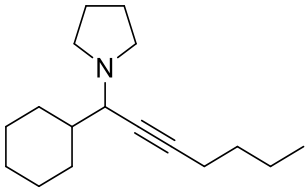

Yellow oil; ^{1}H NMR (500 MHz, $CDCl_3$) δ 3.08 (d, J = 8.2 Hz, 1H), 2.67 – 2.52 (m, 4H), 2.23 (td, J = 6.9, 2.1 Hz, 2H), 2.03 – 1.96 (m, 2H), 1.90 – 1.83 (m, 2H), 1.79 – 1.71 (m, 2H), 1.70 – 1.63 (m, 2H), 1.54 – 1.01 (m, 11H), 0.92 (t, J = 7.2 Hz, 3H). ^{13}C NMR (126 MHz, $CDCl_3$) δ 87.2, 85.5, 60.6, 50.0, 41.4, 31.3, 30.7, 30.0, 29.7, 26.8, 26.4, 26.3, 26.2, 23.6, 22.0, 18.4, 13.6. HRMS for $C_{17}H_{30}N$ [M + 1]: calc. 248.2378, found 248.2373.

1-(1-cyclohexyl-3-(4-(trifluoromethyl)phenyl)prop-2-ynyl)pyrrolidine (C4P23)

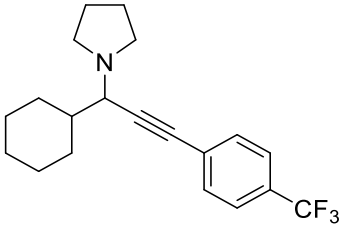

Yellow oil; ^{1}H NMR (500 MHz, $CDCl_3$) δ 7.58 – 7.50 (m, 4H), 3.38 (d, *J* = 8.5 Hz, 1H), 2.78 – 2.70 (m, 2H), 2.69 – 2.61 (m, 2H), 2.11 – 2.06 (m, 1H), 2.01 – 1.95 (m, 1H), 1.81 (s, 1H), 1.73 – 1.55 (m, 2H), 1.36 – 1.04 (m, 8H), 0.93 – 0.87 (m, 2H). ^{13}C NMR (126 MHz, $CDCl_3$)

δ 131.9, 129.5 (q, *J* = 32.6 Hz), 127.5, 127.2, 125.1 (q, *J* = 3.8 Hz), 122.9, 120.7, 90.9, 84.6, 61.2, 60.3, 50.0, 41.3, 31.6, 30.7, 30.3, 26.7, 26.2, 26.1, 23.6, 22.6, 14.0. HRMS for $C_{20}H_{24}F_3N$ [M + 1]: calc: 336.1939, found: 336.1934.

Chapter 5

General catalytic protocol for alkyne-azide cycloaddition (triazole products **C5T1-C5T17**): To a sealed tube containing 0.5 mmol of sodium azide (0.033 g) in 3 mL of ethanol, 0.5 mmol of organic halide or boronic acid, 0.5 mmol of alkyne and 5 mol% of the catalyst were added and the mixture was stirred at reflux for the appropriate time. After completion of the reaction, the mixture was filtered upon a short pad of silica (to withhold any solid material) and the filtrate was evaporated under vacuum. The resulting residue was then separated by column chromatography using silica gel and a mixture of hexane/EtOAc (5/1 ratio for triazoles deriving from organic halides, 10/1 ratio for triazoles deriving from boronic acid) as the eluent, to afford the corresponding triazole product in pure form. The characterization data of the products matched well with those reported in the literature. Supporting Figures for ^{1}H NMR, ^{13}CNMR and ESI-MS may be found in the Appendix.

1-benzyl-4-phenyl-1H-1,2,3-triazole (C5T1)[375]

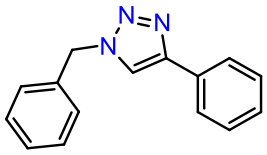

Yellow oil; ^{1}H NMR (500 MHz, $CDCl_3$) δ 7.81 (d, *J* = 7.7 Hz, 2H), 7.68 (s, 1H), 7.42 – 7.30 (m, 8H), 5.59 (s, 2H). ^{13}C NMR (126 MHz, $CDCl_3$) δ 134.5, 129.2, 128.9, 128.8, 128.3, 128.1, 125.8, 54.4. HRMS for $C_{15}H_{14}N_3$ [M + 1]: calc: 236.1182, found: 236.1174.

1-benzyl-4-(4-methoxy)phenyl-1H-1,2,3-triazole (C5T2)[375]

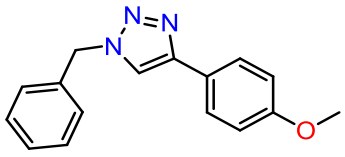

Yellow oil; ^{1}H NMR (500 MHz, $CDCl_3$) δ 7.75 – 7.69 (m, 2H), 7.58 (s, 1H), 7.40 – 7.34 (m, 3H), 7.30 (d, *J* = 7.0 Hz, 2H), 6.92 (d, *J* = 7.7 Hz, 2H), 5.56 (s, 2H), 3.82 (s, 3H). ^{13}C NMR

(126 MHz, $CDCl_3$) δ 159.6, 148.1, 134.7, 129.1, 128.7, 128.0, 127.0, 123.3, 118.7, 114.2, 55.3, 54.2. HRMS for $C_{16}H_{16}N_3O$ [M + 1]: calc: 266.1288, found: 266.1279.

1-benzyl-4-butyl-1H-1,2,3-triazole (C5T3)[375]

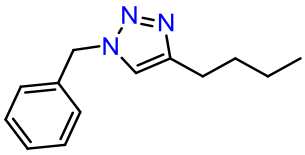

Yellow oil; ^{1}H NMR (600 MHz, $CDCl_3$) δ 7.37 – 7.28 (m, 3H), 7.23 – 7.20 (m, 2H), 7.19 (s, 1H), 5.44 (s, 2H), 2.66 (t, *J* = 7.8 Hz, 2H), 1.60 (p, *J* = 7.7 Hz, 2H), 1.33 (q, *J* = 7.5 Hz, 2H), 0.88 (t, *J* = 7.4 Hz, 3H). ^{13}C NMR (151 MHz, $CDCl_3$) δ 148.8, 135.0, 129.0, 128.5, 127.9, 120.6, 53.9, 31.5, 25.4, 22.3, 13.8. HRMS for $C_{13}H_{18}N_3$ [M + 1]: calc: 216.1495, found: 216.1494.

(1-benzyl-1H-1,2,3-triazol-4-yl)methanol (C5T4)[375]

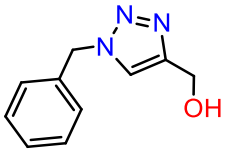

Yellow oil; ^{1}H NMR (600 MHz, $CDCl_3$) δ 7.48 (s, 1H), 7.38 – 7.30 (m, 3H), 7.29 – 7.22 (m, 2H), 5.48 (s, 2H), 4.72 (s, 2H). ^{13}C NMR (151 MHz, $CDCl_3$) δ 148.4, 134.5, 129.1, 128.8, 128.1, 122.2, 56.2, 54.2. HRMS for $C_{10}H_{12}N_3O$ [M + 1]: calc: 190.0975, found: 190.0968.

2-(1-benzyl-1H-1,2,3-triazol-4-yl)ethanol (C5T5)[375]

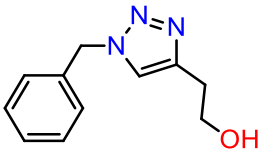

Yellow oil; ^{1}H NMR (600 MHz, $CDCl_3$) δ 7.38 – 7.30 (m, 4H), 7.27 – 7.23 (m, 2H), 5.48 (s, 2H), 3.91 (s, 2H), 2.90 (t, *J* = 6.1, 2.0 Hz, 2H). ^{13}C NMR (151 MHz, $CDCl_3$) δ 146.0, 134.7, 129.1, 128.7, 128.1, 121.5, 61.5, 54.1, 28.7. HRMS for $C_{11}H_{14}N_3O$ [M + 1]: calc: 204.1131, found: 204.1131.

Ethyl 1-benzyl-1H-1,2,3-triazole-4-carboxylate (C5T6)

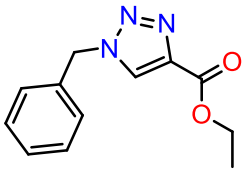

^{1}H NMR (600 MHz, $CDCl_3$) δ 7.97 (s, 1H), 7.31 – 7.27 (m, 3H), 7.23 – 7.17 (m, 2H), 5.58 (s, 2H), 4.40 (q, *J* = 7.2 Hz, 2H), 1.39 (t, *J* = 7.1 Hz, 3H). The found values match well to those in the literature.[375]

1-butyl-4-phenyl-1H-1,2,3-triazole (C5T7)[376]

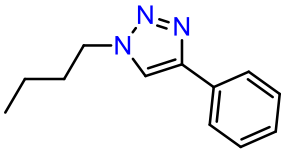

Yellow oil; ^{1}H NMR (500 MHz, $CDCl_3$) δ 7.84 (d, *J* = 7.6 Hz, 2H), 7.76 (s, 1H), 7.42 (t, *J* = 7.6 Hz, 2H), 7.33 (t, *J* = 7.4 Hz, 1H), 4.41 (t, *J* = 7.2 Hz, 2H), 1.99 – 1.89 (m, 2H), 1.45 – 1.34 (m, 2H), 0.97 (t, *J* = 7.4 Hz, 3H). ^{13}C NMR (126 MHz, $CDCl_3$) δ 148.6, 130.7, 128.8, 128.1, 125.7, 119.4, 50.2, 32.3, 19.7, 13.5. HRMS for $C_{12}H_{16}N_3$ [M + 1]: calc: 202.1339, found: 202.1341.

1-butyl-4-(4-methoxy-phenyl)-1H-1,2,3-triazole (C5T8)[376]

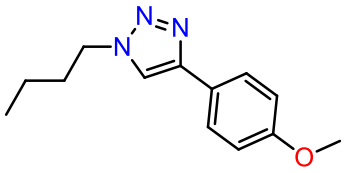

Yellow oil; ^{1}H NMR (500 MHz, $CDCl_3$) δ 7.76 (d, *J* = 8.3 Hz, 2H), 7.66 (s, 1H), 6.96 (d, *J* = 8.3 Hz, 2H), 4.40 (t, *J* = 7.3 Hz, 2H), 3.85 (s, 3H), 1.97 – 1.90 (m, 2H), 1.44 – 1.36 (m, 2H), 0.98 (t, *J* = 7.4 Hz, 3H). ^{13}C NMR (151 MHz, $CDCl_3$) δ 159.6, 150.6, 133.6, 127.0, 118.6, 114.2, 77.2, 77.0, 76.8, 55.3, 50.1, 32.3, 19.7, 13.5. HRMS for $C_{13}H_{18}N_3O$ [M + 1]: calc: 232.1444, found: 232.1447.

1,4-dibutyl-1H-1,2,3-triazole (C5T9)[377]

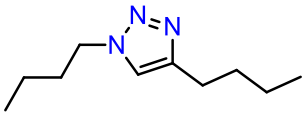

Yellow oil; ^{1}H NMR (500 MHz, $CDCl_3$) δ 7.27 (s, 1H), 4.32 (t, *J* = 7.2 Hz, 2H), 2.71 (t, *J* = 7.7 Hz, 2H), 1.91 – 1.83 (m, 2H), 1.69 – 1.61 (m, 2H), 1.43 – 1.30 (m, 4H), 1.00 – 0.89 (m, 6H). ^{13}C NMR (126 MHz, $CDCl_3$) δ 148.3, 120.4, 49.9, 32.3, 31.6, 25.4, 22.3, 19.7, 13.8, 13.5. HRMS for $C_{10}H_{20}N_3$ [M + 1]: calc: 182.1652, found: 182.1652.

(1-Butyl-1H-1,2,3-triazol-4-yl)methanol (C5T10)[378]

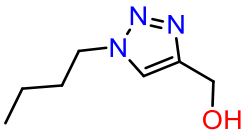

Light yellow oil; ^{1}H NMR (500 MHz, $CDCl_3$) δ 7.54 (s, 1H), 4.80 (s, 2H), 4.36 (t, *J* = 7.2 Hz, 2H), 1.89 (p, *J* = 7.5 Hz, 2H), 1.42 – 1.26 (m, 2H), 0.95 (t, *J* = 7.4 Hz, 3H). ^{13}C NMR (126 MHz, $CDCl_3$) δ 147.6, 121.7, 56.5, 50.1, 32.2, 19.7, 13.4. HRMS for $C_7H_{14}N_3O$ [M + 1]: calc: 156.1131, found: 156.1134.

2-(1-butyl-1H-1,2,3-triazol-4-yl)ethanol (C5T11)

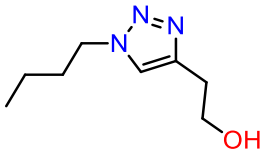

Light yellow oil; ^{1}H NMR (600 MHz, $CDCl_3$) δ 7.40 (s, 1H), 4.32 (t, *J* = 7.2 Hz, 2H), 3.96 (s, 2H), 2.93 (t, *J* = 5.7 Hz, 2H), 1.87 (p, *J* = 7.4 Hz, 2H), 1.38 – 1.24 (m, 2H), 0.95 (t, *J* = 7.3 Hz, 3H). ^{13}C NMR (126 MHz, $CDCl_3$) δ 147.1, 121.6, 61.6, 50.0, 32.2, 28.6, 19.7, 13.4. HRMS for $C_7H_{14}N_3O$ [M + 1]: calc: 170.1288, found: 170.1288.

1,4-Diphenyl-1H-[1,2,3]-triazole (C5T12)[379]

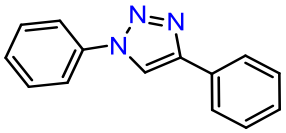

Yellow oil; ^{1}H NMR (600 MHz, $CDCl_3$) δ 8.20 (s, 1H), 7.92 (d, *J* = 7.4 Hz, 2H), 7.80 (d, *J* = 7.6 Hz, 2H), 7.55 (t, *J* = 7.6 Hz, 2H), 7.49 – 7.43 (m, 3H), 7.40 – 7.34 (m, 1H). ^{13}C NMR (151 MHz, $CDCl_3$) δ 148.4, 137.1, 130.2, 129.8, 128.9, 128.8, 128.4, 125.8, 120.5, 117.6, 77.2, 77.0, 76.8. HRMS for $C_{14}H_{12}N_3$ [M + 1]: calc: 222.1026, found: 222.1026.

(1-phenyl-1H-1,2,3-triazol-4-yl)methanol (C5T14)[380]

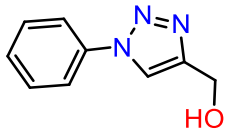

Light yellow oil; ^{1}H NMR (600 MHz, $CDCl_3$) δ 7.98 (s, 1H), 7.73 (d, *J* = 7.6 Hz, 2H), 7.53 (t, *J* = 7.8 Hz, 2H), 7.45 (t, *J* = 7.5 Hz, 1H), 4.91 (s, 2H). ^{13}C NMR (151 MHz, $CDCl_3$) δ 148.2, 135.6, 129.8, 128.9, 120.6, 119.9, 56.7. HRMS for $C_9H_9N_3ONa$ [M + Na]: calc: 198.0638, found: 198.0631.

2-(1-phenyl-1H-1,2,3-triazol-4-yl)ethanol (C5T15)[381]

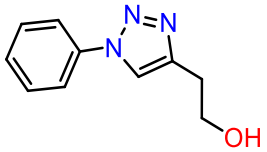

Light yellow oil; ^{1}H NMR (600 MHz, $CDCl_3$) δ 7.85 (s, 1H), 7.73 (d, *J* = 7.9 Hz, 2H), 7.53 (t, *J* = 7.7 Hz, 2H), 7.44 (t, *J* = 7.2 Hz, 1H), 4.03 (t, *J* = 5.9 Hz, 2H), 3.21 (t, *J* = 6.3 Hz, 1H), 3.06 (t, *J* = 5.8 Hz, 2H). ^{13}C NMR (151 MHz, $CDCl_3$) δ 146.2, 135.6, 129.7, 128.7, 120.5, 119.8, 77.2, 77.0, 76.8, 61.6, 28.7. HRMS for $C_{10}H_{11}N_3ONa$ [M + Na]: calc: 212.0794, found: 212.0786.

Chapter 6

General catalytic protocol for A^3 coupling (propargylamine products **C6P1-C6P18**): A mixture of aldehyde (1 mmol), amine (1.1 mmol), alkyne (1.3 mmol), Ag catalyst (0.5 mol%, based on the aldehyde amount) and 2-propanol (5 ml) was added into a sealed tube and stirred

at 90 °C for appropriate time. After completion of the reaction, the mixture was left to cool to room temperature, filtered upon a short pad of silica (to separate any solid material) and the filtrate was evaporated under vacuum. The corresponding propargyl amine was isolated in pure form by column chromatography using silica gel and a solvent mixture of hexane/EtOAc in a ratio of 10/1 as the eluent. The characterization data of the products matched well with those reported in the respective studies in Chapter 4.

General catalytic protocol for alkyne hydration (ketone products **C6K1**-**C6K3**): A mixture of alkyne (1 mmol), water (150 µl), Ag catalyst (3 mol%, based on the alkyne amount) and methanol (1.5 ml) was added into a sealed tube and stirred at 90 °C for 24 hr. The mixture was then allowed to cool to room temperature and filtered upon a short pad of silica (to withhold any solid material). The resulting residue was then loaded to a flash column chromatography using silica gel and the corresponding ketone was isolated in pure form using a mixture of hexane/EtOAc in a ratio of 10/1 (for **C6K1**, **C6K2**) or 3/1 (for **C6K3**), as the eluent. The characterization data of the products matched well with those reported in the literature[337,339]. Supporting Figures for ^{1}H NMR, ^{13}CNMR and EI-MS may be found in the Appendix.

Acetophenone (C6K1)

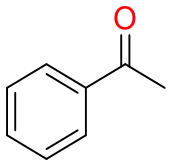

Yellow oil; ^{1}H NMR (500 MHz, $CDCl_3$) δ 7.91 (d, *J* = 8.3 Hz, 2H), 7.50 (t, *J* = 6.6 Hz, 1H), 7.40 (t, *J* = 7.7 Hz, 2H), 2.54 (s, 3H). ^{13}C NMR (126 MHz, $cdcl_3$) δ 198.0, 137.1, 133.0, 128.5, 128.2, 26.5. GCMS (EI) m/z: 120 (M^+).

4-methoxyacetophenone (C6K2)

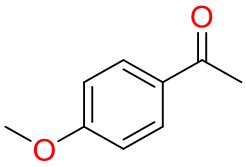

Yellow oil; ^{1}H NMR (500 MHz, $CDCl_3$) δ 7.92 (d, *J* = 8.8 Hz, 2H), 6.92 (d, *J* = 8.8 Hz, 2H), 3.85 (s, 3H), 2.54 (s, 3H). ^{13}C NMR (126 MHz, $CDCl_3$) δ 196.8, 163.5, 130.6, 130.3, 113.6, 55.4, 26.3. MS (EI) m/z: 151 (M^+).

2-hexanone (C6K3)

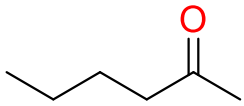

Yellow oil; ^{1}H NMR (600 MHz, $CDCl_3$) δ 2.41 (t, *J* = 7.5 Hz, 2H), 2.12 (s, 3H), 1.53 (p, *J* = 7.5 Hz, 2H), 1.29 (q, *J* = 7.4 Hz, 2H), 0.88 (t, *J* = 7.4 Hz, 3H). ^{13}C NMR (151 MHz, $CDCl_3$) δ 210.5, 43.5, 29.7, 25.9, 22.2, 13.7. GCMS (EI) m/z: 100 (M^+).

Chapter 9: Crystallographic Data

9.1. Crystallographic Data of Ligands

Table 9.1. Crystal data and structure refinement for ligands **L[1]**, **L[3]**, **L[4]**.

Compound	**L[1]**	**L[3]**	**L[4]**
Empirical formula	$C_{20}H_{16}N_6$	$C_{20}H_{16}N_6$	$C_{22}H_{20}N_6$
Formula weight	340.39	340.39	368.44
Temperature/K	100	100(2)	173
Crystal system	monoclinic	triclinic	triclinic
Space group	$P2_1$	P-1	P-1
a/Å	4.6565(3)	6.3881(4)	8.2386(9)
b/Å	29.1915(15)	7.6794(9)	11.8590(11)
c/Å	6.0504(4)	17.8944(12)	19.4033(13)
α/°	90	87.348(7)	90.193(7)
β/°	100.173(6)	89.529(5)	91.897(7)
γ/°	90	67.155(8)	89.882(8)
Volume/Å^3	809.50(9)	808.07(13)	1894.7(3)
Z	2	2	2
ρ_{calc}g/cm^3	1.396	1.399	1.292
μ/mm^1	0.703	0.089	0.639
F(000)	356.0	356.0	776.0
Crystal size/mm^3	0.41 × 0.11 × 0.09	0.12 × 0.06 × 0.04	0.17 × 0.14 × 0.12
Radiation	CuKα (λ = 1.54184)	Mo Kα (λ = 0.71075)	CuKα (λ = 1.54184)
2Θ range for data collection/°	6.056 to 135.36	4.558 to 54.96	8.754 to 142.688
Index ranges	-4 ≤ h ≤ 5, -34 ≤ k ≤ 32, -5 ≤ l ≤ 7	-8 ≤ h ≤ 8, -9 ≤ k ≤ 9, -23 ≤ l ≤ 23	-6 ≤ h ≤ 10, -7 ≤ k ≤ 14, -22 ≤ l ≤ 23
Reflections collected	4039	13024	5180

Independent reflections	2463 [R_{int} = 0.0466, R_{sigma} = 0.0565]	3650 [R_{int} = 0.0484, R_{sigma} = 0.0480]	4563 [R_{int} = 0.0466, R_{sigma} = 0.0683]
Data/restraints/parameters	2463/1/235	3650/0/235	4563/238/485
Goodness-of-fit on F^2	1.038	1.118	2.015
Final R indexes [I>=2σ (I)]	R_1 = 0.0664, wR_2 = 0.1708	R_1 = 0.0994, wR_2 = 0.2643	R_1 = 0.1997, wR_2 = 0.5013
Final R indexes [all data]	R_1 = 0.0708, wR_2 = 0.1819	R_1 = 0.1229, wR_2 = 0.2788	R_1 = 0.2351, wR_2 = 0.5299
Largest diff. peak/hole / e $Å^{-3}$	0.44/-0.24	0.68/-0.44	1.51/-0.81

Table 9.2. Crystal data and structure refinement for ligands **L^5**, **L^7**, **L^8**.

Compound	[**L^5**]·$2H_2O$	[**L^7**]·$2H_2O$	**L^8**
Empirical formula	$C_{24}H_{28}N_6O_2$	$C_{14}H_{18}N_4O_2$	$C_{13}H_{11}N_3$
Formula weight	432.52	274.32	209.25
Temperature/K	173.0	173.0	173.0
Crystal system	orthorhombic	triclinic	monoclinic
Space group	$Pna2_1$	P-1	$P2_1/c$
a/Å	20.4631(9)	8.1128(8)	11.5768(16)
b/Å	4.89861(18)	8.7716(11)	5.9774(8)
c/Å	22.5403(9)	10.9028(11)	16.119(2)
α/°	90	80.648(10)	90
β/°	90	69.951(9)	106.541(14)
γ/°	90	84.374(10)	90
Volume/$Å^3$	2259.45(16)	718.41(15)	1069.3(3)
Z	4	2	4
$\rho_{calc}g/cm^3$	1.271	1.268	1.300
μ/mm^1	0.677	0.716	0.634
F(000)	920.0	292.0	440.0

Crystal size/mm^3	0.4 × 0.26 × 0.14	0.24 × 0.16 × 0.12	0.34 × 0.28 × 0.2
Radiation	CuKα (λ = 1.54184)	CuKα (λ = 1.54184)	CuKα (λ = 1.54184)
2Θ range for data collection/°	7.844 to 142.628	8.716 to 141.898	7.966 to 142.23
Index ranges	-24 ≤ h ≤ 23, -3 ≤ k ≤ 5, -27 ≤ l ≤ 27	-9 ≤ h ≤ 7, -9 ≤ k ≤ 10, -13 ≤ l ≤ 12	-14 ≤ h ≤ 12, -5 ≤ k ≤ 7, -19 ≤ l ≤ 19
Reflections collected	11155	3676	3132
Independent reflections	4091 [R_{int} = 0.0371, R_{sigma} = 0.0393]	2629 [R_{int} = 0.0358, R_{sigma} = 0.0721]	1981 [R_{int} = 0.0368, R_{sigma} = 0.0464]
Data/restraints/parameters	4091/1/299	2629/0/187	1981/0/145
Goodness-of-fit on F^2	1.047	0.986	1.034
Final R indexes [I>=2σ (I)]	R_1 = 0.0484, wR_2 = 0.1263	R_1 = 0.0484, wR_2 = 0.1108	R_1 = 0.0606, wR_2 = 0.1614
Final R indexes [all data]	R_1 = 0.0569, wR_2 = 0.1371	R_1 = 0.0730, wR_2 = 0.1284	R_1 = 0.0753, wR_2 = 0.1860
Largest diff. peak/hole / e $Å^{-3}$	0.21/-0.18	0.20/-0.26	0.20/-0.27

9.2. Crystallographic Data of Coordination Compounds

9.2.1. Chapter 2 Compounds

Table 9.3. Crystal data and structure refinement for **1**-**3**.

Compound	**1**	**2**	**3**
Empirical formula	$C_{44}H_{38}Cl_4Co_2N_{14}$	$C_{40}H_{32}Br_4Co_2N_{12}$	$C_{22}H_{19}Cl_2CoN_7$
Formula weight	1022.54	1118.27	511.27

Temperature/K	173.0	293(2)	173.0
Crystal system	triclinic	triclinic	triclinic
Space group	P-1	P-1	P-1
a/Å	9.2872(6)	9.4548(5)	10.3450(9)
b/Å	11.0385(9)	10.7016(8)	10.6249(10)
c/Å	13.0562(8)	10.7793(9)	12.4219(11)
α/°	67.511(7)	68.392(7)	79.192(7)
β/°	84.255(5)	81.206(6)	72.669(8)
γ/°	79.656(6)	83.475(5)	72.588(8)
Volume/$Å^3$	1215.87(15)	1000.14(13)	1236.4(2)
Z	1	1	2
$\rho_{calc}g/cm^3$	1.397	1.857	1.373
μ/mm^1	7.744	4.873	0.933
F(000)	522.0	550.0	522.0
Crystal size/mm^3	0.08 × 0.06 × 0.03	0.093 × 0.055 × 0.031	0.28 × 0.2 × 0.18
Radiation	CuKα (λ = 1.54184)	MoKα (λ = 0.71073)	MoKα (λ = 0.71073)
2Θ range for data collection/°	8.774 to 142.54	5.616 to 52.744	6.912 to 58.188
Index ranges	$-9 \le h \le 11$, $-13 \le k \le 13$, $-11 \le l \le 16$	$-11 \le h \le 10$, $-13 \le k \le 13$, $-13 \le l \le 13$	$-12 \le h \le 13$, $-13 \le k \le 9$, $-16 \le l \le 16$
Reflections collected	4518	11760	8046
Independent reflections	4518 [R_{int} = 0.0571, R_{sigma} = 0.0893]	4014 [R_{int} = 0.1146, R_{sigma} = 0.0833]	5498 [R_{int} = 0.0248, R_{sigma} = 0.0516]
Data/restraints/parameters	4518/1/290	4014/0/262	5498/24/290
Goodness-of-fit on F^2	1.019	1.385	1.012
Final R indexes [I>=2σ (I)]	R_1 = 0.0717, wR_2 = 0.1813	R_1 = 0.0719, wR_2 = 0.1873	R_1 = 0.0385, wR_2 = 0.0888
Final R indexes [all data]	R_1 = 0.0895, wR_2 = 0.2011	R_1 = 0.0938, wR_2 = 0.1995	R_1 = 0.0495, wR_2 = 0.0954

Largest diff. peak/hole / e Å^{-3}	1.26/-0.52	1.67/-0.82	0.43/-0.48

Table 9.4. Crystal data and structure refinement for **4**-**7**.

Compound	**4**	**5**	**6**	**7**
Empirical formula	$C_{20}H_{16}Cl_2CoN_6$	$C_{44}H_{38}Br_4Co_2N_{14}$	$C_{44}H_{38}CoN_{16}O_6$	$C_{22}H_{19}Cl_2CoN_7$
Formula weight	470.22	1200.38	945.83	511.27
Temperature/K	173	173.0	173.0	173
Crystal system	monoclinic	triclinic	monoclinic	monoclinic
Space group	$P2_1/c$	P-1	$P2_1/c$	$P2_1/c$
a/Å	10.1342(8)	10.4914(10)	10.3683(6)	12.7902(11)
b/Å	21.3347(15)	10.8202(10)	24.1547(10)	8.7966(8)
c/Å	9.7278(11)	12.3408(11)	9.1109(4)	20.363(2)
α/°	90	79.793(8)	90	90
β/°	109.334(10)	73.864(8)	110.136(6)	100.365(10)
γ/°	90	72.821(9)	90	90
Volume/Å^3	1984.7(3)	1278.8(2)	2142.29(19)	2253.6(4)
Z	4	1	2	4
ρ_{calc}g/cm^3	1.574	1.559	1.466	1.507
μ/mm^1	1.154	3.818	3.732	1.024
F(000)	956.0	594.0	978.0	1044.0
Crystal size/mm^3	0.38 × 0.29 × 0.25	0.26 × 0.2 × 0.1	0.2 × 0.1 × 0.08	0.12 × 0.09 × 0.06
Radiation	MoKα (λ = 0.71073)	Mo Kα (λ = 0.71073)	CuKα (λ = 1.54184)	MoKα (λ = 0.71073)
2Θ range for data collection/°	7.14 to 59.038	7.604 to 52.742	10.972 to 140.372	7.296 to 57.968

Index ranges	$-12 \le h \le 12$, $-27 \le k \le 27$, $-13 \le l \le 12$	$-13 \le h \le 12$, $-13 \le k \le 14$, $-7 \le l \le 16$	$-7 \le h \le 12$, $-25 \le k \le 29$, $-11 \le l \le 10$	$-17 \le h \le 17$, $-7 \le k \le 11$, $-26 \le l \le 15$
Reflections collected	8647	5739	6575	8556
Independent reflections	4428 [R_{int} = 0.0812, R_{sigma} = 0.1051]	3973 [R_{int} = 0.0222, R_{sigma} = 0.0514]	3936 [R_{int} = 0.0254, R_{sigma} = 0.0421]	5048 [R_{int} = 0.0326, R_{sigma} = 0.0548]
Data/restraints/parameters	4428/0/262	3973/13/290	3936/0/305	5048/0/290
Goodness-of-fit on F^2	1.013	1.026	1.030	1.040
Final R indexes [I>=2σ (I)]	R_1 = 0.0753, wR_2 = 0.1787	R_1 = 0.0424, wR_2 = 0.1019	R_1 = 0.0389, wR_2 = 0.0960	R_1 = 0.0478, wR_2 = 0.0996
Final R indexes [all data]	R_1 = 0.1242, wR_2 = 0.2174	R_1 = 0.0562, wR_2 = 0.1100	R_1 = 0.0473, wR_2 = 0.1014	R_1 = 0.0742, wR_2 = 0.1175
Largest diff. peak/hole / e $Å^{-3}$	1.08/-1.31	0.53/-0.41	0.42/-0.32	0.33/-0.36

Table 9.5. Crystal data and structure refinement for **8**-**10**.

Compound	**8**	**9**	**10**
Empirical formula	$C_{40}H_{32}Cl_4Co_2N_{12}$	$C_{40}H_{32}N_{12}Co_2Br_4$	$C_{40}H_{32}CoN_{14}O_6$
Formula weight	940.43	1118.27	863.72
Temperature/K	173.0	173.0	173.0
Crystal system	triclinic	triclinic	triclinic
Space group	P-1	P-1	P-1
a/Å	10.0907(18)	10.1947(9)	9.8734(7)
b/Å	10.4778(13)	10.5735(11)	10.0969(7)
c/Å	11.011(2)	11.0714(12)	10.6672(9)
α/°	83.817(13)	81.303(9)	96.504(6)
β/°	77.419(16)	77.374(8)	112.290(7)
γ/°	63.231(16)	62.179(10)	99.774(6)

Volume/$Å^3$	1014.4(3)	1028.3(2)	951.10(13)
Z	1	1	1
$\rho_{calc}g/cm^3$	1.540	1.806	1.508
μ/mm^1	1.129	4.739	4.128
F(000)	478.0	550.0	445.0
Crystal size/mm^3	0.12 × 0.08 × 0.04	0.36 × 0.24 × 0.18	0.4 × 0.28 × 0.14
Radiation	MoKα (λ = 0.71073)	MoKα (λ = 0.71073)	CuKα (λ = 1.54184)
2Θ range for data collection/°	7.584 to 58.59	7.556 to 58.686	9.062 to 142.056
Index ranges	-12 ≤ h ≤ 13, -9 ≤ k ≤ 14, -11 ≤ l ≤ 14	-13 ≤ h ≤ 13, -13 ≤ k ≤ 12, -15 ≤ l ≤ 15	-8 ≤ h ≤ 12, -12 ≤ k ≤ 12, -13 ≤ l ≤ 13
Reflections collected	6761	7075	5125
Independent reflections	4567 [R_{int} = 0.0436, R_{sigma} = 0.1116]	4605 [R_{int} = 0.0352, R_{sigma} = 0.0697]	3503 [R_{int} = 0.0455, R_{sigma} = 0.0624]
Data/restraints/parameters	4567/0/262	4605/0/262	3503/0/277
Goodness-of-fit on F^2	1.033	1.007	1.043
Final R indexes [I>=2σ (I)]	R_1 = 0.0611, wR_2 = 0.1014	R_1 = 0.0427, wR_2 = 0.0813	R_1 = 0.0584, wR_2 = 0.1562
Final R indexes [all data]	R_1 = 0.1082, wR_2 = 0.1274	R_1 = 0.0625, wR_2 = 0.0904	R_1 = 0.0643, wR_2 = 0.1677
Largest diff. peak/hole / e $Å^{-3}$	0.58/-0.52	0.69/-0.84	0.43/-0.70

9.2.2. Chapter 3 Compounds

Table 9.6. Crystal data and structure refinement for **11-13**, **11i**.

Compound	**11**	**12**	**13**	**11i**
Empirical formula	$C_{46}H_{41}Cl_2CuN_{14.5}O_8$	$C_{22}H_{19}CuN_9O_6$	$C_{40}H_{36}Cl_2N_{12}O_{10}Zn$	$C_{21}H_{17}Cl_4CuN_6$
Formula weight	1059.37	569.00	981.08	559.75
Temperature/K	173.0	173	173	100(2)
Crystal system	triclinic	monoclinic	triclinic	triclinic
Space group	P-1	$P2_1/n$	P-1	P-1
a/Å	8.9947(5)	10.8479(3)	9.5360(6)	9.5949(6)
b/Å	11.5251(7)	14.9136(4)	9.6786(7)	10.6656(7)
c/Å	12.2870(7)	15.1286(5)	11.6134(9)	11.3259(6)
α/°	105.528(5)	90	79.785(6)	82.344(5)
β/°	99.583(5)	103.517(3)	78.701(6)	74.965(5)
γ/°	101.062(5)	90	79.075(6)	77.851(6)
Volume/$Å^3$	1172.03(12)	2379.73(13)	1021.03(13)	1090.50(12)
Z	1	4	1	2
$\rho_{calc}g/cm^3$	1.501	1.588	1.596	1.705
μ/mm^1	0.651	0.978	2.694	1.515
F(000)	546.0	1164.0	504.0	564.0
Crystal size/mm^3	0.2 × 0.12 × 0.08	0.28 × 0.16 × 0.08	0.2 × 0.16 × 0.12	0.05 × 0.04 × 0.01
Radiation	MoKα (λ = 0.71073)	MoKα (λ = 0.71073)	CuKα (λ = 1.54184)	MoKα (λ = 0.71075)
2Θ range for data collection/°	6.768 to 65.326	6.888 to 59.034	7.846 to 122.294	5.098 to 54.97
Index ranges	-13 ≤ h ≤ 13, -16 ≤ k ≤ 17, -14 ≤ l ≤ 18	-11 ≤ h ≤ 13, -19 ≤ k ≤ 19, -20 ≤ l ≤ 12	-10 ≤ h ≤ 7, -10 ≤ k ≤ 10, -13 ≤ l ≤ 13	-12 ≤ h ≤ 12, -13 ≤ k ≤ 13, -14 ≤ l ≤ 14
Reflections collected	12030	11083	8034	13369

Independent reflections	7566 [R_{int} = 0.0347, R_{sigma} = 0.0588]	5483 [R_{int} = 0.0295, R_{sigma} = 0.0429]	3110 [R_{int} = 0.0338, R_{sigma} = 0.0330]	4940 [R_{int} = 0.0743, R_{sigma} = 0.1165]
Data/restraints/parameters	7566/2/339	5483/0/344	3110/1/303	4940/0/289
Goodness-of-fit on F^2	1.050	1.042	1.062	0.994
Final R indexes [I>=2σ (I)]	R_1 = 0.0520, wR_2 = 0.1223	R_1 = 0.0359, wR_2 = 0.0859	R_1 = 0.0368, wR_2 = 0.0890	R_1 = 0.0534, wR_2 = 0.0904
Final R indexes [all data]	R_1 = 0.0707, wR_2 = 0.1342	R_1 = 0.0475, wR_2 = 0.0916	R_1 = 0.0443, wR_2 = 0.0951	R_1 = 0.1057, wR_2 = 0.1038
Largest diff. peak/hole / e $Å^{-3}$	0.77/-0.61	0.43/-0.39	0.36/-0.41	0.53/-0.80

9.2.3. Chapter 4 Compounds

Table 9.7. Crystal data and structure refinement for compounds **14**-**17**.

Compound	**14**	**15**	**16**	**17**
Empirical formula	$C_{80}H_{64}Cl_8Cu_4N_{24}$	$C_{40}H_{32}Cl_{10}Cu_5N_{12}$	$C_{88}H_{76}Br_8Cu_4N_{28}$	$C_{44}H_{38}B_2CuF_8N_{14}$
Formula weight	1899.31	1352.97	2419.20	1000.04
Temperature/K	173	173	100.0	100(2)
Crystal system	triclinic	triclinic	monoclinic	triclinic
Space group	P-1	P-1	C2/c	P-1
a/Å	9.5604(6)	10.2604(8)	32.215(2)	8.9788(2)
b/Å	13.9067(7)	10.5576(8)	13.4835(10)	11.4531(3)
c/Å	14.9267(10)	11.3368(8)	25.8172(18)	12.1017(4)
α/°	97.491(5)	101.609(6)	90	105.004(3)
β/°	104.148(6)	104.227(7)	122.782(3)	101.295(3)
γ/°	96.127(5)	91.061(7)	90	101.078(2)

Volume/Å^3	1888.0(2)	1163.05(16)	9428.1(12)	1139.36(6)
Z	1	1	4	1
ρ_{calc}g/cm^3	1.670	1.932	1.704	1.457
μ/mm^1	4.406	8.206	4.341	0.563
F(000)	964.0	671.0	4784.0	511.0
Crystal size/mm^3	0.12 × 0.08 × 0.04	0.24 × 0.16 × 0.12	0.03 × 0.025 × 0.01	0.4 × 0.12 × 0.08
Radiation	CuKα (λ = 1.54184)	CuKα (λ = 1.54184)	MoKα (λ = 0.71075)	Mo Kα (λ = 0.71075)
2Θ range for data collection/°	9.642 to 131.984	8.914 to 142.998	4.882 to 52.746	3.81 to 54.96
Index ranges	-10 ≤ h ≤ 11, -16 ≤ k ≤ 12, -17 ≤ l ≤ 17	-12 ≤ h ≤ 12, -6 ≤ k ≤ 12, -13 ≤ l ≤ 10	-41 ≤ h ≤ 41, -17 ≤ k ≤ 17, -32 ≤ l ≤ 33	-11 ≤ h ≤ 11, -14 ≤ k ≤ 14, -15 ≤ l ≤ 15
Reflections collected	10497	6771	9519	14570
Independent reflections	6406 [R_{int} = 0.0925, R_{sigma} = 0.1081]	4315 [R_{int} = 0.0361, R_{sigma} = 0.0536]	9519 [R_{int} = ?, R_{sigma} = 0.1905]	5202 [R_{int} = 0.0224, R_{sigma} = 0.0255]
Data/restraints/parameters	6406/18/523	4315/0/304	9519/68/579	5202/0/314
Goodness-of-fit on F^2	0.993	1.010	1.053	1.047
Final R indexes [I>=2σ (I)]	R_1 = 0.0646, wR_2 = 0.1512	R_1 = 0.0378, wR_2 = 0.0931	R_1 = 0.1409, wR_2 = 0.3466	R_1 = 0.0335, wR_2 = 0.0867
Final R indexes [all data]	R_1 = 0.1017, wR_2 = 0.1776	R_1 = 0.0499, wR_2 = 0.1025	R_1 = 0.2346, wR_2 = 0.3856	R_1 = 0.0391, wR_2 = 0.0892
Largest diff. peak/hole / e Å^{-3}	0.93/-0.90	0.62/-0.72	1.71/-1.11	0.42/-0.34

Table 9.8. Crystal data and structure refinement for **18**-**20**.

Compound	**18**	**19**	**20**
Empirical formula	$C_{42}H_{32}CuF_6N_{12}O_6S_2$	$C_{44}H_{38}N_{14}Zn$	$C_{52}H_{54}CuF_6N_{12}O_9S_2$
Formula weight	1042.45	828.25	1232.73
Temperature/K	100(2)	173.0	100(2)
Crystal system	triclinic	triclinic	monoclinic
Space group	P-1	P-1	C2/c
a/Å	9.0095(3)	9.1257(4)	21.7957(11)
b/Å	11.1490(4)	11.8008(6)	22.4426(10)
c/Å	12.0186(6)	13.0936(7)	27.7251(19)
α/°	115.336(5)	108.539(5)	90
β/°	104.428(4)	95.030(4)	110.418(6)
γ/°	93.558(3)	101.159(4)	90
Volume/Å^3	1036.89(8)	1294.63(12)	12709.7(13)
Z	1	1	8
ρ_{calc}g/cm^3	1.669	1.062	1.288
μ/mm^1	0.722	0.980	0.485
F(000)	531.0	430.0	5096.0
Crystal size/mm^3	0.07 × 0.03 × 0.01	0.2 × 0.16 × 0.12	0.090 × 0.050 × 0.040
Radiation	Mo Kα (λ = 0.71075)	CuKα (λ = 1.54184)	Mo Kα (λ = 0.71075)
2Θ range for data collection/°	5.166 to 54.968	10.01 to 142.142	4.124 to 50.052
Index ranges	-11 ≤ h ≤ 11, -14 ≤ k ≤ 13, -15 ≤ l ≤ 15	-6 ≤ h ≤ 11, -14 ≤ k ≤ 14, -15 ≤ l ≤ 15	-25 ≤ h ≤ 25, -26 ≤ k ≤ 26, -32 ≤ l ≤ 32
Reflections collected	17458	6991	62999

Independent reflections	4736 [R_{int} = 0.0720, R_{sigma} = 0.0650]	4792 [R_{int} = 0.0278, R_{sigma} = 0.0380]	11194 [R_{int} = 0.1674, R_{sigma} = 0.1259]
Data/restraints/parameters	4736/0/313	4792/0/270	11194/0/748
Goodness-of-fit on F^2	1.028	1.101	0.964
Final R indexes [I>=2σ (I)]	R_1 = 0.0465, wR_2 = 0.1055	R_1 = 0.0798, wR_2 = 0.2063	R_1 = 0.0969, wR_2 = 0.2466
Final R indexes [all data]	R_1 = 0.0733, wR_2 = 0.1153	R_1 = 0.0859, wR_2 = 0.2093	R_1 = 0.1912, wR_2 = 0.3047
Largest diff. peak/hole / e $Å^{-3}$	0.90/-0.66	0.82/-0.65	0.88/-0.44

9.2.4. Chapter 5 Compounds

Table 9.9. Crystal data and structure refinement for compounds **22-24**.

Compound	**22**	**23**	**24**
Empirical formula	$C_{26}H_{22}CuF_6N_8O_6S_2$	$C_{46}H_{36}CuF_6N_8O_6S_2$	$C_{32}H_{31}CuF_6N_9O_6S_2$
Formula weight	784.17	1038.49	879.32
Temperature/K	173.0	173.0	100.0
Crystal system	triclinic	triclinic	monoclinic
Space group	P-1	P-1	C2/c
a/Å	9.3801(5)	9.0686(6)	14.1878(5)
b/Å	13.3284(8)	11.2199(6)	13.3086(5)
c/Å	16.0985(8)	12.0883(8)	40.4807(13)
α/°	107.132(5)	115.102(6)	90
β/°	103.696(5)	104.812(6)	90.608(3)
γ/°	100.131(5)	93.484(5)	90
Volume/$Å^3$	1802.08(18)	1056.48(13)	7643.1(5)
Z	2	1	8

ρ_{calc}g/cm^3	1.445	1.632	1.528
μ/mm^1	2.659	2.439	0.765
F(000)	794.0	531.0	3592.0
Crystal size/mm^3	0.14 × 0.11 × 0.07	0.22 × 0.17 × 0.14	0.1 × 0.06 × 0.05
Radiation	CuKα (λ = 1.54184)	CuKα (λ = 1.54184)	MoKα (λ = 0.71073)
2Θ range for data collection/°	10.024 to 142.2	8.5 to 142.266	4.024 to 52.744
Index ranges	-11 ≤ h ≤ 11, -16 ≤ k ≤ 13, -13 ≤ l ≤ 19	-6 ≤ h ≤ 11, -13 ≤ k ≤ 13, -14 ≤ l ≤ 14	-17 ≤ h ≤ 17, -16 ≤ k ≤ 16, -50 ≤ l ≤ 50
Reflections collected	9434	5327	42305
Independent reflections	6550 [R_{int} = 0.0463, R_{sigma} = 0.0730]	3844 [R_{int} = 0.0921, R_{sigma} = 0.0976]	7794 [R_{int} = 0.0735, R_{sigma} = 0.0429]
Data/restraints/parameters	6550/0/444	3844/1/313	7794/0/506
Goodness-of-fit on F^2	1.048	1.048	1.029
Final R indexes [I>=2σ (I)]	R_1 = 0.0657, wR_2 = 0.1742	R_1 = 0.0682, wR_2 = 0.1736	R_1 = 0.0938, wR_2 = 0.2448
Final R indexes [all data]	R_1 = 0.0890, wR_2 = 0.1921	R_1 = 0.0883, wR_2 = 0.1948	R_1 = 0.1173, wR_2 = 0.2638
Largest diff. peak/hole / e Å^{-3}	1.66/-0.65	1.06/-0.81	1.59/-0.89

Table 9.10. Crystal data and structure refinement for compounds **25-26**.

Compound	**25**	**26**
Empirical formula	$C_{36}H_{42.67}CuF_6N_8O_{9.33}S_2$	$C_{96}H_{88}Cu_4F_{12}N_{24}O_{16}S_4$
Formula weight	978.43	2444.30
Temperature/K	100(2)	100(2)
Crystal system	monoclinic	triclinic
Space group	$P2_1/n$	P-1
a/Å	20.8910(7)	16.6451(3)
b/Å	9.2748(2)	17.1433(2)
c/Å	25.1344(9)	19.1060(3)

α/°	90	90.7040(10)
β/°	114.487(4)	90.0420(10)
γ/°	90	97.2670(10)
Volume/Å^3	4432.0(3)	5407.72(14)
Z	4	2
ρ_{calc}g/cm^3	1.466	1.501
μ/mm^1	2.336	2.420
F(000)	2017.0	2496.0
Crystal size/mm^3	0.1 × 0.08 × 0.03	0.12 × 0.1 × 0.01
Radiation	CuKα (λ = 1.54184)	CuKα (λ = 1.54178)
2Θ range for data collection/°	7.172 to 136.48	6.916 to 133.18
Index ranges	-24 ≤ h ≤ 25, -11 ≤ k ≤ 10, -30 ≤ l ≤ 30	-19 ≤ h ≤ 19, -20 ≤ k ≤ 20, -22 ≤ l ≤ 22
Reflections collected	41244	50455
Independent reflections	8098 [R_{int} = 0.0843, R_{sigma} = 0.0564]	18266 [R_{int} = 0.0517, R_{sigma} = 0.0552]
Data/restraints/parameters	8098/0/616	18266/1296/1442
Goodness-of-fit on F^2	1.007	1.010
Final R indexes [I>=2σ (I)]	R_1 = 0.0606, wR_2 = 0.1638	R_1 = 0.0609, wR_2 = 0.1626
Final R indexes [all data]	R_1 = 0.0765, wR_2 = 0.1744	R_1 = 0.0818, wR_2 = 0.1769
Largest diff. peak/hole / e Å^{-3}	1.48/-1.02	1.06/-0.55

9.2.5. Chapter 6 Compounds

Table 9.11. Crystal data and structure refinement for compounds **27**-**29**.

Compound	**27**	**28**	**29**
Empirical formula	$C_{22}H_{16}AgF_3N_6O_2$	$C_{48}H_{44}Ag_2F_6N_{12}O_8S_2$	$C_{23}H_{22}AgClN_6O_5$
Formula weight	561.28	1310.81	605.78
Temperature/K	173.0	100.0	173
Crystal system	triclinic	monoclinic	monoclinic

Space group	P-1	$P2_1$	$P2_1/n$
a/Å	10.1359(12)	12.9491(3)	15.5196(8)
b/Å	11.0137(13)	9.2308(2)	8.9893(4)
c/Å	11.3295(13)	22.4537(4)	19.5761(8)
α/°	64.447(12)	90	90
β/°	76.865(11)	101.680(2)	92.354(4)
γ/°	72.658(11)	90	90
Volume/$Å^3$	1082.0(3)	2628.33(10)	2728.8(2)
Z	2	2	4
$\rho_{calc}g/cm^3$	1.723	1.656	1.475
μ/mm^1	8.009	7.471	7.194
F(000)	560.0	1320.0	1224.0
Crystal size/mm^3	0.32 × 0.28 × 0.24	0.4 × 0.18 × 0.09	0.25 × 0.11 × 0.08
Radiation	CuKα (λ = 1.54184)	CuKα (λ = 1.54184)	CuKα (λ = 1.54184)
2Θ range for data collection/°	8.708 to 140.52	7.308 to 135.364	10.832 to 140.318
Index ranges	-12 ≤ h ≤ 10, -12 ≤ k ≤ 13, -13 ≤ l ≤ 13	-15 ≤ h ≤ 15, -10 ≤ k ≤ 10, -26 ≤ l ≤ 23	-18 ≤ h ≤ 16, -7 ≤ k ≤ 10, -22 ≤ l ≤ 23
Reflections collected	6366	14247	7997
Independent reflections	3991 [R_{int} = 0.0470, R_{sigma} = 0.0625]	7424 [R_{int} = 0.0323, R_{sigma} = 0.0445]	4931 [R_{int} = 0.0564, R_{sigma} = 0.0819]
Data/restraints/parameters	3991/0/307	7424/37/707	4931/24/327
Goodness-of-fit on F^2	1.008	1.030	1.054
Final R indexes [I>=2σ (I)]	R_1 = 0.0494, wR_2 = 0.1245	R_1 = 0.0603, wR_2 = 0.1591	R_1 = 0.0931, wR_2 = 0.2562
Final R indexes [all data]	R_1 = 0.0626, wR_2 = 0.1348	R_1 = 0.0624, wR_2 = 0.1625	R_1 = 0.1198, wR_2 = 0.2900
Largest diff. peak/hole / e $Å^{-3}$	1.34/-1.00	1.42/-0.67	1.64/-1.21

Table 9.12. Crystal data and structure refinement for compounds **30**-**32**.

Compound	**30**	**31**	**32**
Empirical formula	$C_{24}H_{26}AgBF_4N_6O$	$C_{40}H_{32}Ag_2Cl_2N_{12}O_8$	$C_{20}H_{16}AgN_7O_3$
Formula weight	609.19	1095.41	510.27
Temperature/K	173	173.0	100(2)
Crystal system	monoclinic	triclinic	triclinic
Space group	$P2_1/n$	P-1	P-1
a/Å	11.6635(9)	11.2007(6)	8.3196(2)
b/Å	14.6472(7)	11.2256(5)	10.7490(3)
c/Å	15.5988(13)	17.8129(8)	11.3260(10)
α/°	90	82.719(4)	84.406(5)
β/°	110.943(9)	86.099(4)	68.669(6)
γ/°	90	64.378(5)	73.758(3)
Volume/$Å^3$	2488.8(3)	2002.96(18)	905.81(9)
Z	4	2	2
$\rho_{calc}g/cm^3$	1.626	1.816	1.871
μ/mm^1	7.031	9.686	1.156
F(000)	1232.0	1096.0	512.0
Crystal size/mm^3	0.11 × 0.03 × 0.02	0.14 × 0.08 × 0.02	0.050 × 0.040 × 0.010
Radiation	CuKα (λ = 1.54184)	CuKα (λ = 1.54184)	MoKα (λ = 0.71073)
2Θ range for data collection/°	8.56 to 142.25	8.756 to 143.216	5.45 to 55.16
Index ranges	$-14 \le h \le 13$, $-10 \le k \le 17$, $-15 \le l \le 18$	$-13 \le h \le 13$, $-8 \le k \le 13$, $-21 \le l \le 20$	$-10 \le h \le 10$, $-13 \le k \le 13$, $-10 \le l \le 14$
Reflections collected	7561	13746	4101
Independent reflections	4616 [R_{int} = 0.0385, R_{sigma} = 0.0573]	7557 [R_{int} = 0.0421, R_{sigma} = 0.0606]	4101 [R_{int} = 0.0669, R_{sigma} = 0.0492]
Data/restraints/parameters	4616/0/336	7557/0/577	4101/0/281

Goodness-of-fit on F^2	1.059	1.018	1.086
Final R indexes [I>=2σ (I)]	R_1 = 0.0586, wR_2 = 0.1500	R_1 = 0.0429, wR_2 = 0.0957	R_1 = 0.0666, wR_2 = 0.1736
Final R indexes [all data]	R_1 = 0.0764, wR_2 = 0.1719	R_1 = 0.0590, wR_2 = 0.1034	R_1 = 0.0721, wR_2 = 0.1772
Largest diff. peak/hole / e $Å^{-3}$	1.57/-1.11	1.05/-0.91	3.86/-1.13

Table 9.13. Crystal data and structure refinement for compounds **33-35**.

Compound	**33**	**34**	**35**
Empirical formula	$C_{44}H_{32}Ag_2F_6N_{12}O_4$	$C_{22}H_{16}Ag_2F_6N_6O_6S_2$	$C_{49}H_{38}Ag_2F_{10}N_{12}O_5$
Formula weight	1122.55	854.27	1280.65
Temperature/K	100(2)	173.0	100(2)
Crystal system	monoclinic	monoclinic	triclinic
Space group	$P2_1/c$	$P2_1/n$	P-1
a/Å	11.0493(5)	13.1029(8)	8.3697(3)
b/Å	8.4381(4)	17.2845(5)	13.2918(6)
c/Å	22.4661(10)	13.2948(8)	22.1244(9)
α/°	90	90	102.215(4)
β/°	96.003(5)	109.777(7)	90.352(3)
γ/°	90	90	94.281(3)
Volume/$Å^3$	2083.14(17)	2833.4(3)	2398.28(18)
Z	2	4	2
$\rho_{calc}g/cm^3$	1.790	2.003	1.773
μ/mm^1	1.029	1.619	0.919
F(000)	1120.0	1672.0	1280.0
Crystal size/mm^3	0.3500 × 0.0150 × 0.0100	0.28 × 0.22 × 0.17	0.100 × 0.015 × 0.010

Radiation	Mo Kα (λ = 0.71075)	MoKα (λ = 0.71073)	Mo Kα (λ = 0.71075)
2Θ range for data collection/°	4.92 to 54.958	6.608 to 58.282	4.882 to 54.956
Index ranges	$-14 \leq h \leq 14$, $-10 \leq k \leq 10$, $-29 \leq l \leq 28$	$-17 \leq h \leq 8$, $-23 \leq k \leq 19$, $-11 \leq l \leq 17$	$-10 \leq h \leq 9$, $-17 \leq k \leq 17$, $-28 \leq l \leq 28$
Reflections collected	25576	11474	41994
Independent reflections	4765 [R_{int} = 0.0447, R_{sigma} = 0.0270]	6412 [R_{int} = 0.0370, R_{sigma} = 0.0708]	10947 [R_{int} = 0.0815, R_{sigma} = 0.1026]
Data/restraints/parameters	4765/0/307	6412/0/397	10947/0/705
Goodness-of-fit on F^2	1.042	1.029	1.005
Final R indexes [I>=2σ (I)]	R_1 = 0.0472, wR_2 = 0.1215	R_1 = 0.0594, wR_2 = 0.1113	R_1 = 0.0571, wR_2 = 0.0966
Final R indexes [all data]	R_1 = 0.0563, wR_2 = 0.1268	R_1 = 0.1026, wR_2 = 0.1351	R_1 = 0.1290, wR_2 = 0.1163
Largest diff. peak/hole / e $Å^{-3}$	2.04/-1.15	1.11/-0.72	1.01/-0.74

9.2.6. Chapter 7 Compounds

Table 9.14. Crystal data and structure refinement for compounds **36**-**37**.

Compound	**36**	**37**
Empirical formula	$C_{28}H_{32}CoN_{10}O_8$	$C_{40}H_{32}MnN_{14}O_6$
Formula weight	695.56	859.73
Temperature/K	173	173
Crystal system	triclinic	triclinic
Space group	P-1	P-1
a/Å	8.7772(10)	10.0086(9)
b/Å	9.5437(11)	10.1350(9)

c/Å	10.7337(12)	10.7313(7)
α/°	68.365(11)	97.028(7)
β/°	67.877(11)	112.652(8)
γ/°	76.700(10)	99.700(8)
Volume/Å^3	769.90(17)	969.02(15)
Z	1	1
ρ_{calc}g/cm^3	1.500	1.473
μ/mm^1	4.949	3.350
F(000)	361.0	443.0
Crystal size/mm^3	0.18 × 0.14 × 0.08	0.28 × 0.2 × 0.16
Radiation	CuKα (λ = 1.54184)	CuKα (λ = 1.54184)
2Θ range for data collection/°	9.364 to 141.81	9.046 to 142.154
Index ranges	-6 ≤ h ≤ 10, -8 ≤ k ≤ 11, -11 ≤ l ≤ 12	-11 ≤ h ≤ 12, -12 ≤ k ≤ 12, -8 ≤ l ≤ 12
Reflections collected	4093	5299
Independent reflections	2860 [R_{int} = 0.0377, R_{sigma} = 0.0713]	3563 [R_{int} = 0.0520, R_{sigma} = 0.0667]
Data/restraints/parameters	2860/0/215	3563/0/277
Goodness-of-fit on F^2	1.044	1.056
Final R indexes [I>=2σ (I)]	R_1 = 0.0537, wR_2 = 0.1327	R_1 = 0.0474, wR_2 = 0.1173
Final R indexes [all data]	R_1 = 0.0628, wR_2 = 0.1425	R_1 = 0.0585, wR_2 = 0.1301
Largest diff. peak/hole / e Å^{-3}	0.85/-0.51	0.55/-0.83

9.3. Crystallographic Data of Catalytic Products

9.3.1. 1,4-Dihydropyridine Products

Table 9.15. Crystal data and structure refinement for 1,4-DHP products **C3D4-C3D6, C3D17**.

Compound	**C3D4**	**C3D5**	**C3D6**	**C3D13**
Empirical formula	$C_{28}H_{32}N_2O_8$	$C_{28}H_{32}N_2O_4$	$C_{24}H_{22}Cl_2N_2O_4$	$C_{24}H_{24}N_2O_6$
Formula weight	524.55	460.55	473.33	436.45
Temperature/K	100	173.0	173	173.0
Crystal system	triclinic	triclinic	monoclinic	monoclinic
Space group	P-1	P-1	$P2_1/c$	$P2_1/n$
a/Å	8.6245(3)	10.7636(18)	9.3349(2)	15.5881(6)
b/Å	11.3274(3)	11.3391(17)	27.5175(6)	20.3221(5)
c/Å	14.4275(6)	11.4031(18)	9.3096(2)	33.8600(10)
α/°	101.801(3)	79.397(13)	90	90
β/°	104.493(3)	64.791(16)	107.552(3)	97.853(3)
γ/°	103.978(3)	82.197(13)	90	90
Volume/$Å^3$	1270.46(8)	1235.1(4)	2280.07(10)	10625.7(6)
Z	2	2	4	20
$\rho_{calc}g/cm^3$	1.371	1.238	1.379	1.364
μ/mm^1	0.101	0.664	2.844	0.099
F(000)	556.0	492.0	984.0	4600.0
Crystal size/mm^3	0.1 × 0.05 × 0.04	0.2 × 0.08 × 0.04	0.24 × 0.21 × 0.18	0.19 × 0.03 × 0.03
Radiation	MoKα (λ = 0.71073)	CuKα (λ = 1.54184)	CuKα (λ = 1.54184)	MoKα (λ = 0.71073)
2Θ range for data collection/°	5.07 to 54.966	7.95 to 124.666	10.472 to 142.862	4.65 to 50.056

Index ranges	$-11 \le h \le 11, -14 \le k \le 14, -18 \le l \le 17$	$-10 \le h \le 12, -12 \le k \le 13, -12 \le l \le 12$	$-8 \le h \le 11, -32 \le k \le 33, -11 \le l \le 6$	$-18 \le h \le 17, -24 \le k \le 24, -40 \le l \le 40$
Reflections collected	16762	8369	12792	59833
Independent reflections	5771 [R_{int} = 0.0285, R_{sigma} = 0.0372]	3781 [R_{int} = 0.0876, R_{sigma} = 0.0897]	4373 [R_{int} = 0.0273, R_{sigma} = 0.0220]	18712 [R_{int} = 0.0571, R_{sigma} = 0.0698]
Data/restraints/parameters	5771/0/349	3781/0/314	4373/0/292	18712/0/1461
Goodness-of-fit on F^2	1.031	0.951	1.028	1.022
Final R indexes [I>=2σ (I)]	R_1 = 0.0448, wR_2 = 0.0972	R_1 = 0.0616, wR_2 = 0.1455	R_1 = 0.0524, wR_2 = 0.1418	R_1 = 0.0824, wR_2 = 0.1997
Final R indexes [all data]	R_1 = 0.0624, wR_2 = 0.1045	R_1 = 0.1084, wR_2 = 0.1719	R_1 = 0.0573, wR_2 = 0.1466	R_1 = 0.1485, wR_2 = 0.2438
Largest diff. peak/hole / e $Å^{-3}$	0.27/-0.21	0.24/-0.29	0.38/-0.57	1.06/-0.34

9.3.2. 1,2,3-Triazole Products

Table 9.16. Crystal data and structure refinement for triazole products **C5T1-C5T4**.

Compound	**C5T1**	**C5T2**	**C5T3**	**C5T4**
Empirical formula	$C_{15}H_{13}N_3$	$C_{16}H_{15}N_3O$	$C_{13}H_{17}N_3$	$C_{10}H_{11}N_3O$
Formula weight	235.28	265.31	215.29	189.22
Temperature/K	173.0	173.0	173.0	173.0
Crystal system	orthorhombic	monoclinic	monoclinic	triclinic
Space group	$Pna2_1$	$P2_1$	$P2_1/c$	P-1
a/Å	11.2241(4)	8.1339(8)	13.0813(10)	8.2035(12)
b/Å	19.3350(6)	5.6565(6)	5.4875(3)	11.0403(11)
c/Å	5.5817(2)	14.5299(16)	17.7677(16)	11.2020(11)

α/°	90	90	90	93.064(8)
β/°	90	92.836(9)	108.906(9)	106.687(11)
γ/°	90	90	90	104.934(10)
Volume/Å^3	1211.33(7)	667.69(12)	1206.62(17)	930.1(2)
Z	4	2	4	4
ρ_{calc}g/cm^3	1.290	1.320	1.185	1.351
μ/mm^1	0.619	0.680	0.563	0.744
F(000)	496.0	280.0	464.0	400.0
Crystal size/mm^3	0.24 × 0.18 × 0.1	0.27 × 0.1 × 0.06	0.28 × 0.19 × 0.16	0.12 × 0.08 × 0.06
Radiation	CuKα (λ = 1.54184)	CuKα (λ = 1.54184)	CuKα (λ = 1.54184)	CuKα (λ = 1.54184)
2Θ range for data collection/°	9.11 to 142.246	10.89 to 140.486	10.636 to 140.672	8.32 to 142.388
Index ranges	-12 ≤ h ≤ 13, -15 ≤ k ≤ 23, -6 ≤ l ≤ 6	-9 ≤ h ≤ 9, -5 ≤ k ≤ 6, -17 ≤ l ≤ 14	-15 ≤ h ≤ 15, -4 ≤ k ≤ 6, -21 ≤ l ≤ 20	-10 ≤ h ≤ 8, -11 ≤ k ≤ 13, -13 ≤ l ≤ 11
Reflections collected	3555	1972	3667	5011
Independent reflections	2053 [R_{int} = 0.0254, R_{sigma} = 0.0382]	1586 [R_{int} = 0.0309, R_{sigma} = 0.0578]	2234 [R_{int} = 0.0350, R_{sigma} = 0.0433]	3462 [R_{int} = 0.0266, R_{sigma} = 0.0545]
Data/restraints/parameters	2053/1/163	1586/1/183	2234/0/146	3462/0/255
Goodness-of-fit on F^2	1.069	1.019	1.024	1.052
Final R indexes [I>=2σ (I)]	R_1 = 0.0373, wR_2 = 0.0855	R_1 = 0.0464, wR_2 = 0.1051	R_1 = 0.0469, wR_2 = 0.1150	R_1 = 0.0451, wR_2 = 0.1051
Final R indexes [all data]	R_1 = 0.0418, wR_2 = 0.0892	R_1 = 0.0617, wR_2 = 0.1164	R_1 = 0.0658, wR_2 = 0.1336	R_1 = 0.0688, wR_2 = 0.1216
Largest diff. peak/hole / e Å^{-3}	0.10/-0.17	0.19/-0.19	0.14/-0.19	0.18/-0.24

Chapter 10: Bibliography

1 S. R. Batten, N. R. Champness, X.-M. Chen, J. Garcia-Martinez, S. Kitagawa, L. Öhrström, M. O'Keeffe, M. P. Suh and J. Reedijk, *CrystEngComm*, 2012, **14**, 3001.

2 S. R. Batten, N. R. Champness, X.-M. Chen, J. Garcia-Martinez, S. Kitagawa, L. Öhrström, M. O'Keeffe, M. P. Suh and J. Reedijk, *Pure Appl. Chem.*, 2013, **85**, 1715–1724.

3 O. M. Yaghi, G. Li and H. Li, *Nature*, 1995, **378**, 703–706.

4 O. M. Yaghi and H. Li, *J. Am. Chem. Soc.*, 1995, **117**, 10401–10402.

5 J. C. Bailar Jr., in *Preparative Inorganic Reactions. Volume 1.*, Interscience Publishers, John Wiley and Sons, New York, 1964, vol. 1, pp. 1–25.

6 B. F. Hoskins and R. Robson, *J. Am. Chem. Soc.*, 1989, **111**, 5962–5964.

7 B. F. Hoskins and R. Robson, *J. Am. Chem. Soc.*, 1990, **112**, 1546–1554.

8 S. R. Batten, B. F. Hoskins and R. Robson, *J. Chem. Soc. Chem. Commun.*, 1991, 445.

9 B. F. Abrahams, B. F. Hoskins, J. Liu and R. Robson, *J. Am. Chem. Soc.*, 1991, **113**, 3045–3051.

10 S. Kitagawa, S. Matsuyama, M. Munakata and T. Emori, *J. Chem. Soc. Dalt. Trans.*, 1991, 2869–2874.

11 B. F. Abrahams, M. J. Hardie, B. F. Hoskins, R. Robson and G. A. Williams, *J. Am. Chem. Soc.*, 1992, **114**, 10641–10643.

12 G. R. Desiraju, *J. Am. Chem. Soc.*, 2013, **135**, 9952–67.

13 G. R. Desiraju, *Angew. Chemie - Int. Ed.*, 1995, **34**, 2311–2327.

14 K. R. Seddon and M. Zaworotko, *Crystal Engineering: The Design and Application of Functional Solids, Volume 539*, Springer Science & Business Media, 1999.

15 B. Moulton and M. J. Zaworotko, *Chem. Rev.*, 2001, **101**, 1629–1658.

16 H. Li, M. Eddaoudi, M. O'Keeffe and O. M. Yaghi, 1999, **402**, 276–279.

17 M. Eddaoudi, J. Kim, N. Rosi, D. Vodak, J. Wachter, M. O'Keeffe and O. M. Yaghi, *Science*, 2002, **295**, 469–472.

18 T. J. Prior, D. Bradshaw, S. J. Teat and M. J. Rosseinsky, *Chem. Commun.*, 2003, 500–501.

19 S. I. Noro, R. Kitaura, M. Kondo, S. Kitagawa, T. Ishii, H. Matsuzaka and M.

Yamashita, *J. Am. Chem. Soc.*, 2002, **124**, 2568–2583.

20 O. K. Farha and J. T. Hupp, *Acc. Chem. Res.*, 2010, **43**, 1166–1175.

21 S. Kaskel, *The Chemistry of Metal-Organic Frameworks : Synthesis , Characterization , and Applications*, Wiley-VCH, 1st edn., 2016.

22 J. Rabone, Y. F. Yue, S. Y. Chong, K. C. Stylianou, J. Bacsa, D. Bradshaw, G. R. Darling, N. G. Berry, Y. Z. Khimyak, A. Y. Ganin, P. Wiper, J. B. Claridge and M. J. Rosseinsky, *Science.*, 2010, **329**, 1053–1057.

23 S. L. Anderson and K. C. Stylianou, *Coord. Chem. Rev.*, 2017, **349**, 102–128.

24 Z.-J. Lin, J. Lü, M. Hong and R. Cao, *Chem. Soc. Rev.*, 2014, **43**, 5867–95.

25 M. Wang, M.-H. Xie, C.-D. Wu and Y.-G. Wang, *Chem. Commun.*, 2009, 2396.

26 G. Kumar and R. Gupta, *Chem. Soc. Rev.*, 2013, **42**, 9403.

27 A. Bhunia, M. A. Gotthardt, M. Yadav, M. T. Gamer, A. Eichhöfer, W. Kleist and P. W. Roesky, *Chem. - A Eur. J.*, 2013, **19**, 1986–1995.

28 D. Liu, K. Lu, C. Poon and W. Lin, *Inorg. Chem.*, 2014, **53**, 1916–24.

29 K. deKrafft, Z. Xie, G. Cao, S. Tran, L. Ma, O. Zhou and W. Lin, *Angew. Chemie Int. Ed.*, 2009, **48**, 9901–9904.

30 B. Liu, *J. Mater. Chem.*, 2012, **22**, 10094.

31 Y. Cui, B. Chen and G. Qian, *Coord. Chem. Rev.*, 2014, **273**–**274**, 76–86.

32 M. X. Wu and Y. W. Yang, *Adv. Mater.*, 2017, **29**, 1606134.

33 L. Welte, A. Calzolari, R. Di Felice, F. Zamora and J. Gómez-Herrero, *Nat. Nanotechnol.*, 2010, **5**, 110–115.

34 J. C. Hye, M. Dincă and J. R. Long, *J. Am. Chem. Soc.*, 2008, **130**, 7848–7850.

35 S. R. Caskey, A. G. Wong-Foy and A. J. Matzger, *J. Am. Chem. Soc.*, 2008, **130**, 10870–10871.

36 T. Tian, Z. Zeng, D. Vulpe, M. E. Casco, G. Divitini, P. A. Midgley, J. Silvestre-Albero, J.-C. Tan, P. Z. Moghadam and D. Fairen-Jimenez, *Nat. Mater.*, 2017, **17**, 174–179.

37 R. Matsuda, R. Kitaura, S. Kitagawa, Y. Kubota, R. V. Belosludov, T. C. Kobayashi, H. Sakamoto, T. Chiba, M. Takata, Y. Kawazoe and Y. Mita, *Nature*, 2005, **436**, 238–241.

38 K. Schlichte, T. Kratzke and S. Kaskel, *Microporous Mesoporous Mater.*, 2004, **73**,

81–88.

39 S. S.-Y. Chui, S. M.-F. Lo, J. P. H. Charmant, A. G. Orpen and I. D. Williams, *Science.*, 1999, **283**, 1148–1150.

40 M. H. Zeng, Z. Yin, Y. X. Tan, W. X. Zhang, Y. P. He and M. Kurmoo, *J. Am. Chem. Soc.*, 2014, **136**, 4680–4688.

41 R. A. Agarwal, *Sci. Rep.*, 2017, **7**, 13212.

42 J.-X. Yang, Y.-Y. Qin, J.-K. Cheng, X. Zhang and Y.-G. Yao, *Cryst. Growth Des.*, 2015, **15**, 2223–2234.

43 T. K. Maji, R. Matsuda and S. Kitagawa, *Nat. Mater.*, 2007, **6**, 142–148.

44 C. T. Chen and K. S. Suslick, *Coord. Chem. Rev.*, 1993, **128**, 293–322.

45 W. L. Leong and J. J. Vittal, *Chem. Rev.*, 2011, **111**, 688–764.

46 C. Slabbert and M. Rademeyer, *Coord. Chem. Rev.*, 2015, 288, 18–49.

47 Y. Y. Karabach, A. M. Kirillov, M. Haukka, M. N. Kopylovich and A. J. L. Pombeiro, *J. Inorg. Biochem.*, 2008, **102**, 1190–1194.

48 X. Wang, M. Liu, Y. Wang, H. Fan, J. Wu, C. Huang and H. Hou, *Inorg. Chem.*, 2017, **56**, 13329–13336.

49 S. Lymperopoulou, M. Papastergiou, M. Louloudi, C. P. Raptopoulou, V. Psycharis, C. J. Milios and J. C. Plakatouras, *Eur. J. Inorg. Chem.*, 2014, **2014**, 3638–3644.

50 M. A. Wani, A. Kumar, M. D. Pandey and R. Pandey, *Polyhedron*, 2017, **126**, 142–149.

51 E. Knoevenagel, *Berichte der Dtsch. Chem. Gesellschaft*, 1898, **31**, 2596–2619.

52 A. Karmakar, G. M. D. M. Rúbio, M. F. C. Guedes da Silva, S. Hazra and A. J. L. Pombeiro, *Cryst. Growth Des.*, 2015, **15**, 4185–4197.

53 P. Buchwalter, J. Rosé and P. Braunstein, *Chem. Rev.*, 2015, **115**, 28–126.

54 L. K. G. Ackerman, M. M. Lovell and D. J. Weix, *Nature*, 2015, **524**, 454–457.

55 S. Ko, B. Kang and S. Chang, *Angew. Chemie - Int. Ed.*, 2005, **44**, 455–457.

56 K. Griffiths, A. C. Tsipis, P. Kumar, O. P. E. Townrow, A. Abdul-Sada, G. R. Akien, A. Baldansuren, A. C. Spivey and G. E. Kostakis, *Inorg. Chem.*, 2017, **56**, 9563–9573.

57 G. Kumar, G. Kumar and R. Gupta, *RSC Adv.*, 2016, **6**, 21352–21361.

58 A. A. Mohamed, *Coord. Chem. Rev.*, 2010, **254**, 1918–1947.

59 G. Aromí, L. A. Barrios, O. Roubeau and P. Gamez, *Coord. Chem. Rev.*, 2011, **255**,

485–546.

60 J.-P. Zhang, Y.-B. Zhang, J.-B. Lin and X.-M. Chen, *Chem. Rev.*, 2012, **112**, 1001–1033.

61 F. Tomas, J. Catalan, P. Perez and J. Elguero, *J. Org. Chem.*, 1994, **59**, 2799–2802.

62 A. Escande, J. L. Galigné and J. Lapasset, *Acta Crystallogr. B* , 1974, **30**, 1490–1495.

63 N. Zinin, *Justus Liebigs Ann. Chem.*, 1860, **114**, 217–227.

64 A. Werner and E. Stiasny, *Berichte der Dtsch. Chem. Gesellschaft*, 1899, **32**, 3256–3282.

65 A. Wilh. Hofmann, *Ann. der Chemie und Pharm.*, 1860, **115**, 249–260.

66 A. Ladenburg, *Berichte der Dtsch. Chem. Gesellschaft*, 1876, **9**, 219–223.

67 C. M. P. Pereira, H. A. Stefani, K. P. Guzen and A. T. G. Orfao, *ChemInform*, 2007, **38**, 43–46.

68 A. R. Katritzky and J.-C. M. Monbaliu, *The chemistry of benzotriazole derivatives : a tribute to Alan Roy Katritzky*, Springer International Publishing, 1st edn., 2016.

69 J. K. Beagle, *Top. Heterocycl.Chem.*, 2016, **43**, 177–234.

70 O. I. Bolshakov, *Top. Heterocycl.Chem.*, 2016, **43**, 143–176.

71 K. Bajaj and R. Sakhuja, *Top. Heterocycl.Chem.*, 2016, **43**, 235–284.

72 E. F. V. Scriven and C. A. Ramsden, *Heterocyclic chemistry in the 21st Century : a tribute to Alan Katritzky*, Elsevier, 1st edn., 2017.

73 British Patent, 652339, 1947.

74 J. B. Cotton and I. R. Scholes, *Br. Corros. J.*, 1967, **2**, 1–5.

75 J. Meunier-Piret, P. Piret, J.-P. Putzeys and M. Van Meerssche, *Acta Crystallogr. B* , 1976, **32**, 714–717.

76 J. Reedijk, G. Roelofsen, A. R. Siedle and A. L. Spek, *Inorg. Chem.*, 1979, **18**, 1947–1951.

77 J. Reedijk, A. R. Siedle, R. A. Velapoldi and J. A. M. Van Hest, *Inorganica Chim. Acta*, 1983, **74**, 109–118.

78 F. H. Allen, *Acta Crystallogr. B*, 2002, **58**, 380–388.

79 J. H. Marshall, *Inorg. Chem.*, 1978, **17**, 3711–3713.

80 J. Handley, D. Collison, C. D. Garner, M. Helliwell, R. Docherty, J. R. Lawson and P. A. Tasker, *Angew. Chemie - Int. Ed.*, 1993, **32**, 1036–1038.

81 V. Tangoulis, C. P. Raptopoulou, A. Terzis, E. G. Bakalbassis, E. Diamantopoulou and S. P. Perlepes, *Inorg. Chem.*, 1998, **37**, 3142–3153.

82 S. Biswas, M. Tonigold and D. Volkmer, *Zeitschrift fur Anorg. und Allg. Chemie*, 2008, **634**, 2532–2538.

83 C. Gkioni, V. Psycharis and C. P. Raptopoulou, *Polyhedron*, 2009, **28**, 3425–3430.

84 S. Biswas, M. Tonigold, M. Speldrich, P. Kögerler and D. Volkmer, *Eur. J. Inorg. Chem.*, 2009, 3094–3101.

85 Y. X. Yuan, P. J. Wei, W. Qin, Y. Zhang, J. L. Yao and R. A. Gu, *Eur. J. Inorg. Chem.*, 2007, **2007**, 4980–4987.

86 L. F. Jones, E. K. Brechin, D. Collison, A. Harrison, S. J. Teat and W. Wernsdorfer, *Chem. Commun.*, 2002, 2974–2975.

87 L. F. Jones, G. Rajaraman, J. Brockman, M. Murugesu, E. C. Sañudo, J. Raftery, S. J. Teat, W. Wernsdorfer, G. Christou, E. K. Brechin and D. Collison, *Chem. - A Eur. J.*, 2004, **10**, 5180–5194.

88 L. F. Jones, J. Raftery, S. J. Teat, D. Collison and E. K. Brechin, *Polyhedron*, 2005, **24**, 2443–2449.

89 J. Tabernor, L. F. Jones, S. L. Heath, C. Muryn, G. Aromí, J. Ribas, E. K. Brechin and D. Collison, *Dalton Trans.*, 2004, **4**, 975–976.

90 R. Shaw, R. H. Laye, L. F. Jones, D. M. Low, C. Talbot-Eeckelaers, Q. Wei, C. J. Milios, S. Teat, M. Helliwell, J. Raftery, M. Evangelisti, M. Affronte, D. Collison, E. K. Brechin and E. J. L. McInnes, *Inorg. Chem.*, 2007, **46**, 4968–4978.

91 R. A. Layfield, J. J. W. McDouall, S. A. Sulway, F. Tuna, D. Collison and R. E. P. Winpenny, *Chem. - A Eur. J.*, 2010, **16**, 4442–4446.

92 K. Z. Shao, Y. H. Zhao, Y. Xing, Y. Q. Lan, X. L. Wang, Z. M. Su and R. S. Wang, *Cryst. Growth Des.*, 2008, **8**, 2986–2989.

93 J. C. Rybak, I. Schellenberg, R. Pöttgen and K. Müller-Buschbaum, *Zeitschrift fur Anorg. und Allg. Chemie*, 2010, **636**, 1720–1725.

94 K. Müller-Buschbaum and Y. Mokaddem, *Zeitschrift fur Anorg. und Allg. Chemie*, 2008, **634**, 2360–2366.

95 J.-C. Rybak and K. Müller-Buschbaum, *Zeitschrift für Anorg. und Allg. Chemie*, 2010, **636**, 126–131.

96 K. Müller-Buschbaum and Y. Mokaddem, *Eur. J. Inorg. Chem.*, 2006, **2006**, 2000–2010.

97 J. J. Liu, Z. Y. Li, X. Yuan, Y. Wang and C. C. Huang, *Acta Crystallogr. C* , 2014, **70**, 599–602.

98 Y. Bai, J. Tao, R. Huang and L. Zheng, *Angew. Chemie Int. Ed.*, 2008, **47**, 5344–5347.

99 X. L. Wang, C. Qin, S. X. Wu, K. Z. Shao, Y. Q. Lan, S. Wang, D. X. Zhu, Z. M. Su and E. B. Wang, *Angew. Chemie - Int. Ed.*, 2009, **48**, 5291–5295.

100 J. J. Deng, B. Q. Song, J. Liang, Y. Q. Jiao, X. S. Wu, L. Zhao, K. Z. Shao and Z. M. Su, *Inorg. Chem. Commun.*, 2015, **60**, 82–86.

101 Z. Zhang, S. Xiang, Y. S. Chen, S. Ma, Y. Lee, T. Phely-Bobin and B. Chen, *Inorg. Chem.*, 2010, **49**, 8444–8448.

102 Y.-Q. Chen, Y.-K. Qu, G.-R. Li, Z.-Z. Zhuang, Z. Chang, T.-L. Hu, J. Xu and X.-H. Bu, *Inorg. Chem.*, 2014, **53**, 8842–8844.

103 Y. X. Tan, Y. Zhang, Y. P. He and Y. J. Zheng, *New J. Chem.*, 2014, **38**, 5272–5275.

104 D. C. Zhong, J. H. Deng, X. Z. Luo, H. J. Liu, J. L. Zhong, K. J. Wang and T. B. Lu, *Cryst. Growth Des.*, 2012, **12**, 1992–1998.

105 Y. W. Li, S. J. Liu, T. L. Hu, D. C. Li, J. M. Dou and Z. Chang, *Inorg. Chem. Commun.*, 2014, **47**, 67–70.

106 Y. Y. Qin, J. Zhang, Z. J. Li, L. Zhang, X. Y. Cao and Y. G. Yao, *Chem. Commun.*, 2008, 2532–2534.

107 K. Z. Shao, Y. H. Zhao, X. L. Wang, Y. Q. Lan, D. J. Wang, Z. M. Su and R. S. Wang, *Inorg. Chem.*, 2009, **48**, 10–12.

108 G. X. Liu, L. F. Huang, X. J. Kong, R. Y. Huang and H. Xu, *Inorganica Chim. Acta*, 2009, **362**, 1755–1760.

109 E.-C. Yang, H.-K. Zhao, B. Ding, X.-G. Wang and X.-J. Zhao, *Cryst. Growth Des.*, 2007, **7**, 2009–2015.

110 K. Zhu, H. Chen, S. Nishihara, G.-X. Liu and X.-M. Ren, *Inorganica Chim. Acta*, 2009, **362**, 4780–4784.

111 Y. Dong and G. Xing, *Zeitschrift für Anorg. und Allg. Chemie*, 2015, **641**, 1679–1683.

112 F. Luo, Y. Ning, M. B. Luo and G. L. Huang, *CrystEngComm*, 2010, **12**, 2769–2774.

113 R. Herchel, Z. Indelá, Z. Trávníek, R. Zboil and J. Vančo, *Dalton Trans.*, 2009, 9870–

9880.

114 S. Biswas, M. Tonigold, M. Speldrich, P. Kögerler, M. Weil and D. Volkmer, *Inorg. Chem.*, 2010, **49**, 7424–7434.

115 Y. Y. Liu, M. Grzywa, M. Tonigold, G. Sastre, T. Schüttrigkeit, N. S. Leeson and D. Volkmer, *Dalton Trans.*, 2011, **40**, 5926–5938.

116 S. Biswas, M. Tonigold, M. Speldrich, P. Kögerler and D. Volkmer, *Eur. J. Inorg. Chem.*, 2009, **2009**, 3094–3101.

117 S. Biswas, M. Tonigold, H. Kelm, H. J. Krüger and D. Volkmer, *Dalton Trans.*, 2010, **39**, 9851–9859.

118 A. Lanza, L. S. Germann, M. Fisch, N. Casati and P. Macchi, *J. Am. Chem. Soc.*, 2015, **137**, 13072–13078.

119 C. Qiao, L. Sun, S. Zhang, P. Liu, L. Chang, C. Zhou, Q. Wei, S. Chen and S. Gao, *J. Mater. Chem. C*, 2017, **5**, 1064–1073.

120 H. Y. Ren and X. M. Zhang, *Energy and Fuels*, 2016, **30**, 526–530.

121 J. Xiao, Y. Wu, M. Li, B. Y. Liu, X. C. Huang and D. Li, *Chem. - A Eur. J.*, 2013, **19**, 1891–1895.

122 C. Y. Li, C. J. Yu and B. T. Ko, *Organometallics*, 2013, **32**, 172–180.

123 C. Y. Li, J. K. Su, C. J. Yu, Y. E. Tai, C. H. Lin and B. T. Ko, *Inorg. Chem. Commun.*, 2012, **20**, 60–65.

124 C. H. Chang, H. J. Chuang, T. Y. Chen, C. Y. Li, C. H. Lin, T. Y. Lee, B. T. Ko and H. Y. Huang, *J. Polym. Sci. Part A Polym. Chem.*, 2016, **54**, 714–725.

125 C. Richardson and P. J. Steel, *Dalton Trans.*, 2003, 992–1000.

126 P. Børsting and P. J. Steel, *Eur. J. Inorg. Chem.*, 2004, **2004**, 376–380.

127 Y. Wang, M. C. Hu, Q. G. Zhai, S. N. Li, Y. C. Jiang and W. J. Ji, *Inorg. Chem. Commun.*, 2009, **12**, 281–285.

128 E. V. Lider, D. A. Piryazev, A. V. Virovets, L. G. Lavrenova, A. I. Smolentsev, E. M. Uskov, A. S. Potapov and A. I. Khlebnikov, *J. Struct. Chem.*, 2010, **51**, 514–518.

129 Q.-G. Zhai, X. Gao, S.-N. Li, Y.-C. Jiang and M.-C. Hu, *CrystEngComm*, 2011, **13**, 1602–1616.

130 E. V. Peresypkina, E. V. Lider, A. I. Smolentsev, J. Sanchiz, B. Gil-Hernández, A. S. Potapov, A. I. Khlebnikov, N. A. Kryuchkova and L. G. Lavrenova, *Polyhedron*,

2012, **48**, 253–263.

131 X. Zhou, X. Meng, W. Cheng, H. Hou, M. Tang and Y. Fan, *Inorganica Chim. Acta*, 2007, **360**, 3467–3474.

132 X. L. Tang, W. Dou, J. A. Zhou, G. L. Zhang, W. S. Liu, L. Z. Yang and Y. L. Shao, *CrystEngComm*, 2011, **13**, 2890–2898.

133 A. Sasmal, S. Shit, C. Rizzoli, H. Wang, C. Desplanches and S. Mitra, *Inorg. Chem.*, 2012, **51**, 10148–10157.

134 S. Saha, A. Sasmal, G. Pilet, A. Bauzá, A. Frontera and S. Mitra, *CrystEngComm*, 2014, **16**, 654–666.

135 G. E. Kostakis, P. Xydias, E. Nordlander and J. C. Plakatouras, *Inorganica Chim. Acta*, 2012, **383**, 327–331.

136 G. E. Kostakis, S. P. Perlepes, V. A. Blatov, D. M. Proserpio and A. K. Powell, *Coord. Chem. Rev.*, 2012, **256**, 1246–1278.

137 S. E. Allen, R. R. Walvoord, R. Padilla-Salinas and M. C. Kozlowski, *Chem. Rev.*, 2013, **113**, 6234–6458.

138 G. Fang and X. Bi, *Chem. Soc. Rev.*, 2015, **44**, 8124–8173.

139 X. Liu, P. Cen, H. Li, H. Ke, S. Zhang, Q. Wei, G. Xie, S. Chen and S. Gao, *Inorg. Chem.*, 2014, **53**, 8088–8097.

140 T. Ma, M. X. Li, Z. X. Wang, J. C. Zhang, M. Shao and X. He, *Cryst. Growth Des.*, 2014, **14**, 4155–4165.

141 B. Liu, L. Wei, N.-N. Li, W.-P. Wu, H. Miao, Y.-Y. Wang and Q.-Z. Shi, *Cryst. Growth Des.*, 2014, **14**, 1110–1127.

142 V. R. Thalladi, B. S. Goud, V. J. Hoy, F. H. Allen, J. A. K. Howard and G. R. Desiraju, *Chem. Commun.*, 1996, 401–402.

143 M. du Plessis and L. J. Barbour, *Dalton Trans.*, 2012, **41**, 3895–3898.

144 S. K. Ghosh and S. Kitagawa, *CrystEngComm*, 2008, **10**, 1739–1742.

145 H. Tian, R. Liu, X. Wang, P. Yang, Z. Li, L. Li and D. Liao, *Eur. J. Inorg. Chem.*, 2009, 4498–4502.

146 V. N. Dokorou, C. J. Milios, A. C. Tsipis, M. Haukka, P. G. Weidler, A. K. Powell and G. E. Kostakis, *Dalton Trans.*, 2012, **41**, 12501–12513.

147 R. Bikas, H. Hosseini-Monfared, V. Vasylyeva, J. Sanchiz, J. Alonso, J. M.

Barandiaran and C. Janiak, *Dalton Trans.*, 2014, **43**, 11925–11935.

148 S. K. Henninger, H. A. Habib and C. Janiak, *J. Am. Chem. Soc.*, 2009, **131**, 2776–7.

149 A. K. Chaudhari, B. Joarder, E. Rivière, G. Rogez and S. K. Ghosh, *Inorg. Chem.*, 2012, **51**, 9159–9161.

150 S. Mukherjee, B. Joarder, B. Manna, A. V Desai, A. K. Chaudhari and S. K. Ghosh, *Sci. Rep.*, 2014, **4**, 5761.

151 B. J. O'Keefe and P. J. Steel, *Inorg. Chem. Commun.*, 2000, **3**, 473–475.

152 M. Sun, W.-Z. Zhou, Y.-H. Wang, H.-Q. Tan, Y.-F. Qi, H.-Y. Zang and Y.-G. Li, *J. Coord. Chem.*, 2016, **69**, 1769–1779.

153 M. Kurmoo, *Chem. Soc. Rev.*, 2009, **38**, 1353–1379.

154 M. Murrie, *Chem. Soc. Rev.*, 2010, **39**, 1986–1995.

155 M. Idešicová, J. Titiš, J. Krzystek and R. Boča, *Inorg. Chem.*, 2013, **52**, 9409–9417.

156 H. Drulis, K. Dyrek, K. P. Hoffmann, S. K. Hoffmann and A. Weselucha-Birczynska, *Inorg. Chem.*, 1985, **24**, 4009–4012.

157 A. Bencini and D. Gatteschi, *Inorg. Chem.*, 1977, **16**, 2141–2142.

158 L. Banci, C. Benelli, D. Gatteschi and F. Mani, *Inorg.Chem.*, 1982, **21**, 1133–1136.

159 D. Gatteschi, C. A. Ghilardi, A. Orlandini and L. Sacconi, *Inorg. Chem.*, 1978, **17**, 3023–3026.

160 C. Benelli and D. Gateschi, *Inorg. Chem.*, 1982, **21**, 1788–1790.

161 C. Benelli, D. Gatteschi and G. Speroni, *Inorganica Chim. Acta*, 1984, **90**, 179–183.

162 A. Bencini, C. Benelli, D. Gatteschi and C. Zanchini, *Inorganica Chim. Acta*, 1980, **45**, L127–L128.

163 A. Bencini, C. Benelli and D. Gatteschi, *Inorg. Chem.*, 1978, **17**, 3313–3314.

164 A. W. Addison, T. N. Rao, J. Reedijk, J. van Rijn and G. C. Verschoor, *J. Chem. Soc. Dalt. Trans.*, 1984, 1349.

165 L. Raehm, L. Mimassi, C. Guyard-Duhayon, H. Amouri and M. N. Rager, *Inorg. Chem.*, 2003, **42**, 5654–5659.

166 R. Den Hartog, M. R. Harvey, J. J. A. Hummel, S. T. Van Der Pol, I. Mutikainen, G. A. Van Albada and E. Bouwman, *Inorganica Chim. Acta*, 2011, **376**, 664–670.

167 S. Y. Hao, Y. G. Liu, Z. C. Hao and G. H. Cui, *Zeitschrift fur Anorg. und Allg. Chemie*, 2016, **642**, 618–625.

168 X. X. Wang, Y. G. Liu, Y. H. Li and G. H. Cui, *Transit. Met. Chem.*, 2014, **39**, 461–467.

169 J. Li, L. Li, H. Hou, Y. Fan and L. Gao, *Inorganica Chim. Acta*, 2009, **362**, 4671–4677.

170 J. Li, L. Li, H. Hou and Y. Fan, *J. Organomet. Chem.*, 2009, **694**, 1359–1368.

171 J. Fan, G. T. Yee, G. Wang and B. E. Hanson, *Inorg. Chem.*, 2006, **45**, 599–608.

172 L. Dobrzańska, G. O. Lloyd, T. Jacobs, I. Rootman, C. L. Oliver, M. W. Bredenkamp and L. J. Barbour, *J. Mol. Struct.*, 2006, **796**, 107–113.

173 H. J. Lu, Y. T. Fan, J. Gao and Q. Wang, *Synth. React. Inorganic, Met. Nano-Metal Chem.*, 2005, **35**, 305–309.

174 J. Hu, Z. Zhao, D. Zhao, S. Chen, J. Zhao and H. Zhao, *Zeitschrift fur Anorg. und Allg. Chemie*, 2013, **639**, 821–825.

175 N. F. Chilton, R. P. Anderson, L. D. Turner, A. Soncini and K. S. Murray, *J. Comput. Chem.*, 2013, **34**, 1164–1175.

176 X. Zhu and S. Chiba, *Chem. Soc. Rev.*, 2016, **45**, 4504–4523.

177 S. D. McCann and S. S. Stahl, *Acc. Chem. Res.*, 2015, **48**, 1756–1766.

178 J.-P. Wan and Y. Liu, *RSC Adv.*, 2012, **2**, 9763.

179 D. M. Stout and A. I. Meyers, *Chem. Rev.*, 1982, **82**, 223–243.

180 C. O. Kappe, *Eur. J. Med. Chem.*, 2000, **35**, 1043–1052.

181 C. Safak and R. Simsek, *Mini-Reviews Med. Chem.*, 2006, **6**, 747–755.

182 P. Ioan, E. Carosati, M. Micucci, G. Cruciani, F. Broccatelli, B. S. Zhorov, A. Chiarini and R. Budriesi, *Curr. Med. Chem.*, 2011, **18**, 4901–4922.

183 G. Verma, A. Marella, M. Shaquiquzzaman, M. Akhtar, M. R. Ali and M. M. Alam, *J. Pharm. Bioallied Sci.*, 2014, **6**, 69–80.

184 A. Cukurovali and E. Yilmaz, *J. Mol. Struct.*, 2014, **1075**, 566–578.

185 A. R. Hantzsch, *Justus Liebigs Ann. Chem.*, 1882, **215**, 1–82.

186 S. Sueki, R. Takei, Y. Zaitsu, J. Abe, A. Fukuda, K. Seto, Y. Furukawa and I. Shimizu, *Eur. J. Org. Chem.*, 2014, **2014**, 5281–5301.

187 L. Liu, R. Sarkisian, Y. Deng and H. Wang, *J. Org. Chem.*, 2013, **78**, 5751–5755.

188 P. R. Girling, A. S. Batsanov, H. C. Shen and A. Whiting, *Chem. Commun.*, 2012, **48**, 4893–4895.

189 S. Sueki, R. Takei, J. Abe and I. Shimizu, *Tetrahedron Lett.*, 2011, **52**, 4473–4477.

190 W. Gati, M. M. Rammah, M. B. Rammah, F. Couty and G. Evano, *J. Am. Chem. Soc.*, 2012, **134**, 9078–9081.

191 O. Quinonero, M. Jean, N. Vanthuyne, C. Roussel, D. Bonne, T. Constantieux, C. Bressy, X. Bugaut and J. Rodriguez, *Angew. Chem. Int. Ed.*, 2016, **55**, 1401–1405.

192 D. Hu, Y. Liu and J.-P. Wan, *Tetrahedron*, 2015, **71**, 6094–6098.

193 H. Jiang, R. Mai, H. Cao, Q. Zhu and X. Liu, *Org. Biomol. Chem.*, 2009, **7**, 4943–4953.

194 J. Jiang, J. Yu, X.-X. Sun, Q.-Q. Rao and L.-Z. Gong, *Angew. Chem. Int. Ed.*, 2008, **47**, 2458–2462.

195 J. Safari and S. Gandomi-Ravandi, *RSC Adv.*, 2014, **4**, 46224–46249.

196 S. Rádl, *Aldrichimica Acta*, 1997, **30**, 97–100.

197 J. Verner and M. Potacek, *Molecules*, 2006, **11**, 34–42.

198 A. El-Alali and A. S. Al-Kamali, *Can. J. Chem.*, 2002, **80**, 1293–1301.

199 F. H. Allen, *Acta Crystallogr. B*, 2002, **58**, 380–388.

200 G. O. Jones, P. Liu, K. N. Houk and S. L. Buchwald, *J. Am. Chem. Soc.*, 2010, **132**, 6205–6213.

201 J. Eriksen and C. S. Foote, *J. Phys. Chem.*, 1978, **82**, 2659–2662.

202 N. Narayanaswamy and T. Govindaraju, *Sensors Actuators B Chem.*, 2012, **161**, 304–310.

203 *The redox potential of Cu^{II} to Cu^{I} is +0.15eV, and for ClO_4 to Cl is +0.65eV.*

204 F. Himo, T. Lovell, R. Hilgraf, V. V Rostovtsev, L. Noodleman, K. B. Sharpless and V. V Fokin, *J. Am. Chem. Soc.*, 2005, **127**, 210–216.

205 S. Battula, R. A. Vishwakarma and Q. N. Ahmed, *RSC Adv.*, 2014, **4**, 38375–38378.

206 X. Zhao, Y. Zhang and J. Wang, *Chem. Commun.*, 2012, **48**, 10162–10173.

207 T. Patra, S. Nandi, S. K. Sahoo and D. Maiti, *Chem. Commun.*, 2016, **52**, 1432–1435.

208 A. K. Verma, T. Kesharwani, J. Singh, V. Tandon and R. C. Larock, *Angew. Chemie - Int. Ed.*, 2009, **48**, 1138–1143.

209 C. Gryparis, C. Efe, C. Raptis, I. N. Lykakis and M. Stratakis, *Org. Lett.*, 2012, **14**, 2956–2959.

210 V. a. Peshkov, O. P. Pereshivko and E. V. Van der Eycken, *Chem. Soc. Rev.*, 2012,

41, 3790.

211 W. Fan, W. Yuan and S. Ma, *Nat. Commun.*, 2014, **5**, 3884.

212 S. Kaur, M. Kumar and V. Bhalla, *Chem. Commun.*, 2015, **51**, 16327–16330.

213 P. H. S. Paioti, K. A. Abboud and A. Aponick, *J. Am. Chem. Soc.*, 2016, **138**, 2150–2153.

214 D. De, T. K. Pal, S. Neogi, Senthilkumar, D. Das, S. Sen Gupta and P. K. Bharadwaj, *Chem. - A Eur. J.*, 2016, **22**, 3387–3396.

215 H. Zhao, W. He, L. Wei and M. Cai, *Catal. Sci. Technol.*, 2016, **6**, 1488–1495.

216 M. Varyani, P. K. Khatri and S. L. Jain, *Catal. Commun.*, 2016, **77**, 113–117.

217 H.-B. Chen, Y. Zhao and Y. Liao, *RSC Adv.*, 2015, **5**, 37737–37741.

218 T. Sugiishi, A. Kimura and H. Nakamura, *J. Am. Chem. Soc.*, 2010, **132**, 5332–5333.

219 D. P. Chauhan, S. J. Varma, A. Vijeta, P. Banerjee and P. Talukdar, *Chem Commun*, 2014, **50**, 323–325.

220 A. Arcadi, S. Cacchi, L. Cascia, G. Fabrizi and F. Marinelli, *Org. Lett.*, 2001, **3**, 2501–2504.

221 B. M. Nilsson and U. Hacksell, *J. Heterocycl. Chem.*, 1989, **26**, 269–275.

222 Y. Yamamoto, H. Hayashi, T. Saigoku and H. Nishiyama, *J. Am. Chem. Soc.*, 2005, **127**, 10804–10805.

223 D. F. Harvey and D. M. Sigano, *J. Org. Chem.*, 1996, **61**, 2268–2272.

224 J. J. Fleming and J. Du Bois, *J. Am. Chem. Soc.*, 2006, **128**, 3926–3927.

225 B. M. Trost, C. K. Chung and A. B. Pinkerton, *Angew. Chemie Int. Ed.*, 2004, **43**, 4327–4329.

226 X. Zhang and A. Corma, *Angew. Chemie - Int. Ed.*, 2008, **47**, 4358–4361.

227 B. Karimi, M. Gholinejad and M. Khorasani, *Chem. Commun.*, 2012, **48**, 8961–8963.

228 C. Wei and C.-J. Li, *J. Am. Chem. Soc.*, 2003, **125**, 9584–9585.

229 V. K.-Y. Lo, C.-Y. Zhou, M.-K. Wong and C.-M. Che, *Chem. Commun.*, 2010, **46**, 213–215.

230 C. Wei, Z. Li and C.-J. Li, *Org. Lett.*, 2003, **5**, 4473–4475.

231 Y. Zhao, X. Zhou, T.-A. Okamura, M. Chen, Y. Lu, W.-Y. Sun and J.-Q. Yu, *Dalton Trans.*, 2012, **41**, 5889–5896.

232 N. Salam, A. Sinha, A. S. Roy, P. Mondal, N. R. Jana and S. M. Islam, *RSC Adv.*,

2014, **4**, 10001–10012.

233 N. Sharma, U. K. Sharma, N. M. Mishra and E. V Van Der Eycken, *Adv. Synth. Catal.*, 2014, **356**, 1029–1037.

234 C. Zhao and D. Seidel, *J. Am. Chem. Soc.*, 2015, **137**, 4650–4653.

235 L. Shi, Y.-Q. Tu, M. Wang, F.-M. Zhang and C.-A. Fan, *Org. Lett.*, 2004, **6**, 1001–1003.

236 T. T. T. Trang, D. S. Ermolat'ev and E. V. Van der Eycken, *RSC Adv.*, 2015, **5**, 28921–28924.

237 Y. Zhang, P. Li, M. Wang and L. Wang, *J. Org. Chem.*, 2009, **74**, 4364–4367.

238 L. Rubio-Pérez, M. Iglesias, J. Munárriz, V. Polo, J. J. Pérez-Torrente and L. A. Oro, *Chem. - A Eur. J.*, 2015, **21**, 17701–17707.

239 B. M. Choudary, C. Sridhar, M. L. Kantam and B. Sreedhar, *Tetrahedron Lett.*, 2004, **45**, 7319–7321.

240 C. E. Meyet, C. J. Pierce and C. H. Larsen, *Org. Lett.*, 2012, **14**, 964–967.

241 C. J. Pierce and C. H. Larsen, *Green Chem.*, 2012, **14**, 2672–2676.

242 P. Li, Y. Zhang and L. Wang, *Chem. - A Eur. J.*, 2009, **15**, 2045–2049.

243 W.-W. Chen, R. V Nguyen and C.-J. Li, *Tetrahedron Lett.*, 2009, **50**, 2895–2898.

244 X. Huo, J. Liu, B. Wang, H. Zhang, Z. Yang, X. She and P. Xi, *J. Mater. Chem. A*, 2013, **1**, 651–656.

245 S. Samai, G. C. Nandi and Singh, *Tetrahedron Lett.*, 2010, **51**, 5555–5558.

246 E. Ramu, R. Varala, N. Sreelatha and S. R. Adapa, *Tetrahedron Lett.*, 2007, **48**, 7184–7190.

247 A. W. Addison, T. N. Rao, J. Reedijk, J. van Rijn and G. C. Verschoor, *J. Chem. Soc. Dalt. Trans.*, 1984, 1349.

248 *This process was found to interfere with the first process upon scanning in the anodic direction, possibly due to an electrochemically produced species*.

249 D. Prat, J. Hayler and A. Wells, *Green Chem.*, 2014, **16**, 4546–4551.

250 W. Zhang, N. Saraei, H. Nie, J. R. Vaughn, A. S. Jones, M. S. Mashuta, R. M. Buchanan and C. A. Grapperhaus, *Dalton Trans.*, 2016, **45**, 15791–15799.

251 R. Jain, T. J. Gibson, M. S. Mashuta, R. M. Buchanan and C. A. Grapperhaus, *Dalton Trans.*, 2016, **45**, 18356–18364.

252 R. Huisgen, *Angew. Chemie - Int. Ed*, 1963, **2**, 565–598.

253 R. Huisgen, *Angew. Chemie - Int. Ed*, 1963, **2**, 633–645.

254 C. W. Tornøe, C. Christensen and M. Meldal, *J. Org. Chem.*, 2002, **67**, 3057–3064.

255 V. V. Rostovtsev, L. G. Green, V. V. Fokin and K. B. Sharpless, *Angew. Chemie - Int. Ed.*, 2002, **41**, 2596–2599.

256 M. Meldal and C. W. Tornøe, *Chem. Rev.*, 2008, **108**, 2952–3015.

257 P. Thirumurugan, D. Matosiuk and K. Jozwiak, *Chem. Rev.*, 2013, **113**, 4905–4979.

258 R. L. Weller and S. R. Rajski, *Org. Lett.*, 2005, **7**, 2141–2144.

259 M. D. Best, *Biochemistry*, 2009, **48**, 6571–6584.

260 M. Yang, J. Li and P. R. Chen, *Chem. Soc. Rev.*, 2014, **43**, 6511–6526.

261 M. Yang, A. S. Jalloh, W. Wei, J. Zhao, P. Wu and P. R. Chen, *Nat. Commun.*, 2014, **5**, 4981.

262 W. Xi, T. F. Scott, C. J. Kloxin and C. N. Bowman, *Adv. Funct. Mater.*, 2014, **24**, 2572–2590.

263 J. E. Hein and V. V. Fokin, *Chem. Soc. Rev.*, 2010, **39**, 1302–1315.

264 E. Haldón, M. C. Nicasio, P. J. Pérez, P. J. Pérez, M. A. Pericàs, F. Maseras, M. C. Nicasio, P. J. Pérez, Y. Ji, J.-M. Vincent, H.-J. Youn, D. Y. Chi and N. H. Hur, *Org. Biomol. Chem.*, 2015, **13**, 9528–9550.

265 L. Jin, D. R. Tolentino, M. Melaimi and G. Bertrand, *Sci. Adv.*, 2015, **1**, 1–5.

266 A. Pathigoolla, R. P. Pola and K. M. Sureshan, *Appl. Catal. A Gen.*, 2013, **453**, 151–158.

267 A. N. Semakin, D. P. Agababyan, S. Kim, S. Lee, A. Y. Sukhorukov, K. G. Fedina, J. Oh and S. L. Ioffe, *Tetrahedron Lett.*, 2015, **56**, 6335–6339.

268 K. Tanaka, C. Kageyama and K. Fukase, *Tetrahedron Lett.*, 2007, **48**, 6475–6479.

269 T. R. Chan, R. Hilgraf, K. B. Sharpless and V. V. Fokin, *Org. Lett.*, 2004, **6**, 2853–2855.

270 V. O. Rodionov, S. I. Presolski, S. Gardinier, Y. H. Lim and M. G. Finn, *J. Am. Chem. Soc.*, 2007, **129**, 12696–12704.

271 V. O. Rodionov, S. I. Presolski, D. D. Díaz, V. V. Fokin and M. G. Finn, *J. Am. Chem. Soc.*, 2007, **129**, 12705–12712.

272 G. C. Kuang, H. A. Michaels, J. T. Simmons, R. J. Clark and L. Zhu, *J. Org. Chem.*,

2010, **75**, 6540–6548.

273 A. R. Katritzky, X. Lan, J. Z. Yang and O. V. Denisko, *Chem. Rev.*, 1998, **98**, 409–548.

274 A. R. Katritzky, K. Yannakopoulou, E. Anders, J. Stevens and M. Szafran, *J. Org. Chem.*, 1990, **55**, 5683–5687.

275 A. R. Katritzky, S. Perumal and W.-Q. Fan, *J. Chem. Soc. Perkin Trans. 2*, 1990, 2059–2062.

276 A. R. Katritzky, K. Yannakopoulou, W. Kuzmierkiewicz, J. M. Aurrecoechea, G. J. Palenik, A. E. Koziol and M. Szczesniak, *J. Chem. Soc. Perkin Trans. I*, 1987, 2673–2679.

277 A. R. Katritzky, S. Rachwal, B. Rachwal and J. W. Frankenfeld, *Int. J. Chem. Kinet.*, 1995, **27**, 351–357.

278 J. R. L. Smith and J. S. Sadd, *J. Chem. Soc. Perkin Trans. 1*, 1975, 1181–1184.

279 G. E. Kostakis, P. Xydias, E. Nordlander and J. C. Plakatouras, *Inorg. Chim. Acta*, 2012, **383**, 327–331.

280 R. M. Krishna and S. K. Gupta, *Bull. Magn. Reson.*, 1994, **16**, 239–291.

281 C. Jubert, A. Mohamadou, J. Marrot and J.-P. Barbier, *J. Chem. Soc. Dalt. Trans.*, 2001, 1230–1238.

282 Z. G. Lada, Y. Sanakis, C. P. Raptopoulou, V. Psycharis, S. P. Perlepes and G. Mitrikas, *Dalton Trans.*, 2017, **46**, 8458–8475.

283 M. Massacesi, G. Ponticelli and V. G. Krishnan, *J. Mol. Struct.*, 1980, **69**, 165–181.

284 G. Tabbì, A. Giuffrida and R. P. Bonomo, *J. Inorg. Biochem.*, 2013, **128**, 137–145.

285 Y. C. Wang, Y. Y. Xie, H. E. Qu, H. S. Wang, Y. M. Pan and F. P. Huang, *J. Org. Chem.*, 2014, **79**, 4463–4469.

286 W. Zhu and D. Ma, *Chem. Commun.*, 2004, 888.

287 A. R. Hajipour and F. Mohammadsaleh, *Tetrahedron Lett.*, 2014, **55**, 6799–6802.

288 C. Z. Tao, X. Cui, J. Li, A. X. Liu, L. Liu and Q. X. Guo, *Tetrahedron Lett.*, 2007, **48**, 3525–3529.

289 X. Meng, X. Xu, T. Gao and B. Chen, *European J. Org. Chem.*, 2010, **2010**, 5409–5414.

290 M. Morozova, M. S. Yusubov, B. Kratochvil, V. Eigner, A. Bondarev, A. Yoshimura,

A. Saito, V. V. Zhdankin, M. E. Trusova and P. S. Postnikov, *Org. Chem. Front.*, 2017, **4**, 1–77.

291 J. E. Leffler and R. D. Temple, *J. Am. Chem. Soc.*, 1967, **89**, 5235–5246.

292 B. T. Worrell, J. A. Malik and V. V Fokin, *Science.*, 2013, **340**, 457–460.

293 F. A. Cotton and G. Wilkinson, *Advanced Inorganic Chemistry*, Wiley, 5th edn., 1988.

294 J.-L. Du, T.-L. Hu, S.-M. Zhang, Y.-F. Zeng and X.-H. Bu, *CrystEngComm*, 2008, **10**, 1866.

295 Y. N. Chi, K. L. Huang, F. Y. Cui, Y. Q. Xu and C. W. Hu, *Inorg. Chem.*, 2006, **45**, 10605–10612.

296 R. Tatikonda, E. Bulatov, E. Kalenius and M. Haukka, *Cryst. Growth Des.*, 2017, **17**, 5918–5926.

297 I. Bassanetti, C. Atzeri, D. A. Tinonin and L. Marchiò, *Cryst. Growth Des.*, 2016, **16**, 3543–3552.

298 D. Davarci, R. Gür, S. Beşli, E. Şenkuytu and Y. Zorlu, *Acta Crystallogr. B* , 2016, **72**, 344–356.

299 C. W. Yeh, C. H. Tsou, H. A. Tsai, H. T. Lee, W. H. Yao and M. C. Suen, *Inorganica Chim. Acta*, 2015, **427**, 1–12.

300 G. Lamming, J. Kolokotroni, T. Harrison, T. J. Penfold, W. Clegg, P. G. Waddell, M. R. Probert and A. Houlton, *Cryst. Growth Des.*, 2017, **17**, 5753–5763.

301 C. Janiak, T. G. Scharmann, P. Albrecht, F. Marlow and R. Macdonald, *J. Am. Chem. Soc.*, 1996, **118**, 6307–6308.

302 H.-P. Wu, C. Janiak, G. Rheinwald and H. Lang, *J. Chem. Soc. Dalt. Trans.*, 1999, 183–190.

303 M. Munakata and L. P. Wu, *Adv. Inorg. Chem.*, 1999, **46**, 173–303.

304 A. N. Khlobystov, A. J. Blake, N. R. Champness, D. A. Lemenovskii, A. G. Majouga, N. V. Zyk and M. Schröder, *Coord. Chem. Rev.*, 2001, **222**, 155–192.

305 Y.-L. Wang, Q.-Y. Liu and L. Xu, *CrystEngComm*, 2008, **10**, 1667.

306 L. Y. Du, W. J. Shi, L. Hou, Y. Y. Wang, Q. Z. Shi and Z. Zhu, *Inorg. Chem.*, 2013, **52**, 14018–14027.

307 S. Roy, H. M. Titi, B. K. Tripuramallu, N. Bhunia, R. Verma and I. Goldberg, *Cryst. Growth Des.*, 2016, **16**, 2814–2825.

308 K. S. Min and M. P. Suh, *J. Am. Chem. Soc.*, 2000, **122**, 6834–6840.

309 C. P. Li, H. Zhou, Y. H. Mu, W. Guo, Y. Yan and M. Du, *Cryst. Growth Des.*, 2017, **17**, 2024–2033.

310 M. I. Azócar, G. Gómez, P. Levín, M. Paez, H. Muñoz and N. Dinamarca, *J. Coord. Chem.*, 2014, **67**, 3840–3853.

311 J. M. S. Cardoso, A. M. Galvão, S. I. Guerreiro, J. H. Leitão, A. C. Suarez and M. F. N. N. Carvalho, *Dalton Trans.*, 2016, **45**, 7114–7123.

312 A. Tăbăcaru, C. Pettinari, F. Marchetti, C. Di Nicola, K. V. Domasevitch, S. Galli, N. Masciocchi, S. Scuri, I. Grappasonni and M. Cocchioni, *Inorg. Chem.*, 2012, **51**, 9775–9788.

313 J. Jimenez, I. Chakraborty, M. Rojas-Andrade and P. K. Mascharak, *J. Inorg. Biochem.*, 2017, **168**, 13–17.

314 J. Jimenez, I. Chakraborty, A. M. Del Cid and P. K. Mascharak, *Inorg. Chem.*, 2017, **56**, 4784–4787.

315 S. W. Jaros, M. F. C. Guedes Da Silva, J. Król, M. Conceição Oliveira, P. Smoleński, A. J. L. Pombeiro and A. M. Kirillov, *Inorg. Chem.*, 2016, **55**, 1486–1496.

316 S. W. Jaros, M. F. C. Guedes Da Silva, M. Florek, M. C. Oliveira, P. Smoleński, A. J. L. Pombeiro and A. M. Kirillov, *Cryst. Growth Des.*, 2014, **14**, 5408–5417.

317 X. Y. Wu, H. X. Qi, J. J. Ning, J. F. Wang, Z. G. Ren and J. P. Lang, *Appl. Catal. B Environ.*, 2015, **168**–**169**, 98–104.

318 Z. Zhou, C. He, L. Yang, Y. Wang, T. Liu and C. Duan, *ACS Catal.*, 2017, **7**, 2248–2256.

319 S. Kulovi, S. Dalbera, S. Das, E. Zangrando, H. Puschmann and S. Dalai, *ChemistrySelect*, 2017, **2**, 9029–9036.

320 K. N. Sharma, A. K. Sharma, H. Joshi and A. K. Singh, *ChemistrySelect*, 2016, **1**, 3573–3579.

321 M.-M. Chen, H.-X. Li and J.-P. Lang, *Eur. J. Inorg. Chem.*, 2016, **2016**, 2508–2515.

322 C. L. Ming, Y. H. Li, G. Y. Li and G. H. Cui, *Transit. Met. Chem.*, 2014, **39**, 477–485.

323 G. Abbiati and E. Rossi, *Beilstein J. Org. Chem.*, 2014, **10**, 481–513.

324 U. Halbes-Letinois, J.-M. Weibel and P. Pale, *Chem. Soc. Rev.*, 2007, **36**, 759–769.

325 O. Prakash, H. Joshi, U. Kumar, A. K. Sharma and A. K. Singh, *Dalton Trans.*, 2015,

44, 1962–1968.

326 J. J. Chen, Z. L. Gan, Q. Huang and X. Y. Yi, *Inorganica Chim. Acta*, 2017, **466**, 93–99.

327 M. Trivedi, G. Singh, A. Kumar and N. P. Rath, *Inorganica Chim. Acta*, 2015, **438**, 255–263.

328 M. Trose, M. Dell'Acqua, T. Pedrazzini, V. Pirovano, E. Gallo, E. Rossi, A. Caselli and G. Abbiati, *J. Org. Chem.*, 2014, **79**, 7311–7320.

329 Y. Zhao, K. Chen, J. Fan, T. Okamura, Y. Lu, L. Luo and W.-Y. Sun, *Dalton Trans.*, 2014, **43**, 2252–2258.

330 M. Hassam and W. S. Li, *Tetrahedron*, 2015, **71**, 2719–2723.

331 J. Park, J. Yeon, P. H. Lee and K. Lee, *Tetrahedron Lett.*, 2013, **54**, 4414–4417.

332 P. Mainkar, V. Chippala, R. Chegondi and S. Chandrasekhar, *Synlett*, 2016, **27**, 1969–1972.

333 F. Li, N. Wang, L. Lu and G. Zhu, *J. Org. Chem.*, 2015, **80**, 3538–3546.

334 A. Almássy, C. E. Nagy, A. C. Bényei and F. Joó, *Organometallics*, 2010, **29**, 2484–2490.

335 G. Velegraki and M. Stratakis, *J. Org. Chem.*, 2013, **78**, 8880–8884.

336 N. Marion, R. S. Ramón and S. P. Nolan, *J. Am. Chem. Soc.*, 2009, **131**, 448–449.

337 M. B. T. Thuong, A. Mann and A. Wagner, *Chem. Commun.*, 2012, **48**, 434–436.

338 Z. W. Chen, D. N. Ye, Y. P. Qian, M. Ye and L. X. Liu, *Tetrahedron*, 2013, **69**, 6116–6120.

339 R. Das and D. Chakraborty, *Appl. Organomet. Chem.*, 2012, **26**, 722–726.

340 K. T. Venkateswara Rao, P. S. Sai Prasad and N. Lingaiah, *Green Chem.*, 2012, **14**, 1507–1514.

341 C. Janiak, *J. Chem. Soc. Trans.*, 2000, 3885–3896.

342 A. B. Caballero, J. K. Maclaren, A. Rodríguez-Diéguez, I. Vidal, J. A. Dobado, J. M. Salas and C. Janiak, *Dalton Trans.*, 2011, **40**, 11845–11855.

343 J. Elguero, A. R. Katritzky and O. V. Denisko, *Adv. Heterocycl. Chem.*, 2000, **76**, 1–84.

344 V. I. Minkin, A. D. Garnovskii, J. Elguero, A. R. Katritzky and O. V. Denisko, *Adv. Heterocycl. Chem.*, 2000, **76**, 157–323.

345 D. S. Wofford, D. M. Forkey and J. G. Russell, *J. Org. Chem.*, 1982, **47**, 5132–5137.

346 L. I. Larina and V. Milata, *Magn. Reson. Chem.*, 2009, **47**, 142–148.

347 W. Schilf, L. Stefaniak, M. Witanowski and G. A. Webb, *Magn. Reson. Chem.*, 1985, **23**, 181–184.

348 A. R. Katritzky, X. Lan and W.-Q. Fan, *Synthesis (Stuttg).*, 1994, **1994**, 445–456.

349 A. R. Katritzky and B. V. Rogovoy, *Chem. - A Eur. J.*, 2003, **9**, 4586–4593.

350 H. E. Toma, E. Giesbrecht and R. L. Espinoza Rojas, *Can. J. Chem.*, 1983, **61**, 2520–2525.

351 H. E. Toma, E. Giesbrecht and R. L. E. Rojas, *J. Chem. Soc. Dalt. Trans.*, 1985, **3**, 2469–2472.

352 R. C. Rocha, K. Araki, H. E. Toma, I. De Quõâmica, U. D. S. Paulo, C. Postal and S. Paulo, *Transit. Met. Chem.*, 1998, **16**, 13–16.

353 R. C. Rocha and H. E. Toma, *Transit. Met. Chem.*, 2003, **28**, 43–50.

354 F. Tomás, J. L. M. Abboud, J. Laynez, R. Notario, L. Santos, S. O. Nilsson, J. Catalán, R. M. Claramunt and J. Elguero, *J. Am. Chem. Soc.*, 1989, **111**, 7348–7353.

355 W. (Wim) Dehaen and V. A. Bakulev, *Chemistry of 1,2,3-triazoles*, Springer International Publishing, 2015.

356 A. R. Katritzky, S. Rachwal, B. Rachwal and P. J. Steel, *J. Org. Chem.*, 1992, **57**, 4932–4939.

357 A. R. Katritzky, W. Kuzmierkiewic and S. Perumal, *Helv. Chim. Acta*, 1991, **74**, 1936–1940.

358 M.-T. Chen, B. Landers and O. Navarro, *Org. Biomol. Chem.*, 2012, **10**, 2206.

359 M. Gatto, P. Belanzoni, L. Belpassi, L. Biasiolo, A. Del Zotto, F. Tarantelli and D. Zuccaccia, *ACS Catal.*, 2016, **6**, 7363–7376.

360 I. M. Kolthoff and W. J. Tomsicek, *J. Phys. Chem.*, 1934, **39**, 945–954.

361 S. Stoll and A. Schweiger, *J. Magn. Reson.*, 2006, **178**, 42–55.

362 S. J. Coles and P. A. Gale, *Chem. Sci.*, 2012, **3**, 683–689.

363 O. V Dolomanov, A. J. Blake, N. R. Champness and M. Schröder, *J. Appl. Crystallogr.*, 2003, **36**, 1283–1284.

364 G. M. Sheldrick, *Acta Crystallogr. A* , 2015, **71**, 3–8.

365 G. M. Sheldrick, *Acta Crystallogr. Sect. A*, 2008, **64**, 112–122.

366 L. J. Farrugia, *J. Appl. Crystallogr.*, 1999, **32**, 837–838.

367 A. L. Spek, *J. Appl. Crystallogr.*, 2003, **36**, 7–13.

368 C. F. Macrae, P. R. Edgington, P. McCabe, E. Pidcock, G. P. Shields, R. Taylor, M. Towler and J. Van De Streek, *J. Appl. Crystallogr.*, 2006, **39**, 453–457.

369 P. Rajakumar and V. Murali, *Tetrahedron*, 2000, **56**, 7995–7999.

370 M. A. Macías, N. Nuñez-Dallos, J. Hurtado and L. Suescun, *Acta Crystallogr. E* , 2016, **72**, 815–818.

371 Z. Shi and R. P. Thummel, *J. Org. Chem.*, 1995, **60**, 5935–5945.

372 B. F. Hoskins, R. Robson and D. A. Slizys, *J. Am. Chem. Soc.*, 1997, **119**, 2952–2953.

373 A. W. Gann, J. W. Amoroso, V. J. Einck, W. P. Rice, J. J. Chambers and N. A. Schnarr, *Org. Lett.*, 2014, **16**, 2003–2005.

374 A. Fodor, A. Kiss, N. Debreczeni, Z. Hell and I. Gresits, *Org. Biomol. Chem.*, 2010, **8**, 4575–4581.

375 A. Taher, D. Nandi, R. U. Islam, M. Choudhary and K. Mallick, *RSC Adv.*, 2015, **5**, 47275–47283.

376 Y. Wang, J. Liu and C. Xia, *Adv. Synth. Catal.*, 2011, **353**, 1534–1542.

377 J. Shah, S. Khan, H. Blumenthal and J. Liebscher, *Synthesis (Stuttg).*, 2009, **2009**, 3975–3982.

378 K. Chanda, S. Rej and M. H. Huang, *Chem. - A Eur. J.*, 2013, **19**, 16036–16043.

379 S. Kaur, V. Bhalla and M. Kumar, *Chem. Commun.*, 2015, **51**, 526–529.

380 H. Hagiwara and S. Okada, *Chem. Commun.*, 2016, **52**, 815–818.

381 Y. Jiang, X. He, W. Zhang, X. Li, N. Guo, Y. Zhao, G. Xu and W. Li, *RSC Adv.*, 2015, **5**, 73340–73345.